

Laser-driven ion acceleration from ultrathin solid targets



VNiVERSiDAD
DSALAMANCA

CAMPUS DE EXCELENCIA INTERNACIONAL

Luca Christopher Stockhausen

FACULTAD DE CIENCIAS

Departamento de Física Aplicada. Área de Óptica.

Universidad de Salamanca

A Thesis submitted for the degree of Doctor in Physics

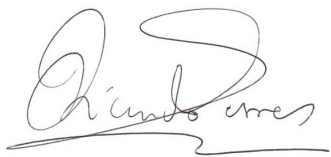
October 2015

RICARDO TORRES LA PORTE, Físico en el QUASAR group del Cockcroft Institute en la University of Liverpool, y

ENRIQUE CONEJERO JARQUE, Profesor Titular del Área de Óptica del Departamento de Física Aplicada de la Universidad de Salamanca,

CERTIFICAN:

Que la presente Memoria, "Laser-driven ion acceleration from ultrathin solid targets" ha sido realizada bajo su dirección en el Área de Óptica del Departamento de Física Aplicada de la Universidad de Salamanca por Don LUCA CHRISTOPHER STOCKHAUSEN y constituye su Tesis Doctoral para optar al grado de Doctor en Física por la Universidad de Salamanca.

A handwritten signature in black ink, appearing to read 'Ricardo Torres La Porte', with a horizontal line underneath.

Ricardo Torres La Porte

Enrique Conejero Jarque

Salamanca, 30 de octubre de 2015.

Abstract

The interaction of high-power (terawatt to petawatt) laser pulses with matter creates a plasma in extreme conditions, capable of sustaining huge electric fields (\sim TV/m). These electric fields may be employed to accelerate charged particles (electrons, protons, ions) to high energies ($>$ GeV for electrons, tens to hundreds of MeV/u for protons and ions). In general these ultra-intense ($>$ 10^{19} Wcm $^{-2}$) laser pulses interact with a target, which could be gaseous, liquid (electron acceleration) or solid (proton and ion acceleration). The presented thesis investigates experimentally and numerically the acceleration of protons and ions from ultrathin solid targets. Laser-driven ion acceleration has become a vivid field of research in the past two decades. In the well-understood Target Normal Sheath Acceleration (TNSA) scheme, ions are accelerated through a large charge-separation field at the rear side of the overdense plasma. These TNSA-generated ion beams compare favourably with conventional acceleration techniques in terms of emittance, brightness and pulse duration. Yet there are many obstacles such as higher cut-off energies and flux rates that have to be overcome to make those laser-driven particle beams useful for applications such as fast ignition or hadron therapy. Beside the TNSA scheme, other promising ion acceleration regimes have emerged. Radiation Pressure Acceleration (RPA), based on the momentum transfer from photons to electrons, offers a much better scaling and produces tens of MeV ions. Other schemes at the onset of relativistically induced transparency like the Breakout Afterburner (BOA), where the interaction changes from surface-dominated to volumetric, have also emerged. While typical TNSA acceleration occurs in micrometre-thick solid targets, both RPA and BOA dominate for ultrathin overdense targets in the range of nanometres.

In the presented thesis, laser-driven ion acceleration from ultrathin targets is explored. Experimental and numerical results from the interaction of single and double laser pulse set-ups with ultrathin targets are presented. The acceleration of ions in the RPA regime with single pulse interaction is investigated, as well as the charged particle dynamics in the relativistic transparency regime. Ion acceleration in a pre-expanded plasma with two linearly polarised pulses and a novel scheme of collisionless shock acceleration with double laser pulses of mixed polarisation is demonstrated. In the latter case a first linearly polarised pulse expands the nanometre overdense plasma, and the second circularly polarised pulse drives a strong collisionless shock into the plasma. This results in an efficient heavy ion acceleration up to 100 MeV/u with relatively moderate laser intensities ($\sim 10^{20}$ - 10^{21} Wcm $^{-2}$). This scheme has been explored in the picosecond and femtosecond regime and is shown to be highly sensitive to the target and laser parameters. Finally, a parameter study for the VEGA Petawatt laser system of the Pulsed Laser Center (CLPU) in Salamanca is presented. The VEGA laser of the CLPU will produce 30 J/30 fs laser pulses with an ultrahigh contrast and a peak power of 1 Petawatt. The obtained results on single and double pulse plasma interaction are used to explore the capability of the VEGA laser systems to efficiently produce multi-MeV ion beams.

To my parents

Acknowledgements

Firstly, I would like to thank my supervisor Ricardo Torres for all his support and encouragement he has provided throughout my PhD, his guidance and for patiently reading through my thesis. Also special thanks go to Enrique Conejero Jarque for supervising and tutoring my project at the University of Salamanca and his great assistance and help during the past years.

I am greatly indebted to Paul McKenna of the University of Strathclyde for giving me the opportunity to work with him and his group and carry out research in the exciting field of laser-driven ion acceleration. It has been a genuine pleasure to work with them during the experimental campaigns at the Central Laser Facility as well as during my visits in Glasgow. So many people have contributed to these experiments, but I would like to thank especially Ross Gray, Haydn Powell, David MacLellan, Martin King, Harry Padda, Bruno Gonzalez Izquierdo, David Carroll, Robbie Wilson and Dean Rusby, with whom I have worked most closely in the lab and in Glasgow.

I also owe gratitude to Luis O. Silva of the Instituto Superior Técnico and his group for giving me access to the OSIRIS code, allowing me to use their computational resources and hosting me in Lisbon. Thanks goes also to Nitin Shukla, Thomas Grismayer, Marija Vranic, Ujjwal Sinha, Bandhu Pathak, Jorge Vieira, Joana Martins, Elisabetta Boella and Paulo Ratinho for the great times in Lisbon.

I am very grateful to Carsten Welsch of the University of Liverpool for the initiation and coordination of the LA3NET project, which has provided an exceptional environment for the realisation of my PhD, facilitating my research stays and contributions to conferences and workshops. I would like to extend the thanks to my co-fellows of LA3NET for all these fantastic

times we had together during our events across the globe. Thanks goes to Rob Ashworth and Magdalena Klimontowska for managing the project and giving assistance whenever needed as well as the rest of the organising team in Liverpool; Samina Faisal, Blaise Guenard and Alexandra Welsch.

Thanks go to the CLPU for enabling the project and hosting me during the past years. Thanks to Andreas Döpp and Alexis Chacón for the good times in our office at the CLPU, discussions and cafe-y-pincho breaks at Oscar's. Also many thanks to Cristina Marcos for her help when I was settling in Salamanca and to the Optics group of the University of Salamanca.

I also acknowledge LaserLab Europe for funding one of my experimental stays at the Central Laser Facility with their staff-exchange scholarship.

My special thanks go to Lisanne, who has patiently supported me during my PhD, also during weeks-long research stays and regular country-hopping for conferences and workshops. I am also very thankful to my friends, near and far, for being there for me, giving support and for all these great and unforgettable times we have shared.

Finally, my deepest gratitude goes to my family, especially my parents Ingeborg and Wolfgang, who have always given me their full support and provided me with endless encouragement throughout my entire life.

I dedicate this thesis to them.

Contents

List of Figures	ix
List of Tables	xiii
1 Introduction	1
1.1 Background	1
1.2 Motivation	3
1.2.1 Hadron therapy	3
1.2.2 Inertial confinement fusion fast ignition	6
1.2.3 Proton radiography	9
1.2.4 Production of radioisotopes for positron emission tomography . .	10
1.3 Thesis structure	12
2 Relativistic laser-matter interaction	13
2.1 Strong field ionisation processes	13
2.2 Motion of a single electron in a laser field	16
2.2.1 Ponderomotive force	20
2.3 Laser propagation in a plasma	21
2.4 Laser absorption in a plasma	24
2.4.1 Resonance absorption	25
2.4.2 Vacuum Heating - Brunel mechanism	25
2.4.3 Relativistic $j \times B$ heating	26
2.5 Relativistically Induced Transparency	26
2.6 Plasma instabilities	29
2.7 Laser-driven ion acceleration	30
2.7.1 Target Normal Sheath Acceleration	31

CONTENTS

2.7.2	Radiation Pressure Acceleration	33
2.7.3	Breakout Afterburner	40
3	Methods	45
3.1	Experimental methods	45
3.1.1	Laser systems	47
3.1.2	Pulse contrast	52
3.1.3	Targets	54
3.1.4	Diagnostics	55
3.2	Numerical methods	67
3.2.1	Simulation method	68
3.2.2	Simulation details	71
3.2.3	Normalisation	73
3.2.4	Simulation remarks	74
4	Single pulse interaction with thin solid targets	77
4.1	Radiation pressure dominated acceleration	78
4.1.1	Simulations with different intensities	81
4.1.2	Simulations with different thicknesses	84
4.1.3	Simulations with different polarisations	88
4.1.4	Simulations with multi-layered targets	93
4.1.5	Summary	95
4.2	Instabilities	96
4.2.1	Experimental set-up	96
4.2.2	Experimental results	100
4.2.3	Simulations	102
4.3	Electron dynamics during relativistic transparency	105
4.3.1	Experimental set-up	111
4.3.2	Experimental results	112
4.3.3	Simulations of the onset of RIT	113
4.3.4	Modelling axial asymmetry in the plasma response to RIT	117
4.3.5	Summary	118

5	Double pulse interaction with thin solid targets	121
5.1	Ion acceleration in a pre-expanded plasma	122
5.1.1	Experimental set-up	122
5.1.2	Experimental results	127
5.1.3	Simulations	128
5.1.4	Energy transfer to ions	132
5.1.5	Sensitivity to the rising edge intensity profile	133
5.1.6	Summary	135
5.2	Ion acceleration with double laser pulses of mixed polarisation	137
5.2.1	Simulations	137
5.2.2	Acceleration in the picosecond regime	138
5.2.3	Acceleration in the femtosecond regime	145
5.2.4	Summary	151
6	Ion acceleration with the VEGA laser	153
6.1	Introduction	153
6.2	Estimations of ion acceleration in VEGA	155
6.2.1	Target Normal Sheath Acceleration	155
6.2.2	Light-Sailing RPA	159
6.2.3	Hole-Boring RPA	160
6.2.4	Experimental data under conditions achievable in VEGA	161
6.3	Requirements for ion acceleration with VEGA	163
6.3.1	Laser pulse parameters	163
6.3.2	Pulse contrast	163
6.3.3	Targets	164
6.3.4	Plasma and particle beam diagnostics	166
6.4	Summary	167
7	Conclusion and outlook	169
7.1	Conclusion	169
7.2	Outlook	171
Bibliography		177

CONTENTS

List of Figures

1.1	Bragg Peak	5
1.2	Heidelberg Ion Therapy Center	5
1.3	ICF direct and indirect drive	8
1.4	Ion fast ignition	8
1.5	Proton radiography	10
2.1	Multiphoton and tunnelling ionisation	15
2.2	Electron trajectories	20
2.3	Relativistically Induced Transparency	27
2.4	Diagnostic RIT	28
2.5	Measurement RIT	28
2.6	Target Normal Sheath Acceleration	32
2.7	Radiation Pressure Acceleration	34
2.8	Hole-Boring	35
2.9	Light-Sailing	38
2.10	Breakout Afterburner	42
3.1	Chirped Pulse Amplification	46
3.2	Vulcan target chamber	48
3.3	Astra Gemini target chamber	49
3.4	VEGA Petawatt	50
3.5	Temporal structure of an intense ultra-short laser pulse	52
3.6	Plasma mirror	54
3.7	Thomson Parabola spectrometer	56
3.8	Thomson Parabola set-up and detection on MCP	57

LIST OF FIGURES

3.9	FujiFilm FLA-5000 scanner and white light source	60
3.10	Microchannel plate detector	62
3.11	Gafchromic HD-V2 film	64
3.12	Ion beam detection with RCF	64
3.13	SRIM calculations	65
3.14	Particle-In-Cell loop	69
4.1	Bunch compression	82
4.2	Intensity scan	83
4.3	Thickness scan	85
4.4	Acceleration comparison	87
4.5	Polarisation comparison	89
4.6	Energy spectra - linear and circular	90
4.7	Overview of simulation run with circular polarisation	91
4.8	Overview of simulation run with linear polarisation	92
4.9	Multi-species simulation run	94
4.10	Experimental set-up Vulcan	97
4.11	Target pre-alignment	98
4.12	RCF stack front	98
4.13	Separation of sheath-driven and laser-driven ion populations	99
4.14	Rayleigh-Taylor instability	101
4.15	Bubble size comparison	101
4.16	High-resolution simulation run for instability study	103
4.17	3D visualisation of high-resolution run	104
4.18	Electron and proton spatial-intensity distributions	106
4.19	Target electron density evolution	107
4.20	Laser pulse transmission and peak electron density	108
4.21	Electron spatial profiles	110
4.22	Electron beam density and Poynting flux	115
4.23	Temporal evolution of electric field and electron density	117
5.1	Laser contrast	123
5.2	Experimental set-up	124
5.3	Proton spatial-intensity profiles	125

LIST OF FIGURES

5.4	Energy spectra	128
5.5	2D simulation results	130
5.6	3D simulation results	130
5.7	2D simulation results	132
5.8	Numerical and experimental energy comparison	134
5.9	Overview linear-linear simulation - picosecond regime	139
5.10	Overview linear-circular simulation - picosecond regime	141
5.11	Al energy spectra - intensity scan	142
5.12	Overview circular-circular simulation - picosecond regime	144
5.13	Double pulse comparison - picosecond regime	145
5.14	Overview linear-circular simulation with 40 nm target - femtosecond regime	148
5.15	Overview linear-circular simulation with 100 nm target - femtosecond regime	149
5.16	Overview linear-circular simulation with 20 nm target - femtosecond regime	150
5.17	Charge density evolution in femtosecond and picosecond regime	151

LIST OF FIGURES

List of Tables

2.1	Critical densities	23
3.1	VEGA laser parameters	51
3.2	Experimental RCF stack design	66
6.1	VEGA laser parameters	155
6.2	Estimations of TNSA acceleration with VEGA	158
6.3	Estimations of RPA light-sailing acceleration with VEGA	159
6.4	Estimations of RPA hole-boring acceleration with VEGA	160
6.5	Experimental results with VEGA 1 parameters	161
6.6	Experimental results with VEGA 2 parameters	162
6.7	Experimental results with VEGA 3 parameters	162

LIST OF TABLES

1

Introduction

1.1 Background

The history of the Light Amplification by Stimulated Emission of Radiation (LASER) started when Albert Einstein first explained the theory of stimulated emission in 1917 (1). After the development of the Microwave Amplification by Stimulated Emission of Radiation (MASER) by Townes in 1953 (2), the first laser was created by Theodore Maiman in 1960 (3), who used a solid-state flashlamp-pumped synthetic ruby laser in his original experiment. Since then the peak powers and intensities have been continuously increasing. The invention of powerful techniques such as Q-switching (4) and mode-locking (5) in the 1960s led to the generation of short pulses (femtosecond to picosecond pulse duration) with high intensity. A breakthrough in laser technology was achieved in 1985, when Donna Strickland and Gerard Mourou invented the concept of Chirped Pulse Amplification (CPA) (6). By temporally stretching the pulse prior to amplification and re-compression, the construction of the first "table-top" laser systems with ultra-high peak powers and ultra-short pulses in the picosecond and femtosecond range was possible. Nowadays, state-of-the-art laser facilities can in general be divided into laser systems delivering long pulses of the order of nanoseconds to picoseconds with energies exceeding kilojoules up to megajoules and short pulses of the order of femtoseconds with sub-kilojoule energies. Long pulses are most often used for fundamental research in plasma physics, laboratory astrophysics, atomic weapons development and inertial confinement fusion. Shorter pulses of the order of femtoseconds are used for the exploitation of X-ray sources, nuclear physics, fast ignition and

1. INTRODUCTION

laser-driven particle acceleration, whose study is addressed in this thesis.

The history of conventional acceleration started in the early 20th century. Rolf Widerøe built and patented the linear accelerator (LINAC) in 1928 (7) and Ernest Lawrence built the cyclotron in 1932 (8). In these machines the particles are accelerated by fast oscillating electric potentials and are capable of generating hundred of MeV proton and ion beams. A milestone in conventional proton acceleration was set with the invention of the proton synchrotron in 1952, allowing acceleration to GeV energies. Nowadays the largest and most powerful particle collider is the Large Hadron Collider (LHC) at CERN, accelerating beams to 13 TeV of energy.

In the 1950s Vladimir Veksler proposed for the first time a plasma-based particle accelerator (9) (before the first laser was created by Theodore Maiman in 1960). Toshiki Tajima and John Dawson showed theoretically that wakefields in a plasma can be driven by an intense laser pulse that is about half a plasma wavelength long, thereby proposing the first Laser Electron Accelerator in 1979 (10). Nowadays electrons can easily be accelerated to energies exceeding 1 GeV (11). Whereas electrons can directly be accelerated to relativistic energies by the laser field with "moderate" laser intensities of the order of 10^{18} Wcm^{-2} (11), this is not the case for the ions. Direct laser-driven ion acceleration requires intensities exceeding 10^{24} Wcm^{-2} , which is at least two orders of magnitude higher than intensities currently achievable by existing laser systems. Therefore, laser-driven proton acceleration, which has become a vivid field of research in the last two decades (12, 13, 14), always relies on the energy transfer from the electrons, which are acting as a mediator. The irradiation of thin (primarily solid) targets with powerful lasers leads to the acceleration of proton beams by electric fields exceeding TV/m with particle energies up to hundred(s) of MeV over short (μm -scale) distances. This stands in strong contrast to ion beams generated by conventional accelerators, which are prone to breakdown voltages to about 100 MV/m and therefore accelerate charged particles over hundreds of metres. Favourable features of laser-driven ion beams include an extremely small effective source size, brightness and short pulse duration. In 2000 Snavely *et al.* (15) attracted international attention when they produced an intense proton beam with a maximum energy of 55 MeV, with a single-shot based experiment as proof-of-principle. Further developments, also in non-laser related fields like target fabrication, led to a further increase as for example the generation of 67 MeV protons by Gaillard *et al.* (16) in 2011 with a tailored cone target. Nowadays a number

of laser facilities operate lasers in the petawatt range (10^{15}W) allowing the laser-based acceleration of particles (e.g. (15), (16), (17), (18), (19)). In the well-understood Target Normal Sheath Acceleration (TNSA) mechanism, ions are accelerated through a large charge separation field at the rear side of an opaque plasma. Typically in the TNSA regime, micrometre thick solid targets are irradiated with intense lasers to produce ion beams with unfavourable features such as low cut-off energies and thermal spectral shapes. More recently the field of laser-driven ion acceleration has somewhat shifted to the study of laser interaction with thinner (nanometre) overdense and near-critical targets (20, 21, 22, 23). The interaction of high intensity lasers with such ultrathin targets shows up a promising route to a more efficient ion beam generation in regimes such as Radiation Pressure Acceleration (RPA) and Breakout Afterburner (BOA). Yet there are still a number of caveats that have to be overcome, e.g. further increasing particle energy, spectral and angular control of the beam, conversion efficiency from laser energy into the ion beam, possible activation issues, as well as stability of the acceleration parameters. However, new experimental routes are emerging to overcome these drawbacks (12, 14).

1.2 Motivation

There are many potential applications for laser-driven ion beams due to their unique characteristics, including small source size, high degree of laminarity and ultra-short duration at the source. In the following some potential applications are discussed.

1.2.1 Hadron therapy

Energetic ion beams generated by conventional accelerators are already frequently utilised for the treatment of cancer. Robert Wilson proposed the radiological use of fast protons in 1946 (24) and the first patients were treated in the 1950s by cyclotron-generated proton beams. Naturally, with the advances in beam quality and achievable energies, laser-driven ion beams have been suggested for the clinical use (25). Global cancer rates increase significantly every year. More than 14 million people were diagnosed with cancer and more than 8 million cancer-related deaths occurred in 2012 (26, 27), clearly demanding affordable and effective treatment. While some cancers are treatable with chemotherapy alone, others need radiotherapy and sometimes surgery.

1. INTRODUCTION

Chemotherapy and radiotherapy are two different approaches of treatment and used in different ways. Chemotherapy refers to the treatment with drugs aiming to stop the cancer cells from reproducing and dividing. It is usually given in a series of sessions before an operation to shrink the tumour and weaken its attachment and is also used to destroy left over cells after an operation. As with any type of medication, there are side effects and healthy tissue can be damaged. Radiotherapy is less severe than chemotherapy. It uses radiation to destroy the cancer cells in a specific spot by damaging the DNA of cancerous cells. The radiation can be directly applied to the tumour instead of injecting drugs into blood vessels. Therefore radiotherapy is a more precise treatment, because it is based on type, location and stage of the cancer. Electrons and γ -rays are widely utilised, but recently carbon ions and protons have been used for treatment. While electron and photon beams are cost-effectively generated, they deposit their energy continuously in matter, thereby causing unwanted damage to healthy tissue during treatment. Opposing the pattern of energy deposition of ions shows a sharp peak, the Bragg peak (figure 1.1). By selecting the initial energy of the ion beam, the dose can be delivered localised to the tumour, sparing healthy cells. Therefore, radiation therapy with fast ion beams is one of the most promising routes to cancer treatment in future. To treat any cancerous tissue in the human body, proton or ion beams of around 200 MeV or 250 MeV/u, respectively, are needed (28). Depending on the tumour, a dose between 2 Gy and 10 Gy ($1 \text{ Gy} = 1 \text{ J/kg}$) is necessary for a successful treatment (25). This corresponds to roughly 2×10^{10} protons at 250 MeV stopped in one kilogram. This could require several thousands of pulses depending on the number of particles available per laser-generated pulse and on the volume of the tumour.

Nowadays, a number of large-scale medical accelerator centres exist, that use linear accelerators, cyclotrons or synchrotrons to generate ion beams with tens to hundreds of MeV energies for cancer treatment. One facility is the Heidelberg Ion Therapy Center (HIT) in Germany (30), which uses a synchrotron seeded by a linear accelerator for the generation of 221 MeV proton and 430 MeV/u carbon beams. HIT features a gantry system (670 metric tons) to allow full rotation of the beam for patient delivery with sub-millimetre precision. Since 2009, patients have been successfully treated with proton and carbon ion radiotherapy. However the building costs of the facility were high (exceeding 115M euro), as well as infrastructure demands. The three-stories building with a footprint of 5027 square metre has nearly the size of a football pitch; the gantry

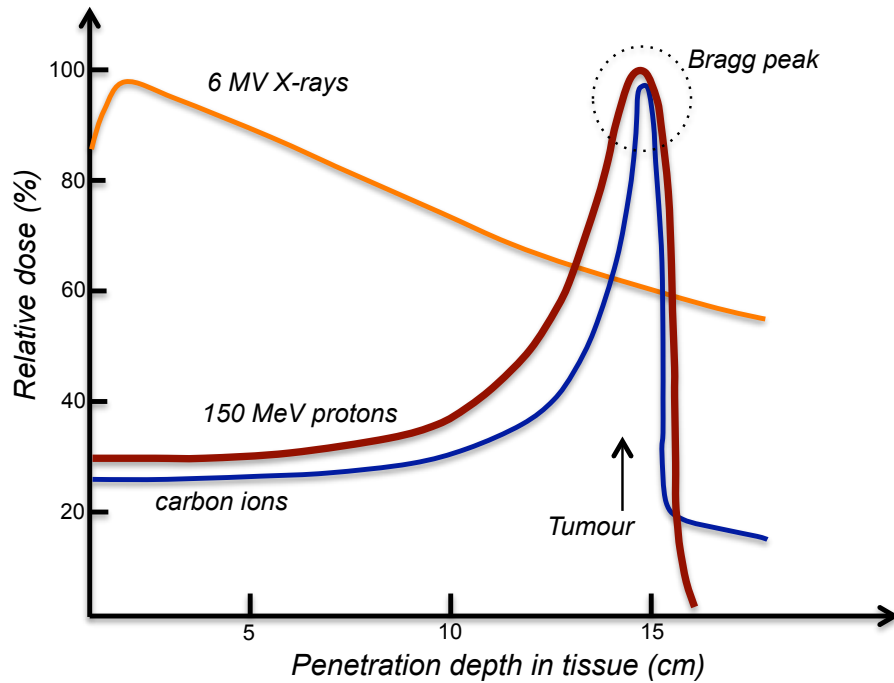


Figure 1.1: Bragg Peak - Dose deposition curves of X-rays, protons and carbon ions in human tissue. While X-rays lose their energy continuously, protons and carbon ions deposit almost their entire energy shortly before being stopped (Bragg peak).

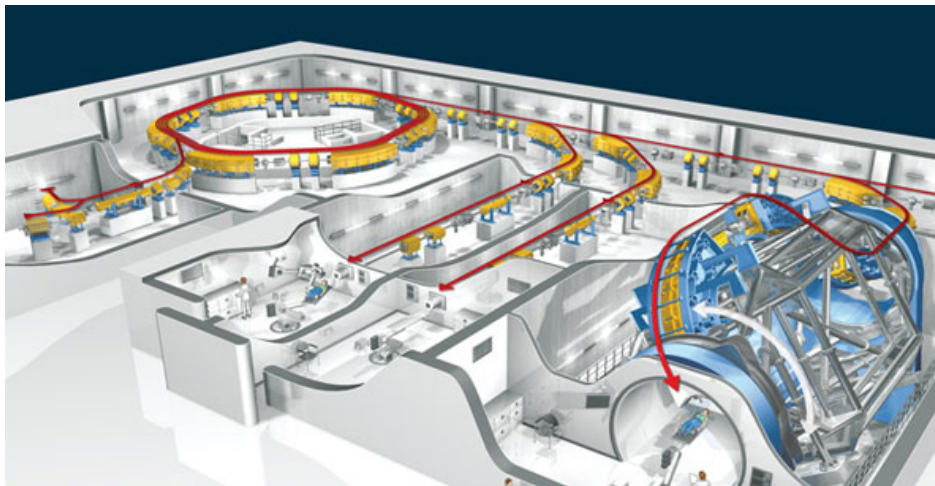


Figure 1.2: Heidelberg Ion Therapy Center - Depiction of the Heidelberg Ion Therapy Center (29). Ion beams are accelerated by a synchrotron to high energies and guided and focused by magnets in vacuum tubes. Three independent beams enter the treatment rooms and irradiate the patients.

1. INTRODUCTION

alone is 25 m long and 13 m in diameter and weighs 670 metric tons (figure 1.2). On average 750 patients per year can be treated with the facility running at full capacity. Laser-driven ion beams could pave the way to smaller treatment facilities due to the acceleration lengths of a few μm opposed to several metres in conventional accelerators (31, 32, 33, 34, 35, 36, 37, 38, 39, 40). This also allows the generation of the ion beam closer to the patient, since a laser-driven system offers advantages in terms of guiding; it is easier to steer a laser beam with mirrors than a particle beam with heavy magnets. Furthermore, laser-based facilities could be more affordable and wider accessible. However, the main drawbacks that have yet to be overcome by laser-driven ion beams include achievable maximum energy, energy spread and reliability. Conventional accelerators offer very stable beams, with a very small energy spread of less than one percent, whereas laser-driven ion beams usually have a thermal spectrum and a energy spread of up to 100 percent. Lastly, the number of protons produced in a single shot is not high enough to treat the cancerous tissue (dependent on target volume), and up to now no robust acceleration mechanism that can operate at a high repetition rate has been demonstrated.

1.2.2 Inertial confinement fusion fast ignition

Laser-driven ion beams have also been proposed for the use in fast ignition with inertial confinement fusion, relaxing the requirements to start the fusion process. With increasing energy demands in the near future, the development of new energy sources will become increasingly important. Fusion power could be one possible solution for clean energy production.

The most promising fusion reaction uses a positively charged deuterium nucleus (one neutron, one proton) and a tritium nucleus (two neutrons, one proton) to fuse them into a heavier helium nucleus with two neutrons and two protons by overcoming the repulsive electrostatic force. This reaction yields 17.6 MeV, but requires a temperature of about 40 million Kelvin to overcome the Coulomb barrier and to start the ignition process. The energy is converted into heat as the generated helium nucleus and the extra neutrons interact with the material around them.

In principle, there are two distinct approaches to generate fusion power; magnetic confinement fusion (MCF) and inertial confinement fusion (ICF).

MCF relies on the use of magnetic fields to confine the hot fusion fuel in the form of a relatively low density plasma ($n_e \approx 10^{15} \text{ cm}^{-3}$) for a rather long time ($t \approx 1 \text{ s}$). One type of magnetic confinement device is the tokamak in the shape of a torus.

In the process of Inertial Confinement Fusion (ICF), high-power laser beams are used to compress and heat hydrogen isotopes to ignite the fuel pellet (see figure 1.3). In the course of ICF the fuel pellet is compressed to ultra-high densities (10^{26} cm^{-3}) and heated within nanoseconds. In the direct ICF approach, several laser beams are focused on a small spherical pellet (μm) containing deuterium and tritium. The rapid heating by the laser beams causes the outer layer of the target to explode. Subsequently, the remaining parts of the pellet are driven inwards in a rocket-like implosion, compressing the fuel inside the capsule and forming a shock wave. This shock wave further heats the fuel until a self-sustaining burn of the core. The fusion burn propagates outward through the cooler, outer regions of the capsule much more rapidly than the capsule can expand. Instead of magnetic fields in the MCF approach, the plasma is confined by inertia, thus the term inertial confinement fusion.

There is another approach to ICF. In the indirect ICF approach, which is used for example at the National Ignition Facility (NIF), laser beams are used to heat the inner walls of a gold cavity (hohlraum), which contains the pellet. This creates an extremely hot plasma, which in turn generates copious amount of soft X-rays. These X-rays rapidly heat the outer surface of the fuel pellet, causing a high-speed ablation, or blow-off, of the surface material and the imploding of the fuel capsule in the same way as if it had been hit with the lasers directly. By symmetrically compressing the capsule with radiation a central hot spot can be formed, where the fusion process can set in. The plasma ignites and the compressed fuel burns before it can disassemble.

At NIF the fuel pellet is a spherical capsule of plastic with 2 mm diameter with the deuterium and tritium being added as gas. The sphere is cooled to 18.6 Kelvins (approximately -255°C), transforming the deuterium and tritium into a thin layer ($70 \mu\text{m}$) of ice inside the pellet. A total of 192 laser beams delivering 1.9 MJ energy are then focused on both sides of the hohlraum within 20 nanoseconds. Therefore a total of 500 Terawatts of power is delivered inside the hohlraum starting the ignition process.

Fast ignition driven fusion by laser-driven particle beam has been identified as a path to high-yield and high-gain for ICF (41, 42, 43, 44, 45, 46). The use of laser-generated proton beams could facilitate the ignition process. In this case the fuel is compressed

1. INTRODUCTION

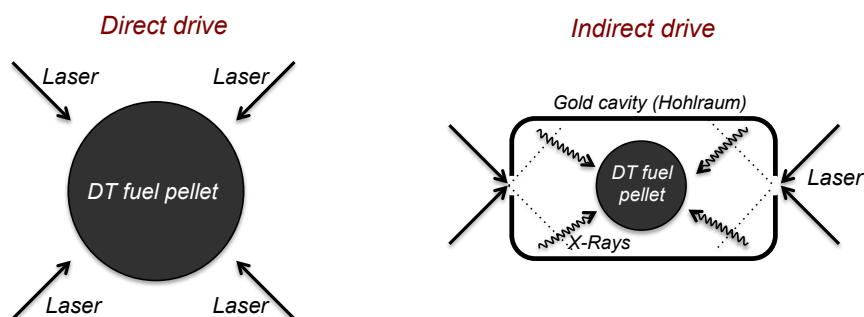


Figure 1.3: ICF direct and indirect drive - Direct-driven and indirect-driven inertial confinement fusion. In the direct-drive the fuel pellet is directly heated by the laser pulses, whereas the indirect-drive relies on secondary-generated X-rays, which heat the pellet.

conventionally by a nanosecond laser pulse and subsequently a laser-generated particle beam delivers energy sufficiently rapidly to ignite the fuel at a much lower peak density (see figure 1.4). A decrease in lower peak density requires much less driver energy to compress the target. One of the biggest caveats of the fast ignition process is the difficulty of depositing enough energy to ignite the hot spot in the pellet before the pressure equilibrium can re-establish itself.

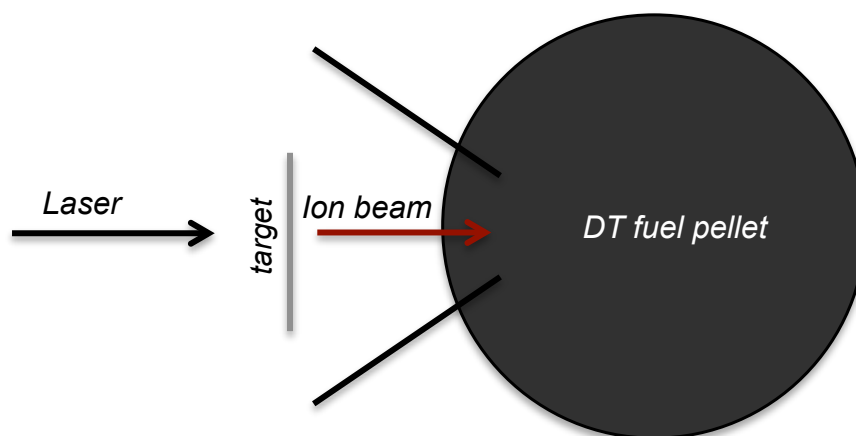


Figure 1.4: Ion fast ignition - Fast ignition-driven fusion. A high-intensity laser pulse is used to produce high-energetic protons from the interaction with a target, which are then guided by a cone onto the pellet.

Although in principle a laser-driven electron beam could be used for the fast ignition process, proton and other ion beams have the inherent advantage of depositing their energy very precisely at the end of their range (Bragg peak). In this way a laser-

generated proton beam directed onto the fuel pellet could ignite it. This beam needs to carry $E_{ig} \sim 10$ kJ to ignite the compressed pellet. The required ion energy E_{ki} depends on the fuel assembly, but is usually ~ 10 MeV for protons and ~ 400 MeV for C. E_{ig} and E_{ki} define then the required number of beam particles, N_P , which is approximately $\sim 10^{16}$ for protons and $\sim 10^{14}$ for carbon ions (47).

1.2.3 Proton radiography

Owing to their unique properties in terms of spatial quality and temporal duration, laser-generated proton beams have already been frequently utilised for radiography. The protons emitted from a laser-irradiated target can be described as virtual, point-like sources (48, 49, 50). Therefore targets placed in front of this source can be easily imaged in high resolution. An image of the object can be obtained through the different attenuation curves of the ions or by scattering. The beams are also used to diagnose electric and magnetic fields by the varying deflections of the produced ion beams (51, 52, 53, 54, 55, 56, 57, 58, 59, 60). The large energy spread of laser-driven ion beams combined with the ultra-short picosecond duration over which they are generated, proves useful for imaging applications. The different energies of the protons allow a "time-of-flight"-probing of the interaction in a time-resolved manner. Multi-layered detectors like Radiochromic Films or CR-32 are used as detector material, so each layer corresponds to the proton spatial intensity distribution for a different energy. In this way, a high temporal resolution can be obtained. The magnitude of the electric field can be inferred from the deflection of the probing beam imprinted with a mesh pattern. Several radiographic applications with laser-generated proton sources have been tested successfully. The proton sources have been used to image small physical objects, meshes and foils (see figure 1.5). Proton probing can also be used to image shock fronts propagating in overdense plasmas.

1. INTRODUCTION

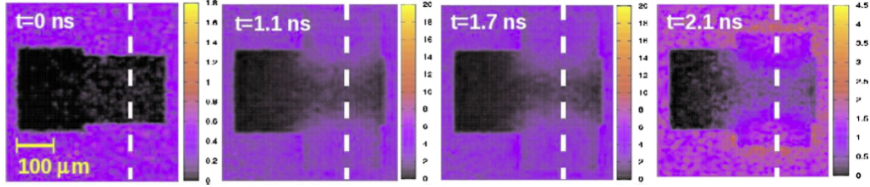


Figure 1.5: Proton radiography - Radiography of a cylinder compression. 2D time-resolved images at 0, 1.1, 1.7 and 2.1 ns (reproduced from (50)).

1.2.4 Production of radioisotopes for positron emission tomography

Laser-generated proton beams can be used for the production of short-lived isotopes for positron emission tomography (PET). PET is an imaging modality that produces three-dimensional images or maps of functional processes in the body. Images are formed by detecting pairs of gamma rays that are emitted indirectly by a positron-emitting radionuclide (tracer). Gordon Brownell, Charles Burnham and William Sweet contributed significantly to the development of PET technology by demonstrating the first annihilation radiation for medical imaging in the 1950s at the Massachusetts General hospital (61). For a PET scan a small amount of a short-lived radioactive tracer is introduced into the patient, typically by intravenous injection. After some uptake time, the tracer has accumulated in the patient and the concentration is measured by the scanner. The radionuclide decays by emitting a positron (positive beta decay). The positron travels a short (3-5 mm) distance before it annihilates with an electron, generating a pair of annihilation gamma rays (each 511 keV) that are emitted in opposite directions. The image acquisition is then based on the external detection in coincidence of the emitted gamma-rays. For a valid annihilation event to be processed, the detection has to occur within a few nanoseconds at the detectors on either side. The detector is commonly a scintillator that creates a light burst upon irradiation, which is detected by a photomultiplier tube. The final count is detected after amplification and determination of energy and spatial position.

Typically radionuclides with short half lives are used for PET scanning such as ^{11}C (~ 20 min), ^{13}N (~ 10 min), ^{15}O (~ 2 min) and ^{18}F (~ 110 min). Due to the short lives of most radioisotopes, the tracers have to be produced in close proximity to the PET imaging facility. Currently the majority of the isotopes are produced by cyclotrons, which also limits the widespread use of PET due to the high costs of

these machines. Laser-driven accelerators may provide a more compact and cheaper alternative to cyclotrons to produce radioisotopes, allowing the on-site installations at hospitals.

The generation of PET-isotopes has been investigated since the early 2000s. Spencer *et al.* produced protons with energies up to 37 MeV with an ultra-intense laser (up to 10^{20} Wcm^{-2}) to induce nuclear reactions in a secondary target to produce β^+ -emitting nuclei of ^{11}C and ^{13}N (activity of order 200 kBq) (62). Fritzler *et al.* produced 10 MeV protons with an intense laser ($6 \times 10^{19} \text{ Wcm}^{-2}$) and numerical simulations supported the generation of GBq sources of PET isotopes (63). In 2004 Ledingham *et al.* reported how intense PET sources of ^{11}C and ^{18}F can be generated using a petawatt laser beam (64). The investigation of laser-based PET-generation is still on-going. In Spain the Laser Laboratory for Acceleration and Applications (L2A2) facility, that is currently in the commissioning phase, will feature a 45 TW laser system capable of delivering pulses with an ultrahigh contrast ($10^{10}:1$ at 100 ps) at 10 Hz and one of the main research lines will be the production of medical-imaging radioisotopes (65).

1.3 Thesis structure

The presented thesis investigates laser-driven ion acceleration from ultrathin solid foils. The work combines experimental and numerical results from particle-in-cell simulations to discuss ion acceleration in overdense and near-critical plasmas with high-intensity lasers.

In chapter 2 high-intensity laser interaction with matter and the relevant theoretical background of laser-driven ion acceleration is presented.

Chapter 3 outlines the experimental and numerical methods, including information on the used laser systems, targetry and diagnostics. The particle-in-cell method is presented with relevant simulation remarks.

Chapter 4 discusses the experimental and numerical results for the interaction of a single high-intensity laser pulse with thin solid targets. In detail the radiation pressure dominated acceleration mechanism is explored with an in-depth parameter study. Also, the electron dynamics in the relativistic transparency regime are studied.

The experimental results in chapter 4 and 5 were obtained from campaigns with the Vulcan and Astra-Gemini laser systems at the Rutherford Appleton Laboratory (Didcot, UK). These experiments were performed in collaboration with the group of Professor Paul McKenna of the University of Strathclyde (Glasgow, UK).

In chapter 5 experimental and numerical results of the interaction of a double-pulse laser set-up are presented. The first part focuses on the interaction with a double pulse of linear polarisation. In the second part a novel acceleration scheme with a double pulse set-up of mixed polarisation is proposed.

Chapter 6 applies the obtained results and, by combining with existing scaling laws, gives estimations of achievable ion beam parameters with the VEGA Petawatt system.

Finally, chapter 7 concludes the results and gives an outlook for future direction of laser-based ion acceleration.

2

Relativistic laser-matter interaction

This chapter gives an overview of the physical processes occurring during the interaction of a high-intensity laser with matter, from ionisation, laser absorption, over propagation and subsequent ion acceleration. Most of this thesis is dedicated to the study of an intense laser pulse impinging on thin solid targets. Only high-intensity lasers are considered, which all have in common that they almost instantaneously ionise any material upon irradiation. This means that usually the target is ionised before the main part of the pulse arrives, subsequently the main part of the pulse always interacts with a plasma. Ionisation with high intensity lasers differs notably from low intensity laser ionisation and the chapter begins with the processes governing ionisation at lower intensities, to put it into context with the ultra-intense lasers utilised in the thesis.

2.1 Strong field ionisation processes

An adequate benchmark for the frontier of high-intensity laser interactions can be derived from the field strength felt by the electrons in an atom. For simplicity the Bohr model of the hydrogen model is considered (66). In that case, the electron sits at a distance from the nucleus given by the Bohr radius, a_B (in SI units)

$$a_B = \frac{4\pi\epsilon_0\hbar^2}{m_e e^2} = 5.3 \times 10^{-11} \text{ m} \quad (2.1)$$

2. RELATIVISTIC LASER-MATTER INTERACTION

with the Dirac constant \hbar , the permittivity in free space ϵ_0 , electron mass m_e and elementary charge e . The electric field strength is then given by

$$E = \frac{e}{4\pi\epsilon_0 a_B^2} \approx 5.1 \times 10^{11} \text{ Vm}^{-1} \quad (2.2)$$

An electromagnetic field with a similar field strength would have an intensity, I_a , given by

$$I_a = \frac{\epsilon_0 c E^2}{2} \approx 3.51 \times 10^{16} \text{ Wcm}^{-2} \quad (2.3)$$

This means that any laser intensity, $I_L > I_a$ will completely ionise the target. However, even at lower intensities ionisation can occur via multiphoton effects. In principle, there are two regimes of interest separated by the Keldysh parameter γ (67).

$$\gamma = \sqrt{\frac{E_{ion}}{2\phi_{pond}}} \quad (2.4)$$

where E_{ion} is the ionisation potential of the atom and

$$\phi_{pond} = \frac{e^2 E_L^2}{4m\omega_L^2} \quad (2.5)$$

is the ponderomotive potential of the laser field. E_L is the field strength of the laser field, and ω_L is the laser frequency. If $\gamma > 1$, this corresponds to multiphoton ionisation, which dominates to intensities up to 10^{13} Wcm^{-2} .

Multiphoton ionisation If the energy of a single photon is not high enough for the ionisation of the atom, an electron can still gain enough energy to overcome the potential barrier of the nucleus by the absorption of several lower frequency photons in a process called multiphoton ionisation (see figure 2.1 (a)). The total energy that is absorbed by the electron through virtual energy levels is

$$E_{electron} = (n + s)\hbar\omega - E_{bound} \quad (2.6)$$

with $n + s = m$ being the sum of photons n , that are necessary for the ejection of the electron, and s of additionally absorbed photons. E_{bound} is the binding energy of the electron to the core.

In case that there are no additionally absorbed photons ($s=0$), the process can be described by perturbation theory, with the n -photon ionisation rate given by

$$W_n = \sigma_n I_L^n \quad (2.7)$$

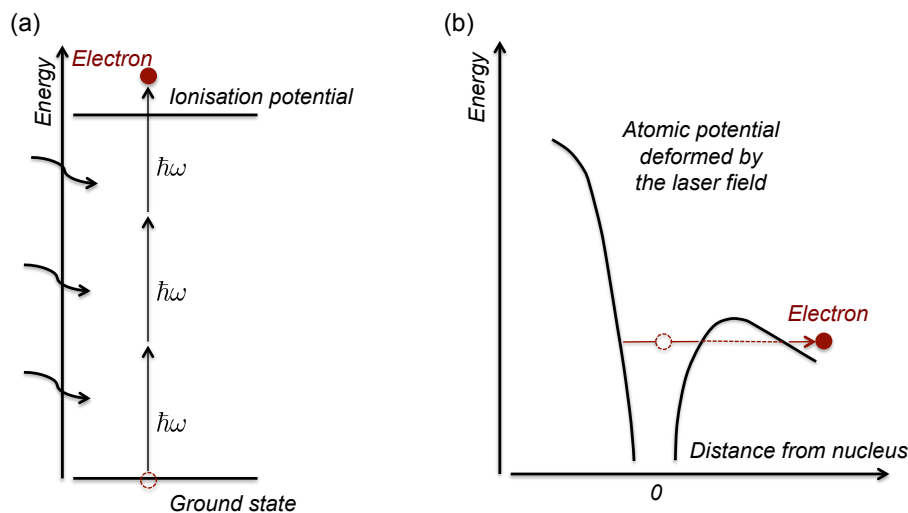


Figure 2.1: Multiphoton and tunnelling ionisation - (a) In case of multiphoton ionisation an electron gains energy by the absorption of multiple low-energy photons to overcome the potential barrier. (b) At high intensities, the laser can also distort the atomic potential allowing tunnelling ionisation.

with σ_n being the cross-section, which is decreasing with n . The process also has a strong dependence on photon density of the incoming laser field; multiphoton ionisation usually occurs at intensities above 10^{10} Wcm^{-2} . In the case that $s \neq 0$, the electron is excited by more photons than necessary, which results in the ejected electron having a higher kinetic energy, visible as distinct peaks separated by the photon energy $\hbar\omega$ in the electron spectrum. This regime is known as *above-threshold ionisation*.

Tunnelling ionisation and barrier suppression For $\gamma \ll 1$ and intensities above 10^{13} Wcm^{-2} (which are still below the direct ionisation threshold) the laser field becomes strong enough to distort the atomic potential. The external laser field can strongly modify the previously purely Coulombic potential. This results in a significant lowering of the Coulomb barrier on side of the potential well to a value close, but still slightly above the binding energy of the electron. Therefore the former bound state is enabled to tunnel through this barrier with a finite probability. This is called *tunnelling ionisation* (see figure 2.1 (b)).

At even higher intensities, between 10^{13} Wcm^{-2} and 10^{15} Wcm^{-2} , the barrier is further suppressed beneath the binding energy, so the electron can escape spontaneously.

2. RELATIVISTIC LASER-MATTER INTERACTION

This process is called *barrier suppression* (BSI). The threshold or appearance intensity for this process can be estimated by assuming a stationary homogeneous electric field that is deforming the atomic potential as

$$I_{app} = 4 \times 10^9 \left(\frac{E_{ion}}{\text{eV}} \right)^4 Z^2 \text{ Wcm}^{-2} \quad (2.8)$$

where E_{ion} is the ionisation potential of the ion or atom with charge ($Z-1$). The simplest case is hydrogen ($Z=1$) for which $E_{ion} = 13.61$ eV, which corresponds to an appearance intensity of $1.4 \times 10^{14} \text{ Wcm}^{-2}$. At intensities above 10^{18} Wcm^{-2} field ionisation (BSI) is the dominant process for all but the most strongly bound electrons. Equation 2.8 underestimates the appearance intensity by more than a factor four for hydrogen-like ions (68), however this simple estimation is useful and sufficiently accurate for many applications.

Collisional ionisation Extending the idea of single electron ionisation to many electrons, as it is the case in real laser-matter interaction, collisional ionisation mechanisms also become important. When enough energetic electrons are excited through field ionisation, these electrons will subsequently ionise other atoms by collisional ionisation. In case of a local thermal equilibrium the ionisation state can be determined by statistical means and the relative ion populations are related by the Saha-Boltzmann equation, assuming the radiative and absorptive events are equal (69). In case that the plasma is produced by a short laser pulse, larger density and temperature gradients have to be taken into consideration as well as radiation that can escape the plasma entirely. Then the assumption of a local thermal equilibrium is not valid any more and the time-dependent atomic rate equations need to be solved in order to determine the charge distribution.

2.2 Motion of a single electron in a laser field

Now the motion of a single electron in the laser field is considered (70, 71). When a laser beam is impinging onto a plasma, an electron will undergo relativistic dynamics in the intense laser field. The particle motion is governed by the Lorentz force (in cgs units)

$$\frac{d\vec{p}}{dt} = -e(\vec{E} + \frac{\vec{v}}{c} \times \vec{B}) \quad (2.9)$$

2.2 Motion of a single electron in a laser field

where $p = \gamma m_e \vec{v}_e$ is the relativistic momentum and $\gamma = 1/\sqrt{1 - v_e^2/c^2}$ is the Lorentz factor of the electrons. The laser field, approximated as a plane wave, propagating in the z-direction can be described by

$$\vec{A}(\vec{r}, t) = \text{Re}[\vec{A}_0 e^{i\phi}] \quad (2.10)$$

where $\phi = \vec{k} \cdot \vec{r} - \omega t$ is the phase of the light wave with ω and λ being the frequency and wavelength of the laser, respectively. $k = 2\pi/\lambda$ is the wave number and \vec{r} and t are the space and time variables. The generic position vector \vec{r} is given as $\vec{r} = x\hat{x} + y\hat{y} + z\hat{z}$. In the case of linear polarisation (LP) $\vec{A}_0 = A_0 e_x$ and $\vec{A}_0 = A_0(e_x \pm ie_y)$ for circular polarisation (CP). The electric and magnetic fields are obtained by

$$\vec{E} = -\frac{1}{c} \frac{\partial \vec{A}}{\partial t} \quad (2.11)$$

$$\vec{B} = \nabla \times \vec{A} \quad (2.12)$$

In the non-relativistic case (neglecting the $v \times B$ term of equation 2.9), the motion of the electron derives to

$$\vec{v} = -\frac{ie}{m_e \omega} \vec{E} \quad (2.13)$$

where m_e is the electron mass. Taking this as the *quiver velocity*, a threshold for relativistic effects can be defined, by equating the quiver velocity to the speed of light, c . This dimensionless parameter, a_0 , is then given as

$$a_0 = \frac{v}{c} = \frac{eE}{m_e \omega c} \quad (2.14)$$

For $a_0 < 1$ the motion is assumed to be non-relativistic, whereas for $a_0 > 1$ relativistic effects have to be taken into account. a_0 can be related to practical parameters such as the wavelength $\lambda = 2\pi c/\omega$ and the intensity, I , defined as the cycle-averaged value of the modulus of the Poynting vector, \vec{S}

$$I = \langle |\vec{S}| \rangle = \left\langle \frac{c}{4\pi} |\vec{E} \times \vec{B}| \right\rangle = \frac{c}{8\pi} |E_0|^2 = \frac{c}{8\pi} \left(\frac{m_e \omega c a_0}{e} \right)^2 \quad (2.15)$$

which yields in practical units

$$a_0 = 0.85 \left(\frac{I \lambda [\mu\text{m}]^2}{10^{18} \text{ W cm}^{-2}} \right)^{\frac{1}{2}} \quad (2.16)$$

2. RELATIVISTIC LASER-MATTER INTERACTION

where for a wave of given irradiance $I\lambda^2$ the peak dimensionless amplitude of the electric field is a_0 for linear polarisation and $a_0/\sqrt{2}$ for circular polarisation. This equation can also be rearranged to give the irradiance in terms of a_0

$$I_0\lambda[\mu m]^2 = \chi\left(1.37 \times 10^{18} \text{ Wcm}^{-2}\right)a_0^2 \quad (2.17)$$

where $\chi = 1$ for linear and $\chi = 2$ for circular polarisation.

Now, the relativistic case is considered, where a_0 exceeds unity and the magnetic term of the Lorentz equation (2.9) cannot be neglected. The electron dynamics is thus described by equation (2.9) to which the equation for electron energy is added.

$$\frac{d}{dt}(\gamma m_e c^2) = -e\vec{v} \cdot \vec{E} \quad (2.18)$$

By using the Lorentz equation (2.9) and equation (2.11) and (2.12), the relation

$$\frac{d}{dt}(\vec{p}_\perp - \frac{e}{c}\vec{A}) = 0 \quad (2.19)$$

is found, where \vec{p}_\perp are the perpendicular vector components of the momentum. This relation states the conservation of canonical momentum due to translational invariance in the transverse plane. By substituting \vec{A} in the z-component of equation (2.9) and (2.18), the momentum in propagation direction is derived to

$$p_z = \frac{\vec{p}_\perp^2}{2m_e c} = \frac{1}{2m_e c} \left(\frac{e\vec{A}}{c}\right)^2 \quad (2.20)$$

From equation (2.19) and (2.20), it is evident that in case of $\vec{A} = 0$ the momentum components vanish, thus no net energy of the wave is absorbed by the electron. This is in agreement with the so-called *Lawson-Woodward theorem*, stating that a charge cannot be accelerated by a radiation field in vacuum extending over an infinite region (as it is the case for a plane wave) (72, 73).

In the following the case of a monochromatic wave of frequency ω is considered. Recalling equation 2.10, the vector potential is given by

$$\vec{A} = A_0[\hat{x}\delta\cos\phi + \hat{y}(1 - \delta^2)^{1/2}\sin\phi] \quad (2.21)$$

with $\phi = \vec{k} \cdot \vec{r} - \omega t$. $\delta \leq 1$ is the polarisation parameter. For $\delta = 1$ or 0 the wave is linearly polarised along \hat{x} or \hat{y} , respectively, while for $\delta = \pm 1/\sqrt{2}$, it is circularly polarised. Other values correspond to elliptical polarisation.

2.2 Motion of a single electron in a laser field

When inserting equation (2.21) in the equations of motion, the phase ϕ must be considered as a function of the particle position, i.e. $\phi = \phi[x(t), t]$. It is convenient to use ϕ as the only variable. The derivative with respect to time is therefore obtained as

$$\frac{d\phi}{dt} = \partial_t \phi + v_z \partial_z \phi = -\omega + \frac{p_z}{m_e \gamma} k = -\omega + \frac{m_e c (\gamma - 1) \omega}{m_e \gamma c} = -\frac{\omega}{\gamma} \quad (2.22)$$

Thus the momentum derives to

$$\vec{p} = m_e \gamma \frac{d\vec{r}}{dt} = m_e \gamma \frac{d\phi}{dt} \frac{d\vec{r}}{d\phi} = -m_e \omega \frac{d\vec{r}}{d\phi} \quad (2.23)$$

From this relation the particle trajectory can be obtained. From equation (2.19) and (2.20) the vector components of the perpendicular momentum and the momentum in the propagation direction are given by

$$\vec{p}_\perp = (p_x, p_y) = \frac{eA_0}{c} (\delta \cos \phi, (1 - \delta^2)^{1/2} \sin \phi) \quad (2.24)$$

$$p_z = \frac{1}{2m_e c} \left(\frac{eA_0}{c}\right)^2 [\delta^2 \cos^2 \phi + (1 - \delta^2) \sin^2 \phi] = \frac{1}{4m_e c} \left(\frac{eA_0}{c}\right)^2 [1 + (2\delta^2 - 1) \cos 2\phi] \quad (2.25)$$

Therefore for a linearly polarised light, transversal oscillations are driven by ω . The motion in propagation direction is split into a longitudinal drift term and a longitudinal oscillation ($\cos 2\phi$) driven by 2ω . When averaging over an oscillation cycle, $\langle \cos 2\phi \rangle = 0$ vanishes and the constant drift of the electron is given by

$$\langle p_z \rangle = \frac{1}{4m_e c} \left(\frac{eA_0}{c}\right)^2 = m_e c \frac{a_0^2}{4} = p_d \quad (2.26)$$

In the case of circular polarisation, $2\delta^2 - 1 = 0$ and $p_x = \langle p_x \rangle$, i.e the high frequency component driving oscillations in the longitudinal direction vanishes. This will become important for the collisionless absorption mechanisms in a plasma, which will be introduced in a later section. By using equation (2.23), the drift velocity derives to

$$v_d = \frac{a_0^2}{a_0^2 + 4} c \quad (2.27)$$

The trajectory is given by

$$\hat{x} = -\delta \sin \phi a_0 \quad (2.28)$$

$$\hat{y} = (1 - \delta^2)^{1/2} \cos \phi \quad (2.29)$$

$$\hat{z} = \frac{1}{4} \left[-\phi - \left(\delta^2 - \frac{1}{2} \right) \sin 2\phi \right] a_0^2 \quad (2.30)$$

2. RELATIVISTIC LASER-MATTER INTERACTION

The trajectories of an electron in a linearly polarised laser field for different intensities are shown in figure 2.2. For circular light the trajectory is helicoidal. Since the electron drifts at a constant velocity along z , transforming to a reference frame moving with velocity $V_z = v_d$ for circular polarisation the orbit is a closed circle. This is also the case for linear polarisation, where the electron orbit is closed in the frame where the average velocity vanishes. This orbit is described by a "figure of eight".

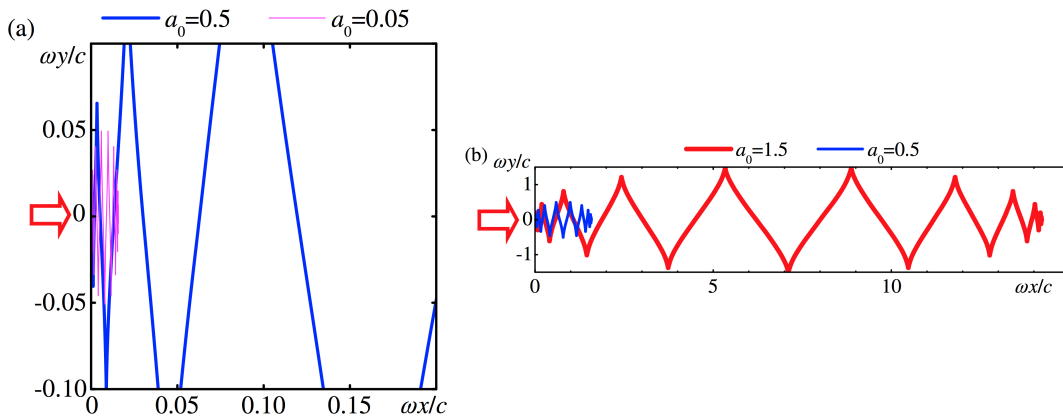


Figure 2.2: Electron trajectories - Trajectories of an electron in vacuum in the given optical fields of ultra-short linearly polarised plane electromagnetic waves representing laser pulses with different dimensionless amplitudes a_0 (equation 2.14) for the pulse duration of $\tau_0 \approx 24/\omega$ (10 fs for $\lambda = 800$ nm); the laser is incident from the left as indicated by the arrows. The maximum electron displacement perpendicular to the pulse propagation is $a_0 c/\omega$, while the forward displacement (along the pulse propagation direction) is proportional to $a_0^2 \tau_0 c$. (a) The amplitudes are $a_0 = 0.05$ and 0.5 (part of the trajectory), (b) $a_0 = 0.5$ and 1.5 (full trajectories). In each frame, the horizontal and vertical scales are equal; however, note the difference in the scales between the frames. At $a_0 = 0.05$, the intensity is much lower than the relativistic intensity, the perpendicular displacement is much larger than the forward displacement in one period. At $a_0 = 1.5$, the intensity is relativistic ($\approx 3 \times 10^{18}$ Wcm $^{-2}$ at the laser wavelength of $1 \mu\text{m}$), the forward displacement in one period exceed the perpendicular one (reproduced from Daido *et al.* (12)).

2.2.1 Ponderomotive force

In the previous section the motion of single electrons in a monochromatic plane wave was described. However, "realistic" electromagnetic waves (laser pulses) are not perfectly monochromatic plane waves, but have finite width and duration. The laser pulse

can be described by an envelope function, describing its transverse and longitudinal profiles, multiplied by an oscillating function.

$$\vec{E}(\vec{r}, t) = \text{Re}[\vec{E}_{env}(\vec{r}, t)e^{-i\omega t}] = \frac{1}{2}\vec{E}_{env}(\vec{r}, t)e^{-i\omega t} \quad (2.31)$$

$$\vec{B}(\vec{r}, t) = \text{Re}[\vec{B}_{env}(\vec{r}, t)e^{-i\omega t}] = \frac{1}{2}\vec{B}_{env}(\vec{r}, t)e^{-i\omega t} \quad (2.32)$$

The envelope functions \vec{E}_{env} and \vec{B}_{env} are supposed to vary with time on a scale slower than the oscillation period $T = 2\pi/\omega$. It is assumed that the field (almost) averages to zero over a period, i.e. $\langle \vec{E}(\vec{r}, t) \rangle \simeq 0$, while for the envelope function $\langle \vec{E}_{env}(\vec{r}, t) \rangle \neq 0$. Therefore two separate time scales are assumed, a slow and a fast one, suggesting to describe the electron motion as a superposition of a slow term and a fast (oscillating) term. The "slow" motion can be described by a dynamic equation with a slowly-varying force, which is named the *ponderomotive force*. It can be expressed as

$$\vec{f}_{pond} = -\frac{e^2}{2m_e\omega^2}\nabla\langle \vec{E}^2(\vec{r}_s(t), t) \rangle \quad (2.33)$$

with r_s referring to the slow motion. In fact, the ponderomotive force is the negative gradient of the previously introduced ponderomotive potential (equation 2.5).

$$\vec{f}_{pond} = -\nabla\phi_{pond} \quad (2.34)$$

The ponderomotive potential can be seen as the cycle-averaged oscillation energy, which is assumed to be a function of the oscillation centre.

$$\phi_{pond} = \frac{e^2}{2m_e\omega^2}\langle \vec{E}^2 \rangle \quad (2.35)$$

The consequence of the ponderomotive force is that electrons are expelled from regions of higher intensity. It is important to note that the force is charge-independent (e^2), therefore it also acts on other charged particles, e.g. ions. However, due to their much higher mass, ions are generally assumed immobile and not affected by this force.

2.3 Laser propagation in a plasma

In section 2.2, the behaviour of a single electron in the laser field has been considered. In this section some fundamental aspects of the interaction of the laser with the plasma electrons are introduced. It is noted that the ions in the plasma bulk are assumed

2. RELATIVISTIC LASER-MATTER INTERACTION

immobile due to their much higher mass; when substituting the ion mass into the equation 2.13, it can be seen that the quiver velocity is much smaller than the speed of light. Also the electron temperature is initially assumed to be close to zero, since the electrons are left with low energies during field ionisation.

The laser propagation in the plasma is determined by the dispersion relation

$$\omega_L^2 = \omega_p^2 + c^2 k^2 \quad (2.36)$$

where ω_L is the laser frequency and ω_p the plasma electron frequency, which is defined as

$$\omega_p = \sqrt{\frac{4\pi n_e e^2}{m_e}} \quad (2.37)$$

where n_e is the electron density of the plasma. The plasma frequency can be seen as the frequency of the oscillations driven by any local charge imbalance between the negative (electron) and positive (ions) charges in the plasma, for instance driven by the laser field. Here, it is assumed that the electron temperature has risen sufficiently, so that collisions can be ignored.

Therefore there are two counteracting effects induced by the laser field. Firstly, the electric field of the laser that drives electrons apart from the plasma ions periodically with the laser frequency ω_L . Secondly, the restoring Coulomb forces of the plasma that tend to bring the negative and positive charges together with the plasma frequency, ω_p . Hence, if $\omega_p < \omega_L$ the first term dominates and the laser can propagate through the plasma. In this case the plasma is said to be *underdense*. Subsequently, in case $\omega_p > \omega_L$, the restoring forces driven by the plasma frequency dominate and the laser gets reflected of the plasma. In this case the plasma is *overdense*. The boundary between the two plasma states is called the *critical density* and can be derived by equating the laser frequency to the plasma frequency, which yields

$$n_c = \frac{\omega_L^2 m}{4\pi e^2} \quad (2.38)$$

or in a more convenient way

$$n_c = 1.1 \times 10^{21} \lambda_{\mu m}^{-2} \text{cm}^{-3} \quad (2.39)$$

It is important to notice that the critical density depends directly on the laser frequency, therefore a plasma that is underdense for a short wavelength laser can be overdense for a long wavelength one (see table 2.1).

2.3 Laser propagation in a plasma

Laser	Typical pulse durations	λ (μm)	n_{cr} (cm^{-3})
KrF	ns	0.248	1.8×10^{22}
Ti:Sapphire	fs	0.800	1.7×10^{21}
Nd:Glass	ps	1.054	9.9×10^{20}
CO ₂	ns	10	1.1×10^{19}

Table 2.1: Critical densities - The critical density depends directly on the laser wavelength. Therefore a plasma that is underdense for a short wavelength laser can be overdense for a long wavelength laser.

In the following, some important plasma length parameters are defined. The focus of the present thesis lies on the interaction of intense laser pulses with thin solid targets, which are initially overdense. For example, solid diamond-like carbon has a density $\rho = 2.7 \text{ g/cm}^3$, which translates to $\sim 500n_{cr}$ for $\lambda = 800 \text{ nm}$ Ti:Sapphire laser. In most cases, it is assumed that the laser pulse impinges on a plasma slab with a step-like density profile. When the laser interacts with an overdense plasma, an evanescent component will penetrate the plasma up to a characteristic length, where the laser electric field has dropped by a factor $1/e$. In the particular case of a step-like density gradient, this collisionless *skin depth*, l_s is defined by

$$l_s = \frac{c}{\omega_p} \tag{2.40}$$

In the interaction with solid targets, the laser pulse duration also plays an important role. Since a ns laser pulse impinging on a overdense plasma allows more time of the on-set of the pulse to drive plasma expansion, the main part of the laser pulse will interact with a lower density plasma, whereas a short fs pulse can access much higher density regions. Again, assuming an initially neutral target with a step-like density profile, a plasma is created at the front surface upon irradiation with a characteristic *scale-length* L , given by (66)

$$L^{-1} = \left. \frac{d}{dx} \log n(x) \right|_{x=x_c} \tag{2.41}$$

Assuming that the plasma expands isothermally, the density profile will take an exponentially decreasing form $n(x) = n_0 e^{x/l}$ with a well-defined scale length

$$L = c_s \tau_L \tag{2.42}$$

2. RELATIVISTIC LASER-MATTER INTERACTION

where τ_L is the pulse duration and c_s is the ion sound speed, given by,

$$c_s = \sqrt{\frac{Zk_B T_e}{m_i}} \approx 3.1 \times 10^7 \sqrt{\left(\frac{T_e}{[\text{keV}]}\right) \left(\frac{Z}{A}\right)} \text{cm s}^{-1} \quad (2.43)$$

where k_B is the Boltzmann constant, T_e is the electron temperature and Z and A are the charge and the mass number of the plasma ions, respectively.

In the simulation of the interaction of high intensity laser pulses with solid targets (as presented for example in section 4.1) the skin depth and scale length compete with another characteristic length of the plasma, called the *Debye length*. It is defined as the distance over which the plasma is shielding against externally applied electric fields. The charged particles will redistribute in such a way to generate an oppositely-directed electric field, to compensate for the externally applied field. This ensures that the plasma maintains the quasi-neutrality. To first order, the electric field due to a charge immersed in a plasma only interacts with other charged particles in the plasma within a volume known as the Debye sphere, where the radius of the sphere is given by the Debye length λ_D .

$$\lambda_D = \sqrt{\frac{k_B T_e}{4\pi e^2 n_e}} \quad (2.44)$$

The Debye length defines the minimum distance over which charge neutrality is ensured (i.e. charged particle essentially feels no electric field effect from the other charges at distances greater than λ_D). Additionally, the Debye length is also a measure of the penetration depth of externally applied electromagnetic fields. For shielding effects to occur, the Debye sphere radius, hence the Debye length, must be much less than the length of the linear dimension, L_{ld} , of the plasma (i.e $\lambda_D \ll L_{ld}$).

2.4 Laser absorption in a plasma

Collisional absorption The absorption of the laser in a plasma is very complicated as there are several mechanisms that depend sensitively on the laser intensity, pulse duration, polarisation, angle of incidence, plasma density and scale length. The absorption mechanisms can be divided into collisional and collisionless. At lower laser intensities ($I_0 < 10^{15} \text{ Wcm}^{-2}$), the collisional absorption or inverse bremsstrahlung heating is the dominant absorption mechanism (66). In this case, the electrons transfer their energy

to the plasma by collisions with the ions. The frequency of these electron-ion collisions is given by

$$v_{ei} \propto \frac{Zn_e}{T_e^{\frac{3}{2}}} \quad (2.45)$$

with Z being the number of free electrons per atom (70). With short laser pulses high densities can be accessed where the plasma is highly collisional, at least at moderate intensities (low electron temperatures), so it can be expected that the inverse bremsstrahlung contributes to the laser absorption. However, as it is evident from equation (2.45), the collision frequency decreases for higher electron temperatures and collisionless absorption mechanisms, which will be described in the next section, start to dominate.

Collisionless absorption

2.4.1 Resonance absorption

Resonance absorption generally requires the incoming laser light to be p-polarised. When the p-polarised light impinges on an oblique incidence onto the plasma, the component of the electric field perpendicular to the surface can reach or tunnel into the plasma. Thereby it is exciting oscillations at the critical surface, which then grow over several laser oscillations. This effect is maximised when the laser equals the plasma frequency, hence the oscillations are rising resonantly. The energy transfer to the plasma is due to the dampening of this excited wave by either wave breaking or collisions. The degree of resonant absorption has been found to be dependent on the plasma density scale length and is higher for longer scale lengths. This process dominates to intensities up to 10^{17} Wcm⁻². At higher intensities resonance absorption is still present, but other mechanisms start to dominate.

2.4.2 Vacuum Heating - Brunel mechanism

Resonance absorption ceases to work for plasmas with a very short density scale length. If the electrons undergo oscillations along the density gradient with an amplitude $x_p \approx \frac{eE_L}{m\omega^2} = \frac{v_{os}}{\omega}$ (v_{os} equivalent to the quiver velocity, equation 2.13), the resonance break down in this amplitude exceeds the scale length L , that is $\frac{v_{os}}{\omega} > L$. The p-polarised laser is obliquely incident on the plasma front surface, but the electric field can not

2. RELATIVISTIC LASER-MATTER INTERACTION

penetrate efficiently past the critical surface. Instead, the electrons near the edge of the plasma-vacuum interface are directly affected by the incoming laser field. The perpendicular component of the laser light drives out electrons, which start to oscillate at the vacuum-plasma boundary. As the field reverses the electrons are accelerated back into the plasma. Because the plasma is overdense and the laser can only penetrate the plasma up to the skin depth l_s , the electrons accelerated back into the plasma are shielded from the laser field. Therefore they can penetrate deeper into the plasma, where they eventually dissipate their energy through collisions.

2.4.3 Relativistic $\mathbf{j} \times \mathbf{B}$ heating

At higher intensities, above 10^{18} Wcm^{-2} , the so-called $\vec{j} \times \vec{B}$ heating becomes important. Similar to the Brunel heating, an almost step like density gradient and linear polarisation of the laser beam is required. In this case the electrons are driven longitudinally by the $\vec{v} \times \vec{B}$ term of the Lorentz force. A linearly polarised wave $\vec{E} = (0, E_0(x)\cos(\omega t), 0)$ gives rise to the longitudinal force

$$\vec{f}_x = -\frac{m}{4} \frac{\partial \vec{v}_{os}(x)}{\partial x} (1 - \cos(2\omega t)) \quad (2.46)$$

The first part describes the electron acceleration in the direction of the laser propagation and the second term describes the fast oscillation of the laser pulse in propagating direction. The second term is responsible for the plasma heating similar to the Brunel mechanisms at twice the laser frequency. The $\vec{j} \times \vec{B}$ heating works for any polarised light wave but circular, and is more effective for normal incidence. In the case of a circularly pulse the driving force has no oscillating component and the plasma heating is suppressed, as it was shown in a previous section. This suppression is relevant in the special cases where plasma expansion by the laser is not desired.

2.5 Relativistically Induced Transparency

When an intense laser pulse interacts with an overdense nanometre thin foil, the plasma can become relativistically transparent during the interaction, which can alter the dynamics of the charged particles. Relativistically Induced Transparency (RIT) (74, 75, 76) occurs due to a combination of two simultaneously occurring processes. Firstly, the plasma is heated by the laser pulse, thereby driving expansion, leading to a

2.5 Relativistically Induced Transparency

broader plasma, which effectively reduces the classical electron density. Secondly, the critical density is relativistically corrected with increasing laser intensity. When the electron density is lower than the relativistically corrected critical density, the laser can propagate through the target (see figure 2.3). RIT can also occur if the laser longitudinal ponderomotive force compresses the target, reducing its thickness to the order of the plasma skin depth (77). This regime has proven promising for some emerging acceleration mechanisms, including the so-called Breakout Afterburner (which will be introduced in section 2.7.3). Because the laser is able to propagate through the target, it can couple more efficiently to the hot electrons that have been generated at an earlier stage of the interaction. Experimentally it is difficult to monitor the on-set of RIT, but cameras looking at the laser fundamental wavelength and second harmonic can be used during experiments, which allows the measurement of light transmission through the plasma, thereby giving an idea of the degree of RIT (see figure 2.4). These experimental measurements can be benchmarked with simulations to verify that RIT has actually occurred.

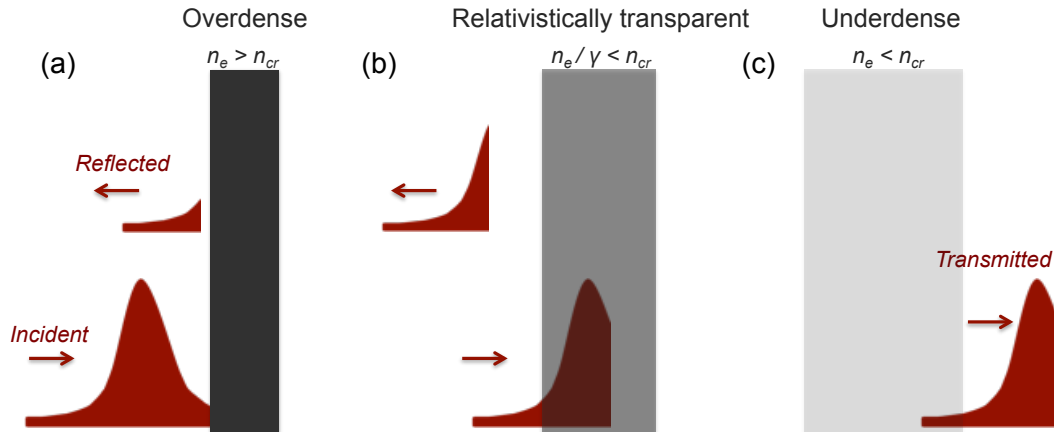


Figure 2.3: Relativistically Induced Transparency - Concept of relativistically induced transparency. In (a) the plasma is classically overdense. (b) When the laser impinges on the front surface, it drives plasma expansion and until (c) with the relativistically corrected plasma density, the target becomes relativistically transparent

The threshold intensity for RIT can be calculated by equating the relativistically corrected critical density with the electron density.

$$\frac{n_e}{\gamma} = n_c \tag{2.47}$$

2. RELATIVISTIC LASER-MATTER INTERACTION

$$\gamma = \sqrt{1 + \frac{a_0^2}{2}} \approx \frac{a_0}{\sqrt{2}} \quad (2.48)$$

$$a_0 \geq \sqrt{2} \frac{n_e}{n_c} \quad (2.49)$$

In practice the threshold intensity for RIT may seem somewhat lower than expected from this equation because a pre-pulse may cause expansion of the plasma, reducing the electron density encountered by the main pulse, and the main pulse itself reduces the local electron density through the ponderomotive force.

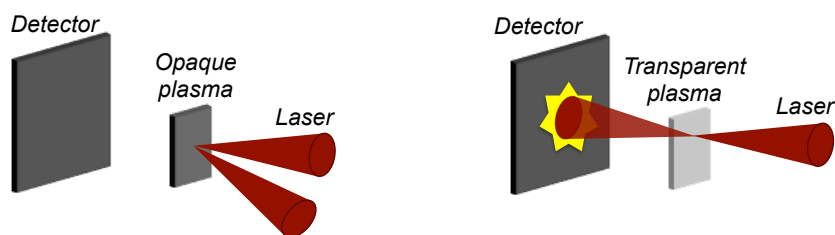


Figure 2.4: Diagnostic RIT - The cartoon shows how RIT was experimentally diagnosed during the campaigns with the Astra Gemini and Vulcan laser systems at the Central Laser Facility. Two cameras were placed at the rear side of the chamber to measure reflected light at the laser fundamental frequency and second harmonic.

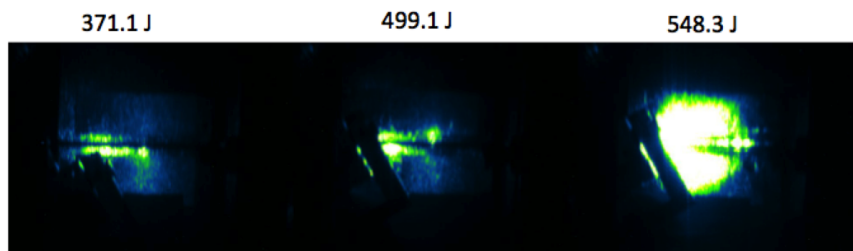


Figure 2.5: Measurement RIT - Three images showing experimental measurements of RIT. The light was reflected of an aluminium foil that was placed on top of the radiochromic film stack. The measurements show that the on-set of transparency is highly sensitive on the laser energy.

2.6 Plasma instabilities

When an ultra-intense laser is interacting with thin solid targets, instabilities can develop. Sometimes these instabilities can have advantageous effect, whereas other impede the generation of ion beams. The following section will describe the two most relevant instabilities that play an active role during thin foil laser interaction.

Rayleigh-Taylor instability The Rayleigh-Taylor instability (RTI) (78) is one of the most prominent ones and occurs when perturbations develop if a light fluid is pushed into a heavy fluid. A key signature of the RTI is the formation of bubbles and spikes at the interface as the lighter fluid is propagating into the heavier fluid. In a classical case the RTI can be seen as a heavier fluid pushing into a less denser fluid under the influence of gravity. The bubbles and spikes are formed when the two fluids, which were maintaining initially an equilibrium, experience a small perturbation which causes pressure variations. This bubble-like structures can be imprinted in the spatial profile of the ion beam. RTI can be counted to the hydrodynamic instabilities, also much like the Richtmeyer-Meshkov instability (79, 80), and is therefore usually associated with fluids. However the same perturbation can occur in a plasma. Therefore the light of the laser is assumed as the lighter photon fluid and the plasma as the heavier fluid.

Streaming or Buneman-type instability The streaming or Buneman-type instability (81) can promote energy transfer from the accelerated electrons to the plasma ions. When a beam of particles or a current drives through a plasma, in a way that different species experience different drifts relative to one another, this is referred to as streaming instability. The drift energy enables the streaming instability, such as the Buneman instability, by exciting wave modes and transferring energy into oscillations. This instability can act as a mediator between the electrons and ions, as proposed in the Breakout-Afterburner ion acceleration mechanism (section 2.7.3) (82). In this case a stream of electrons confined by a magnetic structure driven by the laser through the relativistically transparent target has a significantly larger relativistic velocity to the unmagnetised plasma ions (83). In the non-relativistic case the dispersion relation can be derived from the linearised motions of equations and Poisson's equation as

$$1 = \omega_{pe}^2 \left(\frac{m_e/M_i}{\omega^2} + \frac{1}{(\omega - kv_e)^2} \right) \quad (2.50)$$

2. RELATIVISTIC LASER-MATTER INTERACTION

where ω_{pe} is the electron plasma frequency, v_e the electron drift and m_e and M_i the electron and ion mass, respectively (84). For complex wave modes ω with a positive imaginary part $\text{Im}(\omega)$ the instability grows exponentially. The growth rate follows as $\gamma_i \approx (m_e/M_i)^{1/3}$. In this case, the drift energy of the electrons can be transferred to the plasma ions by exciting wave modes with a phase velocity that is comparable to the velocity of the bulk ions, hence resonantly accelerating them.

2.7 Laser-driven ion acceleration

Laser-driven ion acceleration has been a vivid field of research for almost two decades. The laser-plasma interaction is a very complex process, which depends on many laser and plasma parameters like laser irradiance, target thickness and areal density. Whereas electrons can already be directly accelerated to relativistic energies by the laser field with "moderate" laser intensities of the order of 10^{18} Wcm^{-2} (see equation 2.51), this is not the case for the ions. Replacing the electron mass in equation (2.14) by the proton mass, the relativistic threshold irradiance is given by

$$I_0\lambda[\mu\text{m}]^2 = \chi\left(4.62 \times 10^{24} \text{ Wcm}^{-2}\right)a_0^2 \quad (2.51)$$

where $\chi = 1$ for linear and $\chi = 2$ for circular polarisation. Therefore, currently available laser intensities of the order 10^{22} Wcm^{-2} are at least two orders of magnitude below this threshold intensity. Hence, all currently investigated acceleration mechanisms are based on the energy transfer from the electrons to the ions. A number of different mechanisms have been identified theoretically and some of them have also been experimentally evidenced. The interaction schemes can be divided into processes involving the interaction with an overdense plasma (Target Normal Sheath Acceleration, Radiation Pressure Acceleration), near-critical plasma (Breakout-Afterburner, Radiation Pressure Acceleration) and underdense plasma (pure shock acceleration). In the following sections, the most relevant acceleration mechanisms for the interaction of a short laser pulse with an (initially) overdense solid target are presented. It is important to note that it is not possible to draw an exact line between the on-set of different accelerations mechanisms. Several schemes can act simultaneously or at different stages of the interaction and similar ion energies with similar scaling can be achieved in different regimes. Therefore it is sometimes not trivial to assign the dominant acceleration

regime in simulations and especially in experimental studies. There are a number of existing scaling laws and numerical results, which link the laser and target parameters to the ion beam generation. This will be addressed in more detail in chapter 6 in the context of the feasibility of ion acceleration experiments with the VEGA laser system.

2.7.1 Target Normal Sheath Acceleration

The Target Normal Sheath Acceleration (TNSA) is the most widely studied mechanism and has been tested successfully in experiments and simulations (85, 86, 87). In the TNSA scheme, a linearly polarised intense laser pulse is impinging on a relatively thick solid target of the order of micrometres (as is shown in figure 2.6). The rising edge of the laser pulse is usually intense enough to ionise the target, generating a plasma. The laser energy is then absorbed at the front side of the plasma surface, thereby generating copious amounts of hot electrons with temperature $k_B T$. The energy can be estimated by the absorption through the $\vec{j} \times \vec{B}$ heating to $k_B T = m_e c^2 (\sqrt{1 + a_0^2/2} - 1)$ (88). These hot electrons produced during the interaction then propagate through the target, thereby setting up a large charge separation field of the order of TV/m at the rear side. This drives field ionisation of the atoms located at the rear side. The extent of the charge separation field is given by the Debye length (see equation (2.44)) of the hot electrons, at which electric fields of the plasma are screened out. The ions that are present at the rear side of the plasma are then subsequently accelerated to high energies by this quasi-static sheath field. Electrons are continuously pulled back into the target by the fields and replaced by recirculating hot electrons from the front side. This sheath field is oriented normally to the target, and therefore the ions are accelerated in the perpendicular direction regardless of the incidence angle of the incoming laser pulse; hence the name Target Normal Sheath Acceleration. The electric field scales with $E_{sheath} \approx k_B T_h / e \lambda_D$ and extends over a length of a few micrometres. Protons are preferentially accelerated by TNSA owing to their high charge-to-mass ratio and most of the electron energy will be transferred to the protons, while they electro-statically shield the sheath field to heavier ions. This prevents further ionisation of the bulk ions and their acceleration. Usually the protons originate from surface contaminants on the back side of the target. Heavier ions can also be accelerated by the TNSA mechanisms, however this requires some target preparation, e.g. laser ablation of the rear side of the target to remove hydro-contaminants (89).

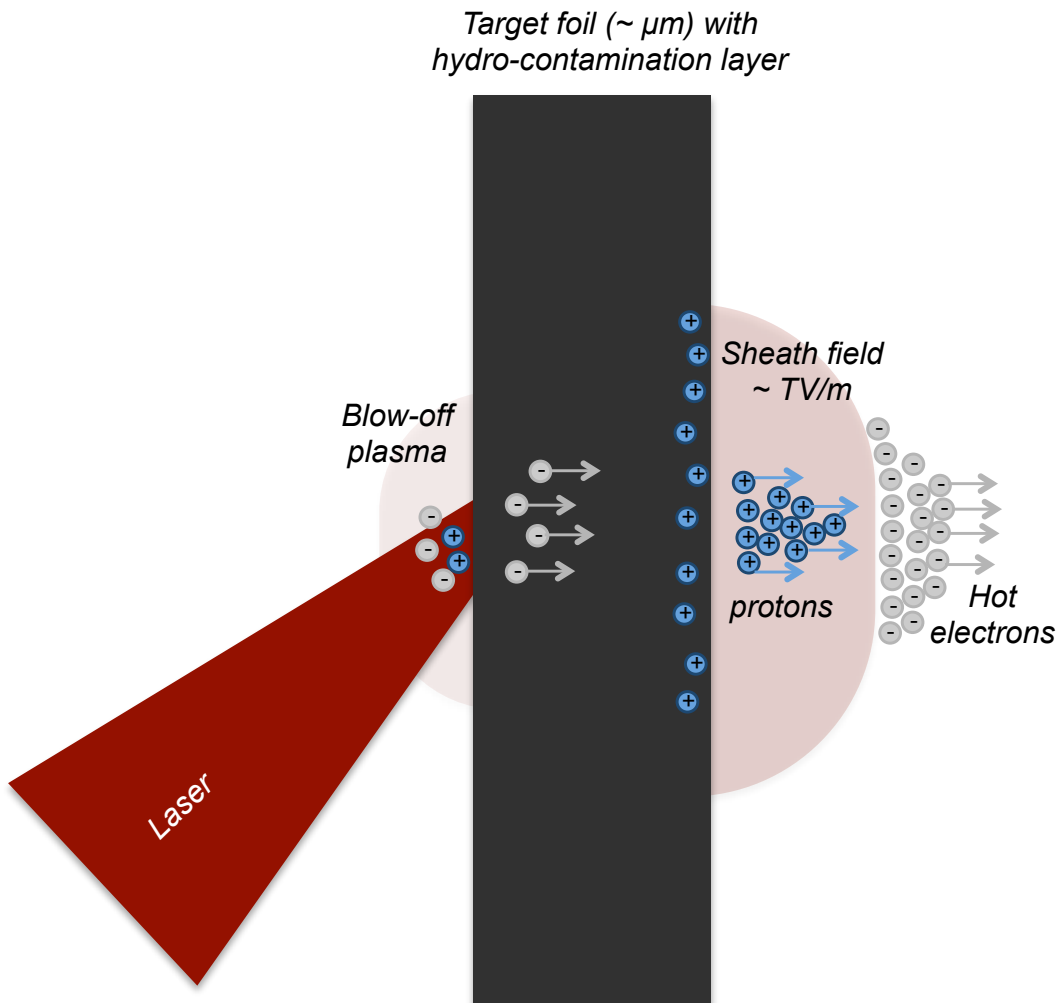


Figure 2.6: Target Normal Sheath Acceleration - Concept of the TNSA mechanism: The incoming high-intensity laser produces copious amounts of hot electrons. The electrons propagate through the micrometre thick overdense plasma and set up a strong charge separation field at the rear side of the target. Protons, present as hydro-contaminants at the back side, are subsequently pulled out and accelerated to high energies.

It is important to note that the plasma stays overdense throughout the interaction, so the laser light is not pushing through the plasma and coupling to the electrons at the rear side. Therefore TNSA is a surface-dominated acceleration mechanism. One of the striking features of TNSA-generated protons is their ultra-low emittance and a small source size of the order of $100\mu\text{m}$ (90). However, this is still much larger than the currently achievable laser focal spots, which are of the order of $10\mu\text{m}$. The difference can be caused by transverse spreading of the hot electrons by deflection in the field or during the recirculation process. The sheath field does not extend perfectly in parallel to the plasma rear surface. Instead the field builds radially, which also impedes the generation of mono-energetic particle beams. The thermal spectrum therefore results from the transversely inhomogeneous charge separation field, that extends over several times the laser focus on the back side. Many scaling laws (e.g. (86) and (87)) have been developed to estimate the obtainable final energies of the ions and usually the maximum energy scales as $E_{max} \propto T_h \propto a_0 \propto \sqrt{I_L}$. The reachable energies with TNSA lie within a range of a few tens of MeV up to more than a hundred MeV. There have been experimental efforts to produce mono-energetic beams by tailoring the targets to restrict the source of ions to a smaller volume. This leads to a more homogeneous accelerating field, however the conversion efficiency is very low.

Some acceleration can also occur at the front side of the target. However due to the strong plasma expansion driven by the pre-pulse of the laser, the scale length is significantly larger, which results in much smaller charge separation fields, resulting in lower ion energies.

2.7.2 Radiation Pressure Acceleration

In recent years the acceleration of ions by means of the Radiation Pressure has been emerging as a promising technique. In principle, the acceleration takes place by pushing the whole plasma bulk by the means of the light pressure for a perfectly reflecting mirror. In contrast to TNSA, which is a surface-dominated mechanism, Radiation Pressure Acceleration (RPA) allows therefore the acceleration of the whole target volume, which could drastically reduce the energy spread of the generated ion beam. Scaling laws for the RPA predict a much more favourable scaling of $E \propto I_L^2$ opposed to the $E \propto I_L^{0.5}$ scaling in the TNSA regime (71, 91). The RPA mechanism can be divided into two distinct regimes; Hole-Boring (92) in case of thicker plasmas (micrometre-scale) and

2. RELATIVISTIC LASER-MATTER INTERACTION

Light-Sailing (93, 94) for thinner plasmas (nanometre-scale) (see figure 2.7). In the following these two will be described.

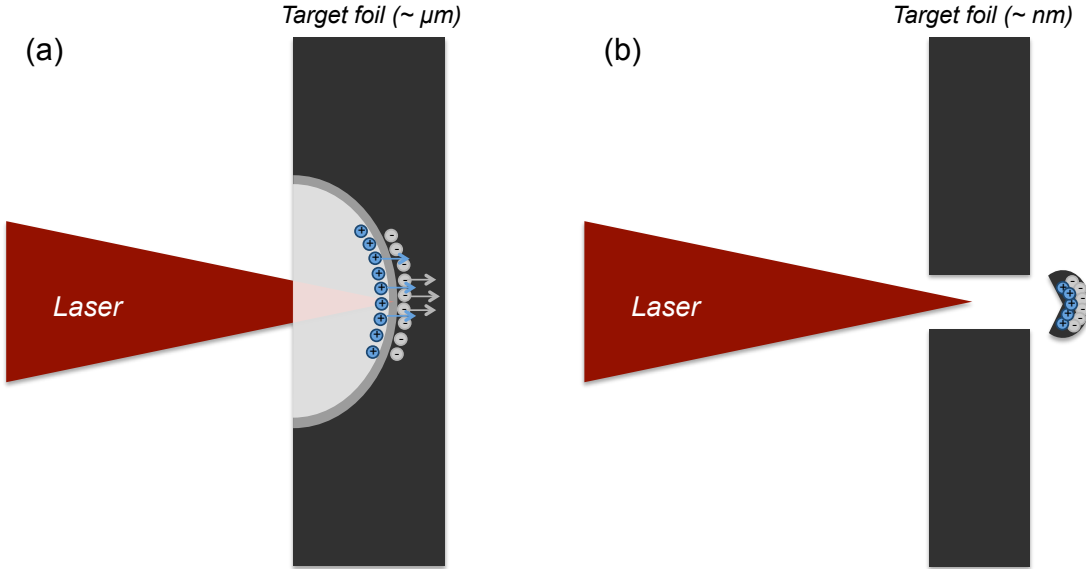


Figure 2.7: Radiation Pressure Acceleration - Hole-Boring (a): Plasma electrons in a micrometre-thick overdense plasma are pushed steadily by the radiation pressure. The ions are collisionless shock-accelerated in the formed strong electrostatic field. **Light-Sailing (b):** In a nanometre-thin overdense plasma, the ions and electrons can be modelled as a moving mirror that is propelled forward by the radiation pressure (like in the sailing paradigm).

2.7.2.1 Hole Boring

For thicker targets of the order of micrometres, the light pressure can give rise to the so-called Hole Boring or collisionless shock acceleration (92). A laser with an intensity of about 10^{19} Wcm^{-2} has an equivalent radiation pressure of tens of GBar. When impinging on a thick target foil, this pressure can steepen the density profile and bend the critical surface inwards and successively drill a hole in the overdense plasma (hole-boring). This results in a snowploughing of the bulk electrons, until the material pressure equals the radiation pressure. In this equilibrium state the velocity of the accelerated ions can be derived by considering a pressure balance. An electron-free area is generated behind the snow-ploughed electron spike. Assuming total reflection of the incoming laser pulse from this electron spike, the ions left behind are then pulled by the arising charge-separation field, forming an ion spike. The unperturbed

ions impinging on these moving spikes are reflected, thus accelerated, by the electric field between the spikes. At the turning points the ion velocity changes sign, and at zero velocity the ion density tends to infinity. This is also the case for the electron spike. Thus, an electro-static shock propagates into the plasma. In the case of highly overdense plasmas, the unperturbed plasma electrons and ions are nearly all reflected by the laser ponderomotive pressure and the longitudinal electric field between the two spikes. Therefore circular polarisation is preferred as it suppresses the heating of the plasma.

Unlike the "light sail" case, which will be discussed in the following section, hole boring has a quasi-stationary velocity because the radiation pressure is balanced by the momentum change of the continuously reflecting particles of the unperturbed plasma, mostly ions due to their larger mass. When the ions accelerated by the shock reach the target rear surface, they can get an additional energy due to the charge-separation field at the target rear side.

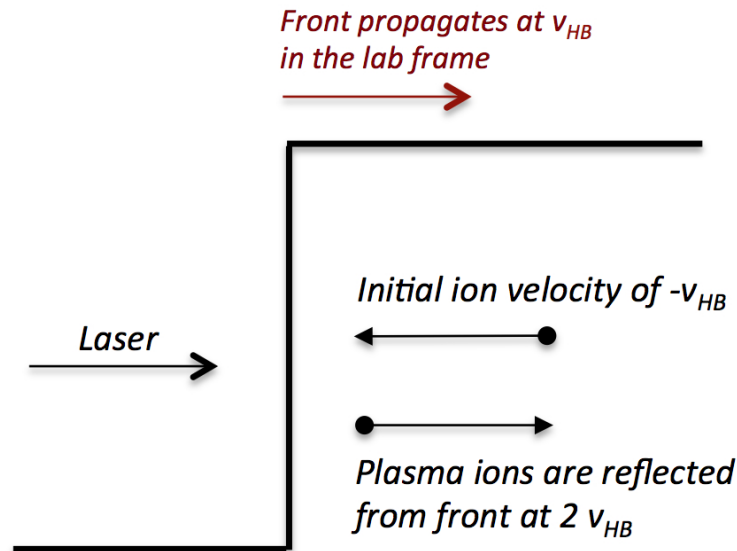


Figure 2.8: Hole-Boring - The ions are accelerated by reflection from the hole-boring front, in the rest frame of the front.

In the simple *non-relativistic case*, the change in momentum of the photons, $\delta p_{photons}$

2. RELATIVISTIC LASER-MATTER INTERACTION

in time, δt , in the *instantaneous rest frame* can be written

$$\delta p_{photons} = (1 + R) \frac{I_L}{c} A \delta t \quad (2.52)$$

with R being the reflection coefficient of the surface, I_L the intensity of the laser and A being the area upon which the laser is incident.

For a plasma with ion density n_i , the change in momentum of the ions in the *instantaneous rest frame* can be written as

$$\delta p_{ions} = 2m_i v_{hb} n_i A v_{hb} \delta t \quad (2.53)$$

where $n_i A v_{hb} \delta t$ is the total number of particles reflected within the time δt . The plasma that is at rest in the *lab frame* approaches the plasma surface with $-v_{hb}$ in the *instantaneous rest frame*. Hence, a beam of plasma is propagating at $+v_{hb}$ away from the plasma surface to ensure particle number conservation. Equating 2.52 and 2.53 (assuming perfect reflectivity, $R=1$) gives the momentum balance in the *instantaneous rest frame* by (95)

$$2n_i m_i v_{hb}^2 = \frac{2I_L}{c}, \quad (2.54)$$

where n_i and m_i are the number and mass of the plasma ions, respectively. The *dimensionless pistoning parameter* Ξ is defined as

$$\Xi = I_0 / m_i n_i c^3 = 1 / \rho c^3, \quad (2.55)$$

where ρ is the mass density of the plasma. From equation 2.54 the non-relativistic ion velocity or hole boring velocity, v_{hb} , in the *instantaneous rest frame* can be determined

$$v_{hb} = \sqrt{\frac{I_L}{n_i m_i c}} = \sqrt{c^2 \Xi} \quad (2.56)$$

In the *lab frame* the velocity of the accelerated ions is twice the hole boring velocity, i.e. $v_i = 2v_{hb}$ (see figure 2.8)

$$v_i = 2\sqrt{\frac{I_L}{n_i m_i c}} = 2\sqrt{c^2 \Xi} \quad (2.57)$$

The non-relativistic ion energy ϵ_i in the *lab frame* is therefore given by

$$\epsilon_i = \frac{2I_L}{n_i c} = 2m_i c^2 \Xi \quad (2.58)$$

In the *relativistic case*, the momentum balance of the plasma surface in the *instantaneous rest frame* is given by

$$\frac{2I_L}{c} \left(\frac{1 - v_{hb}/c}{1 + v_{hb}/c} \right) = 2\gamma_{hb}^2 m_i n_i v_{hb}^2, \quad (2.59)$$

where $\gamma_{hb} = (1 - v_{hb}^2/c^2)^{-1/2}$.

The relativistic ion velocity in the *instantaneous rest frame* can be derived to

$$\beta_{hb} = \frac{v_{hb}}{c} = \frac{\sqrt{\Xi}}{1 + \sqrt{\Xi}}, \quad (2.60)$$

The relativistic kinetic ion energy in the *lab frame* is calculated by using the appropriate Lorentz transformation for the ion velocities and is given by

$$\epsilon_i = m_i c^2 \left[\frac{1 + \beta_{hb}^2}{1 - \beta_{hb}^2} - 1 \right] \quad (2.61)$$

or in terms of the pistoning parameter,

$$\epsilon_i = m_i c^2 \left[\frac{2\Xi}{1 + 2\sqrt{\Xi}} \right] \quad (2.62)$$

2.7.2.2 Light Sailing

When the target becomes sufficiently thin or the hole boring front is reaching the target rear, the so-called Light Sailing phase begins. In this case the thickness becomes comparable to or less than the skin depth. The target is accelerated as a whole by the incoming radiation pressure (see figure 2.9). The light pressure P_R can be related to the laser intensity via

$$P_R = \frac{2I_L}{c} \quad (2.63)$$

This scheme is accessible with short laser pulses (~ 30 fs) with high intensity and an ultra-high contrast (to prevent target destruction). The target foil is accelerated as a whole purely by the pressure of light. Again, in the first stage, the laser energy is mediated to the target electrons (ideally all of them) whereas the ions remain at rest due to their higher mass. The charge separation field quickly rises and once it is strong enough it pulls the ion layer as a whole, thereby accelerating them to high energies. In the second stage, the electron and ion layer are ideally co-propagating with the laser pulse, just like the light-sail paradigm. At the final acceleration phase, the ions moving

2. RELATIVISTIC LASER-MATTER INTERACTION

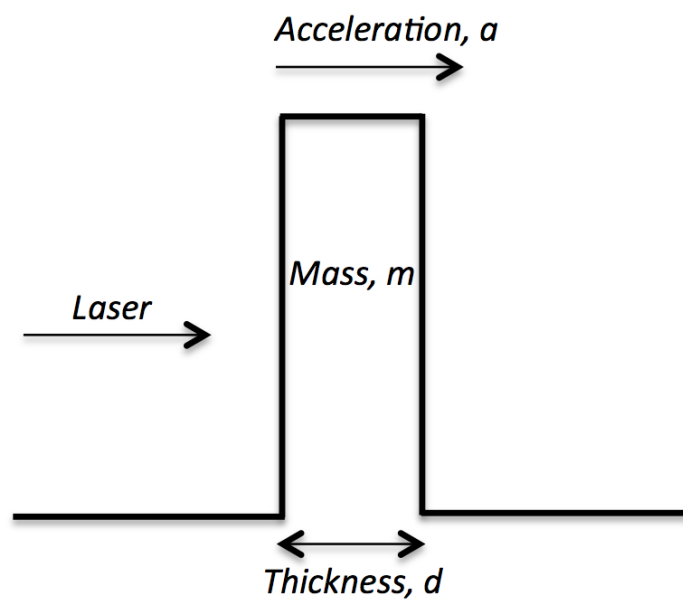


Figure 2.9: Light-Sailing - The plasma slab is pushed as a whole by the radiation pressure of the laser pulse, accelerating the ions.

with nearly the same velocity as electrons take most of this energy due to their much larger mass (12).

In the simple non-relativistic 1D case, the acceleration of the ions within a plasma slab with total mass, M , and area, A , can be found using Newton's second law and the incoming radiation pressure P_R .

$$\frac{dp_i}{dt} = Ma = \frac{(1+R)I_L}{c}A \quad (2.64)$$

The mass can also be expressed in terms of the density, ρ and thickness d , of the target. Therefore the acceleration is given by

$$a = \frac{(1+R)I_L}{\rho dc} \quad (2.65)$$

Approximating the temporal profile of the laser intensity as a Gaussian the ion velocity can be shown to scale linearly with intensity, and consequently the energy of the accelerated ions scales as $E \propto I_L^2$. Relativistically the Light Sailing acceleration is modelled as a relativistically accelerated plasma mirror, taking into account the Doppler downshift of the laser radiation experienced by the receding target. In the lab frame the plasma mirror is undergoing acceleration, therefore for simplicity, the velocity at a particular point during the acceleration is picked and used as the instantaneous velocity of the frame in which the calculations can be performed. The momentum of the ions within the plasma can be determined by equating the radiation pressure due to the relativistically (Doppler) adjusted laser intensity with the gain in momentum of the ions (96)

$$\frac{dp}{dt} = \frac{(1+R)(1-\beta)I_L}{c(1+\beta)} \quad (2.66)$$

This leads to an individual ion momentum given by,

$$p_i = n_i m_i c \left(\sinh(\psi) - \frac{1}{4\sinh(\psi)} \right) \quad (2.67)$$

where $\psi = \frac{1}{3} \sinh^{-1} \left[\frac{6It}{m_i n_i I_d c^2} + 2 \right]$.

Increasing the thickness above this optimum value leads to an increase in overall mass of the target and therefore a reduction in the acceleration. However, below the optimum the required balance between radiation pressure and the resultant charge separation cannot be established and the electrons are stripped from the target, leaving the remaining ions to undergo Coulomb explosion.

2. RELATIVISTIC LASER-MATTER INTERACTION

The ions must be quickly accelerated up to relativistic velocities in order to suppress the development of instabilities. In case of longer pulses the Rayleigh-Taylor instabilities destroy the foil, and the simple "light sail" scenario is no longer valid. The instability effectively reduces the target areal density with time, which leads to larger maximum energy, albeit the number of ions with this energy is much smaller. As the foil becomes relativistic, the optimum condition cannot be always satisfied if the areal foil density is constant, because in the boosted frame co-moving with the foil the laser amplitude remains the same (it is relativistically invariant) but the dimensionless areal density increases due to the laser frequency downshift. It turns out that the gradually decreasing areal density can indeed provide larger ion energies and larger efficiencies. The relativistic ions obtained in the radiation pressure acceleration can be further accelerated in the wakefield.

The laser polarisation is a crucial parameter. In the case of linearly polarised light, the laser drives plasma expansion, which effectively reduces the plasma density. For ultra-intense interaction, this could lead to a near-critical plasma, in which case parts of the laser light will propagate through the plasma. Light-Sailing RPA however requires a highly overdense plasma. In the case of circular polarisation the Brunel heating, resonance absorption and $\vec{j} \times \vec{B}$ heating can be efficiently suppressed and the plasma can be accelerated as a whole. This is due to the vanishing longitudinal oscillating term with 2ω , as shown previously (see equation 2.25) Esirkepov *et al.* (97) showed that it is also possible to accelerate protons to relativistic energies with a linearly polarised laser, however this requires an intensity above 10^{23} Wcm^{-2} (97). In this case the force of the laser pushes and compresses the electrons into the target, which set up an ultra-high charge separation field accelerating the ions rapidly within one laser cycle, making it independent of the polarisation.

2.7.3 Breakout Afterburner

All aforementioned ion acceleration mechanisms have assumed the interaction of an intense laser with an overdense plasma, which stays opaque throughout the entire interaction. As explained previously, the interaction is fundamentally different when the target goes relativistically transparent. The so-called Breakout Afterburner (BOA) mechanism takes place at this stage. It has been proposed as a novel mechanism for the efficient acceleration of ions by Yin *et al.* (82, 98) and Albright *et al.* (99). Whereas

Target Normal Sheath Acceleration is a surface-dominated mechanism, the interaction in BOA changes to volumetric, since all electrons present in the bulk of the plasma can couple to the laser that is propagating through the target. Analogously to the TNSA mechanism, BOA requires a linearly polarized laser pulse that interacts with the initially overdense plasma. The different absorption mechanisms produce hot electrons that propagate through the plasma and set up a sheath field (enhanced TNSA), while the opaque bulk of the target provides cold electrons for the return current in the laser conversion region, where they are subsequently converted to hot electrons. The skin depth is increasing during the process, allowing more of the laser field to reach into the plasma and provoke further hot electron generation. When the target is initially thin enough (nanometre), eventually all of the bulk electrons are volumetrically heated and introduce a huge longitudinal electric field (TV/m) in the target by means of a plasma wave.

In figure 2.10 the BOA process is illustrated. In the initial TNSA acceleration phase, the linearly polarised laser pulse generates copious amount of hot electrons, that propagate through the target and set up the rear sheath field. There are two distinct populations of electrons; laser-heated and cold background electrons. The acceleration of the ions by the sheath field is modest compared to the later acceleration stages.

During the second "enhanced TNSA" stage, almost the entire bulk of cold background electrons is converted into hot electrons (for ultra-thin targets). The plasma is still overdense, but the skin depth becomes comparable to the target thickness, during this on-set of relativistically induced transparency. At this stage, the entire layer of electrons within the target oscillates in the laser field, reinforcing the electron heating to a point where there are almost no cold electrons left. The ions experience an electric field which consists of a space-charge separation from the sheath and a ponderomotive drive from the laser. In sufficiently thin targets, the ions are accelerated as a solitary bunch peaked around a well defined mean-energy.

In the Breakout Afterburner (BOA) phase, the plasma, turns classically underdense and the laser can propagate through the plasma. This results in an enhanced longitudinal electric field compared to the earlier stages of the interaction, that co-propagate with the ions. The ions are accelerated as a bunch to high energies. The enhanced electric field at this stage is attributed to the electron dynamics in the penetrated laser field. According to plasma kinetic theory, a large relative drift between the electrons

2. RELATIVISTIC LASER-MATTER INTERACTION

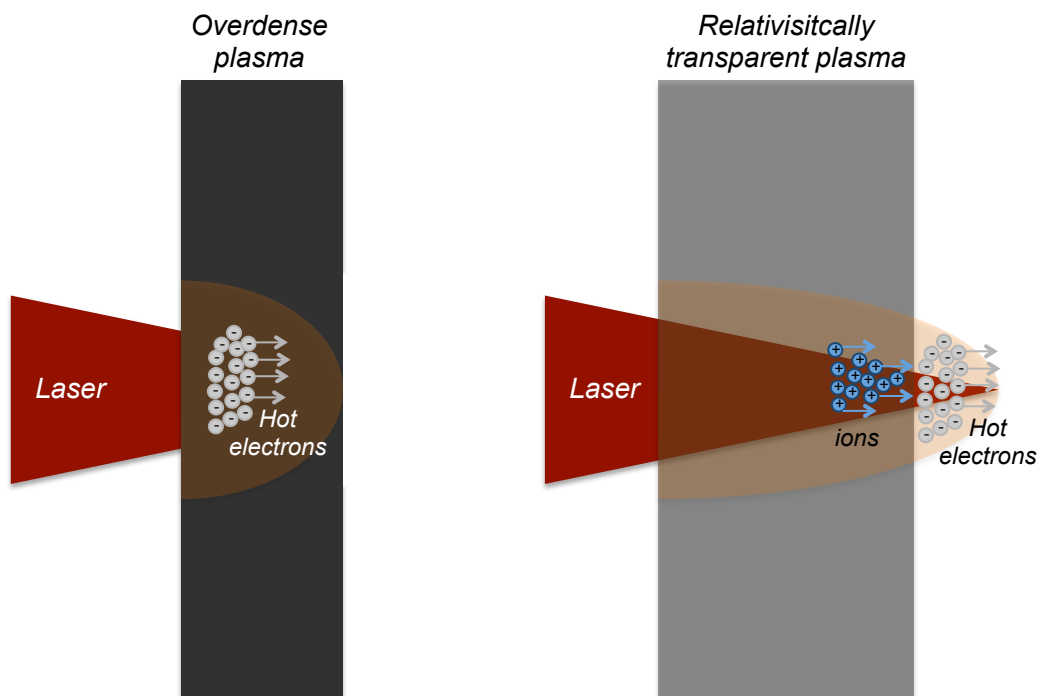


Figure 2.10: Breakout Afterburner - Concept of the Breakout Afterburner mechanism. The acceleration occurs in several steps. See text for details.

and ions gives rise to a Buneman-like instability (see section 2.6). While the electron beam moves with relativistic speeds, the ions are assumed to be cold and slowly (non-relativistic) moving. The Buneman-instability grows rapidly to reduce the relative drift between the electrons and ions. The phase velocity of the Buneman instability is resonant with the ions and results in an acceleration and eventual heating of the ions. The streaming and momentum transfer from the electrons to ions results in the electrons re-gaining their energy from the penetrating laser field. Therefore the instability can be maintained for a longer period, reinforcing the energy transfer to the ions.

After the BOA phase, the non-linear interaction among the light wave and particles, as well as possibly the relaxation of the ion distribution as a result of the Buneman instability causes the ion distribution to lose its monoenergetic character and break into smaller populations of lower energies. Finally the ions relax into an almost Boltzmann-like distribution with high cut-off energy, but low particle flux.

2. RELATIVISTIC LASER-MATTER INTERACTION

3

Methods

In the following, the methods used in the scope of this thesis will be laid out. The chapter is split into a description of the experimental techniques, including the laser systems, diagnostics and targets used, and numerical methods. The latter will lay out the fundamental equations of the particle-in-cell method and the assumptions made in the presented simulations.

3.1 Experimental methods

In the framework of this thesis a number of experimental campaigns were conducted with the laser systems Vulcan and Astra-Gemini of the Central Laser Facility at the Rutherford Appleton Laboratory in Oxfordshire, UK. The Vulcan laser delivers relatively long picosecond pulses with high energies (more than 500 Joules), whereas Astra-Gemini generates short 30 femtoseconds pulses with energies up to 30 Joules. Both belong therefore to the class of Petawatt lasers. The VEGA laser system that is currently being installed in Salamanca delivers also 30 femtoseconds short pulses with similar energies like Astra-Gemini. High-power laser systems generally comprise a low-power front-end and one or more amplification stages. The front-end produces typically a high repetition rate (\sim MHz) train of ultra-short (\sim tens of fs) pulses. Pulses are picked from the train at lower repetition rate and subsequently amplified by techniques such as Chirped Pulse Amplification (CPA) or Optical Parametric Chirped Pulse Amplification (OPCPA).

3. METHODS

Chirped Pulse Amplification If the ultra-short pulses were directly amplified, they would soon start to induce non-linear effects down the amplifier chain and damage the optical systems. In order to overcome this limitation the Chirped Pulse Amplification (CPA) technique was introduced in 1985 by Donna Strickland and Gerard Mourou (6). In principle, CPA follows three consecutive steps; stretching of the initially short laser pulse, subsequent amplification to high intensity and re-compression of the pulse (see figure 3.1). The seed pulse is stretched and dispersed into the frequency components of the pulse over different optical path lengths using a pair of diffraction gratings (alternatively prisms or fibres can also be used to stretch the pulse). By stretching the duration of the pulse the peak power is reduced and its energy can therefore be safely amplified without producing any damage or non-linear effects in the optics. Therefore the frequency of the pulse becomes linearly time-varying and a chirp is produced. This longer pulse can then be conventionally amplified in a regenerative (100) or multi-pass laser amplifier (101). In the final stage, the pulse is re-compressed with another set of dispersive optics. By using the CPA technique nowadays a number of laser systems are able to produce ultra-short, high-intensity (10^{22} Wcm⁻²) laser pulses in successive amplification stages, with peak powers in the petawatt range.

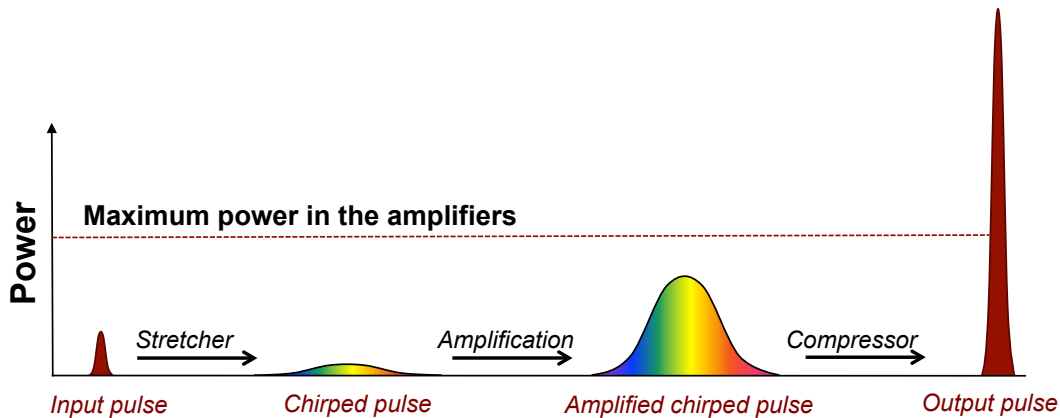


Figure 3.1: Chirped Pulse Amplification - Illustration of the CPA concept: Stretching of the initially short laser pulse, amplification to high intensity and re-compression of the pulse.

Optical Parametric Chirped Pulse Amplification As shown above, Chirped Pulse Amplification is used to generate laser pulses with high peak powers overcoming

the limitations imposed by non-linearities and damage threshold of the laser optics. However the amplification is affected by gain-narrowing (102) which limits the pulse bandwidth and therefore limits the shortest pulse length achievable. To overcome this caveat, the Optical Parametric Chirped Pulse Amplification (OPCPA) was invented by Dubietes *et al.* in 1991 (103).

In OPCPA the seed pulse is stretched and then amplified by an optical parametric amplifier (OPA), where the energy of a high-energy narrow-band long-pulse from a pump laser is parametrically transferred to the low-energy chirped seed pulse in a non-linear crystal. This technique allows the amplification of laser pulses with a very large bandwidth reducing the minimum pulse length possible. Also, as the pump laser is not absorbed by the crystal, OPAs support higher average pump energies than most laser media.

By combining the concept of CPA and OPA, pulses with high intensities and ultra high peak powers can be achieved.

3.1.1 Laser systems

3.1.1.1 Vulcan

The Vulcan laser is a Nd:Glass laser system with a central wavelength of 1054 nm. It provides eight beam lines, of which two can be operated either in short (~ 0.5 ps) or long (\sim ns) pulse mode, with the remaining six operating only in a long pulse mode. In the experiments that were carried out in the framework of the thesis, only the Petawatt arm of Vulcan was used operating in its short-pulse mode. It delivers around 500 Joules in half a picosecond, producing a peak power of a Petawatt, by using the optical parametric chirped pulse amplification (OPCPA) technique. The system is capable of delivering intensities up to 10^{21} Wcm⁻² depending on the size of the focal spot. The seed pulse is generated by a Ti:Sapphire Kerr-lens mode-locked oscillator. The crystal passively mode-locks the pulse focusing the higher intensity laser light more than the lower intensities. The seed pulse is stretched by a Öffner stretcher to 2.4 nanoseconds, before it is sent to the optical parametric amplifier (OPA). The pump lasers are Q-switched frequency-doubled Nd:YAG lasers providing pulses of 532 nm with an energy of 1 J in 15 ns. The amplification occurs in three stages to reduce the amount of amplified spontaneous emission.

3. METHODS

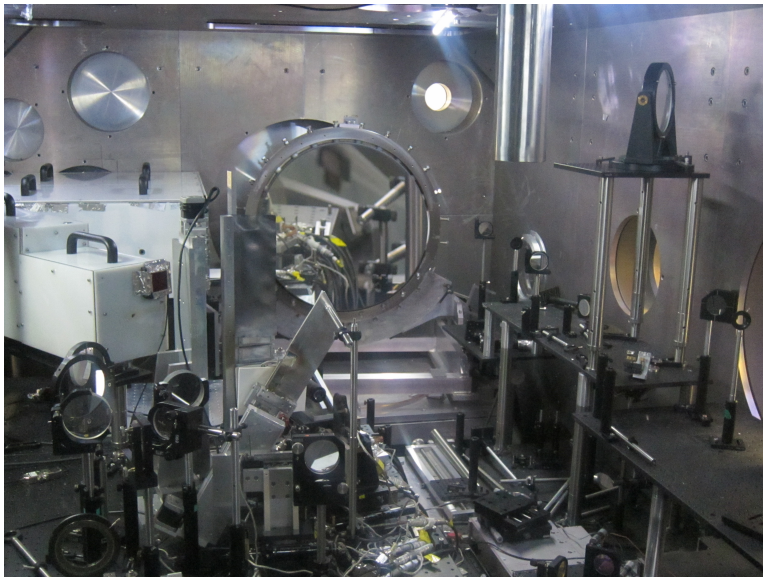


Figure 3.2: Vulcan target chamber - Picture inside the Vulcan target chamber. In the background, the $f/3$ off-axis parabolic mirror is seen. The target holder and plasma mirror arrangement are seen in the centre. The white boxes on the left contain the Thomson Parabola spectrometers.

The main amplification of the Petawatt combines Nd:silicate and Nd:phosphate amplifiers. By using this combination the effect of bandwidth narrowing can be reduced and the wavelength is centred around $\lambda = 1054.5$ nm. After passing through the Nd:silicate rod amplifiers (high gain) pumped by flash lamps, the pulse follows through the main Nd:phosphate rod and disc amplifiers. At the final stage of the amplification the pulse energy is around 650 J. To improve the final compression of the beam and the focus of the pulse, adaptive optics are used to correct any aberration picked up by the thermal changes during the amplification. This is done by a wave front detector, that detects the aberrations, and a deformable mirror using piezoelectrically controlled elements which adjusts the beam profile. The amplified beam is then fed to the target area (Vulcan Target Area Petawatt), where it is compressed under vacuum to a pulse duration of about 0.5 ps. The diameter of the grating ensures that the laser fluence is below the damage threshold of the following optics. The beam with a final diameter of about 600 mm then enters the target chamber and after hitting a turning mirror the beam is focused by a $f/3$ off-axis parabolic mirror (see figure 3.2) to a focal spot of 5-7 μm . In order to extract information on the pulse contrast and final energy on

the target, a leak through the back of the turning mirror is used to enable the use of a second-order auto-correlator to measure the pulse duration. The energy throughput is measured with calorimetry and usually found to be about 50% through the compressor.

3.1.1.2 Astra-Gemini

Astra-Gemini is a Ti:Sapphire laser with a central wavelength of 800 nm. It provides two beams, that each deliver 15 J in pulses in about 30 fs at a repetition rate of 0.05 Hz (i.e one shot every 20 seconds). The Gemini amplifiers use Ti:Sapphire crystals with a small signal gain of around 4.2 per pass to achieve the output energy of 25 J. The beam is mainly compressed by two gratings and a plane mirror. The bandwidth of the Gemini beam is around 35 nm, which exceeds the height of the second grating after dispersion by the first grating. Therefore the compressor uses a double pass, to correct the spatial dispersion. The compressed pulse is steered onto a mirror, which directs the beam to the interaction chamber (see figure 3.3).

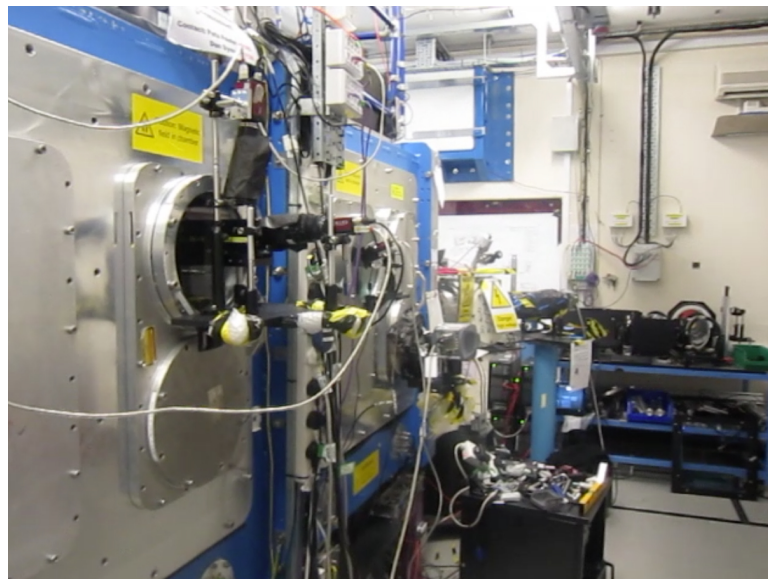


Figure 3.3: Astra Gemini target chamber - Picture showing the outside of the Astra Gemini target chamber.

The beam can be focused to a spot size of $3 \mu\text{m}$ at FWHM with an energy of about 2 Joules on target. The strong decrease in energy on target is due to the necessary employment of plasma mirrors to increase the pulse contrast, and also to transport

3. METHODS

optics (see section 3.1.2 for an explanation of how plasma mirrors work). The double plasma mirror arrangement enhances the intensity contrast to 10^{11} and 10^{10} , at 1 ns and 10 ps, respectively, prior to the peak of the pulse. The pulse can be focused using an $f/2$ parabolic mirror, to a calculated peak intensity of about $7 \times 10^{20} \text{ Wcm}^{-2}$. A deformable mirror is employed prior to focusing to ensure a high quality focal spot.

3.1.1.3 VEGA

The main laser system of Centro de Láseres Pulsados (CLPU) is the VEGA laser. VEGA is a Ti:Sapphire system with a wavelength centred around 800 nm. The laser will offer three independent outputs, at 20 TW (VEGA 1), 200 TW (VEGA 2) and 1 PW (VEGA 3) (parts of the amplification stage are shown in figure 3.4). Beside the achievable peak power, the two most striking features will be the high repetition rate of 10 Hz (VEGA 1 and 2)/1 Hz (VEGA 3) and the extremely high contrast of $10^{10} : 1$ at 1 ps. This will allow the study of laser interaction with ultrathin targets without the use of plasma mirrors. The simultaneous outputs will also allow pump-probe experiments.



Figure 3.4: VEGA Petawatt - Picture of the on-going installation of the VEGA Petawatt laser system. This shows the optical tables with parts of the amplification stage.

The front-end of the CLPU laser starts with the oscillator and uses a double-CPA

3.1 Experimental methods

architecture. Pulses are amplified by a regenerative amplifier and multi-pass amplifier both pumped by a CFR 200 YAG laser carrying 13 mJ and 100 mJ, respectively. The pulse is then fed into the first compressor, followed by a XPW for pulse contrast enhancement. With an energy of 30-50 μJ , the pulse is passed through a dazzler and subsequently amplified by another regenerative amplifier and mazzler (pumped by an ULTRA laser with 13 mJ) to about 0.8 mJ. After pulse cleaning, the final amplification in the front end is carried out by a multi-pass amplifier (pumped by a CFR 200 YAG laser), generating an output pulse with 25 mJ, $10^{12} : 1$ pulse contrast. The three outputs of VEGA share the same output pulse. In the following the amplification chain only of the Petawatt arm is described.

VEGA System	Energy	Pulse duration	Wavelength	Peak Power	Repetition rate
VEGA 1	600 mJ	30 fs	800 nm	20 TW	10 Hz
VEGA 2	6 J	30 fs	800 nm	200 TW	10 Hz
VEGA 3	30 J	30 fs	800 nm	1 PW	1 Hz or single shot

Table 3.1: VEGA laser parameters - Overview of the VEGA laser system parameters. All exits share the same front-end, thereby allowing the synchronisation of the different outputs for pump-probe experiments.

After the first splitter (one beam to VEGA 1) the pulse with then 22 mJ is amplified by a multi-pass amplifier (pumped by Propulse laser with 2.5 J) to 700 mJ. After the next beam splitter (200 mJ through-put) the pulse is picked by Pockel cells D20 and passes through a fast shutter. The 160 mJ beam is again amplified by two TITAN 3J pump lasers (together 7 J) to 2.4 J. After this stage, the beam passes through another Pockels D50 cell preventing back reflection down the laser chain. The final amplification from 2.2 J to 45 J is performed by 12 Titan 10 J (delivering together 120 J) pump laser. After the final compression a deformable mirror is employed for beam quality enhancement. The final petawatt output pulse carries 30 J in 25 fs with a pulse contrast of up to $10^{10}:1$. See table 3.1 for an overview of the VEGA parameters.

3. METHODS

3.1.2 Pulse contrast

No laser pulse is perfect. In practice an ultra-short femtosecond laser pulse is mounted on a picosecond long pedestal, accompanied by a nanosecond long amplified spontaneous emission (ASE) and low intensity replicas of the main pulse at specific times before and after the main laser pulse, the so called pre- and post-pulses (see figure 3.5). The intensity ratio between the ASE, the pedestal and the pre-pulses is called pulse contrast and it has different values for each of these contributions. The typical values range between 10^4 (poor contrast) to 10^{10} (high contrast). The pulse contrast is a very important parameter and defines to which extent the target is perturbed before the arrival of the main pulse (104). For the interaction of an intense laser with thin targets, the pulse contrast plays a crucial role. At intensities above 10^{20} Wcm^{-2} , the accompanying pre-pulse and amplified spontaneous emission pedestals are often intense enough to ionise or destroy the target prior to the arrival of the main pulse.

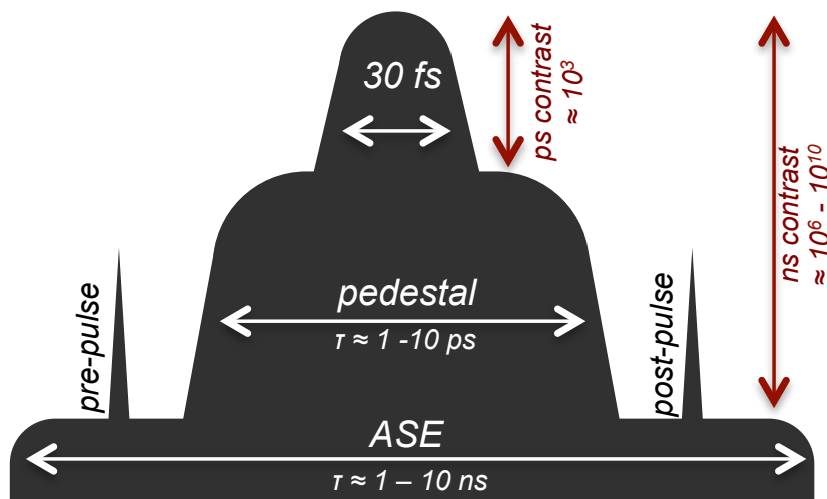


Figure 3.5: Temporal structure of an intense ultra-short laser pulse - Typical temporal structure of an intense ultra-short laser pulse, showing the different components contributing to the contrast at the nanosecond to picosecond range. Leakage from the regenerative amplifier; amplified spontaneous emission, picosecond pedestal and pre-pulses.

Since the rising edge of the laser pulse significantly influences the induced plasma heating, the interaction of ultra-intense laser pulses with solid targets and especially with ultra-thin targets requires very high contrasts.

For relatively thick (few tens of μm) targets, scale length pre-plasma contributes positively to the ion acceleration due to stronger main pulse absorption and self-focusing, while the sufficient target thickness prevents rear surface deterioration. In the case of nanometre foils, this is not the case and a low pulse contrast causes the target to be destroyed before the arrival of the main pulse.

A common device to increase the contrast is a plasma mirror (105, 106), which acts on the compressed pulse as a picosecond gated temporal switch and thus reflects only the ultra-short high intensity pulse. A plasma mirror is created by focusing the high-power laser pulse onto an optical flat material (usually made of glass). The ASE and pre-pulse are not intense enough to ionise the material and are therefore transmitted through the glass. The incoming pulse eventually reaches a critical intensity and the front surface of the glass substrate is ionised. Thereby an overdense plasma is formed, which reflects the main part of the pulse. This way the pulse is "cleaned" of the unfavourable pre-pulse and the contrast is significantly increased (see figure 3.6). However, this improvement comes with a reduction in total laser energy on target. The ionisation has to occur at a time-scale of picoseconds prior to arrival of the main pulse to suppress the development of plasma expansion and instability growth, which would affect the quality of the transmitted beam. A single (or double) plasma mirror system provides a contrast ratio improvement of the order of 10^2 (10^4) (107, 108). The pulse contrast is often measured with delay-scanning cross-correlators such as Sequoia (Amplitude Technologies) or recently with single-shot cross-correlators (109).

The Sequoia works by splitting the laser beam into two parts. One of them is converted into the second harmonic in a non-linear crystal. The second-harmonic generation process yields a pulse that is relatively clean and free from additional pulses. This cleaned pulse is mixed with the remainder of the original pulse in a second crystal tuned for sum- or difference-frequency generation. The contrast can then be mapped as a function of the delay between the two pulses by one of two methods. In the first one, one or both of the pulse fronts is tilted in order to give a spatially-varying delay, thereby mapping a time window onto the spatial coordinate. Imaging the third harmonic signal then yields a single-shot measurement of the intensity profile as a function

3. METHODS

of delay, which is most useful for laser systems with low repetition rates. In the second method, the pulses are scanned through one another using an adjustable relative delay, and the third harmonic signal recorded for each delay to give a plot of contrast versus time (110).

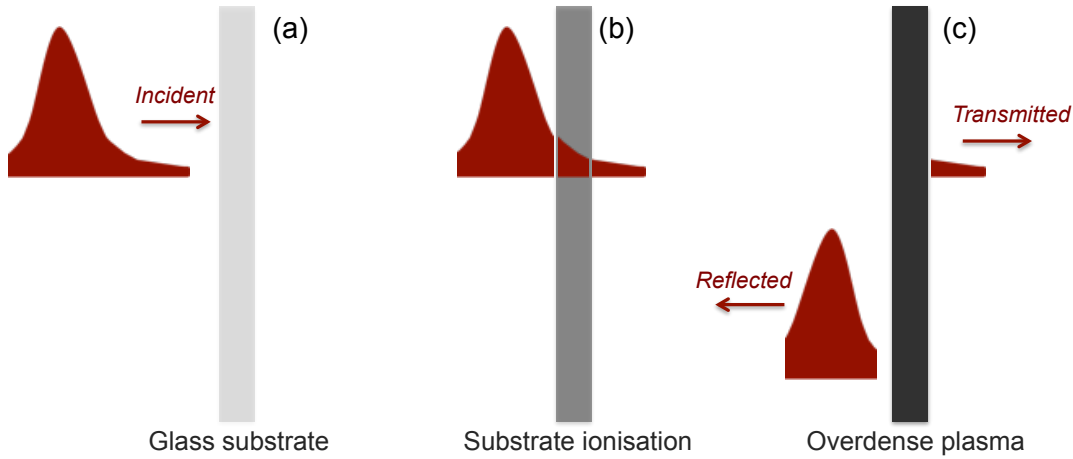


Figure 3.6: Plasma mirror - Single plasma mirror set-up. (a) The ASE and pre-pulses are not intense enough to ionise the glass substrate and are transmitted through. (b) The rising edge of the pulse eventually ionises the substrate and turns it into an overdense surface, (c) which reflects the cleaned pulse.

3.1.3 Targets

There are many different types of targets, overdense and underdense, that are commonly used in laser plasma interactions. Overdense, solid targets usually include thin foils (from few nanometres to micrometres), double layer targets and structured targets (thin foils with nanogrooves, dots, etc.). Also, mass-limited targets and micro-assembled targets (e.g. nanospokes, cones) can be used. Underdense targetry usually includes aerogels, foams, droplets and gas jets (111, 112). However, it is important to recall that the critical density, which divides underdense and overdense, depends on the wavelength of the laser (see table 2.1). Hence, a dense gas jet that appears underdense for a Ti:Sapphire laser ($\lambda = 800$ nm), could be overdense for a CO₂ ($\lambda = 10$ μ m) laser.

Gas targets usually consist of noble gases at high pressure (several tens of atmosphere) expanded through a pulsed valve. Clusters are produced when mixing another

gas (e.g. CO₂) with the noble gas and expanding the mixture at high pressure through a pulsed valve.

Solid targets can consist of any metal (Al, Cu, Ti, Au, etc.) (113) or plastic (Mylar, PTFE, etc.). Diamond-like carbon (DLC) is frequently utilised for thin foil interaction. DLC is an important form of amorphous carbon consisting of a mixture of sp^3 and sp^2 coordination. The beneficial properties of DLC are due to the sp^3 constituents that make DLC mechanically hard, infra-red (IR) transparent and chemically inert. High quality DLC coatings can rival crystalline diamond in terms of mechanical performance. The hardness of crystalline diamond is approximately 100 GPa, its Young's modulus being approximately 1000 GPa. Furthermore DLC targets offer high resistivity to radiation damage, thermal conductivity, as well as extreme heat resistance (114). Therefore DLC combines the advantage of high mechanical strength with high laser-induced damage threshold, which makes it an ideal candidate for laser interaction with nanometre foils due to its lower contrast-demands.

The ideal thickness of thin foils for ion acceleration depends on many factors, especially on the desired regime of acceleration. The aforementioned TNSA mechanisms, relying on hot electron generation and a sheath-field on the rear side, with long pulses works best for micrometre thick targets, which provide more bulk electrons in absolute numbers.

On the contrary, RPA works best for ultra-short pulses and ultra-thin targets. However the optimum thickness is limited by the contrast parameters of the laser pulse as well as the effective areal density.

The *dimensionless areal density* is defined as

$$\sigma = \left(\frac{n_e}{n_{nc}} \right) \left(\frac{d}{\lambda} \right), \quad (3.1)$$

where n_e is the plasma density, n_{cr} the critical density, d the target thickness and λ the laser wavelength.

Chapter 6 includes estimations for the ideal target conditions in the interaction of an ultra-short laser pulse with thin plasmas.

3.1.4 Diagnostics

In all the experimental campaigns a number of diagnostics were employed to monitor the plasma and generated particle beams by the interaction. In the following sections

3. METHODS

the main diagnostics that were used are explained.

3.1.4.1 Thomson Parabola

The Thomson Parabola (TP) is a type of spectrometer that is used to analyse the energy spectrum of multiple-species ion beams, separating the charged particles with different charge to mass (q/m) ratios and different energies into different trajectories (115). In the most basic layout it consists of an entrance pinhole to reduce the cross section of the beam, a magnet and two electrodes, giving rise to parallel magnetic and electric fields, and a detector (see figure 3.7). The incoming charged particle beam passes through the fields, where it is deflected according to the Lorentz force. Due to the deflection in the orthogonal direction by the magnetic and electric field, the beams imprint as parabolic traces on the detector with a curvature that depends on their energy and their charge-to-mass ratio (see figure 3.8 for sample ion tracks).

The choice of the dimensions of the TP is non-trivial, since the different ion species tend to merge their paths, making it difficult to distinguish them. The neutral particles pass through the electric and magnetic field without any deflection, producing the so-called zero-point. This zero-point serves as reference when producing the energy spectra from the parabolic traces. The TP used in the experiments within the scope of this thesis, used a yoked pair of permanent magnets for the generation of the magnetic field. The field strength (~ 1 T) was measured with a Hall probe and the fringe fields have been found to be negligible. Two copper plates with high-voltage supplies (each ~ 10 kV) were used to generate the electric field.

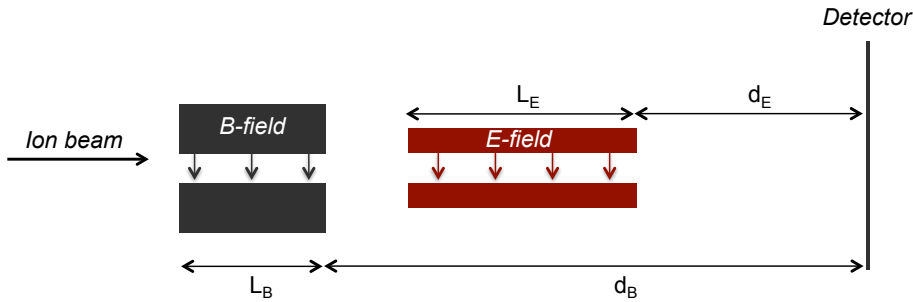


Figure 3.7: Thomson Parabola spectrometer - Geometry of the Thomson Parabola spectrometer. The incoming ion beams are deflected according to the Lorentz force by the parallel magnetic and electric fields and detected down-stream. The beams are separated by their charge-to-mass ratio and imprint as parabolic traces on the detecting material

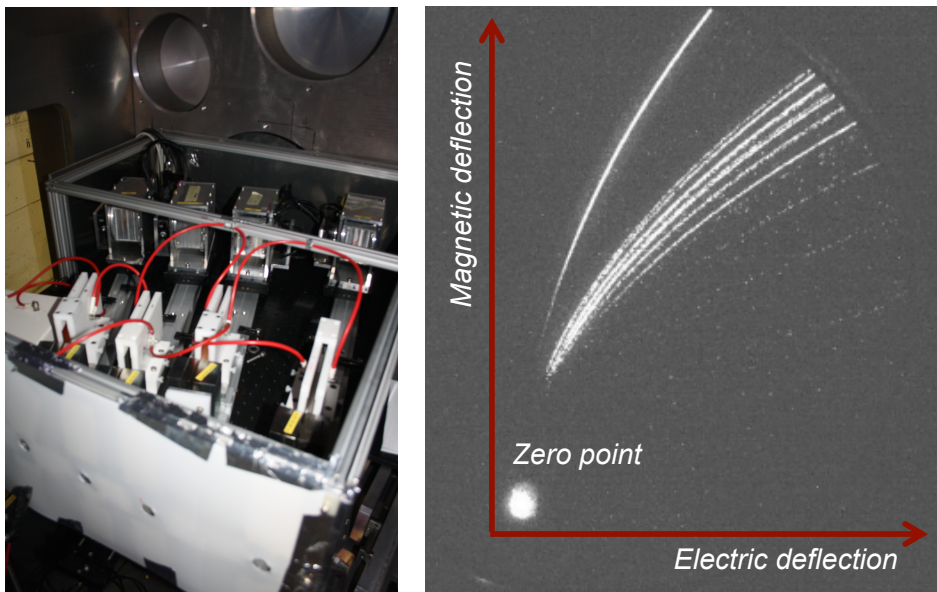


Figure 3.8: Thomson Parabola set-up and detection on MCP - Left: Picture of the Thomson Parabola spectrometer set-up during the experimental campaigns. In the foreground the permanent magnets and the electrodes (high-voltage supplied through the red cables) are seen. In the back the drums for holding the image plates are seen. Right: Picture of sample parabolic ion tracks on a phosphor screen coupled to a MCP. The ion beams are deflected by the magnetic and electric fields of the Thomson Parabola spectrometer.

The shape of the parabolic traces can be derived analytically starting from the Lorentz force (here given in SI units)

$$\vec{F} = q(\vec{E} + \vec{v} \times \vec{B}) \quad (3.2)$$

Considering an ion beam travelling in the z -direction, with \vec{E} and \vec{B} fields oriented in the x -direction, the displacement induced by the magnetic and electric fields can be derived by

$$x = \frac{qE_0L_E}{mv_z^2} \left(\frac{1}{2}L_E + d_E \right) \quad (3.3)$$

$$y = \frac{qB_0L_B}{mv_z} \left(\frac{1}{2}L_B + d_B \right) \quad (3.4)$$

where x and y are the displacements due to the electric and magnetic field, respectively, of an ion with charge q , mass m and velocity v in the z -direction. The lengths

3. METHODS

of the magnetic and electric field parallel to the laser propagation direction are given by L_B and L_E , respectively, and d_B and d_E are the distances between the end of the fields and the detector plane.

The two equations can be combined and by eliminating the velocity component, the parabolic deflection is obtained as

$$y^2 = \frac{qB^2L_B^2}{mEL_E} \frac{(\frac{1}{2}L_B + d_B)^2}{(\frac{1}{2}L_E + d_E)} x \quad (3.5)$$

The kinetic energy can then easily be derived at any position $[x, y]$ on the detector plane by using either the deflection of the electric field or the magnetic field. Although both values should be consistent, normally the deflection by the magnetic field is used to extract the final energy. With $E_{kin} = \frac{1}{2}mv^2$ and substituting in y from the above equation, the energy of the ion is given by

$$E_{kin} = \frac{(qBL_B)^2}{2m} \left(\frac{1}{2}L_B + d_B\right)^2 \frac{1}{y^2} \quad (3.6)$$

These equations are derived for the non-relativistic case, which is sufficient for the ion energies currently achieved in laser-plasma interactions.

The maximum dispersion defines the range of detectable energies. For most experiments, a TP with high charge-to-mass and energy resolution is needed. There is in principle no limitation in dispersion in the magnetic field, since the ions are deflected orthogonally to the magnetic field due to the cross-product term in the Lorentz force. However, there is a limit in the electric field, since the positively charged ions are deflected towards the negative electrode. For this reason, the incoming particle beam is directed as close as possible to the negative electrode (without clipping of the beam) to ensure maximum deflection. As mentioned previously, for the energy extraction of the ions, the inhomogeneities of the electric and magnetic fields have been neglected. However numerical studies taking into account the inhomogeneous field components and especially the fringe fields towards the edges, have shown that the dispersion does not differ significantly. To increase the detectable range and resolution, in the experimental campaign with the Astra-Gemini laser system, a modified version of the Thomson parabola was employed. In this design the magnetic field is still parallel to the beam propagation, but the electrodes are placed in a wedged configuration (116). In this case the separation between the copper plates increases along the beam propagation axis to

increase the detectable energy range. The electric field components at any given point can then be calculated according to

$$E_x = \frac{zV}{(x^2 + z^2)\theta_0} \quad (3.7)$$

$$E_y = 0 \quad (3.8)$$

$$E_z = \frac{-xV}{(x^2 + z^2)\theta_0} \quad (3.9)$$

where E_x , E_y and E_z are the field components of the electric field V is the applied voltage, θ_0 the angle between the plates and s_{min} the minimum separation of the plates. The distance between the vertex of the electrodes, coordinate origin, and the front of the detector is z_0

$$z_0 = \frac{s_{min}}{\tan(\theta_0)} \quad (3.10)$$

The Thomson parabola can be coupled to a wide range of detectors. Examples for off-line detectors include Columbia Resin 39 (CR-39) nuclear track detector or image plates. Micro Channel Plates (MCP) coupled with a CCD camera can be used as on-line diagnostics for high repetition laser systems.

The ion spectra are extracted with a custom-built Matlab graphical user interface. By selecting the neutral zero point and specifying the magnetic field strength, the parabolic traces can be fitted.

3.1.4.2 Image Plate

Image Plate (IP) detectors are commonly employed in the field of medicine, material science and biology as an alternative to photographic X-ray plates. They are highly sensitive for a broad range of ionising radiation, including electrons, gamma rays and ions and thereby also often used in experiments to detect charged particles. In the experiments conducted within the framework of this thesis the IPs were employed as detector material for the Thomson Parabola ion spectrometer as well as stand-alone diagnostic to measure the spatial intensity profile of the produced charged particle beams. For this purpose, commercially available plates from Fujifilm were used. These IPs consist of multiple layers. The top layer is a protective coating, followed by an active layer and the polyester support film. The active layer contains a high-emission, phosphorescent

3. METHODS

material, precisely barium fluorobromide with a small fraction of bivalent europium as a luminescence centre, formulated as (BaFBr:Eu^{2+}) , which in form of small crystals is coated evenly on the supporting film. The europium ions are excited into a metastable state, thereby trapping and storing the incident energy. To retrieve the data stored on the IP, the plate has to be irradiated at 632.8 nm with a special readout scanner (see figure 3.9) which excites the Eu ions to a higher energy state, which then returns to the ground state by emitting a photon. This process is called photo stimulated luminescence (PSL). The emitted photon is detected by the scanner and amplified by a photomultiplier tube, which in turn converts it into an electric signal.

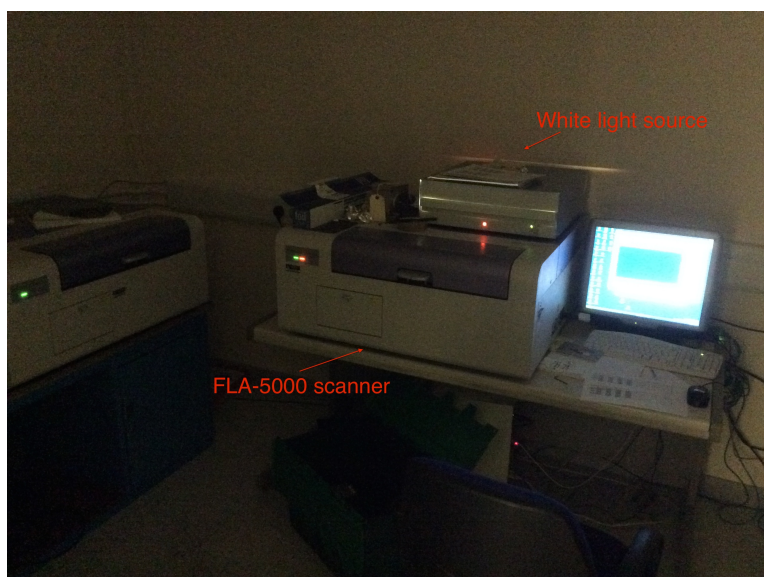


Figure 3.9: FujiFilm FLA-5000 scanner and white light source - This picture shows the FujiFilm FLA-5000 scanner and the white light source for erasing the image plates in the scanning room situated above the user control room of the Target Area Petawatt of the VULCAN laser system at the Rutherford Appleton Laboratory

The scanner used in the scope of this thesis was the model FLA-5000 manufactured by FujiFilm, capable of reading out with a resolution of 25-50 μm . In case that the output signal is saturated the IP can be re-scanned until the PSL value falls below the saturation level. There are a number of advantages of using the IP compared to other detector material like the CR-39 nuclear track detector for example. These include the high sensitivity (several tens times more sensitive than film), the large dynamic range (10^4 to 10^5 over the 10^2 range of the photographic method) and the superior linearity,

which ensures that the recorded PSL signal is proportional to the incident dose in the entire detector range. Furthermore, the image plate can be reused after any remaining information is erased by the irradiation with a high brightness white light source. The response of IPs to the irradiation of high-energetic charged particle beams has been studied extensively and calibration curves for electrons and ions can be found in the existing literature (117, 118, 119, 120).

3.1.4.3 Micro Channel Plate

The micro channel plate (MCP) (see figure 3.10) is another particle beam diagnostic tool. It is closely related to an electron multiplier, as both intensify single particles or photons by the multiplication of electrons via secondary emission. A MCP is a slab made from highly resistive material of typically 2 mm thickness with a regular array of tiny tubes or slots (microchannels) leading from one face to opposite, densely distributed over the whole surface in order to increase the chances of an incoming particle to hit the wall of the channel. The channel diameter varies usually between six and ten micrometres depending on the resolution and are spaced apart by approximately 15 μm . The channels are parallel to each other and often enter the plate at a small angle to the surface. Each microchannel is a continuous-dynode electron multiplier, in which the multiplication takes place under the presence of a strong electric field. The impact starts a cascade of electrons that propagate through the channel amplifying the original signal by several orders of magnitude depending on the electric field strength and the geometry of the micro-channel plate. After the cascade, the microchannel takes some time to recover (or recharge) before it can detect another signal. This dead time is given by the ratio of the output charge per channel over current per channel.

The electrons exit the channels on the opposite side where they are detected by additional means. For example, the signal from the whole MCP may be integrated by a single metal anode measuring the total current. In some applications however the spatial information of the detected beam has to be preserved. In that case a phosphor screen is placed behind the MCP to produce an image, which in turn is detected by a CCD camera. In the experiments reported in this thesis a Hamamatsu model F2226-14PGFX MCP coupled to a P43 phosphor screen was used. The image was recorded with an Andor CCD camera.

3. METHODS

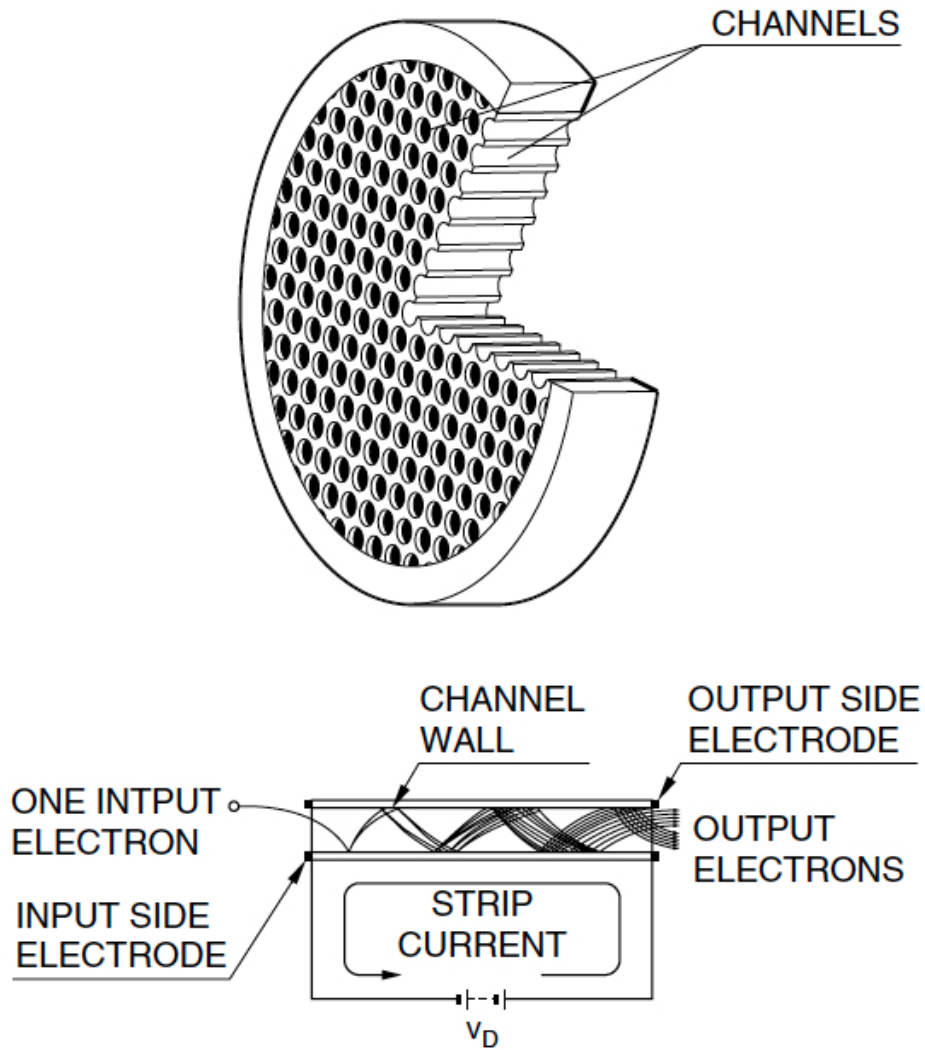


Figure 3.10: Microchannel plate detector - Working principle of a microchannel plate. In the experiments reported in this thesis the Hamamatsu model F2226-14PGFX (121) coupled to a P43 phosphor screen was used (121).

3.1.4.4 CR-39

Columbia Resin Number 39 (CR-39) (122) belongs to the group of solid state nuclear track detectors. It consists of an allyl diglycol carbonate polymer and is commercially available. While being insensitive to the irradiation of photons and electrons, it is highly sensitive to proton and ion beams. When an energetic ion beam collides with the polymer structure, it leaves a trail of broken chemical bonds within the CR-39. These have a characteristic diameter, which in turn is a direct measure of the particle energy loss and therefore the diameter increases towards the Bragg peak and decreases further down. After exposure, the CR-39 is etched in a six-molar alkaline solution (NaOH) at a temperature of 80°C for about an hour to reveal the ion tracks. Because of the difference in the etching rate between the plastic and damaged regions, pits are formed and the size of the hole grows with etching time. After the etching the pits can be counted with a scanning microscope and as long as the signal is not saturated, the number of pits corresponds to the absolute number of incoming ions, making it advantageous for flux measurements. Despite the capability of measuring absolute numbers of ions and being insensitive to the irradiation of electrons and photons, the main disadvantage of CR-39 is the time-consuming post-processing. Furthermore, CR-39 can only be used once, therefore it does not compare favourably with other detectors. However, CR-39 can be used in conjunction with other detectors like radiochromic films and image plates to give an absolute calibration of the number of incident ions.

3.1.4.5 Lanex screen

Lanex[®] is a scintillating material, that can also be used for the detection of charged particle beams. In the experimental campaigns reported in this thesis it has frequently been employed in the electron spectrometer to monitor the electron yield. Like other scintillating materials, Lanex emits light due to luminescence when struck by ionizing radiation. A CMOS camera was pointed towards the Lanex screen and light-tightened, to collect the emitted light.

3.1.4.6 Radiochromic film

Radiochromic Film (RCF) is a commonly used detector material for radiography imaging and dosimetry measurements, but also finds wide application in laser plasma ex-

3. METHODS

periments as a dose measuring device for charged particle beams (123). In most of the experiments reported in this thesis the Gafchromic[®] HD-V2 Dosimetry Film (figure 3.11) was used, complemented with the EBT2 film for some shots. The dynamic dose range of the HD-V2 film is between 10 Gy and 1000 Gy and it develops itself in real time without any post-exposure treatment. The film can be used to cover a wide energy range from 100 keV up to MeV and offers a high spatial resolution to at least 5 μm .

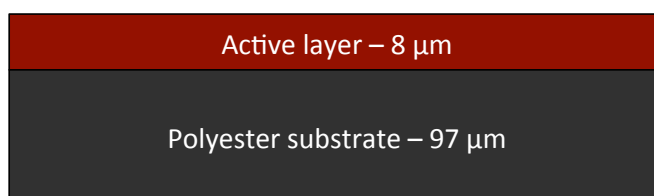


Figure 3.11: Gafchromic HD-V2 film - This shows the active layer and supporting polyester layer of which the HD V2 film consists

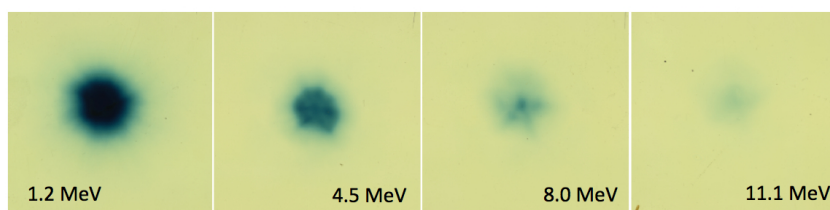


Figure 3.12: Ion beam detection with RCF - Sample ion beam detected with a RCF stack. The layers correspond to different energies according to their attenuation curves.

The active layer of the RCF consists of radiation-sensitive organic micro-crystal monomers appearing yellow, which upon irradiation undergo a polymerisation to form a dye of darker blue colour. The degree of the colour density depends on the absorbed dose, therefore higher doses appear darker than light doses (see figure 3.12). The active micro-crystal structure has a very small scale allowing extremely high micrometre resolutions, which gives an accurate dose profile. For a precise measurement of the absorbed dose, a calibration measurement with a well-known dose is required beforehand. Apart from measuring the absorbed dose, the RCF films give the spatial profile of the ionising particle beams, allowing detailed insight into the particle dynamics. When used in a stack configuration, the RCF layers can be used to measure the energy distribution of

the charged particle beams. Because ions lose their energy very precisely at the end of their penetrating range due to the Bragg peak, a layered stack of RCF films can be used to reconstruct the discrete energy spectrum with a data point per layer and thereby also gives a very good indication of the maximum cut-off energy of the charged particle beam. The Bragg peak occurs due to a rapid increase in nuclear scattering at low particle velocities. Depending on the desired measurement, the RCF films can be separated with filter material to cover a larger range of energies. The highest resolution stack is one just composed of active layers, hence each layer corresponding to a specific energy. An example stack design that was used in the experiments reported in this thesis is shown in table 3.2.

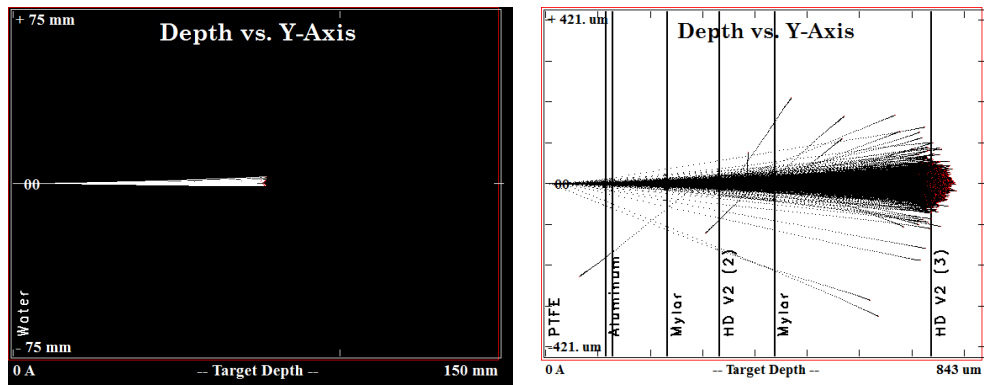


Figure 3.13: SRIM calculations - Simulation results from SRIM calculations. On the left, 70 MeV protons are stopped in water. On the right, the penetration of 9.5 MeV protons in a RCF stack is simulated.

In order to calculate the energies for each corresponding layer, the software package SRIM (Stopping Ranges of Ions in Matter) was used (124). SRIM is based on a Monte-Carlo simulation method, using the binary collision approximation with a random selection of the impact parameter of the next colliding ion. SRIM uses the Bethe-Bloch formula, derived in the Born approximation, to calculate the stopping power (energy over distance). Figure 3.13 shows the stopping range of 70 MeV protons in 15 cm of water, which is often used as a test material in clinical studies.

3. METHODS

Material	Purpose	Thickness (μm)	Stopping energy (MeV)
PTFE	Reflector	115	-
Al	Filter/Protective	13	-
HD V2 (1)	RCF	105	2.7
Mylar	Filter	100	-
HD V2 (2)	RCF	105	5.3
Mylar	Filter	300	-
HD V2 (3)	RCF	105	8.5
Mylar	Filter	400	-
HD V2 (4)	RCF	105	11.6
Mylar	Filter	500	-
HD V2 (5)	RCF	105	14.5
Cu	Filter	250	-
HD V2 (6)	RCF	105	18.7
Cu	Filter	250	-
HD V2 (7)	RCF	105	22.5
Cu	Filter	250	-
HD V2 (8)	RCF	105	25.9
Cu	Filter	250	-
HD V2 (9)	RCF	105	28.9
Cu	Filter	250	-
EBT2 (10)	RCF	285	32.1
Cu	Filter	250	-
EBT2 (11)	RCF	285	35.1
Cu	Filter	500	-
EBT2 (12)	RCF	285	40.1

Table 3.2: Experimental RCF stack design - This shows a sample RCF stack design that was used during the experiments.

3.1.4.7 Optical transmission diagnostics

The energy of the portion of laser light transmitted through the target due to relativistically induced transparency was monitored both by optical spectrometer measurements and by measuring the 2D spatial-intensity profile of transmitted laser beam on a PTFE screen positioned behind the target, with an Andor CCD camera. The transmitted and reflected light was recorded in the laser fundamental frequency and second harmonic using inferential filters. Neutral density filters are used to dim the light and prevent destruction of the CCD camera.

3.2 Numerical methods

A complete comprehensive understanding of any physical process requires the synergy of theory, simulations and experiments. In the framework of this thesis, beside the experimental work, particle-in-cell (PIC) simulations were performed to model the interaction of a laser pulse with matter and the subsequent acceleration of ions. These simulations were carried out with the OSIRIS PIC code.

OSIRIS is a three-dimensional, relativistic, massively parallel, object oriented PIC code developed by UCLA and Instituto Superior Tecnico (IST), which has been used for modelling plasma based accelerators (125).

For some simulations, additional calculations with the PIC code EPOCH have been carried out by the University of Strathclyde to model the field-ionisation and to identify the dominant ion species.

PIC codes are used to simulate many different phenomena, including the simulation of charged particles propagation through a plasma. This is achieved by discretising the plasma in a finite number of cells, solving Maxwell's equations and then pushing each particle to a new cell in position and momentum space via self-consistently calculated fields. The simulations can be carried out in up to three dimensions. The presented results in this thesis were obtained with 1D3V and 2D3V simulations. This means that the configuration space is one- or two-dimensional, while the velocity space is three-dimensional. While these plasmas are different from true one- or two-dimensional (i.e., 1D1V or 2D2V) plasmas, they are widely used in PIC simulations because they can be regarded as three dimensional models with some restrictions or translational symmetries in relevant directions and they may include more physics of real three-dimensional

3. METHODS

plasmas than the true one- or two-dimensional (126). The enormous advantage of using the particle-in-cell method instead of particle-particle interaction is the reduction in computational resources.

In the particle-in-cell method, the forces are exchanged between the particles through electromagnetic fields. In this case the field is represented by a regular array of mesh points and the field values at particle positions are obtained by interpolating on an array of mesh-defined values. The mesh defined densities for the calculation of the fields are obtained by the opposite process of depositing the particle attributes to nearby mesh-points.

3.2.1 Simulation method

In the following the main equations governing the transport of charged particles in a plasma upon laser irradiation are explained.

Charged particles are pushed through the plasma by solving the Lorentz equation, given in cgs units as

$$\frac{d\vec{p}}{dt} = q(\vec{E} + \frac{\vec{v}}{c} \times \vec{B}) \quad (3.11)$$

with $q_{cgs} = \frac{qSI}{\sqrt{4\pi\epsilon_0}}$, $\vec{E}_{cgs} = \vec{E}_S\sqrt{4\pi\epsilon_0}$ and $\vec{B}_{cgs} = \vec{B}_S\sqrt{\frac{4\pi}{\mu_0}}$. The fields are given by Maxwell's equation, which in cgs units are

$$\nabla \cdot \vec{E} = 4\pi\rho \quad (3.12)$$

$$\nabla \times \vec{B} = \frac{1}{c} \frac{\partial \vec{E}}{\partial t} + \frac{4\pi}{c} \vec{j} \quad (3.13)$$

$$\nabla \times \vec{E} = -\frac{1}{c} \frac{\partial \vec{B}}{\partial t} \quad (3.14)$$

$$\nabla \cdot \vec{B} = 0 \quad (3.15)$$

with ρ being the charge density and \vec{j} being the current density. The charge density and current density can be represented as

$$\vec{j}(\vec{x}) = \sum_{i=1}^n q_i v_i \delta(\vec{x} - \vec{x}_i) \quad (3.16)$$

$$\rho(\vec{x}) = \sum_{i=1}^n q_i \delta(\vec{x} - \vec{x}_i) \quad (3.17)$$

These equations are sufficient to describe a plasma and predict its behaviour within the limits of classical physics. The Particle-in-cell code solves these equations in four distinct steps (see figure 3.14).

Firstly, given an initial configuration of particles with certain positions and momenta, the sources of the electromagnetic field are found, i.e. the current and the charge density are deposited onto the grid. Secondly, the sources are used to advance the electromagnetic fields in time by one time step via Maxwell's equations. Thirdly, the updated fields are used to evaluate the force on the particles. In the last step of the loop, the equations of motion are integrated to move the charged particles.

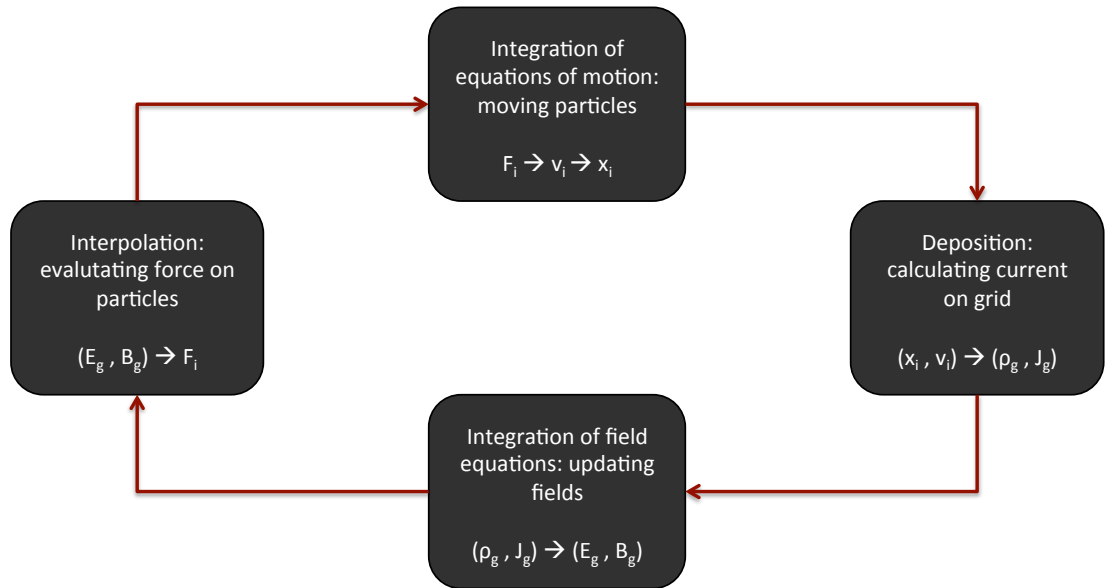


Figure 3.14: Particle-In-Cell loop - This shows the four steps of a Particle-In-Cell simulation. See text for details.

Field solving The fields in OSIRIS are solved in three different steps, by using Faraday's equation 3.14 and Ampere's equation 3.13 can be re-written as

$$\frac{\partial E}{\partial t} = 4\pi j - c\nabla \times B \quad (3.18)$$

3. METHODS

and

$$\frac{\partial B}{\partial t} = -c\nabla \times E \quad (3.19)$$

Therefore only the current density \vec{j} is required to advance the fields. The continuity equation, which can be derived using Gauss equation, is used to ensure charge conservation.

The rotational operator is replaced by a finite-difference approximation on the mesh and \vec{E} , \vec{B} and \vec{j} are defined on shifted meshes for higher accuracy. This means in 1D, \vec{E} and \vec{j} are defined on points x_i and \vec{B} on points $x_{i+\frac{1}{2}}$.

At the beginning, \vec{E} and \vec{B} are centred at time t_n and \vec{j} is centred at $t_{n+\frac{1}{2}}$. The magnetic fields are then advanced by a half time step ($\vec{B}^n \rightarrow \vec{B}^{n+\frac{1}{2}}$), the electric field by a full time step ($\vec{E}^n \rightarrow \vec{E}^{n+1}$) and finally the magnetic field by another half time step ($\vec{B}^{n+\frac{1}{2}} \rightarrow \vec{B}^{n+1}$).

Particle push The fields as calculated above are then interpolated to a particle position by weighting each field component linearly from the particle's nearest grid points for which each component of \vec{E} and \vec{B} is known. The particle advancement (updating the momentum) is done by solving the Lorentz equation with the Boris pusher (127), using the field values interpolated at the particle initial position x^n . For a relativistic generalisation of Lorentz equations $\vec{u} = \gamma\vec{v}$ is used with the γ being the relativistic Lorentz factor. Hence the equation becomes

$$\dot{\vec{u}} = \frac{q}{m} \left(\vec{E} + \frac{1}{c} \frac{u}{\gamma} \times \vec{B} \right) \quad (3.20)$$

To advance one full time step δt , the code starts from $\vec{u}^{n-\frac{1}{2}}$ and time-centred fields \vec{E}^n and \vec{B}^n are used. To advance the particles, the following four steps are executed consecutively: First, half the electric impulse is added to obtain \vec{u}' . Second, \vec{u}' is rotated with half the magnetic impulse, giving \vec{u}'' . Then the other half of the magnetic impulse is added, before the remaining half of the electric impulse is given.

Explicitly this means:

1. $\vec{u}' = \vec{u}^{n-\frac{1}{2}} + \frac{q}{m} \frac{\delta t}{2} \vec{E}^n$
2. $\vec{t} = \frac{q}{m} \frac{\delta t}{2} \frac{\vec{B}^n}{\gamma^n} \Rightarrow \vec{u}'' = \vec{u}' + \vec{u}' \times \vec{t}$
3. $\vec{s} = \frac{\vec{t}}{1+t^2} \Rightarrow \vec{u}''' = \vec{u}'' + \vec{u}'' \times \vec{s}$

$$4. \vec{u}^{n+\frac{1}{2}} = \vec{u}''' + \frac{q}{m} \frac{\delta t}{2} \vec{E}^n$$

$$\text{with } \gamma^n = (1 + u'^2)^{\frac{1}{2}}.$$

The updated momentum is used to update particle positions through

$$\gamma^{n+\frac{1}{2}} = \left[1 + (u^{n+\frac{1}{2}})^2 \right]^{\frac{1}{2}} \quad (3.21)$$

$$x^{n+1} = x^n + \frac{u^{n+\frac{1}{2}}}{\gamma^{n+\frac{1}{2}}} \Delta t \quad (3.22)$$

3.2.2 Simulation details

The input deck provides all necessary information for the simulation, including the laser and plasma parameters. The laser is defined by its dimensionless amplitude a_0 , which represents the laser intensity, the spatial and temporal pulse shape, the pulse duration, focal spot size, focal point, polarisation and pulse delay in case of multiple pulses. The plasma is assumed to be pre-ionised. The spatial profile is defined by points in space with assigned density values. The electron density has to match the ion density, to allow the simulation to start. For step-like density profiles, the rise to the maximum value occurs over several cells, to avoid miscalculation of the fields in the transit space. The diagnostics for each particle species are also defined in the input deck. These include the charge density and phase spaces. The diagnostics can also be specified as time- or space-averaged quantities, which helps to reduce the size of the output data. The input deck also defines the simulation space (box), as well as temporal and spatial resolution. In the following some of the most important simulation details will be explained. Since the interaction of a laser with an overdense plasma is always computationally demanding, some compromise between realistic parameter choice, resolution and available resources must be made.

3.2.2.1 Courant condition

The numerical stability of PIC simulations is limited in the time domain by the Courant condition. In a 2D simulation with a box defined over xy -space, the maximum time step must be

$$c\Delta t < \frac{1}{\sqrt{\frac{1}{\Delta x^2} + \frac{1}{\Delta y^2}}} \quad (3.23)$$

3. METHODS

where $\Delta x(y) = \frac{L_{x(y)}}{n_{c,x(y)}}$, with $L_{x(y)}$ being the length of the box in $x(y)$ -direction and $n_{c,x(y)}$ being the number of cells along the $x(y)$ -direction. The Courant condition requires the time step Δt to be shorter than the time required for an electromagnetic wave to traverse a cell.

3.2.2.2 Particles per cell

To resolve the whole physics, an appropriate choice of particles per cell is very important. For this reason, at initial higher densities, a higher number of particles per cell is needed. This ensures that there will be enough particles per cell when the density is significantly reduced compared to the initial density. This is especially important to resolve the transition between overdense and underdense plasma regions.

3.2.2.3 Thermal velocity and temperature distribution

The initial electron temperature is defined by the thermal velocity and expressed in terms of momentum, given by $\gamma \times v$. The relativistic kinetic energy (kinetic energy = total energy - rest energy) is given by

$$K_E = \sqrt{p^2 c^2 + m^2 c^4} - mc^2 = \frac{1}{2} k_B T \quad (3.24)$$

Solving this for the momentum, p .

$$pc = \sqrt{\frac{1}{4}(k_B T)^2 + k_B T mc^2} \quad (3.25)$$

Therefore since $p = \gamma m v$,

$$\gamma v/c = \frac{\sqrt{\frac{1}{4}(k_B T)^2 + k_B T mc^2}}{mc^2} \quad (3.26)$$

For $k_B T = 1$ keV and $mc^2 = 511$ keV, $\gamma v = 0.045c$.

3.2.2.4 Spatial resolution

To capture the physics of the interaction, the cell size has to be chosen to resolve the smallest inhomogeneities. This means that the cell has to be small enough to resolve the following four scales: First, the laser wavelength has to be resolved. Second, the target itself has to be resolved at all times. Third, the skin depth as defined in equation 2.40.

As a rule of thumb, the cell size must be at least as small as the shortest skin depth during the simulation. Note that this quantity is independent of the initial electron temperature. Fourth, the shortest Debye length (see equation 2.44) has to be resolved. The initial Debye length can be increased by raising the initial temperature. It has to be noted that a laser pulse can drive significant plasma expansion, resulting in a decrease in electron number density, which also increases the Debye length. Therefore, for the non-relativistic electron temperatures, i.e. $k_B T_e < 511$ keV the Debye length is shorter than the skin depth. Not resolving the Debye length can result in numerical heating. However, in the case of an ultra-short laser pulse interacting with the plasma, the heating by the laser field occurs much faster than numerical heating.

3.2.3 Normalisation

Normalisation offers tremendous benefits when running PIC simulations. Firstly, the multiplication by several common constants, like m_e , e and c can be avoided. By expressing simulation quantities in terms of fundamental plasma quantities, the results are general and not bound to specific units that may have been chosen. In laser-plasma physics it is common to either normalise to the plasma frequency or to the laser frequency. For underdense plasmas (plasma electron density is lower than critical density), usually the plasma frequency is chosen as normalising frequency. Since in the framework of this thesis, the plasma is mostly (initially) overdense, the laser frequency was chosen as normalising frequency. Furthermore all quantities were normalised to the electron mass, m_e , the speed of light, c , and the electron charge, e . In cgs units the corresponding values are $m_e = 9.109 \cdot 10^{-28}$ g, $e = 4.803 \cdot 10^{-10}$ StatC and $c = 2.998 \cdot 10^{10}$ cms⁻¹. This means that the quantities can be expressed in physical (cgs) units by applying the following transformation.

- Position: $x_{sim} = \frac{\omega_L}{c} x_{phy}$
- Linear momentum: $p_{sim} = \frac{p_{phy}}{m_{sp} c} = \frac{\gamma v}{c} = \frac{u}{c}$
- Electric field: $E_{sim} = e \frac{c}{m_e c^2} E_{phy}$
- Magnetic field: $B_{sim} = e \frac{c/\omega_L}{m_e c^2} B_{phy}$

3. METHODS

where m_{sp} is the mass of the considered species. In practical units the physical units will relate to the simulation quantities as:

- Position: x [cm] = $2.998 \times 10^{10} x_{sim} \omega_L^{-1}$ [rad/s]
- Linear momentum: p [g cm/s] = $2.731 \times 10^{-17} \frac{m_{sp}}{m_e} p_{sim}$
- Electric field: E [GV/cm] = $1.704 \times 10^{-14} E_{sim} \omega_L$ [rad/s]
- Magnetic field: B [gauss] = $5.681 \times 10^{-8} B_{sim} \omega_L$ [rad/s]

For high kinetic energies $p \gg m_{sp}c$, the relativistic energy is reduced to $E \approx m_{sp}c^2 p_{sim}$, where $m_{sp}c^2$ is the rest mass energy for the species being considered.

Recalling the previous chapter, the dimensionless laser amplitude a_0 (equation 2.14) is used to express laser intensity.

3.2.4 Simulation remarks

Targets in higher dimensional simulations expand more rapidly and thus shorten the time interval over which enhanced acceleration occurs; consequently, 1D simulations tend to systematically over-predict ion energies. In 2D, the target could become transparent to the laser earlier than in 1D because of transverse non-uniformity of laser intensity and the combination of lateral expulsion of plasma from behind the laser spot and self-focusing (98). Kinetic simulations of laser interaction with highly overdense targets in higher dimensions is challenging, because of the initially small skin depth and Debye length scales. However, as plasma and relativistic effects take place, the local skin depth and Debye lengths become larger during the later stages of the interactions. This means the skin depth is well resolved during the main acceleration phase. Also, the electron temperature changes from an initial keV level to MeV as the initially highly overdense plasmas approach the critical density. This causes the Debye length to increase significantly.

Another important aspect to take into account in the input deck is the choice of number of particles per cell as it affects the overall dynamics of the simulation. This is because there might be initially enough particles at the beginning of the simulation, but at a latter stage, despite the well resolved Debye length and skin depth, there could be none. When modelling the interaction of an ultra-intense laser with thin solid targets,

3.2 Numerical methods

the on-set of transparency, which sensitively alters the ion acceleration mechanisms, is highly dependent on the initial density. Therefore, a realistic value for the ion densities in terms of the critical density has to be used as well.

3. METHODS

4

Single pulse interaction with thin solid targets

In the early days of laser-driven ion acceleration research efforts were mostly focused on the study of high-intensity lasers ($> 10^{18} \text{ Wcm}^{-2}$) impinging on micrometre thick solid foils. Under these conditions, Target Normal Sheath Acceleration (TNSA) (128), was found to be the dominant mechanism for the acceleration of the ions. In TNSA models, ions are accelerated through a large charge-separation field at the rear side of an opaque plasma, resulting in the generation of ion beams following a thermal energy distribution with moderate cut-off energies (around 50 MeV) (128).

TNSA is a relatively reliable technique, because it is experimentally easier to shoot with a moderately intense ($\sim 10^{18} - 10^{19} \text{ Wcm}^{-2}$) laser onto micrometre targets than with ultra-high intensity ($\sim 10^{21} - 10^{22} \text{ Wcm}^{-2}$) laser onto nanometre foils. It allows the reproducible generation of multi-MeV ions, but the maximum energy scales with intensity as $E_{max} \propto \sqrt{I}$ (91), which unfavourably compares to the proposed scaling in other mechanisms such as Radiation Pressure Acceleration ($E_{max} \propto I^2$) (129).

Also TNSA-generated beams are not well-suited for the envisioned practical applications such as hadron therapy, because of their poor properties in terms of cut-off energy, energy spread and flux rates. Hadron therapy for deep-seated tumours requires energies of $\sim 250 \text{ MeV}$ for protons, $\sim 400 \text{ MeV/u}$ for carbon ions and an energy spread below 1%. Opposed to this, TNSA generated ions beam have a thermal energy spectrum (with an energy spread up to 100%) and cut-off energies around 50 MeV for protons.

4. SINGLE PULSE INTERACTION WITH THIN SOLID TARGETS

Recently, efforts in laser-driven ion acceleration have therefore been drifting from the TNSA regime (micrometre targets) towards other acceleration schemes with much thinner targets (nanometres), which predict higher energies and more advantageous scaling with laser parameters. One of the most promising mechanisms is laser-driven ion acceleration by means of the radiation pressure (RPA) (96, 97, 130) which was introduced in chapter 2 alongside other schemes such as the Breakout Afterburner (BOA). BOA operates best at the on-set of relativistically induced transparency, and therefore also depends very sensitively on the laser and target parameters (82, 98).

In the following, numerical and experimental results from the interaction of high-intensity laser pulses with ultrathin solid targets are presented. In the first part, the efficient generation of ion beams in the RPA regime with an intense single laser pulse is investigated in detail with PIC simulations, including a scan of several laser and target parameters.

The RPA regime investigated in the simulations works best at the threshold of relativistically-induced transparency (RIT). The on-set of RIT is not well understood as it is accompanied by a complex electron dynamics that critically affects the acceleration of ions. The second part of this chapter reports an experimental investigation of the electron dynamics at the on-set of RIT, providing new insight into the collective response of charged particles to intense laser fields over an extended interaction volume. This influences the ion dynamics, which are mediated by the plasma electrons.

4.1 Radiation pressure dominated acceleration

The inherent brittle structure of nanometre foils demands a number of requirements to be fulfilled for a stable and efficient acceleration with ultra-thin foils. In the present high-intensity regimes, where laser intensity exceeds values of 10^{21} Wcm⁻², the pre-pulse that usually accompanies the main pulse will be sufficiently intense to fully ionise the target and cause the plasma to expand (131). In some cases the expansion could cause the target to blow up before the arrival of the main pulse. In this case the main pulse cannot couple efficiently to the plasma electrons, which in turn drive the ion acceleration. Radiation Pressure Acceleration (RPA) in the light-sailing mode operates optimally with very short pulses (femtosecond pulses) interacting with nanometre-scale solid targets. RPA may also work with longer laser pulses (picosecond range) (132),

4.1 Radiation pressure dominated acceleration

however the longer pulse duration would induce more plasma expansion, which has to be taken into account when choosing the optimum target thickness.

Consequently, for longer pulse durations the experimentally observed optimum thickness is larger than predicted by the empirical scaling law for the normalised electron areal density $\sigma_{opt} \approx 3 + 0.4a_0$ derived by Esirkepov *et al.* (133).

There are already a number of laser systems which can produce the required high-intensity pulses, but lack in good contrast. This requires the use of contrast-enhancing measures, e.g. plasma mirrors (134) during experiments, which significantly alters the interaction. While the general pulse shape can usually be maintained, polarisation can be affected and more importantly the total energy throughput on target is much lower (losses of up to 50% are not unusual). Therefore, advances in pulse cleaning and contrast enhancement could immensely favour the condition of the interaction and improve the production of laser-produced ion beams. Future laser-systems, including the VEGA Petawatt laser at CLPU, will offer true petawatt laser power interaction with targets with short pulses in the femtosecond range by offering an ultra-high contrast of more than 10^{12} :1 at 1 ps.

As explained in a previous chapter, a circularly polarised laser pulse at normal incidence can cause the radiation pressure acceleration to become the dominant mechanism (135). Because of the missing oscillating term of the $\vec{j} \times \vec{B}$ force, electron heating is strongly suppressed. Also the other absorption mechanisms like Brunel heating and resonance absorption are absent in the circular case. Instead, the electrons are compressed to a highly dense layer in front of the laser pulse (snow-ploughing), creating a charge separation field, which in turn accelerates the plasma ions. By a careful choice of laser and target parameters, the radiation pressure ideally balances out the restoring force given by the charge separation field. In this case the interaction changes from surface-dominated to volumetric and the plasma bulk eventually propagates ballistically as a quasi-neutral plasma bunch, continuously gaining energy from the laser field. In this manner, all ion species are accelerated to the same energy, theoretically producing mono-energetic ion beams. This stands in stark contrast to sheath-driven acceleration, which preferentially acts on hydro-contaminants present at the rear surface of the target. In the RPA regime with a low electron temperature, a phase-stable acceleration can be maintained, and the process is expected to lead to high conversion efficiencies ($\sim 3\%$ for carbon ions) and much more advantageous scaling of maximum

4. SINGLE PULSE INTERACTION WITH THIN SOLID TARGETS

energy against laser intensity ($E_{max} \propto I^2$) compared to TNSA-produced beams (132). The presented work was published in Nuclear Instruments and Methods A (136) and SPIE conference proceedings (137).

The two-dimensional simulations of a laser impinging normally on a semi-infinite slab of plasma were performed with the fully relativistic particle-in-cell (PIC) code OSIRIS (125) for a Ti:Sapphire laser with a wavelength centred at $\lambda = 800$ nm. This corresponds to a laser frequency of $\omega_L = 2.5 \times 10^{15}$ s⁻¹. Therefore simulation units in the time and space domains are converted to physical units by multiplying by $1/\omega_L = 0.425$ fs and $c/\omega_L = 127.57$ nm. The longitudinal direction x_1 is defined by the propagation of the laser. The transversal direction is denoted as x_2 . The simulation box has a size of $x_1 = 157.75 c/\omega_L$ by $x_2 = 220.02 c/\omega_L$, which is equivalent to $20.12 \mu\text{m}$ times $28.07 \mu\text{m}$. The interaction is assumed to be quasi-1D, with the important physics occurring in the longitudinal direction. Therefore the box is split in the x_1 direction into 39133 cells and in x_2 direction in 168 cells. While the overall physical behaviour is accurately modelled due to the quasi-1D approximation, the limited transverse resolution can suppress some features, e.g. transverse instability development, which will be addressed later. The pulse is modelled with a realistic duration of 40 fs at full width with a \sin^2 pulse shape, which simplifies computing due to its sharp edges while being a good enough approximation to a Gaussian pulse. The laser was focused down to a focal spot of $\approx 5 \mu\text{m}$ and focused on the plasma slab with normal incidence. The shape of the laser pulse directly affects the shape of the plasma density gradient at the front side of the plasma.

The intensity was varied from moderate intensities, 10^{19} Wcm⁻², up to intensities of 10^{22} Wcm⁻². The simulations were carried out for different targets, but presented results are mainly from the interaction with diamond-like carbon (DLC) targets. It was assumed that any pre-pulse would be of sufficient intensity to fully ionise the target entirely. Therefore a fully ionised plasma slab with a step-like profile has been modelled, with a sharp gradient over a few simulation cells. The fully ionised diamond-like carbon targets with an initial temperature of 1 keV is modelled with a solid density of $460 n_{cr}$ (close to DLC density at room temperature, $\rho = 2.7$ g/cm⁻³) (132). Further runs with pure hydrogen and carbon bulk with a hydrogen contamination layer, as commonly present in real experiments, were also performed. To ensure accurate simulations,

4.1 Radiation pressure dominated acceleration

each cell initially contains 1000 particles, which is sufficient to observe the on-set of transparency.

The choice of number of particles per cell (N_p) is critical. Assuming the density to be initially constant and equal to n_0 , an isolated particle would yield in the overlapping cells a density $\sim n_0/N_p$, which may be considered the smallest density value that can be resolved accurately. A high number of particles per cell is therefore needed to resolve large density gradients and describe low density regions. This is particularly necessary in the case of plasma expansion and the on-set of relativistically-induced transparency. Using many particles per cell also helps to reduce statistical noise and to take into account tails of very energetic particles (71).

Several diagnostics were employed in the simulation including records of all electric and magnetic fields, the charge density of all species, as well as several phase spaces. The computational domain (i.e. the simulation box size) was chosen sufficiently large (four times the FWHM of the laser pulse) so that the constraints at the boundaries do not cause any unphysical behaviour in the area of interest. This was confirmed by analysing the output and only a negligible amount of particles was found near the boundary. In principle the stated times are given relative to $t=0$, when the laser pulse impinges on the plasma.

4.1.1 Simulations with different intensities

The ion dynamics in the interaction of an ultra-intense laser with ultra-thin targets are highly sensitive to the laser parameters. Whereas in the Target Normal Sheath Acceleration model (which works best with micrometre thick targets), the maximum cut-off energy scales with intensity as $E_{max} \propto \sqrt{I}$, Radiation Pressure Acceleration models predict is much more favourable scaling with I^2 . Therefore, a set of simulations with aforementioned parameters and 40 nm targets was performed with a circularly polarised laser pulse. The laser intensity was varied between 10^{21} Wcm $^{-2}$ and 10^{22} Wcm $^{-2}$. Because of the large computational requirements, a few runs with most realistic and highest achievable resolutions were performed rather than a full limited-resolved scan with a larger number of intensity values.

Figure 4.1 (a)-(d) shows the bunch compression of the ion charge density, with the laser ($I = 10^{22}$ Wcm $^{-2}$) impinging from the left side of the simulation box at six different time steps. The incoming laser drives the density to highly overdense values

4. SINGLE PULSE INTERACTION WITH THIN SOLID TARGETS

(up to $8000 n_{cr}$ at 4.1 (d)-(f)) and pushes the particles purely by its radiation pressure. It is important to note that this process occurs in only a few femtoseconds, a time scale much shorter than the pulse duration.

As it can be seen in figure 4.2, a change in intensity strongly modulates the ion spectra and cut-off energies, with a non-thermal ion energy distribution showing some prominent population at the highest energies for the highest intensity simulation (4.2(f)). The favourable scaling is confirmed by comparing the maximum energies. Doubling the laser intensity results in a four-fold increase in cut-off energy as can be seen when comparing the spectra obtained at $5 \times 10^{21} \text{ Wcm}^{-2}$ (10 MeV/u cut-off energy) and 10^{22} Wcm^{-2} (40 MeV/u cut-off energy), which is consistent with the predicted $E_{max} \propto I^2$ scaling.

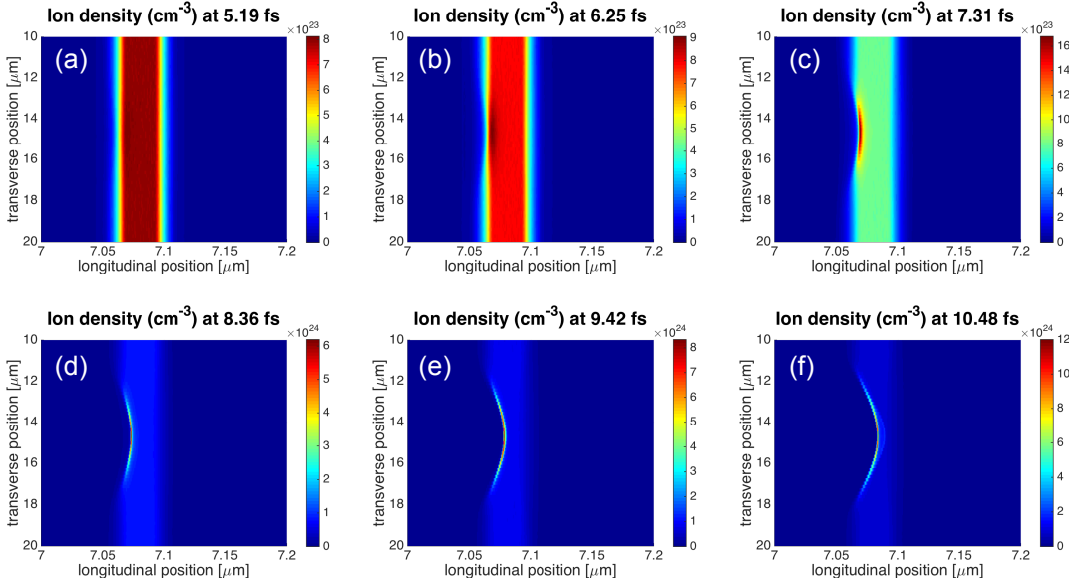


Figure 4.1: Bunch compression - This illustrates the compression of the ions induced by a 40 fs circularly polarised laser pulse of $I = 10^{22} \text{ Wcm}^{-2}$ on a 40 nm thin DLC target by the radiation pressure. The time evolution of the ion density is shown in (a)-(f) as the circularly polarised laser impinges normally from the left side on the target. Note that the colour scale is changing, because the difference in initial density and maximum density is very high.

4.1 Radiation pressure dominated acceleration

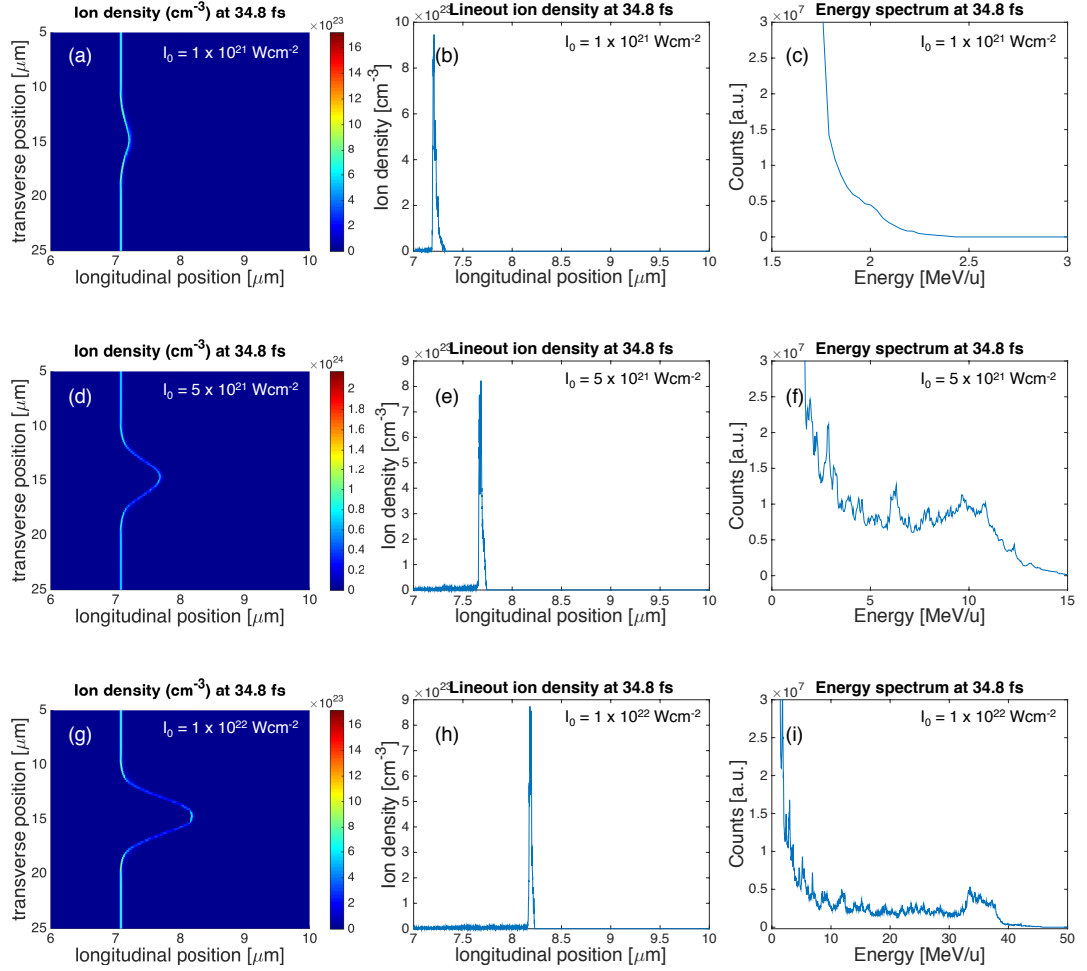


Figure 4.2: Intensity scan - Intensity scan for 40 nm carbon targets under otherwise identical conditions (see text for details). The charge densities at three time steps [(a),(d),(g)] and ion spectra [(b),(e),(h)] are shown. The time corresponds to the time after the laser pulse impinges on the target. The ion spectra corresponds to the time step 34.8 fs. The cut-off energies increase significantly with increasing intensity. The light blue colour in the bunch corresponds to high densities, whereas the purple colour indicates low density regions. The line-outs [(c),(f),(i)] are the ion densities in the target centre. Note that the scale of the colour bar changes.

4. SINGLE PULSE INTERACTION WITH THIN SOLID TARGETS

4.1.2 Simulations with different thicknesses

The cut-off energy of the ions also depends very sensitively on the target thickness. In the simplified Light Sailing (LS) model it is assumed that the target acts as a perfectly reflecting mirror and therefore all of the plasma ions are accelerated to the same velocity, giving rise to a monoenergetic beam. This peak arises due to the finite width of the laser pulse. It drives a cocoon deformation and transverse expansion of the targets. This leads to the eventual breakthrough of the laser pulse and the termination of the LS stage (138).

Considering the reflectivity of the plasma foil, the intensity threshold for self-induced transparency can be defined in terms of the dimensionless laser amplitude as $a_0 = \sqrt{1 + (\pi\sigma)^2} \simeq \pi\sigma$ for $\pi\sigma \gg 1$, where σ is the dimensionless areal density defined in chapter 3 (equation 3.1). Therefore the radiation pressure P_{rad} on target

$$P_{rad} = 2RI/c = 2m_e c^2 n_c a_0^2 R \approx 2\pi^2 m_e c^2 n_{nc} \sigma^2 \quad (4.1)$$

becomes independent of a_0 for $a_0 > \pi\sigma$.

Three simulations with 20, 40 and 60 nm thin carbon targets with an impinging laser pulse of intensity $I = 10^{22} \text{ Wcm}^{-2}$ under otherwise identical conditions as in the previous section were performed. The maximum energy increases as the thickness approaches the optimum around 40 nm. For thickness 20 nm, which is below the optimum the target blows up and only a small number of ions reaches the highest energies (4.3(i)).

The maximum radiation pressure is obtained for $a_0 < \pi\sigma$ and the reflectivity approaches unity. From this the optimum areal density and therefore target thickness is determined by $\sigma_{opt} \simeq a_0/\pi$, which yields the highest ion energies (97). This can be seen in figure 4.3. It is important to note that when the foil becomes relativistic, the optimum condition cannot always be satisfied if the areal density is constant. This is due to the fact that a_0 remains constant in the boosted frame co-moving with the foil, but the areal density σ' increases due to the laser frequency downshift. Therefore the optimum condition becomes velocity-dependent

$$a \approx \pi\sigma' = \pi \frac{n_e l}{n_{cr} \lambda_0} \sqrt{\frac{c+V}{c-V}} \quad (4.2)$$

with the mirror velocity, V . It has been shown that a gradually decreasing areal density could even improve the energy cut-off of the accelerated ions. This is also consistent

4.1 Radiation pressure dominated acceleration

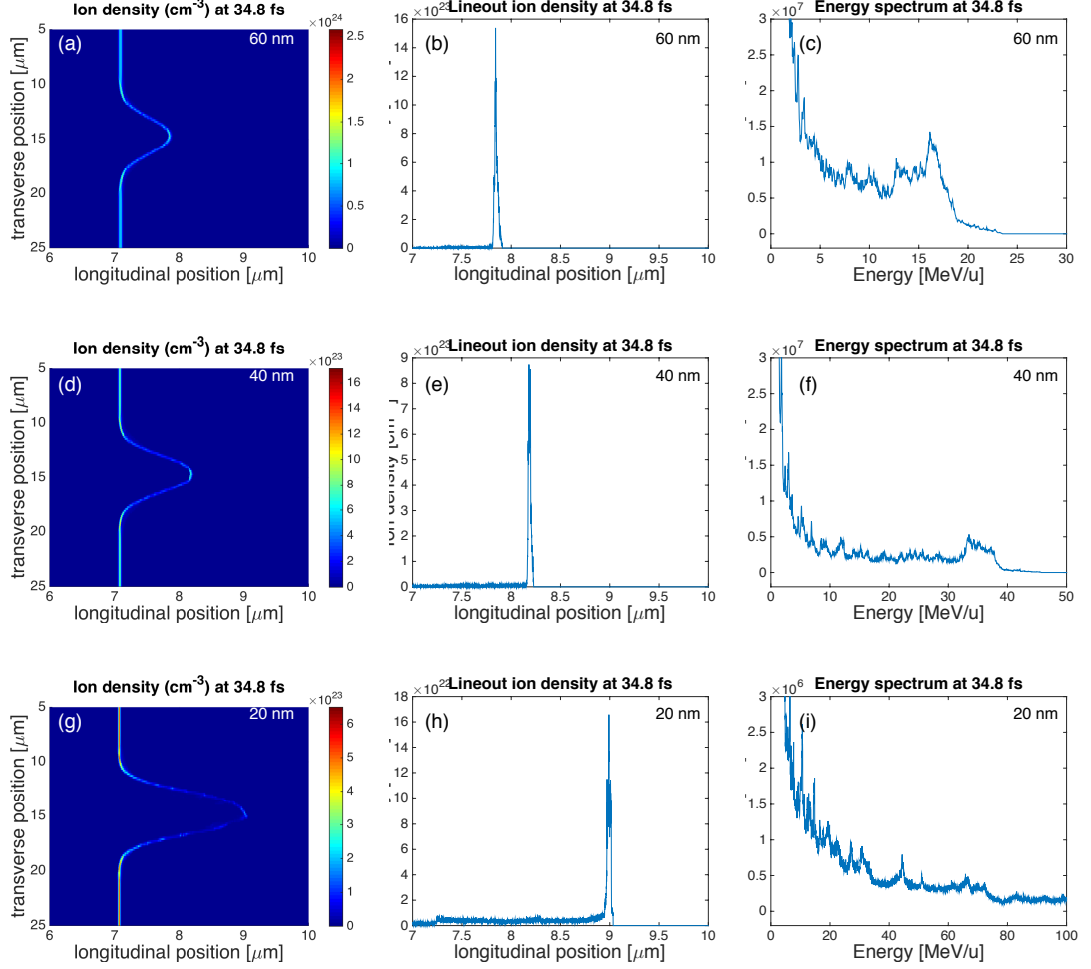


Figure 4.3: Thickness scan - Target thickness scan for carbon targets under otherwise identical conditions as in figure 4.2 ($I = 10^{22} \text{ Wcm}^{-2}$, circular polarisation. See text for details). The charge densities at three time steps [(a),(d),(g)] and ion spectra [(b),(e),(h)] are shown. The time corresponds to the time after the laser pulse impinges on the target. The ion spectra corresponds to the time step 34.8 fs. The cut-off energies increase significantly with decreasing target thickness and ion spectra shows stronger modulations for the thinnest target. The light blue colour in the bunch corresponds to high densities, whereas the purple colour indicates low density regions. The line-outs [(c),(f),(i)] are the ion densities in the target centre. Note that the scale of the colour bar changes.

4. SINGLE PULSE INTERACTION WITH THIN SOLID TARGETS

with the simulations. Various processes can facilitate the decreasing of the areal density. This includes instability development, which will be discussed in a following section, and transverse foil expansion caused by the ponderomotive force.

Even a circularly polarised laser pulse cannot suppress all the heating mechanisms driven by the oscillating part of the ponderomotive force. In multi-dimensional simulations, collisionless absorption of the circularly polarised intense laser pulses normally impinging on the overdense plasma can lead to the vacuum heating of the electrons at the sharp vacuum-plasma interface. The suggested mechanism could lead to the heating of plasma at the periphery of the laser spot rather than at its centre (139). Therefore a small portion of the laser light still gets absorbed and drives some expansion, especially in the transverse direction.

Figure 4.4 shows line-outs of the 2D charge density along the centre of the transverse direction and their evolution in time for different values of intensity [(a)-(c)] and target thickness [(d)-(f)] explored so far. It shows the increasing acceleration with increasing intensity and decreasing target thickness. Furthermore it indicates the formation of the monoenergetic features as observed in the corresponding energy spectra in figure 4.2(i) and 4.3(f). The fine blue line above the bulk of the ion population in the interaction of a $I_0 = 10^{22} \text{ Wcm}^{-2}$ laser pulse with 40 nm target (see figure 4.4(c) and (e)) corresponds to a distinct prominent population towards the end of the energy spectrum. This line is not visible in the case of the interaction of a $I_0 = 10^{21} \text{ Wcm}^{-2}$ laser pulse with 40 nm target (figure 4.4(a)), which is consistent with the observed spectrum. In the case of the $I_0 = 10^{22} \text{ Wcm}^{-2}$ laser pulse impinging on a 20 nm target it can be seen that the increase in cut-off energy comes along with a spreading of the prominent population towards the end of the spectrum, as evidenced by the disintegration in multiple lines at the charge density front (figure 4.4(f)).

4.1 Radiation pressure dominated acceleration

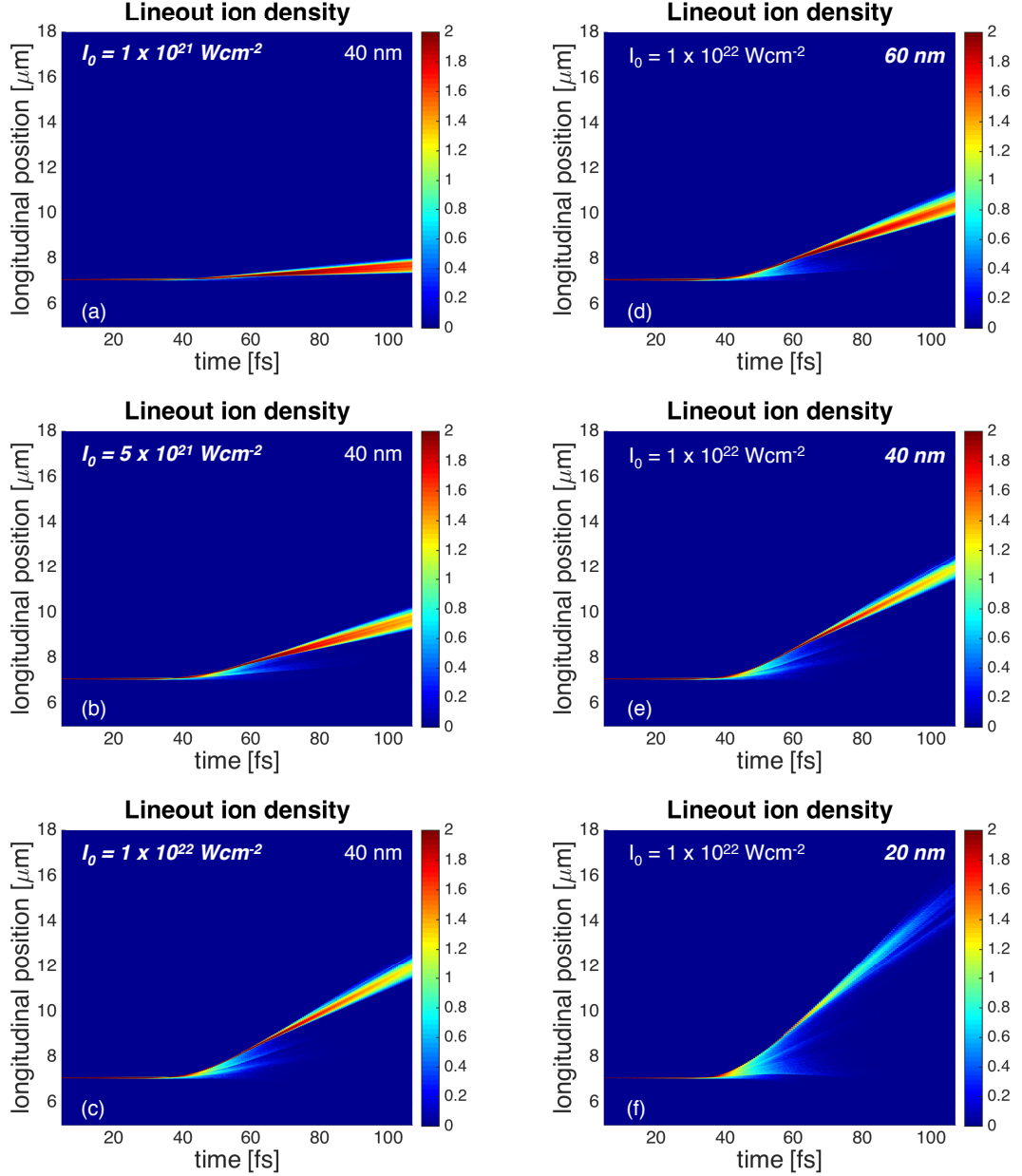


Figure 4.4: Acceleration comparison - Comparison of acceleration for the intensity [(a)-(c)] and target [(d)-(f)] scan. Shown are line-outs through the 2D charge density at the centred transverse position and its evolution with time. The fine light blue line above the main population in the 40 nm, $I_0 = 10^{22} \text{ Wcm}^{-2}$ simulation corresponds to the monoenergetic feature that is observed in the energy spectra (see also main text).

4. SINGLE PULSE INTERACTION WITH THIN SOLID TARGETS

4.1.3 Simulations with different polarisations

Another set of simulations was carried out to study the effect of different laser polarisations. For the generation of fast electrons at a steep laser-plasma interface, an oscillation force across the boundary is required. At normal incidence, this is the fast oscillating $2\omega_L$ component along the longitudinal direction of the $\vec{j} \times \vec{B}$ force (introduced in chapter 3, equation 2.46). In the case of circular polarisation, the $2\omega_L$ term vanishes and the electron oscillations are suppressed (140). On the contrary, a linearly polarised pulse will generate a fast electron population with a temperature $T_h \sim \phi_{pond}$ (141). The high electron temperature causes the plasma to expand before a shock front may be formed (4.5(c)). Simulations with linearly and circularly polarised laser pulses were carried out to study the particle dynamics in each case.

The simulation with the linearly polarised pulse yet produces high-energetic particles, but the number of particles at these energies are almost negligible (figure 4.5(d)). Furthermore, the spectrum shows no distinct peaks, suggesting that the ions distribute in a rather thermal way, which is not favourable for applications such as hadron therapy. Only at higher intensities exceeding $I_0 = 10^{23} \text{ Wcm}^{-2}$, as shown by Esirkepov *et al.* (97), the linearly polarised pulse can be used to accelerate ions in the radiation pressure regime efficiently.

On the contrary, a circular polarised pulse effectively suppresses hot electron generation and as it can be observed in the charge density plots, an isolated distinct ion population emerges at the rear side of the target (figure 4.6). By comparing the propagation of both the electron and ion population, it can be seen that both layers are compressed and co-propagate to higher energies. The different particle dynamics induced with different polarisations are most prominently observed in the charge density distribution. In the case of circular polarisation, the electron population stays highly overdense while being pushed by the laser light (4.5(g)). The carbon ions are subsequently co-propagating with the electron sheet and the whole focal volume is radiation pressure accelerated as a quasi-neutral plasma bunch. In this scenario all ion species are accelerated to equal velocity.

Figure 4.7 and 4.8 illustrate the aforementioned dynamics clearly. In the case of the circular polarised pulse (figure 4.7), the 2D charge density plot and line-out [(a)-(b)] show how the electrons and ions are compressed and maintain the highly

4.1 Radiation pressure dominated acceleration

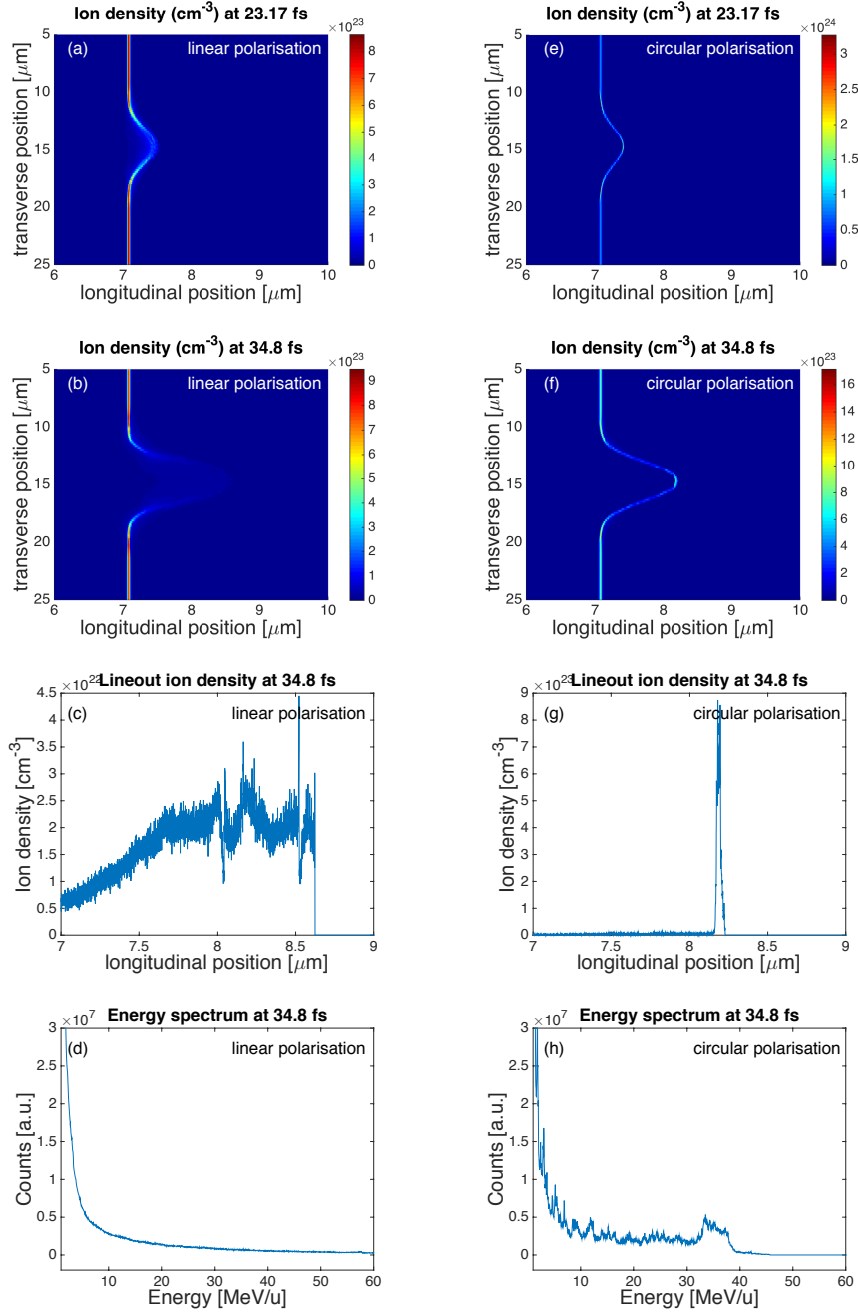


Figure 4.5: Polarisation comparison - Linear and circular polarisation comparison for carbon targets under otherwise identical conditions ($I = 10^{22} \text{ Wcm}^{-2}$, 40 nm thick target. See main text for details). The charge densities at two time steps and ion spectra are shown for linear polarisation [(a),(b),(d)] and circular polarisation [(e),(f),(h)]. The time corresponds to the time after the laser pulse impinges on the target. The ion spectra [(d),(h)] correspond to the time step 34.8 fs. The linearly polarised laser pulse strongly heats the plasma electrons and drives target expansion (c) to near-critical density values. While high cut-off energies are reached, the spectrum has a thermal shape with no sharp peaks. The circularly polarised pulse efficiently pushes the plasma inwards and drives a compressed ion bunch (g) to high energies.

4. SINGLE PULSE INTERACTION WITH THIN SOLID TARGETS

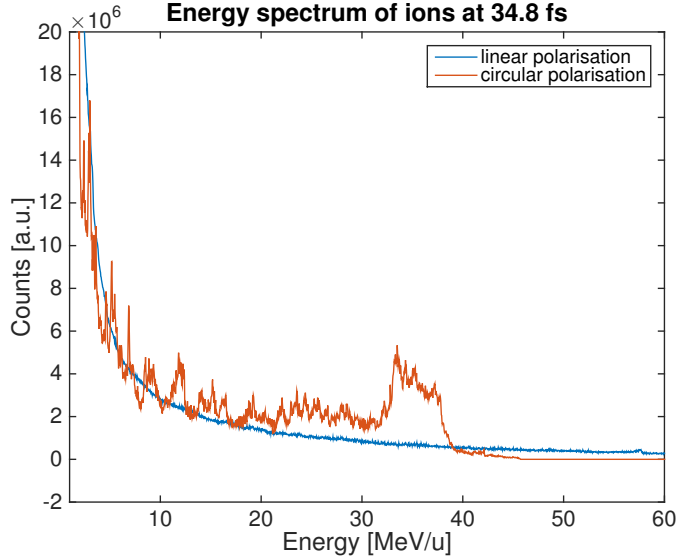


Figure 4.6: Energy spectra - linear and circular - This shows the energy spectra of the linear and circular polarised simulation runs. The monoenergetic peak in the spectrum of the circular polarised run can be clearly observed. In case of the linearly polarised laser pulse, the spectrum follows a thermal distribution without distinct peaks.

overdense nature of the plasma. This results in the volumetric acceleration of copious amounts of bulk ions, as imprinted in the phase space (c) and clearly visible as distinct prominent population towards the end of the energy spectrum (d). The behaviour of the transversal electric field [(e)-(f)] is consistent with the other diagnostics. Because the plasma stays highly overdense, the laser field gets reflected from the plasma surface.

Contrarily, in the linearly polarised case (figure 4.8), the laser pulse drives a significant expansion as observed in the 2D charge density plot and line-out [(a)-(b)]. The subsequent disintegration of the plasma leads to an expanded phase space with no distinct populations (c). The spectrum follows a thermal distribution, with only a negligible fraction of ions carrying energies above 30 MeV (d). Since the plasma turns underdense throughout the interaction, a part of the laser field is transmitted through the plasma as seen in the transversal electric field diagnostic [(e)-(f)].

Front acceleration in the linearly polarised case In the case of a linearly polarised laser, another energetic ion population at the front side of the plasma is observed. In addition to the previously explained rear-surface acceleration, a smaller

4.1 Radiation pressure dominated acceleration

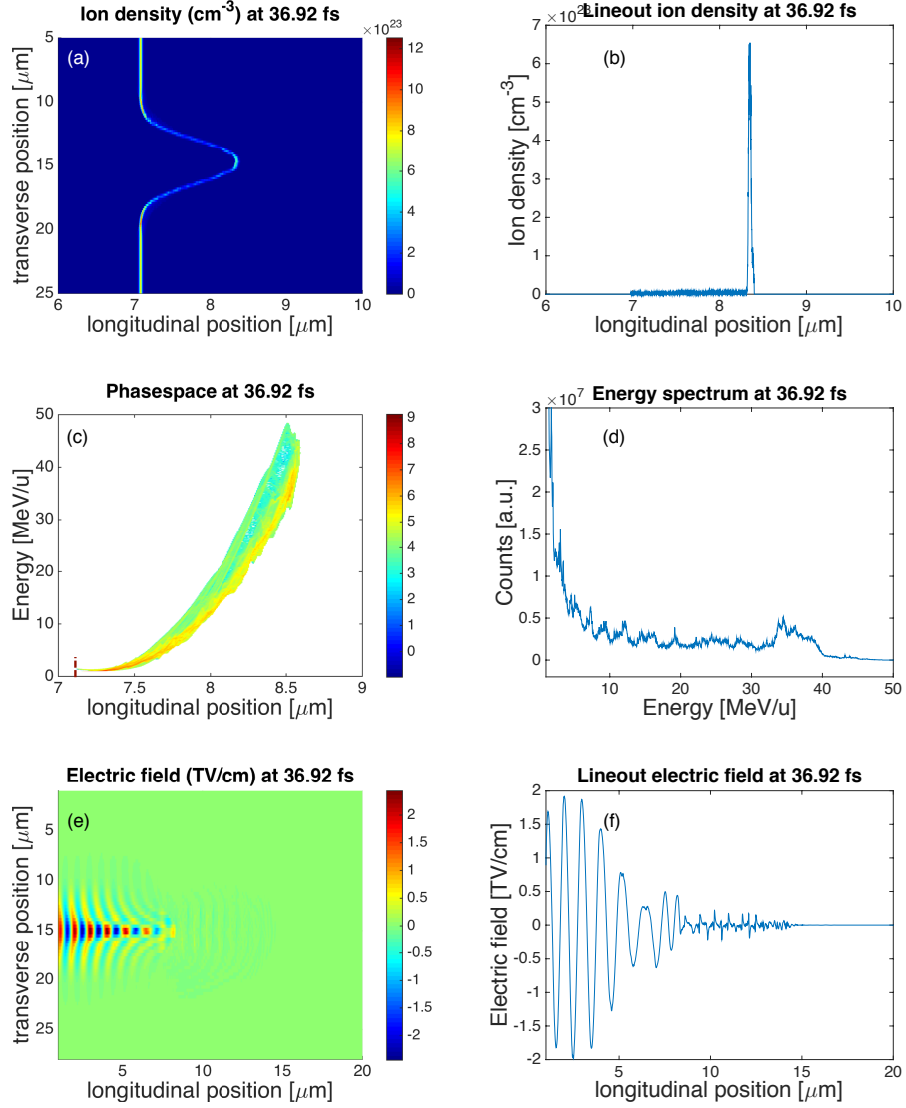


Figure 4.7: Overview of simulation run with circular polarisation - Overview diagnostics of a simulation with 40 nm DLC target [(a) ion density, (b) lineout of ion density, (c) phasespace, (d) energy spectrum, (e) transversal electric field, (f) lineout electric field]. The circularly polarised laser impinges with an intensity, $I = 10^{22} \text{ Wcm}^{-2}$. The diagnostics correspond to time 36.92 fs after the laser impinging on the target. The red-dotted line in the phase space indicates the initial position of the target. See main text for discussion of the results.

4. SINGLE PULSE INTERACTION WITH THIN SOLID TARGETS

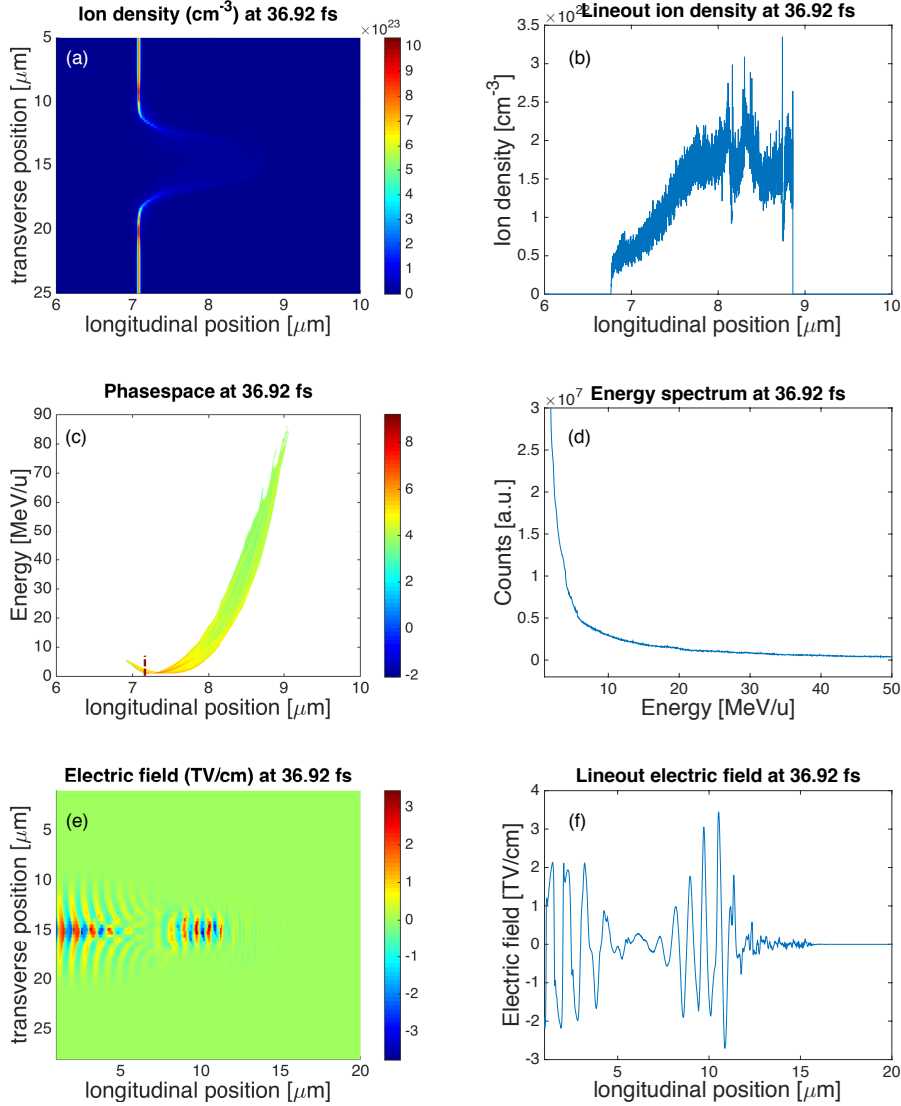


Figure 4.8: Overview of simulation run with linear polarisation - Overview diagnostics of a simulation with 40 nm DLC target [(a) ion density, (b) lineout of ion density, (c) phasespace, (d) energy spectrum, (e) transversal electric field, (f) lineout electric field]. The linearly polarised laser impinges with an intensity, $I = 10^{22} \text{ Wcm}^{-2}$. The diagnostics correspond to time 36.92 fs after the laser impinged on the target. The red-dotted line in the phase space indicates the initial position of the target. See text for discussion of the results.

charge separation field is generated due to the strong plasma expansion driven by the leading edge of the laser (4.8(e)). This results in a significantly larger scale length, causing a fraction of the bulk plasma ions to be accelerated in the opposite direction of the incoming laser pulse. However the absolute energies of these front-side accelerated ions are relatively low and they experience a strong angular spread.

4.1.4 Simulations with multi-layered targets

In real-life experiments, thin foil films are usually coated by a hydro-carbon or water contamination layer. This is beneficial in the Target Normal Sheath Acceleration scheme, since the protons present in the hydro-contamination layer are preferentially accelerated owing to their high charge-to-mass ratio. The accelerated proton layer also effectively shields the plasma bulk ions from being accelerated at a range of the Debye length (see chapter 3, equation 2.44). For an acceleration of heavier ions (e.g. carbon ions), the contamination layers have to be removed by processes such as laser-ablation (89).

The Radiation Pressure Acceleration model differs from this as the acceleration process is carried out rather volumetrically than surface-dominated, involving all ion species of the plasma bulk throughout the interaction. In this manner, heavier ions can be accelerated without the need of sometimes cumbersome target preparation. Therefore another set of simulation was performed to study the acceleration process with two ion species. In this case the target consisted of 40 nm carbon (C^{6+} ions) with a 5 nm hydrogen contamination layer. The circularly polarised laser pulse has an intensity of 10^{22} Wcm^{-2} under otherwise identical conditions as used in the previous sections. The dynamics of both ion species as observed in the charge density distribution are very similar (4.9(a)-(d)). The electrons are compressed to a dense layer and co-propagate with the C^{6+} ions and protons. The spectral features between the proton and C^{6+} ions are very similar as it can be seen in figure 4.9(f). The similar dynamics observed in the proton and C^{6+} ions distinguish the radiation pressure acceleration scheme from the Target Normal Sheath Acceleration as explained previously.

4. SINGLE PULSE INTERACTION WITH THIN SOLID TARGETS

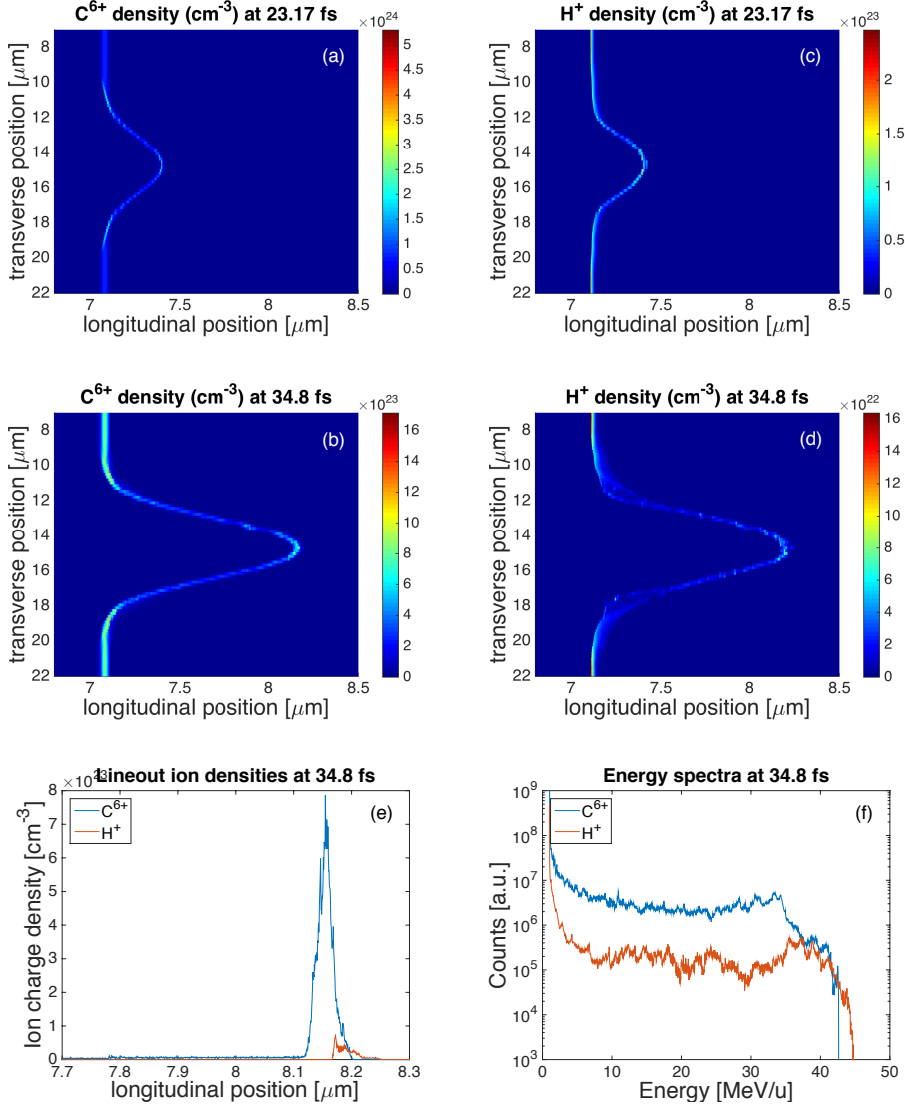


Figure 4.9: Multi-species simulation run - Interaction of a laser pulse with a 40 nm carbon target with a 5 nm hydrogen contamination layer. The simulation parameters are otherwise identical to the second run in Figure 4.3. (a)-(b) and (c)-(d) show the charge densities at two different time steps for carbon ions and protons, respectively. A lineout of the charge densities and energy spectrum are shown in (e) and (f). The similarity in spectral features suggests an efficient acceleration of both ion species. Note that the y-axis in (f) is displayed with a logarithmic scale to facilitate comparison between both species.

4.1.5 Summary

In the first part of this chapter, the production of high-energy ion beams from the interaction of ultra-intense laser pulses with ultra-thin targets has been numerically investigated.

The simulations show signatures of the RPA model of ion acceleration, as imprinted in the formation of shock fronts and non-thermal ion energy distributions showing some prominent population at the highest energies. The cut-off energies of these ion beams scale favourably as $E_{max} \propto I^2$ as predicted by the RPA model. Simulations with multi-species targets have shown that the RPA mechanism acts volumetrically on all ion species in the plasma bulk, which favours the acceleration of heavier ions without the need of extensive target preparation.

Therefore, short femtosecond, high-contrast laser systems like Astra-Gemini and VEGA are well-suited to accelerate ions efficiently in the radiation pressure dominated regime. The spectral shape of the produced ion beams is strongly dependent on both laser and target parameters. The highest energies are obtained with the thinnest targets, circular polarisation and the highest intensities.

From this it can be concluded that the RPA regime would be accessible to the VEGA 3 laser at CLPU provided it can reach a pulse contrast larger than $10^{12} : 1$ in a time scale shorter than 1 ps, while keeping the intensity larger than 10^{21} Wcm^{-2} . In that case proton energies of 100 MeV and C^{6+} ions energies of 100 MeV/u could be produced, with a potential for a sharp energy increase for higher laser intensities, and a relatively higher population of high energy ions than TNSA-produced ion beams. However, an increased transverse resolution in the simulations reveals the occurrence of instabilities which hinder the generation of truly monoenergetic ion beams as it will be shown in the next section.

4.2 Instabilities

During the interaction of an ultraintense laser with an overdense plasma, instabilities can grow. A commonly observed instability is the Rayleigh-Taylor instability (RTI), which occurs when a heavier fluid pushes against a lighter fluid (see chapter 2.6). In the Radiation Pressure Acceleration regime, the laser light (light fluid) pushes against the dense target (heavy fluid), and can be shown to be analogously Rayleigh-Taylor unstable. The formation of the instability manifests as rippling and eventual breaking up of the interface between the two fluids. These perturbations can grow in the form of bubbles, visible in the spatial-intensity profile of the accelerated ions, and have been observed theoretically and experimentally (78, 142, 143, 144).

The observation of the Rayleigh-Taylor instabilities (as imprinted in the form of bubbles in the spatial profile) is an important confirmation of radiation-pressure driven ion beams and allows to identify these direct laser-driven ion populations. The occurrence of RPA ion beams in the interaction of an ultraintense laser with an ultrathin target was studied experimentally and numerically.

Experimentally, this was achieved by tilting the target with respect to the incoming laser incidence. In this manner it was possible in an experimental campaign with the Vulcan laser system to spatially separate the radiation-pressure driven ion beam (along the laser axis) and sheath-driven ion beam (along the target normal) to study the bubble structure. The signatures of RTI were investigated from the data recorded in radiochromic film stacks and presented in the following.

The breaking up of the electron layer that pulls the plasma ions due to these instabilities, reduces the efficiency of the acceleration. It also causes a reduced number of high-energetic ions and broadens the energy spectrum (78, 80). This was studied numerically by performing particle-in-cell simulations with the OSIRIS code.

4.2.1 Experimental set-up

The Vulcan laser at the Rutherford Appleton Laboratory (described in section 3.1.1.1) was used to investigate radiation-pressure dominated ion acceleration and study the development of Rayleigh-Taylor instabilities. The laser delivers light with a central wavelength $\lambda = 1.054 \mu\text{m}$ in pulses of (1.0 ± 0.2) ps, with a total laser pulse energy $E_L = (200 \pm 15)$ J. The light is focused by an f/3 off-axis parabolic mirror on target. The

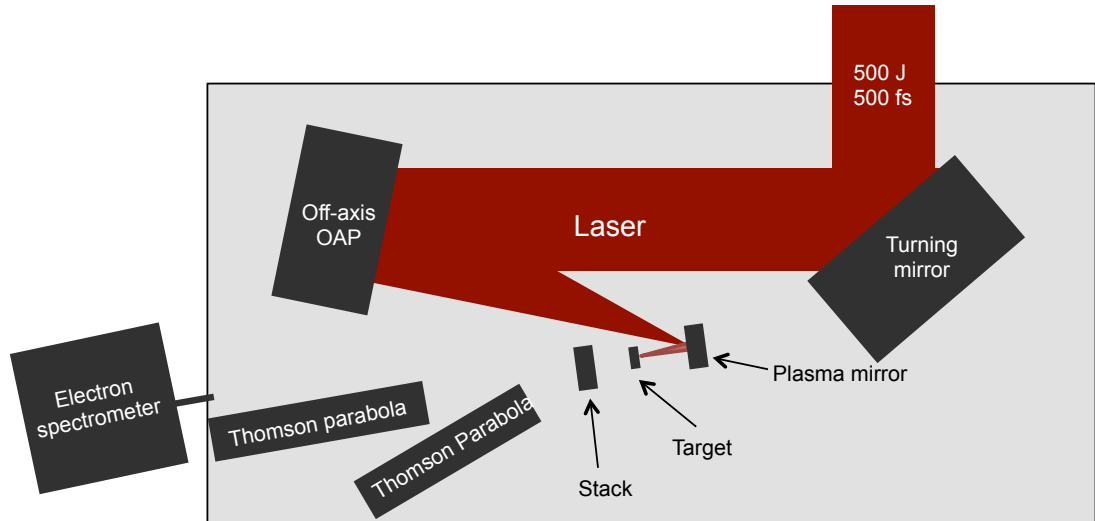


Figure 4.10: Experimental set-up Vulcan - Experimental set-up used in the Vulcan campaign in May 2013. The incoming laser pulse is turned and focused by a $f/3$ off-axis parabolic mirror onto the target. A single plasma mirror set-up is used to increase the pulse contrast. Sample electron and ion diagnostics are shown.

focal spot FWHM diameter was $7.3 \mu\text{m}$, giving a calculated peak intensity, $I_L = 2 \times 10^{20} \text{ Wcm}^{-2}$. A flat slab of glass was placed in the converging beam a few centimetres before the focus to create a plasma mirror that reflected the laser beam onto the target with an enhanced contrast of $10^{10} : 1$. Figure 4.10 shows the experimental set-up.

The target foils were Al with thickness, L , between 10 nm and 100 nm. The foils were attached to a copper plate with a circular hole and placed on top of a pin (see figure 4.11). Protons and carbon ions are produced from hydro-carbon contamination layers on the target surfaces.

The target was mounted on a motorised rotating wheel with capacity to hold five targets (figure 4.11). The motorised stage allows to change and align the target without the need to open the chamber, thus sparing the lengthy process of letting up and pumping down the vacuum interaction chamber. The chamber has an inner volume of about 20 m^3 and is covered with lead and PTFE and sits behind concrete walls for radiation shielding purposes. During the laser shot the chamber is pumped down by roughing pumps and turbo pumps to about 10^{-4} mbar or below.

The target was positioned either normally or angled at 30° with respect to the incoming laser. This was achieved by pre-aligning the target outside the target chamber

4. SINGLE PULSE INTERACTION WITH THIN SOLID TARGETS

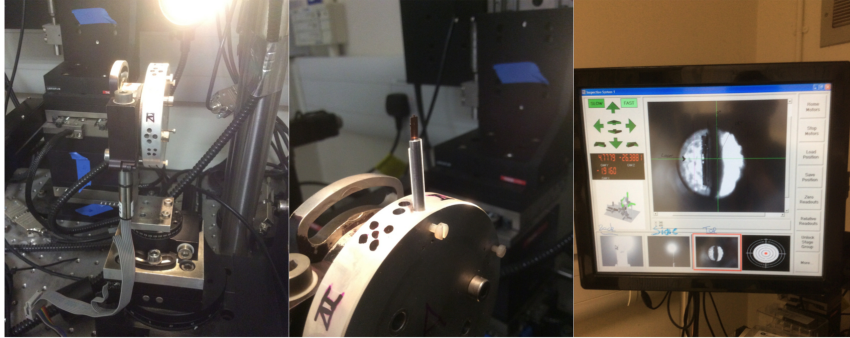


Figure 4.11: Target pre-alignment - The picture shows the target wheel and alignment stage. The targets were pre-aligned outside the target chamber to either normal incidence or 30° with respect to the incoming laser pulse.

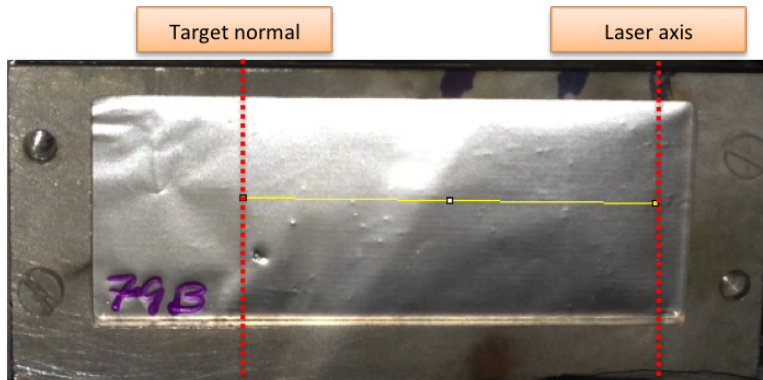


Figure 4.12: RCF stack front - The front of the RCF stack is shown. A protective layer of aluminium is added to block low-energetic electrons and to reflect laser light at the on-set of induced transparency. The red-dotted lines indicate the laser axis and target normal for targets at 30° .

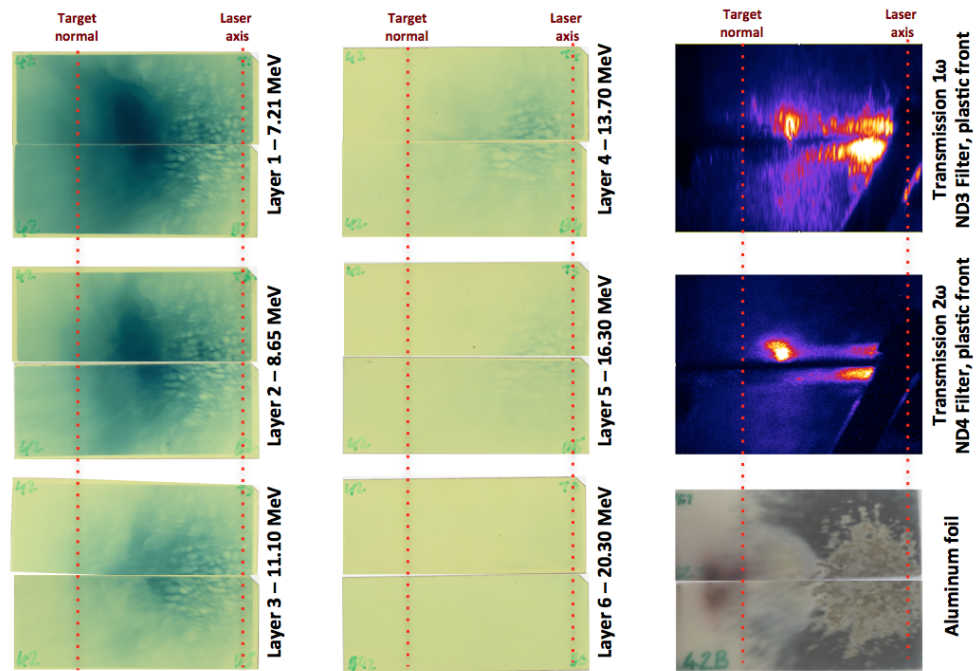


Figure 4.13: Separation of sheath-driven and laser-driven ion populations - Overview of the RCF stack and transmission diagnostic. Six layers of RCF corresponding to different energies are shown. The red-dotted lines indicated the target normal and laser axes. Two distinct ion populations can be identified, clearly separating sheath-driven ions and radiation pressure-driven ions along the laser axis. The burn-pattern on the aluminium foil confirms this. The transmission diagnostics shows that laser light is partially transmitted.

4. SINGLE PULSE INTERACTION WITH THIN SOLID TARGETS

in a target alignment rig (figure 4.11). Radiochromic film (RCF) stacks were used to record the spatial profile of the proton beams. For the same reason, all off-line diagnostics were placed on motorised mounts allowing to record up to five laser shots without opening the chamber. The RCF stack ($6.4 \text{ cm} \times 5.0 \text{ cm}$) was positioned 7.5 cm from the target. A slot in the stack provided a line-of-sight to other diagnostics (e.g. Thomson Parabola spectrometer). A real-life picture of the front side of the stack (bottom part, top part looks identical) is shown in figure 4.12.

4.2.2 Experimental results

When the target normal was positioned at 30° from the incoming laser two distinct proton beams were recorded in the radiochromic film stacks, one along the laser axis and one along the target normal. This can be seen in figure 4.12 and 4.13. In figure 4.13 the dark areas show the spatial distribution of protons in the beam. Each layer of the RCF stack corresponds to a different energy. Stacks with different filtering were used to adjust the detection to predicted proton energies. An example stack design is shown in table 3.2.

The existence of two distinct proton beams points to the presence of two different acceleration mechanisms. The target normal beam is characteristic of TNSA, whereas the beam along the laser axis can be directly associated to RPA protons. Therefore it was possible to separate the ion beams originating from the different acceleration mechanism. As stated above, the formation of a bubble structure due to the development of Rayleigh-Taylor instabilities is an important signature of RPA-driven ion beams. These structures are clearly visible in the spatial intensity profile and confirm the RPA origin of this ion beam.

As previously stated, the RCF stack consists of various layers of active material to allow also some energy resolution measurements along with the spatial profile. A set of reference bubbles at different layers of the RCF diagnostics was selected and measured in size, in order to identify the origin of the instability formation.

As it can be seen in figure 4.14 the size of the bubbles stays roughly constant through multiple layers. The preservation of the structure implies that it is reasonable to assume that laminar beam propagation is maintained due to the charge neutralising presence of co-propagating electrons (90).

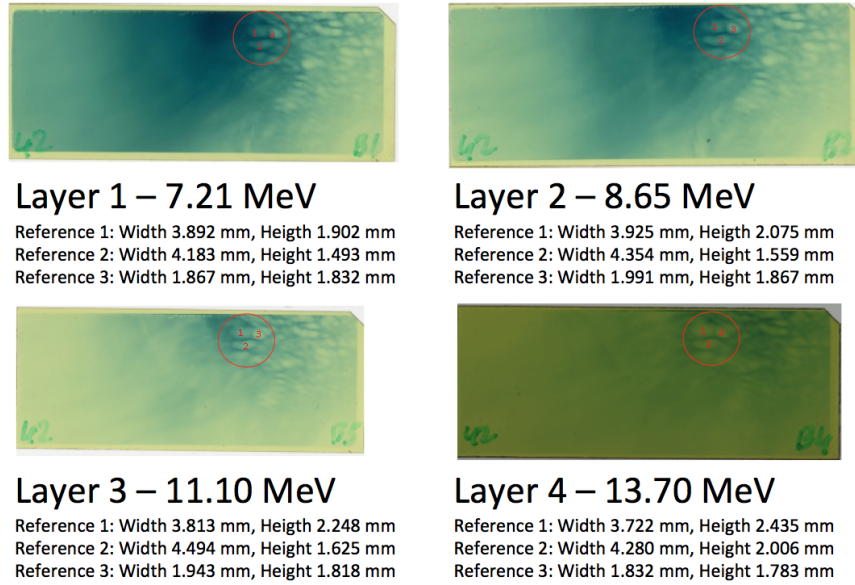


Figure 4.14: Rayleigh-Taylor instability - Four layers of the RCF stack down-stream are shown. The bubble formation on the right side indicates the development of Rayleigh-Taylor instabilities. The sizes of three reference-bubbles are measured to investigate the growth-rate.

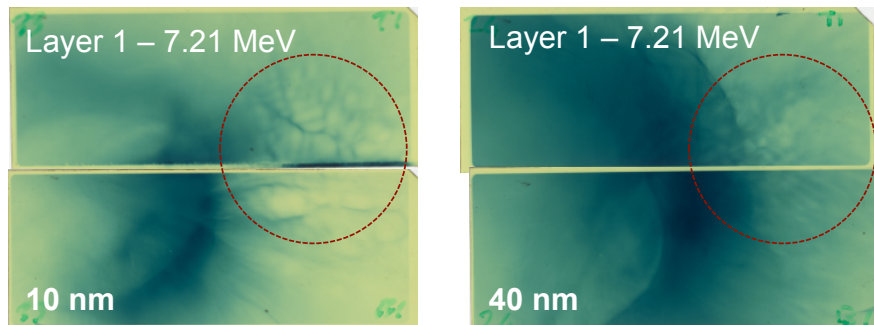


Figure 4.15: Bubble size comparison - The first layer of the RCF stack shown for a 10 nm and 40 nm thick Al foil. The bubble size increases for decreasing target thickness.

4. SINGLE PULSE INTERACTION WITH THIN SOLID TARGETS

The formation of the instabilities depends on the target thickness. The bubble size is larger for thinner targets, as it can be observed when comparing the 10 nm and 40 nm target as seen in figure 4.15.

The cut-off energy of the sheath-driven ion beams is also very sensitive to the incoming laser energy. Higher laser energies lead to higher cut-off energies, which can be attributed to the reinforced energy transfer to the plasma bulk electrons, which then traverse the target and set up the sheath-field. A monoenergetic proton dot surrounded by ring is observed (see figure 4.15). This ring structure will further be addressed in the next chapter.

4.2.3 Simulations

The transverse instabilities were also studied with two-dimensional particle-in-cell simulations with varying transverse resolution. The simulation box and parameters are identical to the presented scaling simulations in section 4.1. The laser is circularly polarised with an intensity of $1 \times 10^{22} \text{ Wcm}^{-2}$. A 40 nm thick purely hydrogenic target with $n_e = 460n_{cr}$ was used for the simulation. Due to the high computational requirements of the high-resolution run, the target was placed closer to the left border of the simulation box (see figure 4.16) without affecting the physical behaviour of the simulation. Two snapshots of the proton charge density and corresponding energy spectra are shown in figure 4.16. The top row corresponds to the simulation run with 168 cells in the transverse direction and the bottom row a run with an eight-fold increase in cells, 1344 in total, under otherwise identical conditions. Both simulations follow the characteristic dynamics of the RPA mechanism as explained in section 4.1. At the late stage of the interaction, the rippling at the charge density front can be clearly observed, which eventually leads to the break-up of the density front (figure 4.16(c)). Since RTI develops in the transverse direction, the simulation with eight-fold increase in number of cells in the transverse x_2 -direction should highlight the signature (i.e. rippling of the surface) of the instability.

While the overall dynamics are in principle maintained in the high resolution, it can be seen that the charge density in the envelope of the density profile stays overdense, whereas for the lower resolution runs, it approaches near-critical values quicker. The higher resolution run shows a proton spectrum with a larger modulation than the

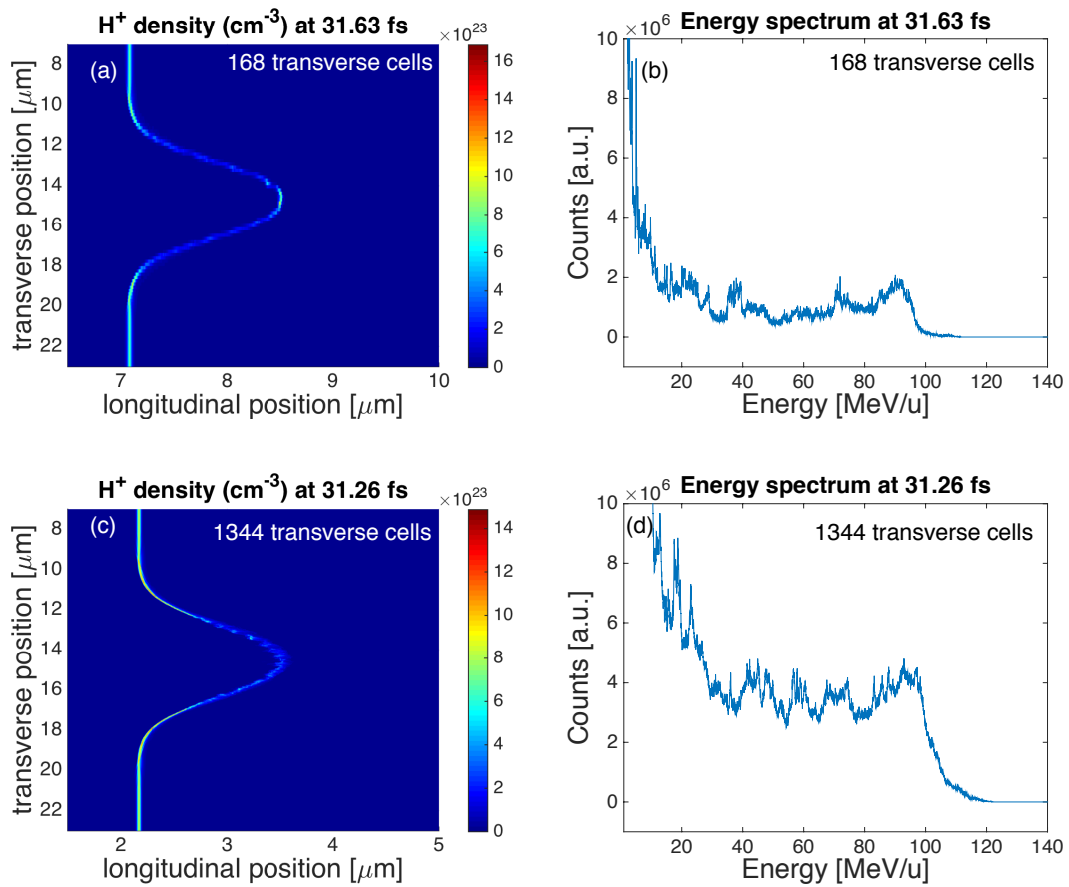


Figure 4.16: High-resolution simulation run for instability study - Comparison of a low-resolution [(a)-(b)] and high-resolution [(c)-(d)] 2D simulation. The transverse cell number is eight-fold increased from 168 to 1344 with otherwise identical parameters. The high-resolution run reveals the instability development in more detail (c).

4. SINGLE PULSE INTERACTION WITH THIN SOLID TARGETS

spectrum obtained with the lower resolution one (figure 4.16). The evolution of the proton charge density in time is also shown as a 3D picture in figure 4.17.

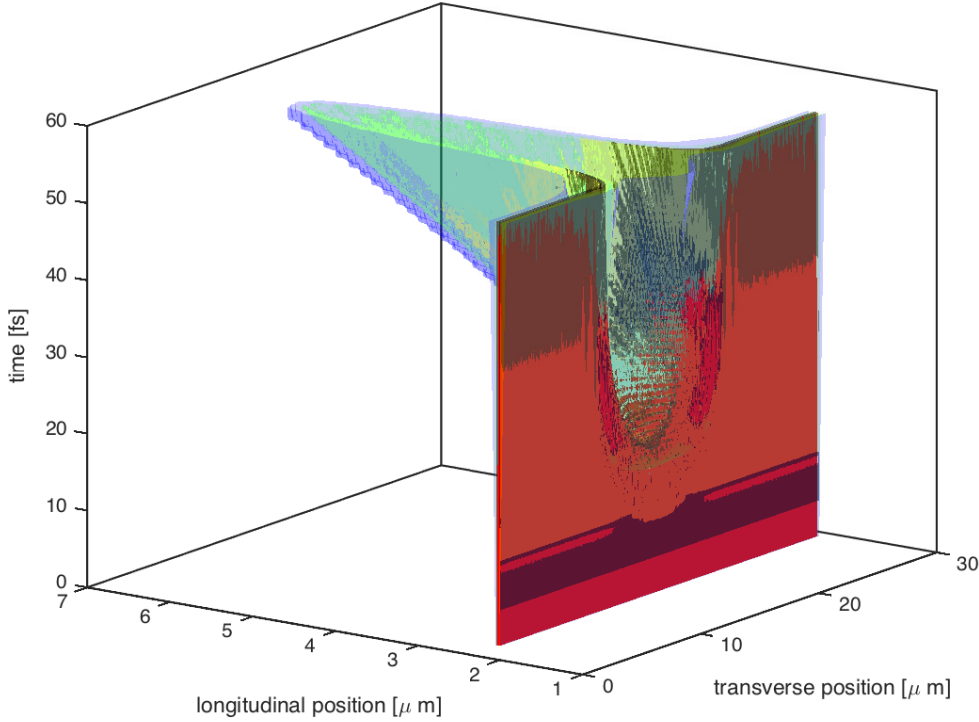


Figure 4.17: 3D visualisation of high-resolution run - 3D plot showing the evolution of carbon ion charge density in time. Clearly the acceleration and instability development as evidenced in the rippling of the density front are observed.

In summary, the development of transverse instabilities was numerically studied with OSIRIS particle-in-cell simulations. It confirmed the existence of bubble structures as experimentally observed, which are a key signature for radiation-pressure accelerated ion and proton beams.

To suppress the transverse RTI in the RPA regime, the use of elliptically polarised lasers has been proposed (145). A moderate $\vec{j} \times \vec{B}$ heating of the elliptically polarised pulse can thermalise the local electrons, inducing a transverse diffusion of ions and resulting in the stabilisation of the short-wavelength perturbations of RTI. This could lead to an improved ion beam, whose beam divergence is not severely affected by the transverse smoothing mechanism (145).

4.3 Electron dynamics during relativistic transparency

As stated in section 2.7, with the currently available laser systems, a direct acceleration of the ions is not possible. Therefore the laser energy is always transferred to the ions via the plasma electrons. This makes the study of the electron dynamics during laser-plasma interaction necessary.

In the following, the collective response of plasma electrons to intense laser fields over an extended interaction volume in the onset of relativistically induced transparency is presented. As it was shown previously, RIT is a particularly important factor in the frame of radiation pressure acceleration as it sets a limit to the intensity with which an electron density shock front can be driven. It also underpins a range of other intense laser-plasma physics, including high energy x-ray generation (Bremsstrahlung (146), synchrotron (147, 148) and betatron (149) production), high-harmonic generation (150), high-field physics (151) and the production of intense magnetic fields (152). The results presented in this section were published in the *New Journal of Physics* (153).

The behaviour of ponderomotively-driven electrons during the interaction of an ultraintense laser pulse with thin solid targets is studied, which is important for the development of promising new ultraintense laser-driven ion acceleration mechanisms involving ultrathin targets. One interesting mechanism is the so-called Breakout Afterburner (as introduced in section 2.7.3). Numerical studies of Yin *et al.* predicted an asymmetry in the collective response of electron in the interaction of an ultraintense laser with nanometre foils (98).

This asymmetry in the collective dynamics is demonstrated experimentally, as the plasma turns relativistically transparent. The 2D spatial-intensity profile of the accelerated electrons changes from an ellipse aligned along the laser polarisation direction in the case of limited transparency, to a double-lobe structure aligned perpendicular to it when a significant fraction of the laser pulse co-propagates with the electrons. The temporally-resolved dynamics of the interaction are investigated via particle-in-cell simulations. These numerical results were obtained with the particle-in-cell code EPOCH (154) and were carried out by the group of Professor Paul McKenna of the University of Strathclyde.

4. SINGLE PULSE INTERACTION WITH THIN SOLID TARGETS

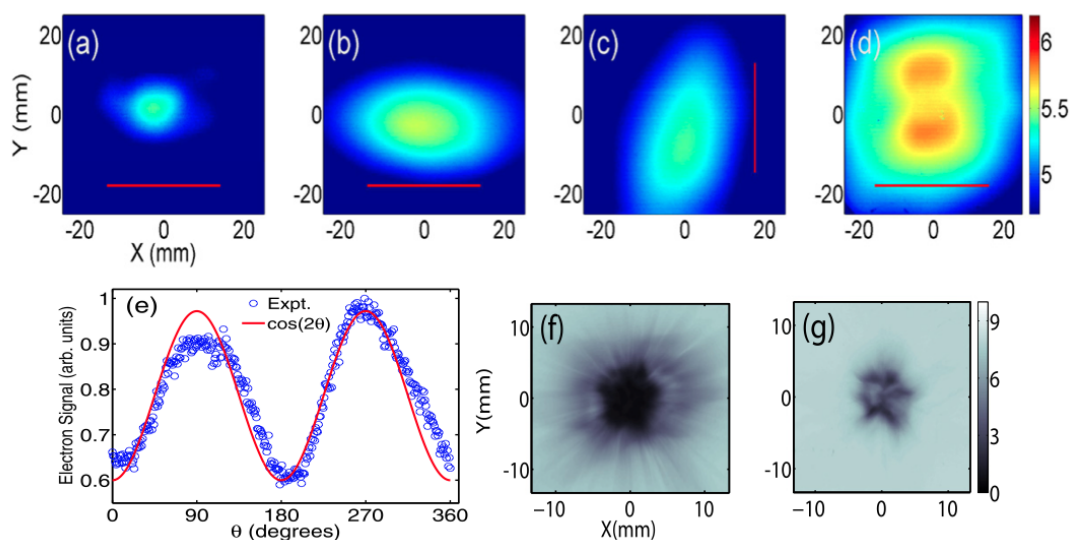


Figure 4.18: Electron and proton spatial-intensity distributions - (a)-(d) 2D spatial-intensity distribution of the electron beam, for energy > 5 MeV, as measured with imaging plate, for: (a) $L = 800$ nm with polarisation in the x-axis; (b) $L = 40$ nm with polarisation in the x-axis; (c) $L = 40$ nm with polarisation in the y-axis; and, (d) $L = 10$ nm with polarisation in the x-axis. The laser polarisation axis is shown as a red line. (e) Modulation in the electron signal as a function of θ (angle of the laser polarisation) at 10 mm radius, corresponding to the lobe centre. (f)-(g) 2D spatial-intensity distribution of the proton beam, at ~ 1 MeV (f) and ~ 3 MeV (g), for $L = 10$ nm and polarisation on the x-axis (the same laser shot as the electron distribution in (d))

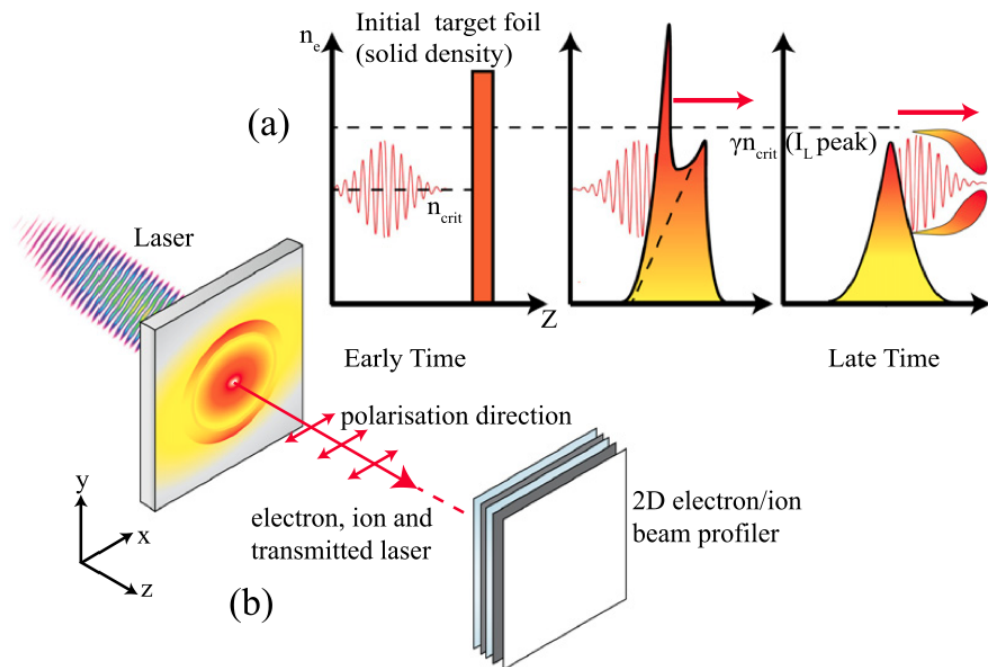


Figure 4.19: Target electron density evolution - (a) Schematic illustrating the target electron density evolution and induced transparency. (b) Schematic showing the laser foil interaction and the position of the electron and proton spatial-intensity distribution detector.

4. SINGLE PULSE INTERACTION WITH THIN SOLID TARGETS

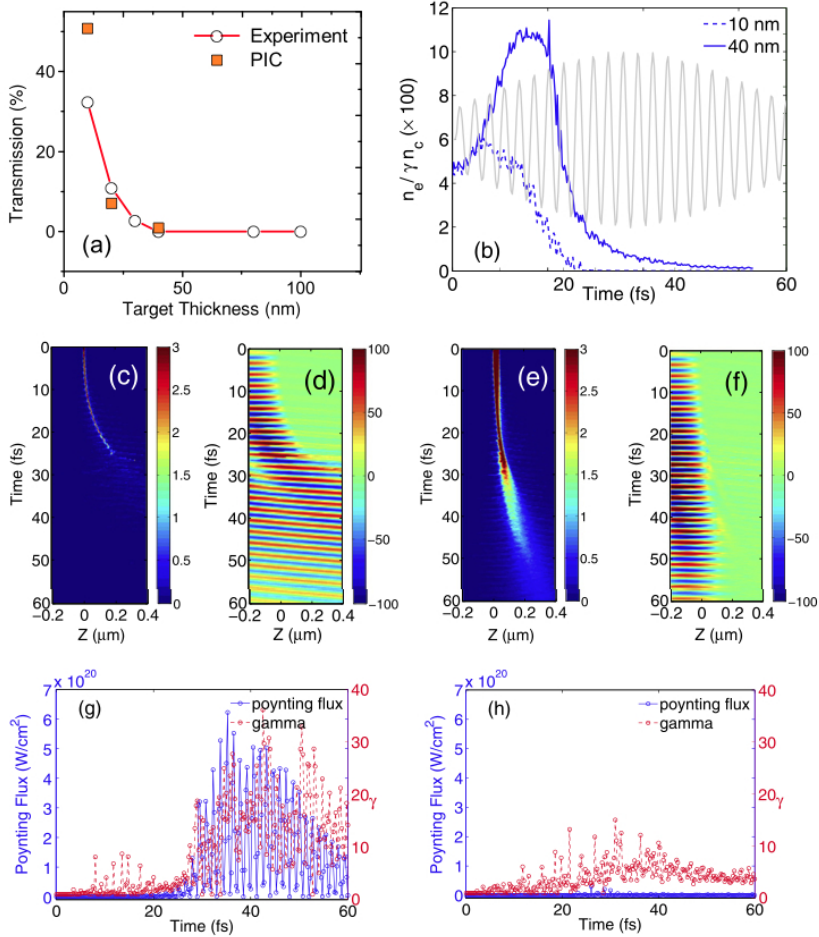


Figure 4.20: Laser pulse transmission and peak electron density - (a) Comparison between experiment and simulation results for the transmitted percentage of the laser as a function of target thickness. (b) Evolution of the peak electron density in the PIC simulation (at any position across the evolving electron density profile.) for $L = 10$ nm and 40 nm. The laser pulse temporal profile is shown in the background for reference. (c) Electron density (in units of $100 n_e/n_{cr}$) and (d) laser electric field (in units of TVm^{-1}) along the laser propagation (z) axis as a function of time, for $L = 10$ nm; (e) and (f) are the corresponding plots (same units) for $L = 40$ nm; (g) evolution of the laser Poynting flux and the electron Lorentz factor 600 nm from the target rear surface for $L = 10$ nm; (h) corresponding plots for $L = 40$ nm.

4.3 Electron dynamics during relativistic transparency

In a foil target, electrons are driven forward from the region of the critical density n_{cr} , beyond which the laser light cannot propagate, by the first component of the ponderomotive force (section 2.2.1), with a 2ω oscillation induced by the second component (155). In the specific case of targets in which relativistically induced transparency (RIT) occurs, the transmitted part of the laser pulse also ponderomotively drives a significant electron momentum in the perpendicular (radial) direction.

The RIT process (in detail explained in section 2.5) is illustrated schematically in 4.19, which also shows the longitudinal propagation of a ponderomotively-driven local region of enhanced electron density ahead of the laser pulse (156). Transparency changes the nature of the interaction from surface-dominated to volumetric (22), such that the collective electron response to the laser field continues over an extended distance.

An understanding of the charged particle dynamics in the RIT regime is particularly important for the development of the Break-Out Afterburner (BOA) (82) and RIT-acceleration (RITA) (156), and for schemes for which it is harmful, such as radiation pressure acceleration (RPA) (157), which is most effective just before transparency occurs.

Usually, the beam of electrons expelled by the ponderomotive force of an intense laser with a symmetric intensity profile has also a cylindrical symmetry along the laser propagation axis. However, in a theoretical study of BOA featuring 3D particle-in-cell simulations, Yin *et al.* (20) predicted an asymmetry in the collective response of the electrons in thin foil targets undergoing RIT.

A variation in the electron response to the laser ponderomotive force scaling as $\cos(2\theta)$, where θ is the angle between the electron radial momentum vector and the polarisation axis, is predicted to lead to the formation of electron density lobes in the direction orthogonal to the laser polarisation and propagation axes. Although signatures of an annular profile in BOA-ion acceleration had been reported (158, 159), the predicted azimuthal asymmetry in the electrons had not been measured directly.

Results from one of the experimental campaigns with the Astra Gemini laser demonstrate this asymmetry in the collective electron response to the radial ponderomotive force during RIT, as manifested in the formation of lobe structures in the spatial-intensity profile of the beam of electrons accelerated. The electron dynamics is shown, both experimentally and via PIC simulations, to be highly sensitive to the polarisation

4. SINGLE PULSE INTERACTION WITH THIN SOLID TARGETS

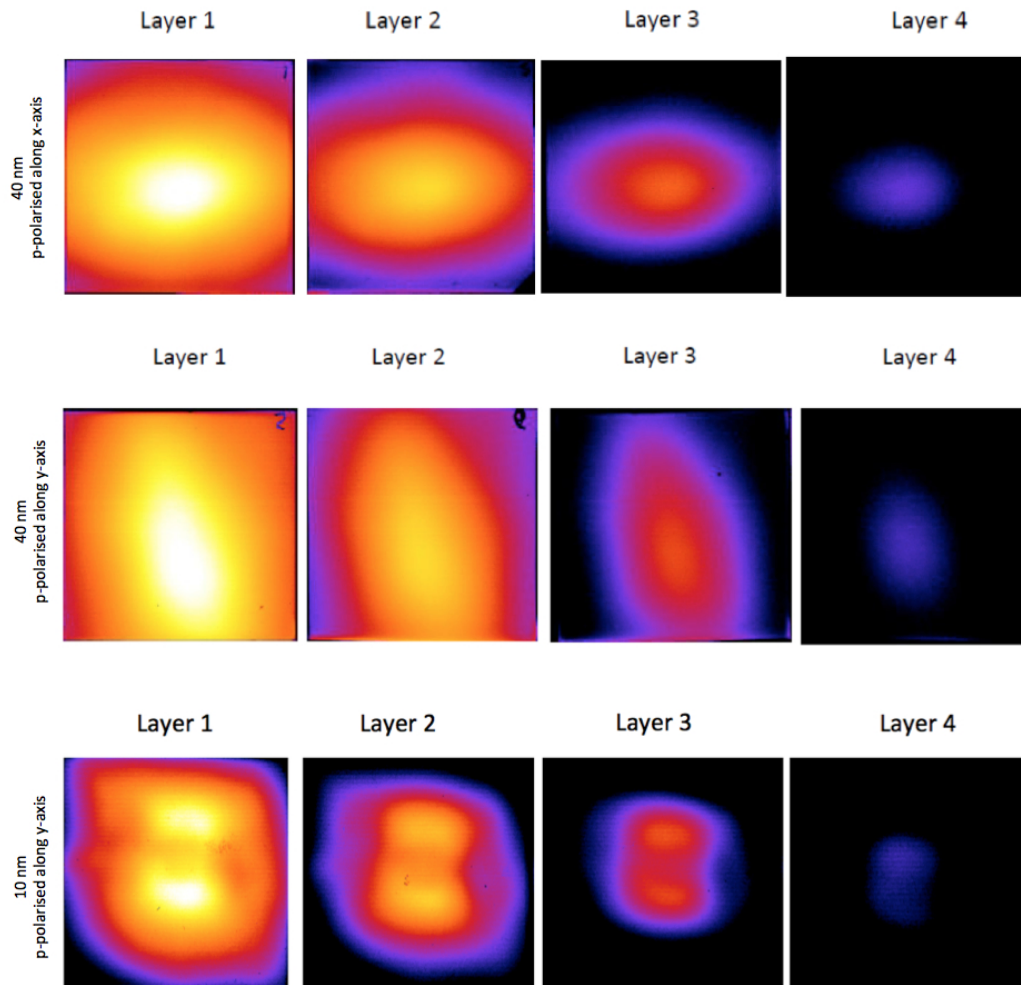


Figure 4.21: Electron spatial profiles - This shows the electron spatial profiles as imprinted on image plates for p-polarised laser light impinging on 40 nm and 10 nm Al foils. The polarisation axis is varied, thereby controlling the elliptic beam profile of the electrons

4.3 Electron dynamics during relativistic transparency

of the drive laser pulse and the degree of transparency induced. These results highlight the potential to control the collective electron dynamics, the formation of resulting electrostatic fields, and hence the spatial intensity profile of the beam of ions accelerated by these fields.

4.3.1 Experimental set-up

The Astra-Gemini Ti:Sapphire laser at the Rutherford Appleton Laboratory was used to produce pulses of 800 nm with typical duration, $\tau = 40$ fs (FWHM). For some shots, the laser pulse duration was varied in the range 40-160 fs by adding group velocity dispersion to the pulse via an acousto-optic modulator. A double plasma mirror set-up in-built in the Astra-Gemini transport system, enhanced the intensity contrast to $\sim 10^{11}$ and $\sim 10^9$, at 1 ns and 10 ps, respectively, prior to the peak of the pulse. The pulse was focused using an f/2 off-axis parabolic mirror, to a spot size of $3 \mu\text{m}$ (FWHM), yielding a calculated peak intensity, I , of $7 \times 10^{20} \text{ Wcm}^{-2}$. The pulse delivered ~ 2 J of energy on-target (i.e. the energy after the plasma mirrors and transport optics). A deformable mirror was employed prior to focusing to ensure a high quality focal spot.

The laser light was linearly polarised, with the direction of polarisation varied using a thin mica $\lambda/2$ wave-plate. The target was an aluminium foil, with thickness, L , varied in the range of 10-800 nm. It was placed in the laser focus, with the target normal in the direction of incidence of the laser.

Up to 15 targets were mounted on a motorised target wheel, allowing to change and align the target without the need to open the chamber (inner volume $\sim 5 \text{ m}^3$). The Astra-Gemini laser can in principle deliver a shot every 20 seconds, however the actual shot time is limited by the target alignment procedure, which can take up to 20 minutes. The targets are aligned with a retro-focusing system or white light illumination of the front surface and the use of a focal spot camera.

Due to the higher shot rate compared to the Vulcan system described in the previous section, primarily on-line diagnostics (such as a Thomson Parabola spectrometer coupled to a micro-channel plate with a phosphor screen and CCD camera) were employed (see section 3.1.4). All off-line diagnostics (such as Radiochromic Film stacks) were also mounted on motorised mounts for the same reasons stated above. During laser shots, the vacuum chamber was kept at a pressure of 10^{-4} mbar accomplished by roughing and turbo pumps.

4. SINGLE PULSE INTERACTION WITH THIN SOLID TARGETS

The energy of the laser light transmitted through the target (due to RIT) was monitored both by optical spectrometer measurements and by measuring the 2D spatial-intensity profile of the transmitted laser beam on a PTFE screen positioned behind the target, with a CCD camera. The energy transmission as measured by both diagnostics was calibrated by comparing the recorded signal to the energy measured on a calorimeter on shots for which there was no target in the beam path.

The 2D spatial-intensity profile of the beam of ponderomotively accelerated electrons by the laser pulse was measured 3 cm downstream from the target using passive stacked layers of Fujifilm image plates (IP), interleaved with iron filters¹, and in separate shots, in real-time using a Kodak Lanex screen detector, with equivalent iron filtering. The 2D spatial-intensity and spectral profile of the beam of accelerated protons was simultaneously measured using stacked layers of radiochromic film, placed immediately in front of the IP stack, filtered for energy selection with thin layers of Mylar and copper. The stacks were centred on the laser propagation (z -) axis, as illustrated in figure 4.19.

4.3.2 Experimental results

Figure 4.18 shows representative measurements of the spatial-intensity profiles of both the electron and proton beams, and exhibits the most salient features of the experimental results. The only laser pulse parameter varied for this data set is the direction of polarisation ($\tau = 40$ fs and $I = 7 \times 10^{20}$ Wcm⁻²). For $L = 800$ nm, for which induced transparency does not occur, the electron beam is circular and relatively small. For $L = 40$ nm, a larger number of electrons are detected and the beam is highly elliptical, with the major axis parallel to the laser polarisation. This is clear when comparing figures 4.18 (b) and (c) and 4.21, for which the laser polarisation vector is along the x -axis and y -axis, respectively. Similar polarisation-sensitive electron beam ellipticity has been previously observed in laser-underdense plasma interactions(160) (but not with overdense targets) and indicates strong electron interaction with the laser electric field.

Figure 4.18(d) shows the corresponding case for polarisation in x and a $L = 10$ nm target, for which a double-lobe structure, centred on the laser propagation axis and oriented in the axis perpendicular to the laser polarisations, is measured. In figure

¹RCF stacks with varying filtering were used, see table 3.2 for example stack design

4.3 Electron dynamics during relativistic transparency

4.18(e) the electron signal at a radius corresponding to the peak of the lobes is plotted as a function of θ (angle with respect to the polarisation axis). The variation in the distribution has a $\cos(2\theta)$ dependence, which is in good agreement with the theoretical predictions of Yin *et al.* (20). The double-lobe structure in the electron density arises due to the plasma response to the propagating laser field. Although the radial ponderomotive force is axisymmetric, as described in (20), a $\cos(2\theta)$ variation arises in the collective response of the electrons to the combined radial force and the laser E-field (the angular variation arising from a dot product in the momentum component terms).

The double lobe structure is only measured for the thinnest targets explored ($L = 10$ nm). Figure 4.18(f) and (g) shows the corresponding proton beam profile at two proton energies sampled. Generally with decreasing target thickness the proton beam becomes more structured, with evidence of hollowing for $L = 10$ -40 nm. The highest proton flux is typically measured off-axis, which is a signature of BOA-ion acceleration (158, 159). At low proton energies radial spoke features are also clearly observed for $L = 10$ nm, and the prominence of this feature also decreases with increasing L . By considering the magnitude and evolution of the charge separation-induced electrostatic fields, as determined from numerical simulations discussed in the next section, it is calculated that the measured double-lobe electron distribution could give rise to proton lobes separated by ~ 6 mm at the position of the RCF detector. The features observed in figure 4.18(g) are separated by about this scale, but a double-lobe structure is not clearly observed. The separation of the expected proton lobes will increase with the duration of the electrostatic field and hence the drive laser pulse. The theoretical study in which a double-lobe ion distribution is predicted was performed for laser pulses with $\tau > 150$ fs (20).

Figure 4.20(a) shows the measured percentage of laser light transmitted as a function of L . Only a few percent is transmitted for $L = 40$ nm, rising to $\sim 10\%$ for $L = 20$ nm and $\sim 30\%$ for $L = 10$ nm. The measured changes to electron and proton beam profiles are thus shown to be correlated with the onset of RIT.

4.3.3 Simulations of the onset of RIT

To investigate this correlation in more detail, 2D3V simulations were performed using the fully relativistic electromagnetic PIC code EPOCH by the Strathclyde group. Full 3D PIC simulations at the required spatial and temporal resolutions and solid density

4. SINGLE PULSE INTERACTION WITH THIN SOLID TARGETS

requires high performance computing resources much beyond those available for this study. However, 2D3V simulations enable core aspects of the collective effects governing RIT and the resulting electron dynamics to be explored. The simulation grid comprised a total of 7.2 million cells with ten particles per cell and a spatial resolution of 0.5×0.8 nm. The laser had a Gaussian profile both temporally and spatially. The target consisted of two species, electrons and Al^{13+} ions at a density $n_e/n_{cr} = 447$. In order to resolve the Debye length, the initial electron and ion temperatures were $T_e = 10$ keV and $T_i = 40$ eV, respectively. Simulations were performed as a function of laser polarisation, target thickness (10, 20 and 40 nm), laser intensity (up to 6×10^{20} Wcm^{-2}) and pulse duration ($\tau = 40$ -160 fs). The simulation plane is y-z, the laser is incident along the target normal (z-axis) and propagates only 200 nm in vacuum before reaching the target front surface (laser light therefore reaches the target 1.5 fs after the start of the simulation, ensuring interaction with an initially solid density target).

The predicted onset of transparency occurs at a target thickness of 20 nm, in good agreement with the experimental results figure 4.20(a), although the percentage of transmitted light is higher than that measured for the 10 nm thick target case. Simulations for $L = 40$ nm exhibit minimal transparency. As shown in figure 4.20(b), for this case the peak electron density increases by more than a factor 2 in response to the laser ponderomotive drive, and decreases to γn_c only very later in the laser pulse (which is included as a background plot). By contrast, for $L = 10$ nm significant transparency occurs as the peak density decreases to γn_{cr} on the rising edge of the laser pulse. The temporal evolution of the electron density and the laser electric field along the laser propagation axis ($y=0$) are shown in figure 4.20(c) and (d), respectively, for $L = 10$ nm, and in figure 4.20(e) and (f), respectively, for $L = 40$ nm. The effects of radiation pressure are observed in both cases, with the $L = 10$ nm target becoming transparent after 30 fs. The $L = 40$ nm case remains overdense throughout the simulation time.

The evolution of the electron Lorentz factor and the Poynting flux (which is a measure of laser energy) at an example distance of 600 nm downstream from the initial rear surface of the target, are shown in figures 4.20(g) and (h), for $L = 10$ nm and 40 nm, respectively. For the $L = 10$ nm case transparency occurs after ~ 30 fs, and the Lorentz factor increases by more than a factor of two in response to the transmitted laser pulse. There is no appreciable increase in the electron Lorentz factor downstream for the $L = 40$ nm case. The results presented in figure 4.20 all involve polarisation in

4.3 Electron dynamics during relativistic transparency

the plane of the simulation box. These results confirm that for the parameters of the experiment, significant transparency occurs for $L = 10$ nm and that the propagated portion of the laser pulse continues to act on the accelerated electrons over an extended volume at the target rear.

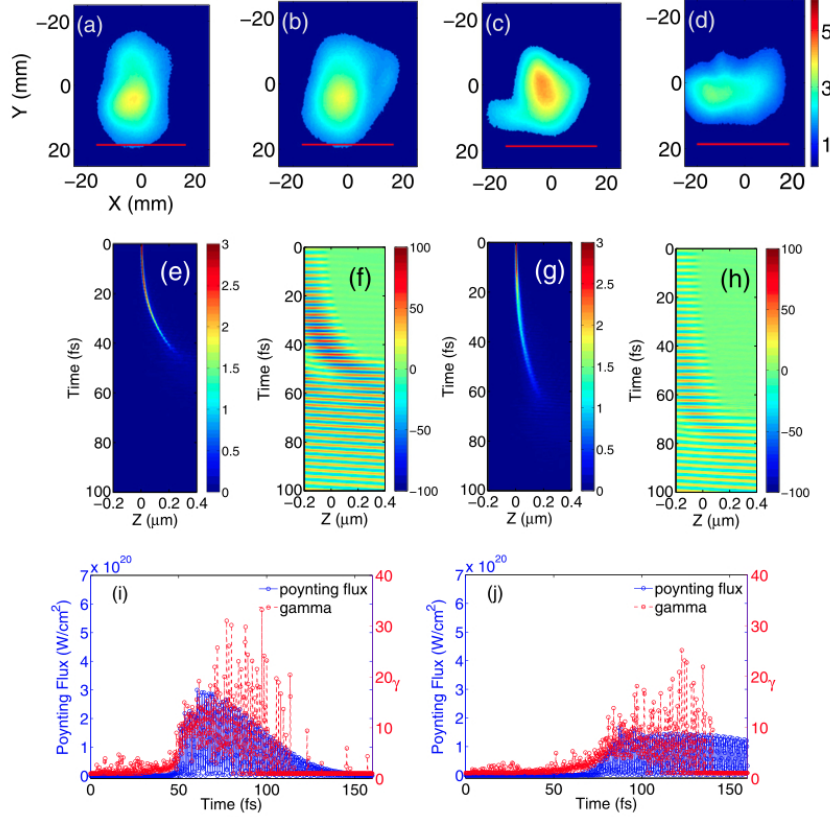


Figure 4.22: Electron beam density and Poynting flux - (a)-(d) Experimental results: 2D spatial-intensity distribution of the electron beam density (in arbitrary units) for energy > 5 MeV, as measured with a Lanex screen, for: (a) $\tau = 40$ fs; (b) $\tau = 80$ fs; (c) $\tau = 120$ fs, and (d) $\tau = 160$ fs. The laser is polarised along the x-axis in all four cases and the target thickness is 10 nm; (e)-(j): simulation results: (e) electron density (in units of $100 n_e/n_{cr}$) and (f) laser electric field (in units of TVm^{-1}) along the z-axis as a function of time, for a $\tau = 160$ fs pulse; (i) evolution of the laser Poynting flux and the electron Lorentz factor 600 nm downstream from the target rear surface for a $\tau = 80$ fs pulse; (j) corresponding plots for a $\tau = 160$ fs pulse.

To further confirm that the degree of RIT occurring defines the spatial-intensity distribution of the electron beam, both the experiment and simulation studies were ex-

4. SINGLE PULSE INTERACTION WITH THIN SOLID TARGETS

panded to investigate the sensitivity to the laser pulse duration, for fixed laser energy and target thickness $L = 10$ nm. Figures 4.22(a)(d) show that the orientation of the major axis of the resulting elliptical electron beam (measured on the Lanex screen) changes from being aligned perpendicular to the laser polarisation for a $\tau = 40$ fs pulse to being parallel for $\tau = 160$ fs. Corresponding simulation results for the temporal evolution of the electron density and laser electric field along the laser propagation axis are shown in figures 4.22(e)(h) for two example cases, $\tau = 80$ fs and 160 fs. The Poynting flux and Lorentz factor (as for the $\tau = 40$ fs results in figure 4.20(g)), are shown in figures 4.22(i) and (j), for $\tau = 80$ fs and 160 fs, respectively. In all cases the laser polarisation vector is in the plane of the simulation. The simulations confirm that the degree of transparency decreases with increasing pulse duration, because of the decreasing peak laser intensity. These results, when considered together with those in figure 4.20, demonstrate that the orientation of the electron spatial-intensity distribution is sensitive to the degree of laser light transmission.

In the discussion so far, the onset of transparency is described in terms of the combined effect of the increasing electron Lorentz factor, on the rising edge of the laser pulse, coupled with the thermal expansion of electrons into vacuum resulting in a reduced peak electron density, such that laser pulse propagation can occur part way through the interaction (74, 75). This physical picture is rigorously true for infinite plasmas. In the case of target thickness comparable to the plasma skin depth, the transparency conditions are modified due to additional effects such as the longitudinal ponderomotive force at the plasma interface (161). Vshivkov *et al.* (77) derive the conditions for relativistic transparency in a thin slab of overdense plasma as $a_0 \gg \omega_p^2 L / 2c\omega$, where ω and ω_p are the laser and plasma frequency, respectively, L is the target thickness and a_0 is the light amplitude (equation (50) in reference (77)). For the parameters of the present experiment, this condition is satisfied only for $L < 20$ nm (with the terms on the right side equal to a_0 for $L = 70$ nm). Thus the obtained results are also in good agreement with the analytical model of RIT in thin plasma slabs (77).

Also the role of light pressure compressing the electrons in the thin target such that the effective target width as seen by the laser becomes of the order of, or less than the skin depth has been considered. Whereas this can contribute to inducing transparency in thin foils in the case of circularly polarised laser light, due to the constant light pressure and reduced electron heating, in the case of linear polarisation and the other

4.3 Electron dynamics during relativistic transparency

laser and target parameters considered here the presented simulations indicate that RIT occurs predominately through plasma expansion reducing the peak electron density.

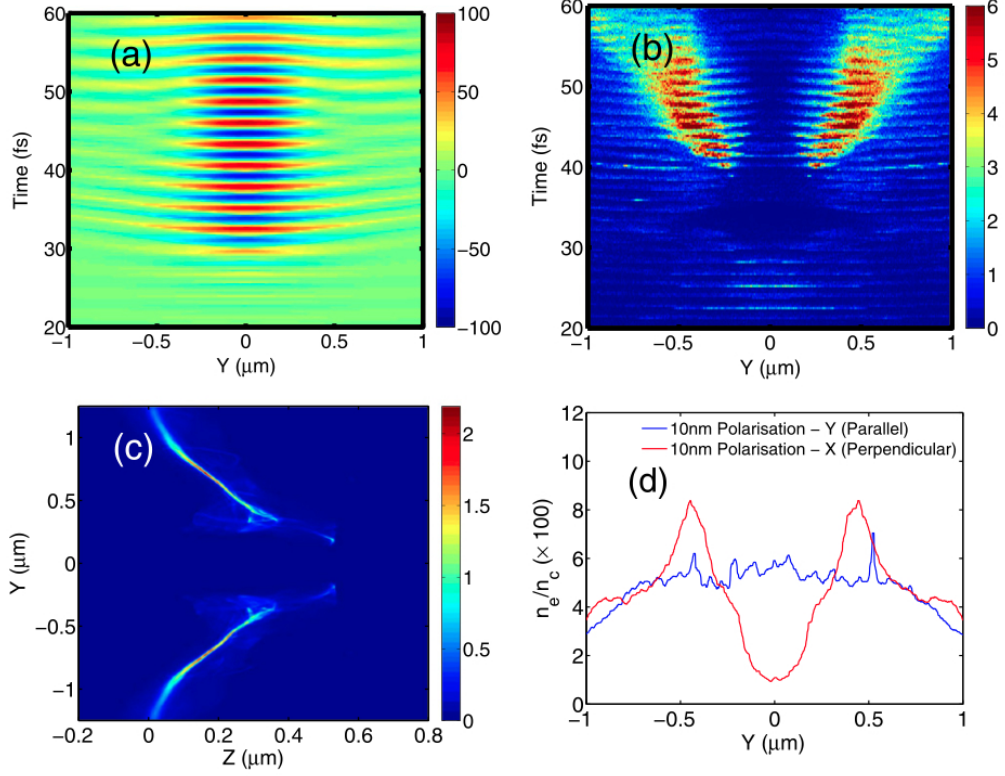


Figure 4.23: Temporal evolution of electric field and electron density - PIC simulation results showing the temporal evolution of (a) E_x , the laser E-field (in TVm^{-1}) and (b) the electron density (in units of n_e/n_{cr}), along the y -axis, at 600 nm downstream from the rear surface of a $L = 10$ nm target; (c) example 2D profile of the electron density at 35 fs, just after RIT has occurred (in units of $100n_e/n_{cr}$); (d) time-integrated electron density profile along the y -axis (at 600 nm from the rear surface) for the two polarisation directions.

4.3.4 Modelling axial asymmetry in the plasma response to RIT

Detailed numerical investigation of the asymmetry in the collective electron response to the onset of transparency requires high resolution 3D simulations with an initially solid density target, which were computationally too demanding. However, the 2D3V EPOCH code used employs a 2D simulation plane with 3 field and velocity components,

4. SINGLE PULSE INTERACTION WITH THIN SOLID TARGETS

which enables aspects of the asymmetry to be explored by comparing the 1D electron density profiles along the y -axis in simulation runs with the polarisation parallel (y -polarised) and perpendicular (x -polarised) to the simulation plane.

In figure 4.23 the electron response for the $L = 10$ nm case is explored. Figures 4.23(a) and (b) show the temporally-resolved E-field of the transmitted laser light and the electron density, respectively, as measured 600 nm downstream from the target rear surface. The laser is polarised in the x -axis (i.e. perpendicular to the plane of the simulation), and, as before, $t = 0$ corresponds to the start of the simulation. Electrons ponderomotively driven forward (longitudinally) by the laser pulse are ejected first from the target and detected downstream after about 20 fs. This population is relatively small in number compared to the dense population which arrives later and as a result shows up as a relatively weak signal along the $y = 0$ axis in figure 4.23(b). Before the target undergoes RIT it is driven forward by laser radiation pressure, to a maximum on-axis displacement of ~ 300 nm. After 30 fs the target is relativistically transparent and the remainder of the laser pulse is transmitted, as shown in figure 4.23(a). Figure 4.23(c) shows an example 2D profile of the target at 35 fs (just after RIT has occurred).

The simulations reveal strong radial expulsion of the electrons due to the radial ponderomotive force of the transmitted laser light and a longitudinal oscillation of the electrons in response to the 2ω component of the ponderomotive force, which results in bunches of electrons being ejected forward towards the diagnostic point downstream. As shown in figure 4.23(b), the density distribution of the radially expelled electrons (detected 600 nm downstream after 40 fs) is modulated at 2ω . Temporally integrated electron density profiles for the cases in which the distribution is sampled parallel and perpendicular to the laser polarisation vector are compared in figure 4.23(d). The double-peak feature observed perpendicular to the laser polarisation (x -polarised), which changes to a more uniform distribution for the parallel case (y -polarised), is qualitatively consistent with the experimental results in figure 4.18(d).

4.3.5 Summary

In summary, the dynamics of electrons in a relativistically transparent foil driven by a linearly polarised laser field were studied in this section. The onset of RIT for a 20 nm thin target was reproduced with particle-in-cell simulations for given laser parameters and target characteristics. RIT occurs mainly due to plasma expansion, which agrees

4.3 Electron dynamics during relativistic transparency

with the analytical model. The orientation of the spatial intensity distribution of the electrons is correlated with the degree of laser light transmission. The collective dynamics of electrons in a relativistically transparent foil driven by a linearly polarised laser field is experimentally shown to exhibit a $\cos(2\theta)$ dependence, as manifested in a double lobe formation in the electron density distribution. This was predicted theoretically by Yin *et al.* (98) and reproduced with particle-in-cell simulations. The degree of structure in the proton beam, the the form of radial spokes in the beam is also found to be correlated to the onset of transparency, showing signatures of the BOA acceleration model.

4. SINGLE PULSE INTERACTION WITH THIN SOLID TARGETS

5

Double pulse interaction with thin solid targets

From the early days of laser acceleration research there has been a continuing effort to further understand and harness the rich variety of phenomena that arise in the laser-plasma interaction, by varying in a controlled manner the myriad of parameters that determine them. These include the target size, shape, and composition (16, 162), the geometry of the interaction (163) and laser parameters (intensity, polarisation, pulse duration, and pulse shape) (91, 132, 164, 165).

Among the latter the use of a controlled pre-pulse has been proposed as an effective way to tailor and optimise the target density profile (166, 167). For instance, an intense enough pre-pulse may initiate an expansion of the target so that some time afterwards the main pulse may encounter a near critical density plasma. Such near critical density plasmas are particularly well suited for sustaining the hole boring mechanism of ion acceleration (92, 168).

In the following chapter, the investigations of ion acceleration using double laser pulse schemes are presented.

Experimental campaigns were carried out with ultrathin solid aluminium targets to study the feasibility of enhanced acceleration of ions with a double laser pulse set-up (both pulses linearly polarised). The results led to the investigation and proposal of a novel scheme of acceleration using a double pulse with mixed polarisations (linear and circular).

5. DOUBLE PULSE INTERACTION WITH THIN SOLID TARGETS

Extensive simulations with the particle-in-cell code OSIRIS were performed in order to find the best practical conditions for this new accelerations scheme.

The first part of the chapter presents an enhanced proton acceleration in the relativistic transparency regime. It includes experimental results from one of the campaigns carried out with the Vulcan laser and numerical results obtained with the particle-in-cell code EPOCH by the Strathclyde group. The presented work was published in the New Journal of Physics (169). In the second part of the chapter, the results obtained with the OSIRIS code are presented. These simulations were firstly carried out for long picosecond pulse durations to allow comparison to the experimental and numerical results presented in the first part, and then extended to a feasibility study with short femtosecond pulses.

5.1 Ion acceleration in a pre-expanded plasma

As discussed in previous chapters, the interaction of an intense-laser with ultrathin targets may generate ion beams by a variety of mechanisms. An enhanced energy coupling is mediated by a self-generated plasma channel, leading to absorption over an extended length of near-critical density plasma. The final maximum ion energy in the vicinity of the channel can be increased, and this increase is highly sensitive to the intensity profile of the rising edge of the laser pulse, which varies the extent of overlap between the channel and the expanding proton layer.

5.1.1 Experimental set-up

The experimental results were obtained with the Vulcan Petawatt laser (described in section 3.1.1.1). Figure 4.10 shows the experimental arrangement. Beside the normal single shot operation as employed in the previous set of measurements, the pulse was also configured to deliver double pulses separated by a delay of 1.5 ± 0.1 ps.

This mode was achieved by introducing a pre-pulse after the first stage of pre-amplification and before the pulse stretcher, using a polariser and polarising beam splitter to control the energy. Therefore the first pulse effectively acts as a controlled pre-pulse with a variable intensity ratio. The rest of the experimental arrangement, focusing system, plasma mirror, target mount and beam diagnostics, were the same as described before in section 4.2.

5.1 Ion acceleration in a pre-expanded plasma

Taking into account the beam losses on-route to the target by optics and plasma mirror, a total of 200 J energy was delivered on target. The measured focal spot at FWHM diameter was $7.3 \mu\text{m}$, which combined gave a peak intensity, I_L , of $2 \times 10^{20} \text{ Wcm}^{-2}$ ($a_0 = 13$) in the single pulse case. In the double pulse case the energy was divided between the first and second pulse, therefore the total intensity was the same.

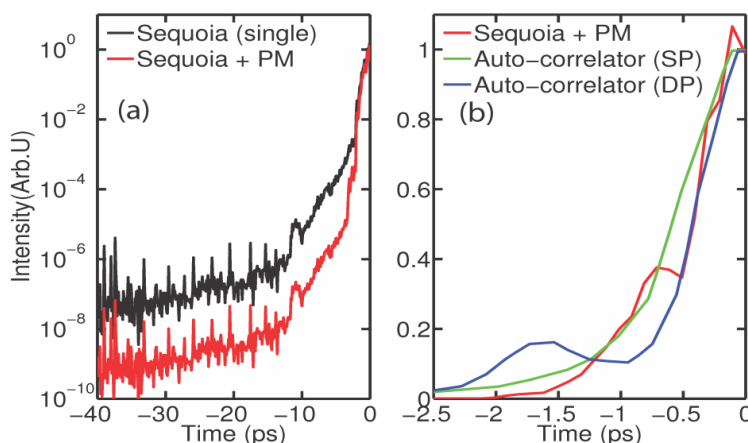


Figure 5.1: Laser contrast - (a) Third-order autocorrelation measurement of the rising edge profile of the laser pulse (black line); modelled contrast enhancement due to plasma mirror (red line). (b) Same plot as the modelled contrast enhancement in (a), but on a linear intensity axis and scaled to view the picosecond rising edge of the pulse

Due to the relatively long pulse duration of Vulcan, the amplified spontaneous emission can drive significant plasma expansion before the arrival of the main pulse. In order to remove the unwanted ASE and improve the contrast of both the wanted pre-pulse and the main pulse a plasma mirror has been employed. It was placed after the off-axis parabola. In figure 5.1 an example temporal contrast is shown made of the pre-amplifiers, stretcher and compressor systems using a third order cross-correlator (Sequoia) (see section 3.1.2 for details). This detailed scan was made with low power pulses and represents the inherent intensity contrast of the laser pulses, i.e. without plasma mirrors. The contrast enhancement produced by the plasma mirror cannot be measured using the same scanning technique due to the requirement to operate the plasma optics with full power pulses and therefore in single-shot mode. Therefore, the calculated pulse intensity profile after the plasma mirror, as modelled using measurements of the plasma mirror reflectivity as a function of peak intensity (170), is shown in

5. DOUBLE PULSE INTERACTION WITH THIN SOLID TARGETS

figure 5.1. The corresponding plot in the picosecond region of the laser pulse is shown in figure 5.1(b) on a linear axis.

To quantify changes to the intensity on the rising edge the parameter I_{RE} is used, which is the intensity 1.5 ps before the peak of the main pulse. With the plasma mirror, $I_{RE} \sim 0.04I_L$. The addition of a variable intensity pre-pulse increases I_{RE} up to a maximum value of $0.2 I_L$. Example on-shot autocorrelation measurements in the single and double pulse modes are also shown in figure 5.1(b), together with a reference Gaussian pulse.

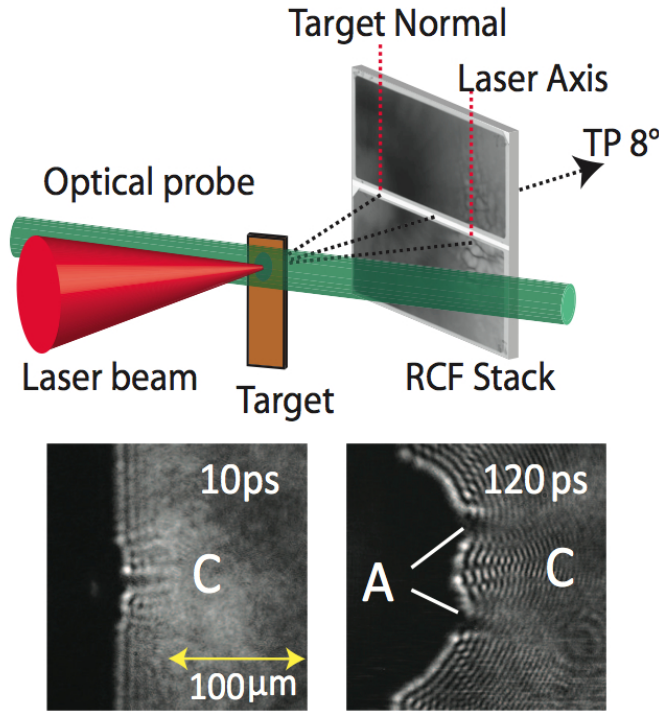


Figure 5.2: Experimental set-up - Experimental set-up (top) and example optical probe images (bottom) of rear-surface plasma expansion for a $L = 40$ nm target after 10 ps and 120 ps. Features consistent with channel formation and ring-like expansion are labelled C and A, respectively.

The laser either impinged normally or with an incidence angle, θ_L of 30° with respect to the target normal. The laser was linearly polarised (p-polarisation for the 30° incidence case). The oblique incidence angle was chosen to be sufficiently large to clearly separate the proton beam components directed along the target normal (i.e. TNSA) and

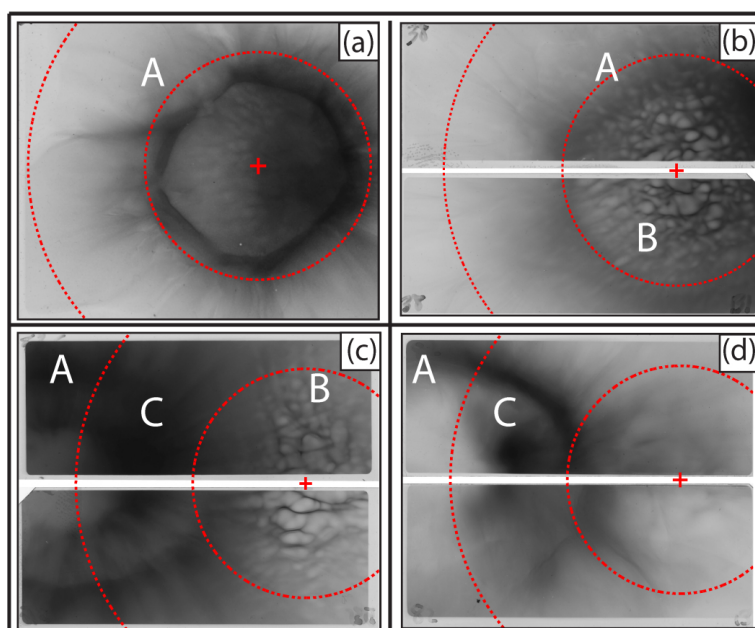


Figure 5.3: Proton spatial-intensity profiles - Proton spatial-intensity profiles in the range 5-7 MeV. (a) [$\theta_L = 0^\circ$, $I_{Re} = 0.04 I_L$, $L = 10$ nm]; (b) [$\theta_L = 0^\circ$, $I_{Re} = 0.1 I_L$, $L = 10$ nm]; (c) [$\theta_L = 30^\circ$, $I_{Re} = 0.1 I_L$, $L = 40$ nm]; (d) [$\theta_L = 30^\circ$, $I_{Re} = 0.2 I_L$, $L = 40$ nm]. The red cross marks the laser propagation axis and the circles mark the radii at 15° and 30° . See text for details on labels A, B and C.

5. DOUBLE PULSE INTERACTION WITH THIN SOLID TARGETS

along the laser axis (i.e. RPA in expanded plasma), while ensuring complete collection of all components on the detector. A schematic of the experimental arrangement is shown in figure 4.10 and 5.2.

The target foils consisted of aluminium with thickness, L , varying between 10 and 40 nm. As it was found in the experiments, in both cases relativistically-induced transparency occurs to different extents. Protons and carbon ions arise from hydro-carbons on the target surfaces. The transparency was measured at the back side of the chamber (i.e. on the right side of the chamber in figure 4.10), collecting the transmitted light with two CCD cameras at the back side of the chamber, that is, in front of the target from the point of view of the incident laser. The cameras were fitted with interference filters at the laser fundamental wavelength and second harmonic respectively. It was found that the laser energy transmission was typically a factor of 2.5 higher for the 10 nm foils compared to the 40 nm case. Some shots with 100 nm and thicker aluminium have not shown any transparency.

Various diagnostics were employed to monitor the charged particle dynamics. The spatial-intensity distribution of the protons accelerated by the various acceleration schemes was measured in coarse energy steps using a stack of radiochromic films (RCF), positioned 7.5 cm behind the target (sample stack composition is shown in table 3.2. The dimensions of the RCF were 6.4 cm \times 5.0 cm.

A slot in the RCF stack provided a line-of-sight to a Thomson parabola spectrometer (see section 3.1.4.1) (171) with calibrated image plate detectors (172). This was used to measure the charge-to-mass (q/m) ratio of the different ion species and the energy spectra of the ions accelerated along a sample angle of 8° from the laser axis. The low energy threshold of the Thomson Parabola for protons was 5 MeV and the spectral measurements were background-subtracted.

The plasma expansion depends sensitively on the initial target thickness as well as the incoming laser parameters. A transverse optical probe was used to monitor the plasma expansion profile by shadowgraphy (173), Mach-Zehnder interferometry (174) and Nomarski interferometry (175). Example probe interferograms are shown in figure 5.2. The figures shows features in the plasma expansion which are consistent with the proton beam measurements and simulations.

5.1.2 Experimental results

In figure 5.3 representative measurements of the spatial-intensity profile of the proton beam are shown for both normal and 30° incidence, different pre-pulse intensity ratios, $I_{RE} = 0.04I_L$ (single pulse) and $I_{RE} = 0.1 - 0.2I_L$ (double pulse), respectively and target thickness $L = 10$ nm and 40 nm.

The red cross marks the laser axis, and each dotted circumference marks the intersection of the RCF with 0° and 30° aperture cones originating at the point of interaction. The $[\theta_L = 0^\circ; I_{RE} = 0.04I_L; L = 10$ nm] in figure 5.3 (a) is dominated by an annular ring profile with divergence half-angle of $\sim 12^\circ$. A similar feature has been observed with diamond-like carbon foils undergoing relativistically-induced transparency (158, 176). Signatures of this feature are referred to as 'A' in the following text.

As shown in figure 5.3(b) for $[\theta_L = 0^\circ; I_{RE} = 0.1I_L; L = 10$ nm], when increasing I_{RE} , bubble-like structures are formed, which are referred to as feature 'B'. These are attributed to transverse instabilities (78) and clearly observed in the ring.

As described in chapter 4.1 a radiation pressure driven acceleration mechanism produces a particle beam in the direction of the laser whereas the TNSA produces a beam in the direction of the target normal. Therefore, if both mechanisms coexist in the interaction it is possible to distinguish their contributions by tilting the target with respect to the incoming laser, hence creating two angularly separated particle beams. This can be seen in figure 5.3 (c) and (d).

Figure 5.3(c) shows the proton beam profile obtained after tilting the target by 30° , with $I_{RE} = 0.1I_L$ and $L = 10$ nm. The bubbles only occur along the incoming laser axis which is consistent with the prediction that they only appear in case of radiation pressure accelerated protons, but not for sheath-accelerated protons. The ring however is centred along the target normal axis in all shots.

An enhanced region of proton density and maximum energy is observed near the edge of the ring at an angle of $15-20^\circ$ from the laser axis. This feature is labelled 'C' in figure 5.3. This feature is more clearly observed for the 40 nm targets $[\theta_L = 30^\circ; I_{RE} = 0.2I_L; L = 40$ nm]. Feature 'C' moves around from shot-to-shot within an approximately 10° angular range. On many shots it overlaps with the localised region of the ring, giving rise to an arc-shaped population of higher energy protons on the RCF,

5. DOUBLE PULSE INTERACTION WITH THIN SOLID TARGETS

and in other shots, where it does not overlap the ring, it is approximately circular as shown in 5.3(d).

Due to the movement of feature 'C' it was not possible to measure the corresponding proton spectrum with a fixed spectrometer sampling a small angular range. Instead, the spectrum in the region of this feature was obtained from the RCF stack and is shown in figure 5.4. Corresponding spectra measured using the spectrometer at 8° are shown in figure 5.4. Both sets of measurements show an extension of the spectrum to higher energies as the pulse intensity ratio is increased, highlighting an overall enhancement in ion energies in the angular region between the laser axis and target normal. The largest enhancement is measured in the region of feature 'C'. In order to explain these phenomena a set of PIC simulations were performed, which are presented in the following section.

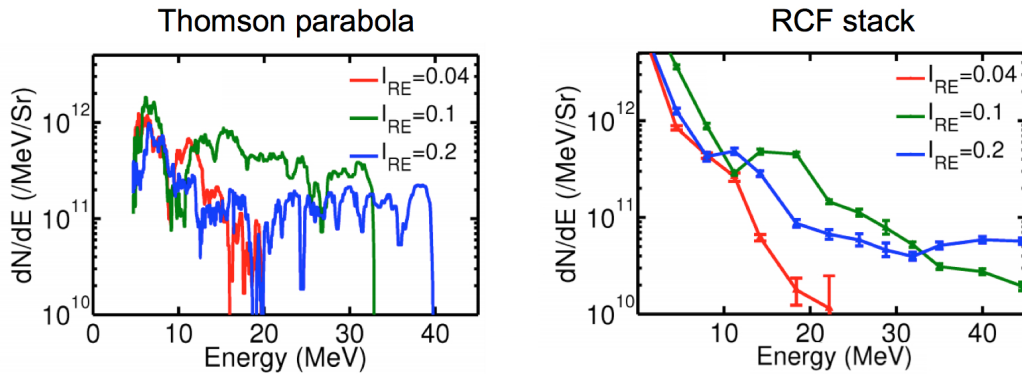


Figure 5.4: Energy spectra - Proton energy spectra in the region of feature 'C', as measured using the RCF stack (right), for three example I_{RE} (all for $\theta_L = 30^\circ$ and $L = 40$ nm. Left: Corresponding proton energy spectra as measured using the Thomson parabola spectrometer at 8° to the laser axis.)

5.1.3 Simulations

The underpinning physics was investigated by performing 2D and 3D PIC simulations with the EPOCH code (154) with parameters chosen to be comparable with the experiment.

The simulation box for the 2D runs was $175 \mu\text{m} \times 65 \mu\text{m}$, using 26000×3840 mesh cells and 50 particles per cell. The target is angled at 30° to the laser axis and was

5.1 Ion acceleration in a pre-expanded plasma

initialised as a 40 nm thick layer of Al^{11+} with an ion density of $60 n_{cr}$, with 8 nm thick hydrocarbon contamination layers with $60 n_{cr}$ H^+ and $20 n_{cr}$ C^{6+} on both surfaces. Test simulations with the EPOCH code incorporating an ionisation model showed that for the explored parameter range, the predominant ionisation state reached in aluminium and carbon is $q = +11$ and $+6$, respectively. The initial electron temperature was set to 10 keV. The laser pulse had a Gaussian temporal envelope with a FWHM of 0.5 ps and was focused to a Gaussian intensity profile with FWHM $6 \mu\text{m}$. The peak intensity was $2 \times 10^{20} \text{ Wcm}^{-2}$. The rising edge profile was varied by using a pre-pulse of same duration with peak-to-peak separation of 1 ps. I_{RE} was varied up to $0.5 I_L$, reducing the peak intensity to keep the energy fixed.

Due to computational restraints, the numerically intensive 3D run used a $60\mu\text{m} \times 20\mu\text{m} \times 20\mu\text{m}$ simulation box with $3000 \times 360 \times 360$ cells. To compensate for the reduction in resolution and box size, the target consisted of the equivalent of 20 nm Al^{11+} at a density of $60n_{cr}$, expanded to a Gaussian profile with a peak density of $5n_{cr}$ (informed by the 2D results). Similarly the H^+ and C^{6+} layers were expanded to peak densities of $5n_{cr}$ and $1.67n_{cr}$, respectively. The initial electron temperature was 10 keV. The two laser pulses were again focused to $6 \mu\text{m}$, but the pulse durations were reduced to 0.2 ps (FWHM) with a 0.5 ps separation, to make the 3D simulations feasible. Test simulation with pulse durations from 0.2 to 0.8 ps showed similar behaviour in all cases for which relativistically-induced transparency occurs. Example results are shown in figure 5.5 and 5.6 for the 2D and 3D simulations, respectively. The electrons heated at the target front side propagate through the plasma and create a Debye sheath at the back of the target that accelerates the protons in the target normal direction. The higher q/m species expand faster than the lower ones. This results in the layering of the ion species in the beam, where the protons take the lead. RIT occurs near the peak of the pulse, which drives additional electron heating over the target volume. As shown in figure 5.5(b,f), electrons are heated over a radius of tens of micrometres at the target rear. This occurs because the radial ponderomotive force due to the propagating part of the laser pulse drives the electrons radially outwards. This behaviour is clearly observed in the 3D simulations and is consistent with previous observations (82, 153). As discussed in the context of BOA (82, 158), in addition to a general enhancement in the acceleration electric field, energy exchange from the electrons to the ions can occur via relativistic Buneman-like instabilities (99) (see section 2.6).

5. DOUBLE PULSE INTERACTION WITH THIN SOLID TARGETS

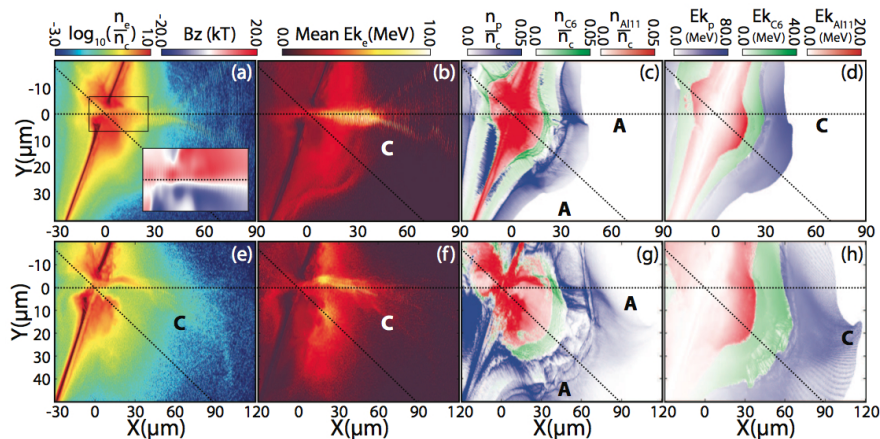


Figure 5.5: 2D simulation results - Top row: 2D PIC results showing (a) electron density and magnetic field (inlet), (b) mean electron energy, (c) ion density (protons -blue; C^{6+} - green; Al^{11+} - red) and (d) mean ion energy, all for $I_{Re} = 0$ at an example time of 1 ps. The laser is incident from the left along the $Y = 0$ axis. The dotted lines mark the laser and target normal axis. Bottom row: Same for $I_{Re} = 0.2 I_L$ at the same time relative to the peak of the main pulse.

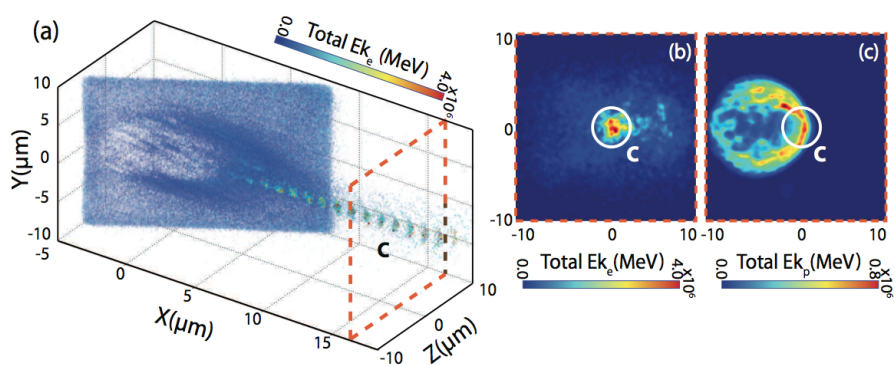


Figure 5.6: 3D simulation results - 3D PIC results showing (a) an example 3D plot of the total electron energy at 0.4 ps, and 2D maps of the total (b) electron and (c) proton energies in the Y-Z plane at $X = 16 \mu\text{m}$. At this relatively small distance from the target the channel (C) is on-axis and overlaps with one side of the expanding proton ring distribution. At larger distances it steers off-axis as shown in figure 5.5(f)

5.1 Ion acceleration in a pre-expanded plasma

In agreement with the experimental results, the simulation exhibit a ring-like proton distribution centred along the target normal, labelled 'A', in figure 5.5(c,g). This feature is not directly induced by the additional heating or radial expansion of the electron population (which is centred along the laser axis), but is produced by the RIT-boosted acceleration of heavier (C and Al) ions into the expanding TNSA proton population (this is discussed in the following section). The transverse optical probe measurements in figure 5.2(d) show a region of enhanced density either side of the target normal, consistent with a ring (labelled 'A'). A comparison of probe images at different times with respect to the peak of the laser pulse shows that this ring feature expands outwards.

A salient feature of the simulation results is the observation that the onset of RIT is accompanied by the formation of an energetic electron jet extending into the expanded ion layers - feature 'C' in figures 5.5 and 5.6. The jet is bounded by a magnetic field, which is shown in the inset of figure 5.5(a) for the region around the target bounded by the rectangular box. Jet-like current filaments of this type can be produced in magnetised channels or magnetic vortex-driven current structures generated when fast electrons are turned around in the sheath field formed at the rear of the plasma slab (177). A plasma channel or jet-like feature extending from the rear of the target is observed experimentally in the transverse optical probe measurements of figure 5.2(d), at early times after the interaction (at 10 ps). Due to the co-propagation of the transmitted part of the laser pulse with the jet, direct acceleration of electrons occurs over an extended distance, resulting in electron energies significantly higher than the surrounding plasma, as shown in both the 2D and 3D simulations (e.g. figure 5.6(a)). Note that electron bunching is observed within the jet at the laser frequency, as clearly observed in figure 5.6(a).

The additional electron energy is in turn coupled to protons in the vicinity of the jet. Figure 5.7 shows a plot of the longitudinal component of the electric fields induced by the particles (i.e. with the laser field removed) for the simulation reported in figure 5.5(a-d). The electrostatic fields formed at the interfaces between the three ion species layers produces a buffering acceleration effect (167, 176) over the full angular range. Discontinuities in these fields occur where the carbon ions, further accelerated by the RIT-driven volumetric heating of plasma electrons, are driven into the proton layer and produce the measured proton ring. Also, a strong longitudinal electric field is

5. DOUBLE PULSE INTERACTION WITH THIN SOLID TARGETS

produced along the plasma jet and extends into the proton layer. This field overlaps with the highest energy protons (c.f. figure 5.5(d)) and typically occurs at one side of the expanding proton ring.

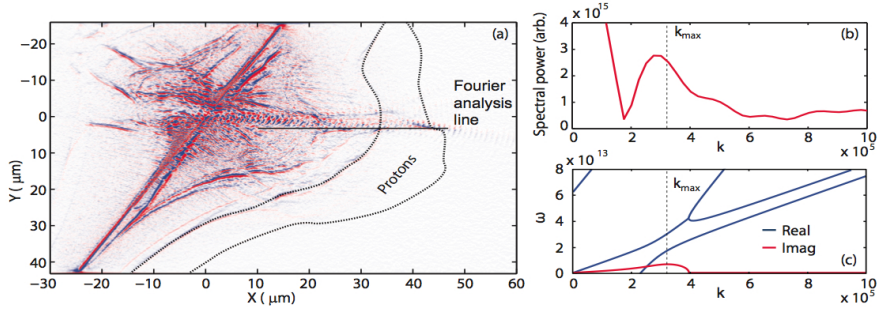


Figure 5.7: 2D simulation results - (a) 2D PIC results showing the longitudinal electric field for $I_{Re} = 0$ at an example time of 1 ps. The dashed region mark the extent of the front and rear of the proton layer and the field driven by the jet is observed to extent into it; (b) Spectral power as a function of wave number k along the solid line in (a), which marks the region along the jet at which the highest energy protons are produced (as shown in figure 5.3(d)); (c) Analytic solutions to the linear dispersion relation for the Buneman instability, as discussed in the text. The maximum wave growth occurs at k_{max} .

Initially directed along the laser axis, after tens of micrometres the jet steers by 10 to 15° due to the local asymmetry in the plasma density arising from the target tilt. This results in the highest energy protons being produced in a narrow off-axis region, amongst a broader angular distribution of lower energy ions, as shown in figure 5.5(d) and (h) and in figure 5.6(c). This is fully consistent with the experimental results for which the highest energy protons are measured in the RCF at or near the edge of the proton ring (feature 'C' in figure 5.3(c) and (d)). The simulations show that the jet radius increases towards the limit of the expanded plasma because the magnetic field strength decreases due to the lack of background electrons to provide a neutralising return current.

5.1.4 Energy transfer to ions

Although a magnetised channel or vortex structure may account for the production of the electron jet, the parameters are unsuitable for accelerating ions via the magnetic vortex acceleration scheme (178). That scheme requires a well-defined localised

5.1 Ion acceleration in a pre-expanded plasma

magnetic field structure, such as produced at a plasma boundary, which moves in a non-uniform plasma producing a localised moving longitudinal electric field structure. In the case as described in the previous sections, the expansion characteristics of the target produce non-localised magnetic and electric field structures. To explore the energy transfer between the electrons and ions a Fourier analysis was performed along the longitudinal electric field in the region of maximum proton energy enhancement and in the vicinity of the electron jet (shown by the line in figure 5.7(a)), to measure the spatial structures present. Figure 5.7(b) shows a strong spatial structure in the region of wave numbers, k , between 2×10^5 and $4 \times 10^5 \text{ m}^{-1}$ which grows over time after the target has gone transparent. This structure appears to be correlated to the relativistic Buneman instability. Using mean proton and electron plasma frequencies, ω_p , and velocities, v , along the analysis line the following linear equation for the Buneman instability is solved:

$$\frac{\omega_{pi}^2}{(\omega - kv_i)^2} + \frac{\omega_{pe}^2}{(\omega - kv_e)^2} = 1 \quad (5.1)$$

This results in the dispersion relation shown in figure 5.7(c). The real solutions correspond to waves that can propagate due to the coupling of the plasma oscillations of the different particle populations. Instabilities grow in the region where there are complex solutions to the dispersion equation. It can be seen that the maximum growth occurs at $k_{max} \sim 3.2 \times 10^5 \text{ m}^{-1}$ (given by the imaginary component of the complex solution). These dispersion solutions are indicative of a set of fixed plasma frequencies and velocities, whereas in the simulation these values are evolving. Nevertheless, this approximation is in good agreement with the spatial structure growing in the simulations. This suggests that the energy transfer mechanism from the electron jet to the protons is related to the Buneman instability.

5.1.5 Sensitivity to the rising edge intensity profile

The measured maximum proton energy of feature 'C' increases with I_{RE} , as shown in figure 5.8(a), doubling over the range $I_{RE} = 0.04 - 0.2I_L$. Both the 2D and 3D simulations also exhibit an increase over this range. Compared to experiment, the predicted energies are higher in the 2D and lower in the 3D case, but these absolute values depend on the laser pulse duration and simulation times (which are shorter for

5. DOUBLE PULSE INTERACTION WITH THIN SOLID TARGETS

the more computationally intense 3D runs). With an increasing I_{RE} the expanded near-critical density plasma becomes more favourable for extended jet formation, resulting in higher laser energy coupling to electrons, as shown in figure 5.8(a). The case $I_{RE} = 0$ corresponding to an idealised laser pulse, is an exception. Higher proton energies are predicted because limited ion expansion prior to RIT results in the jet extending over the full dense proton layer, as shown in figure 5.5(a-d) (where the proton front reaches $X=60\mu\text{m}$ and the jet extends beyond this). Energy coupling to protons is particularly effective in this scenario.

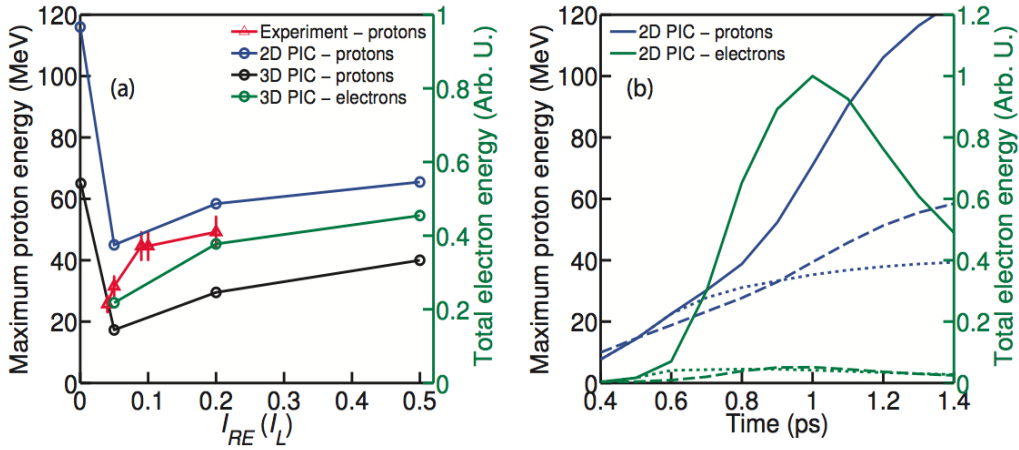


Figure 5.8: Numerical and experimental energy comparison - (a) Comparison of the maximum proton energy in the experiment and in the 2D and 3D simulations, and total electron energy in the region of the channel 3D simulations, as function of I_{Re} . (b) Temporal evolution of the maximum proton energy and total electron energy behind the target. Solid line corresponds to $L = 40$ nm with RIT; dotted line corresponds to $L = 40$ nm with the laser pulse truncated immediately prior to RIT; dashed line corresponds to $L = 800$ nm with the full laser pulse (no RIT)

Figure 5.8(b) shows the evolution of the total electron energy, which rapidly increases when RIT occurs at 0.6 ps, and decreases as the laser pulse decays and energy is transferred to fields and ions. There is a corresponding increase in the proton acceleration (significant change in the slope at 0.8 ps), resulting in an overall maximum energy enhancement of a factor of ~ 3 over the TNSA-protons set in motion before RIT occurs. The increase is a factor ~ 2 over TNSA driven by the full laser energy on a target which does not undergo RIT. Even with a relatively small inherent I_{RE} level

of a few percent of I_L , the proton layer expands significantly before RIT occurs and thus the jet is formed mainly within the lower q/m ion layers.

5.1.6 Summary

In summary ion energy enhancement in ultrathin foils undergoing relativistic induced transparency was investigated in this section using a double pulse laser scheme. It is shown that TNSA, RPA and transparency-enhanced/BOA acceleration can all occur, at different stages in the laser pulse interaction with the target. The individual mechanisms can be investigated angularly separating the ion beams produced by tilting the target foil with respect to the incident laser. Also, the highest energy ions are measured in a narrow angular range and result from additional acceleration driven by a transparency-induced jet of high energy electrons. In the absence of an ideal drive laser pulse with a very sharp picosecond rising edge, a controlled target expansion tailoring of the rising edge intensity profile produces an extended plasma jet and thus better energy coupling to the expanded proton population.

2D and 3D PIC simulations performed with the EPOCH code revealed a novel three-stage mechanism: 1) sheath expansion 2) hole boring shock wave acceleration, and 3) energy transfer by two-stream instabilities. The latter causes a resonant energy transfer between the ions species at the later stage of the interaction. The process begins with the arrival of a first lower energy laser pulse, which heats the target electrons, driving plasma expansion and TNSA. Ions of differing charge-to-mass ratios expand at different rates, resulting in a spatial layering of ion species. As expansion continues and the sheath field decays, the second, more intense laser pulse propagates into the near-critical (but still overdense) plasma. A layer of target electrons is ponderomotively compressed and driven forward, inducing a strong longitudinal electrostatic collisionless shock wave which reflects the Al ions forward. These fast SWA-ions begin to stream through the slower expanding Al layer, resulting in the growth of an electrostatic field due to the well-known ion two-stream instability (99). As this field grows in time there is a resonant energy exchange between the two ion populations whereby the wave eventually reaches a saturation point in which a component of the fast aluminium population begins to decelerate resulting in an acceleration of the slower aluminium ions. This acceleration would, ordinarily, result in the dampening of the electric field. However, due to the onset of self-induced transparency at a critical point on the rising edge of

5. DOUBLE PULSE INTERACTION WITH THIN SOLID TARGETS

the laser field of the main pulse, the field of the propagating laser pulse volumetrically heats the electron population in the expanded particle layers, resulting in an increase in the ion acoustic velocities and thus an additional increase in particle expansion and shock velocities. When the fast SWA-aluminium ion population streams through the expanded carbon ion layer further streaming instability grow due to the existence of multiple populations with differing relative velocities. Importantly, one such instability occurs when the accelerated aluminium ions reach the expanded proton layer.

The results also highlight the importance of diagnosing and controlling the intensity contrast, not only in the tens of picosecond to nanosecond temporal range explored previously (162, 179), but also on the picosecond rising edge of the laser pulse. This task is non-trivial and requires significant investment. However, given the demonstrated importance of the pulse picosecond rising edge profile and the fact that ultrathin foil targets are used in a number of new laser-acceleration schemes, in particular RPA and BOA, this step is important for the development of future applications of laser-ion sources.

5.2 Ion acceleration with double laser pulses of mixed polarisation

In the previous section it was shown that a linearly polarised laser pre-pulse could create a near-critical plasma in which the coupling of the linearly polarised main pulse energy to the electrons would be enhanced. This idea was extended to study the differences with a circularly polarised main pulse. In this case the second pulse would drive a shock in the near-critical density plasma instead of a RIT-enabled volumetric heating and subsequent jet formation. The efficiency of the hole-boring process increases as the density of the plasma is reduced to just above the critical density (180). Previous works have exploited the pre-pulse that often accompanies a high power laser pulse to somehow prepare the plasma and optimise its conditions for the acceleration of ions, but in these schemes laser pulses of the same polarisation were used (166, 167).

In the work presented in the following, simulations with the particle-in-cell code OSIRIS were firstly carried out for linearly polarised double pulses in the picosecond regime. These simulations were compared to the experimental and numerical results from EPOCH presented in the first part of the chapter in order to validate them.

The polarisation of the main pulse was then changed to circular to test the idea proposed above in a set of conditions similar to the ones used in the previously reported experiments. Simulations with femtosecond pulses were then carried out to investigate the feasibility of this new scheme with Ti:Sapphire lasers. In order to find the optimum conditions, simulations with different pulse durations, pulse delays and target thickness were performed.

5.2.1 Simulations

One-dimensional simulations were performed with the fully-relativistic particle-in-cell (PIC) code OSIRIS. The Vulcan laser parameter set was used for the picosecond regime calculations. Therefore the wavelength was set at 1054 nm. The laser pulses had a \sin^2 pulse envelope with a duration of 800 fs FWHM each and were delayed by 1 ps. Both pulses were focused to a diameter of 7.3 μm . The pre-pulse and main pulse carried intensities of $0.2 \times 10^{20} \text{ Wcm}^{-2}$ and $1.8 \times 10^{20} \text{ Wcm}^{-2}$, respectively.

For the femtosecond regime, a Ti:Sapphire laser (800 nm wavelength) with pulse durations between 40 fs and 100 fs FWHM was used. The pulse delay was varied

5. DOUBLE PULSE INTERACTION WITH THIN SOLID TARGETS

between 250 fs and 750 fs. Both pulses were again focused to a diameter of $7.3 \mu\text{m}$. The pre-pulse and main pulse carried intensities an order of magnitude higher, but kept the same 10:1 intensity ratio, i.e. $0.2 \times 10^{21} \text{ Wcm}^{-2}$ and $1.8 \times 10^{21} \text{ Wcm}^{-2}$, respectively.

The layered target consists of aluminium, carbon and hydrogen. Field ionisation simulations showed that the dominant charge state of aluminium is Al^{11+} . Carbon and hydrogen are assumed to be fully ionised. The plasma is modelled as a plane slab of plasma with a step density profile of $n_{\text{al}} = 660n_{\text{cr}}$, $n_{\text{c}} = 120n_{\text{cr}}$ and $n_{\text{p}} = 60n_{\text{cr}}$. The initial electron temperature is set to 1 keV, while ions are assumed to be cold. All simulations are performed with a realistic mass to charge ratios $m_{\text{Al}}/q_{\text{Al}} = 4471$, $m_{\text{C}}/q_{\text{C}} = 3645$ and $m_{\text{p}}/q_{\text{p}} = 1836$. The laser pulses always impinged normally onto the plasma slab.

The simulations were carried on a grid line with 450099 cells. The box is $361 \mu\text{m}$ long. Each cell contains initially 5000 particles and they are pushed with a time step of 0.00263887 fs. The energies in the figures have been extracted according to $E_i = (\gamma - 1)m_i c^2$, where γ is the relativistic factor of the ions.

5.2.2 Acceleration in the picosecond regime

Linear-linear double pulse Figure 5.9 shows the phase space (a-d) and longitudinal electric field (e-h) at four times corresponding to the peak of the first pulse (0.8 ps after the start of the simulation), the peak of the main pulse (1.8 ps), the trailing edge of the main pulse (2.5 ps) and a later stage of the interaction (5 ps). The first pulse drives initially an expansion of the plasma (a), with the second pulse intensifying this effect and further lowering the density of the plasma. The plasma goes transparent at an early stage and allows the rest of the pulse to propagate through. The longitudinal electric field shows that a large component of the laser field propagates through the relativistically transparent plasma (f-g), effectively coupling to the heavy-ion species. Here one can clearly see the initial expansion, a shock-driven ion component, and the energy transfer. The layered structure of the ion beam is maintained throughout the expansion and acceleration [(a) and (d)]. After the pulses have passed, the protons at the rear side of the target are driven to high energies (h). Similar spectra have previously been observed in the Breakout Afterburner (BOA) regime (98). The ion spectra draws many analogies to the BOA case. This is manifested in the multicomponent shape of the spectra (figure 5.9), where the leading species (protons) reach energies

5.2 Ion acceleration with double laser pulses of mixed polarisation

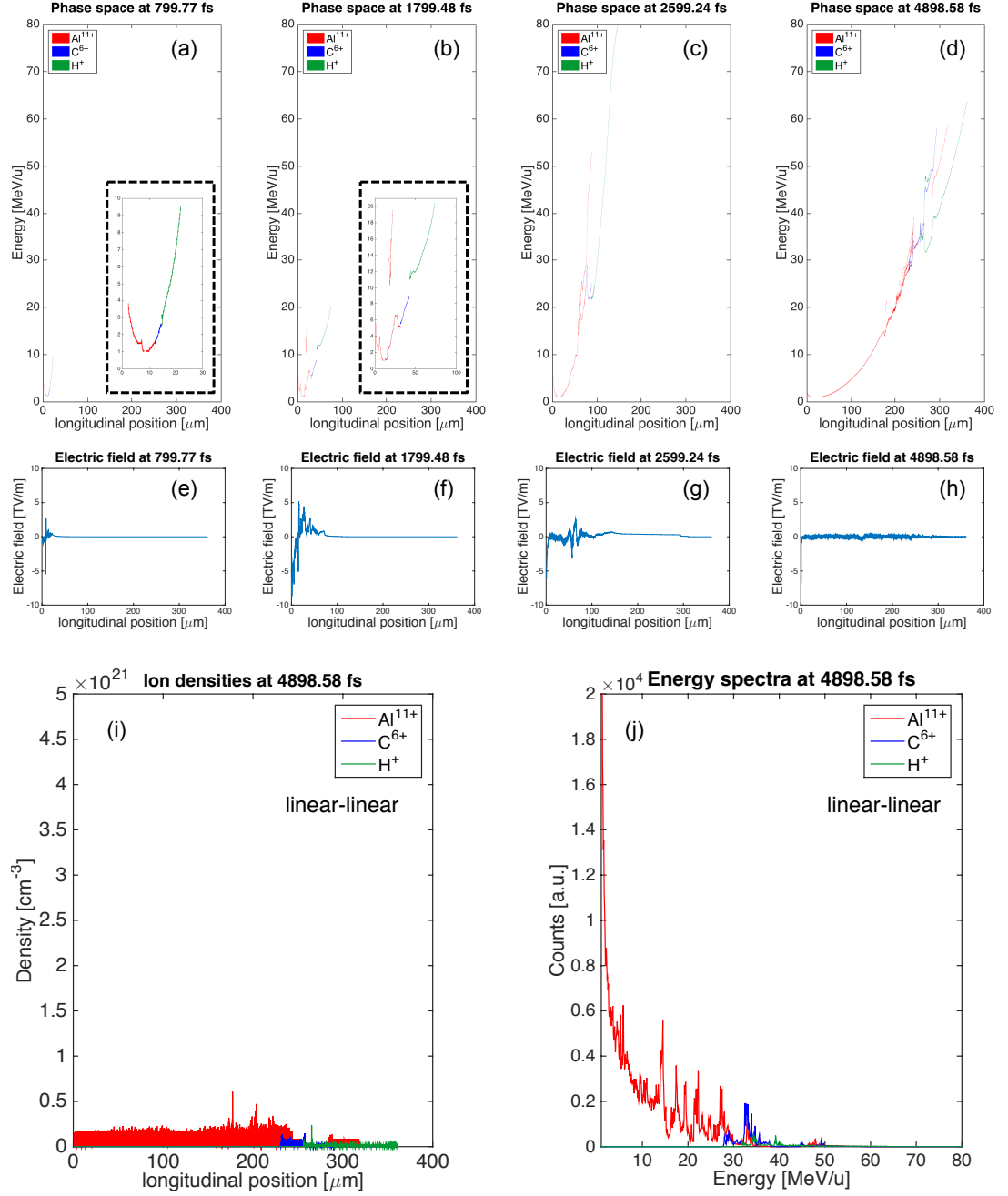


Figure 5.9: Overview linear-linear simulation - picosecond regime - Overview of the linear-linear double pulse run with picosecond-range pulses. The phase spaces at four time steps [(a)-(d), inlets in (a) and (b) show dynamics in more detail] are shown with their corresponding longitudinal electric field values [(e)-(h)]. The charge densities and energy spectra at the last time step are displayed in (i) and (j), respectively. See text for details.

5. DOUBLE PULSE INTERACTION WITH THIN SOLID TARGETS

of 49 MeV, followed by the carbons with 49 MeV/u, and finally the Al ions with 48 MeV/u (h).

Linear-circular double pulse After the conditions of the simulations were validated by reproducing the two-stream instability process with linearly polarised double pulses, the polarisation of the main pulse was made circular while maintaining the rest of the parameters the same. With this mixed polarisation a remarkable enhancement is observed in the acceleration of the heavy ions. The spectrum in figure 5.10(j) shows a prominent feature around 25 MeV/u with an energy spread of around 20%. This feature was absent in the case of the linear-linear double pulse (see figure 5.9(j)).

In the phase space plots in figure 5.10(a)-(d) it can be seen that after the expansion driven by the first linearly polarised pulse (a), the different ion species maintain their layering. While the plasma density is still fairly overdense, the circularly polarised main pulse launches a strong shock wave that further accelerates the slower ions (b). As the plasma continues to expand, it becomes underdense, letting part of the laser pulse to be transmitted through. The formation of the shock wave is also manifest in the plots of the longitudinal electric fields in figure 5.10(f)-(g). At its strongest (1800 fs after the rising edge of the first pulse impinges on the target (f)), the longitudinal electric field peaks at around 10 TV/m. At the trailing edge of the pulse, the shock wave accelerated Al¹¹⁺ ions punch through the leading ion layers, eventually overtaking the protons. This suggests this mechanism could be particularly efficient for heavy ion acceleration. This stands in stark contrast to the linear-linear case as evident when comparing the energy spectra in figure 5.13, where no preferential acceleration of the heavier ions can be observed.

The density plot in figure 5.10(i) at almost 5 ps after the impinging of the first pulse, shows that the accelerated bunch of Al¹¹⁺ stays slightly overdense ($\sim 2.5 n_{cr}$), whereas in the linear-linear case, the plasma at the same stage of the interaction was completely transparent (see figure 5.9(i)).

5.2 Ion acceleration with double laser pulses of mixed polarisation

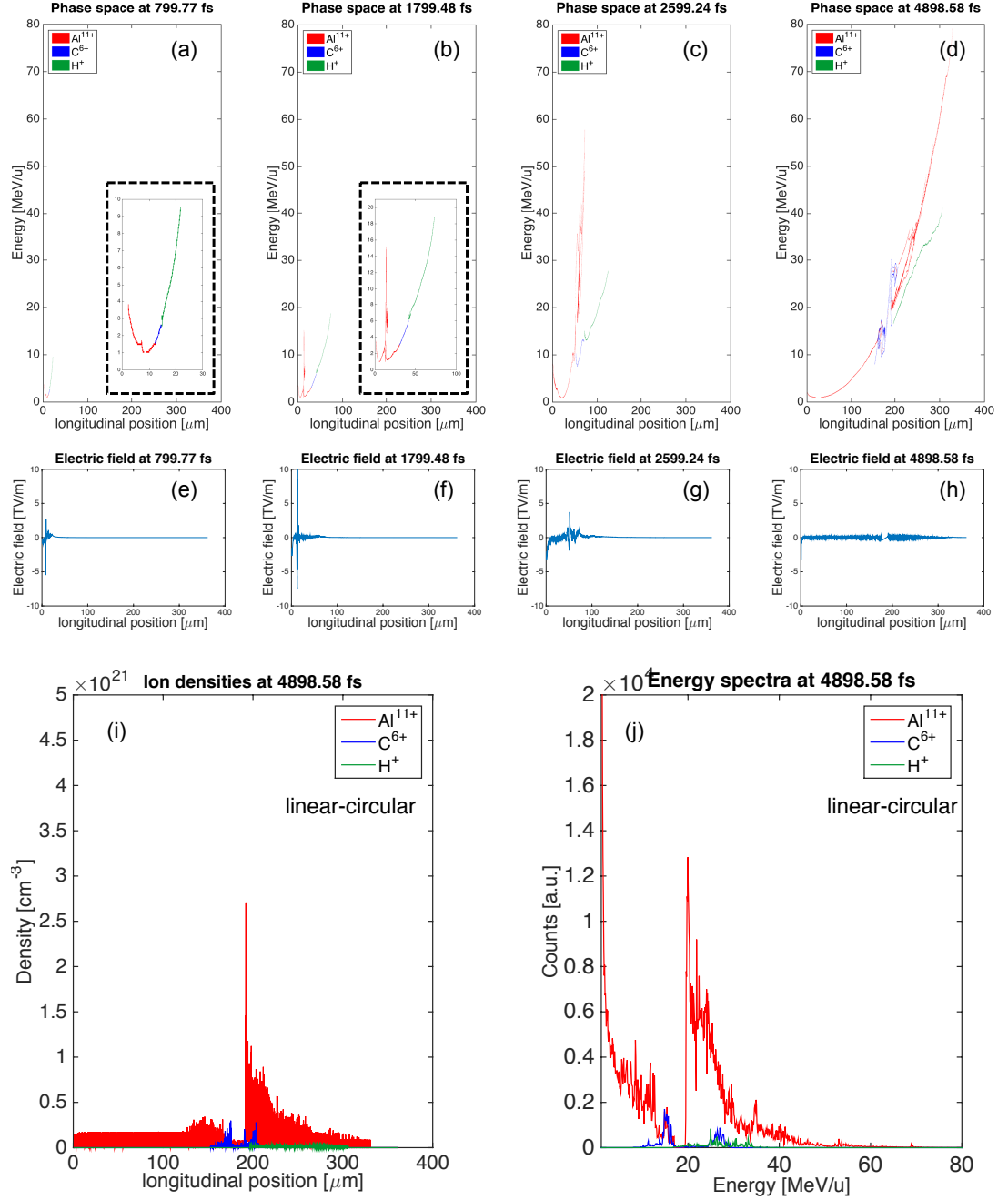


Figure 5.10: Overview linear-circular simulation - picosecond regime - Overview of the linear-circular double pulse run with picosecond-range pulses. The phase spaces at four time steps [(a)-(d), inlets in (a) and (b) show dynamics in more detail] are shown with their corresponding longitudinal electric field values [(e)-(h)]. The charge densities and energy spectra at the last time step are displayed in (i) and (j), respectively. See text for details.

5. DOUBLE PULSE INTERACTION WITH THIN SOLID TARGETS

Intensity scaling In order to further investigate this mechanism, a set of simulations was performed with different intensities of the main pulse and a constant pre-pulse of intensity $0.13 \times 10^{20} \text{ Wcm}^{-2}$ under otherwise identical conditions. Figure 5.11 shows that, when increasing the main pulse intensity from $1.15 \times 10^{20} \text{ Wcm}^{-2}$ to $2.30 \times 10^{20} \text{ Wcm}^{-2}$ and $3.45 \times 10^{20} \text{ Wcm}^{-2}$, the energy of the Al^{11+} bunch increased from 25 MeV/u to 80 MeV/u and 150 MeV/u, respectively. That means, the maximum ion energy scales approximately linearly with the laser intensity as predicted for the hole-boring mechanism of ion acceleration for low values of the dimensionless pistoning parameter ($\Xi \ll 1$) The pistoning parameter is defined as $\Xi = I_0/m_i n_i c^3$, where $n_i = n_e/Z_i$ is the ion density (95, 181). The energy spread of the Al^{11+} bunch can be as narrow as $\sim 10\%$.

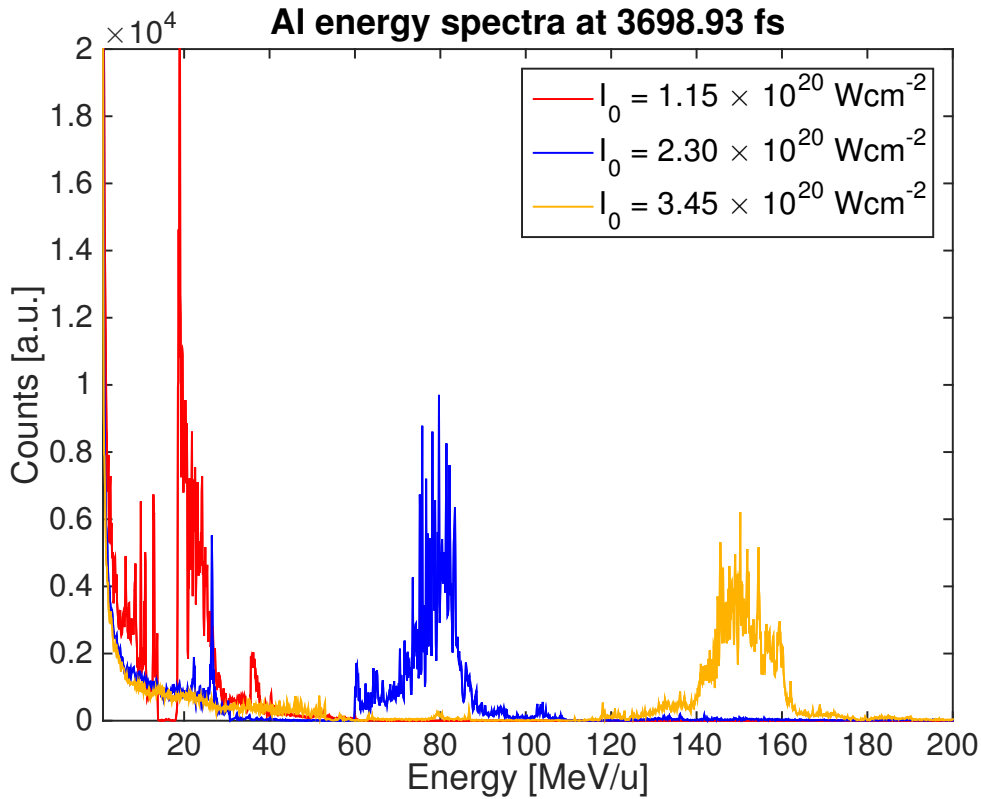


Figure 5.11: Al energy spectra - intensity scan - Al energy spectra for a linear-circular double pulse set-up. The intensity of the first pulse is kept constant at $0.13 \times 10^{20} \text{ Wcm}^{-2}$. The intensities of the second pulse are $1.15 \times 10^{20} \text{ Wcm}^{-2}$, $2.30 \times 10^{20} \text{ Wcm}^{-2}$ and $3.45 \times 10^{20} \text{ Wcm}^{-2}$.

5.2 Ion acceleration with double laser pulses of mixed polarisation

Circular-circular double pulse For comparison with the other set-ups, a simulation with a circular-circular double pulse set-up was performed (see figure 5.12). In this case, the first pulse drives almost no expansion and only a minimal increase in energies is observed (see figure 5.12(a)). When the second pulse rises a strong shock wave is driven into the target (b), producing a distinct population of ions. Since no plasma expansion is enabled by electron heating during the interaction of the first laser pulse, the plasma stays overdense throughout the interaction. The second pulse gets almost fully reflected and the different layers are strongly compressed (i). Overall the ion energies are much lower than in the linear-circular case, making this set-up less favourable for the production of high-energy ion beams. However it has to be noted, that the ion spectra shows a distinct population of heavy ions at lower energies (around ~ 10 MeV/u in (j)), which could be useful for the generation of low-energy beams.

5. DOUBLE PULSE INTERACTION WITH THIN SOLID TARGETS

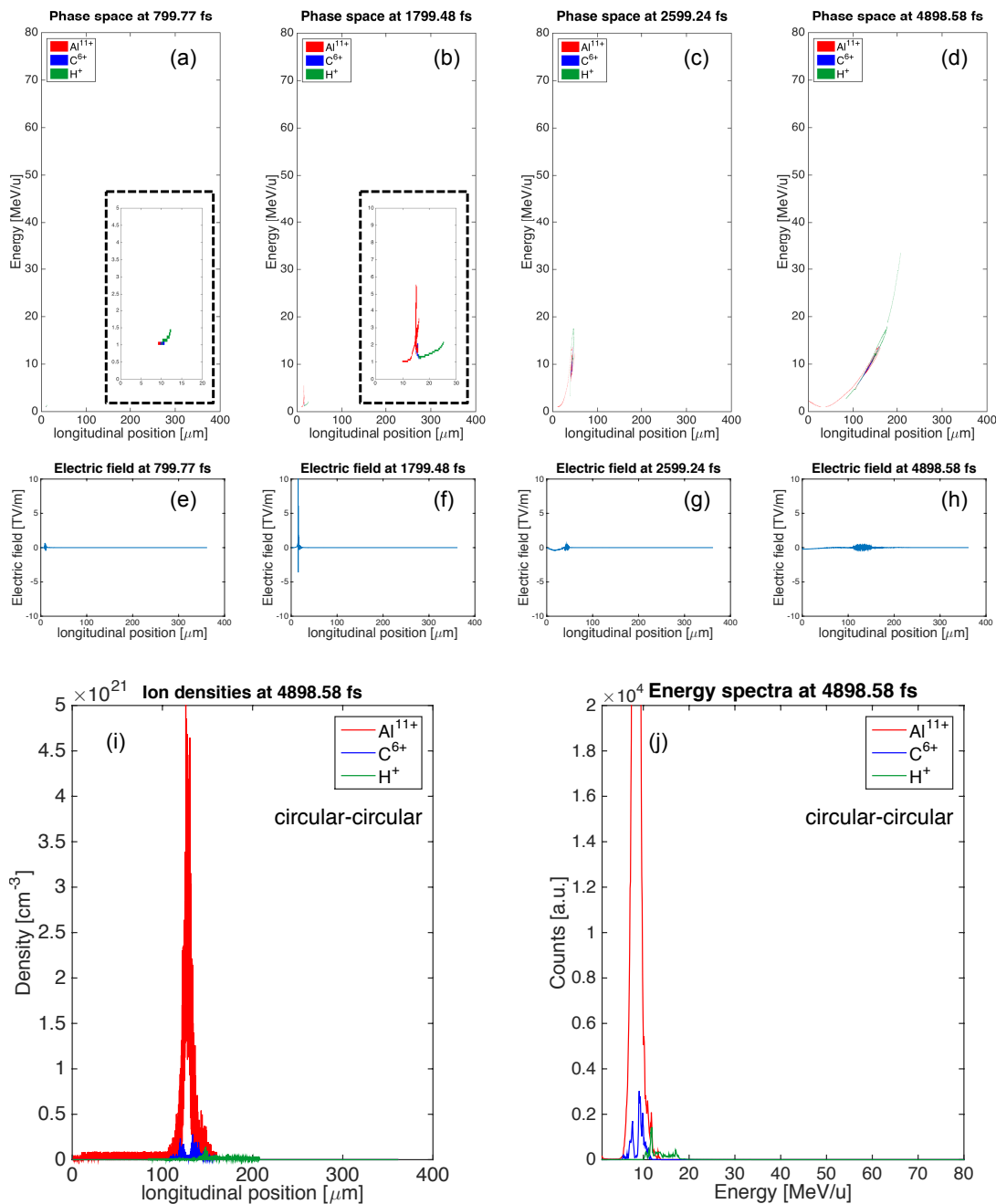


Figure 5.12: Overview circular-circular simulation - picosecond regime - Overview of the circular-circular double pulse run with picosecond-range pulses. The phase spaces at four time steps [(a)-(d), insets in (a) and (b) show dynamics in more detail] are shown with their corresponding longitudinal electric field values [(e)-(h)]. The charge densities and energy spectra at the last time step are displayed in (i) and (j), respectively. See text for details.

5.2 Ion acceleration with double laser pulses of mixed polarisation

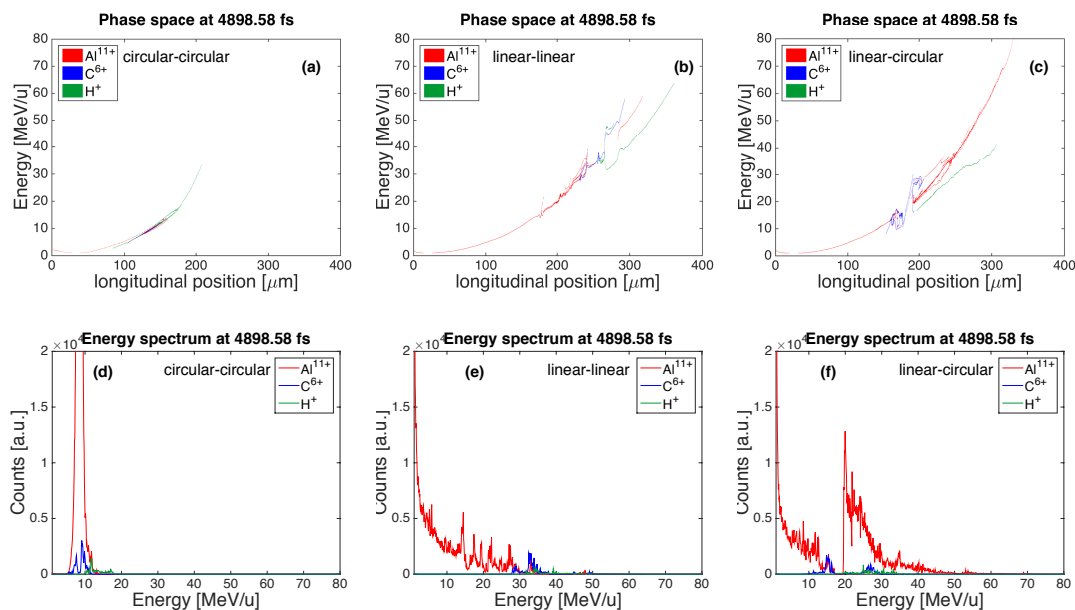


Figure 5.13: Double pulse comparison - picosecond regime - Comparison of phase space and energy spectrum of circular-circular [(a),(d)], linear-linear [(b),(e)] and linear-circular [(c),(f)] simulation runs. Except the different polarisations, the simulations were performed under identical conditions.

5.2.3 Acceleration in the femtosecond regime

The results of the simulations with double pulses of mixed polarisation in the picosecond regime reveal a promising route to efficient heavy ion acceleration, which gives rise to high energies with moderately intense laser pulses. It does not have the stringent pulse contrast requirements as demanded by other acceleration mechanisms, but relies on the introduction of a controlled pre-pulse. However the implementation of this scheme in practice is currently not achievable. In the previously reported experiments the double pulse was generated at the front end of the laser system before the pre-amplification. The only practical way nowadays to combine two laser pulses with different polarisations and such short delay is by using two separate amplification lines. Currently that possibility is offered only by a few Ti:Sapphire laser systems working in the femtosecond regime, like Astra-Gemini at the Rutherford Appleton Laboratory and, in the future, the VEGA system at CLPU.

Without the guidance of the double pulse experiment reported in section 5.1 different parameters (pulse duration, pulse delay, and target thickness) had to be scanned.

5. DOUBLE PULSE INTERACTION WITH THIN SOLID TARGETS

The objective was to identify the conditions that reproduced the phenomena observed in the picosecond-long mixed polarisation double pulses, that is, plasma expansion to near-critical densities followed by shock acceleration, using femtosecond pulses instead.

In order to compensate for the shorter pulse duration the intensity of the pulses was an order of magnitude higher than in the picosecond case.

The first pulse drives a layered plasma expansion similar to the long pulse case (see figure 5.14(a)) for 100 fs FWHM pulses, impinging on a 40 nm thin target. Calculations performed with shorter pulses (not shown here) do not give the plasma enough time to expand, and give rise to lower quality ion beams.

The target thickness is also critical and its optimum value is related to the pulse duration. If the target is too thick, the short duration of the first pulse is not sufficient to effectively heat the bulk of the target and prepare it for the arrival of the second. Figure 5.15 shows the interaction with a 100 nm target. Although the first pulse drives some plasma expansion (a), it can be seen in the phase space plot at 641.32 fs that the induced shock is much weaker compared to the 40 nm case (see figure 5.14(a)), resulting in much lower energies of the heavier ions as visible in the late-stage phase space plots (d) and energy spectrum (j).

On the other hand, a target too thin disintegrates quickly, diminishing the effectiveness of the second pulse shock and impeding the acceleration of heavy ions. In case of a 20 nm thin target (see figure 5.16(b)-(d)) the phase space plots indicate that the plasma disintegrates quickly and no shock accelerating structure can be established.

The optimum target thickness for 100 fs FWHM mixed polarisation double pulses with the intensities mentioned above was found to be around 40 nm (see figure 5.14), providing the most suitable conditions for an efficient heavy ion acceleration.

In order to reproduce the mechanism observed in the long pulse case, the circularly polarised main pulse has to arrive at a time when the plasma density has relaxed enough for the shock wave to be formed efficiently while being still slightly overdense. The optimum delay was found at around 500 fs. For shorter delays, e.g. 250 fs, the plasma does not have enough time to expand (streaming effects after the first pulse has passed further lower the density) in order to create the necessary conditions for the shock-induction by the second pulse. A longer pulse delay, e.g. 750 fs, was found to provide similar conditions like the 500 fs in the case of 40 nm targets. It is expected

5.2 Ion acceleration with double laser pulses of mixed polarisation

that there is an upper limit for the pulse delay given by the continuously decreasing charge density due to free-streaming effects of the plasma.

Figure 5.17 shows the charge density evolution of the plasma during the interaction with the mixed polarisation double pulse in the picosecond regime (under the conditions specified in 5.10) and in the femtosecond regime under the best conditions found (100 fs pulse duration, 500 fs pulse delay, 40 nm thin target). The energy ratio between the main pulse and the pre-pulse is 10:1 for both picosecond and femtosecond regime.

It can be seen, from the similarity of both plots, that the best conditions found in the femtosecond regime manage to reproduce the same density evolution as the picosecond regime albeit in a shorter time scale, i.e expansion of the plasma from solid to near-critical, followed by the formation of a shock wave peaking at a density of $\sim 130n_{cr}$.

Similarly to the picosecond regime case, the shock wave created by the 100 fs long circularly polarised main pulse drives the aluminium ions to higher energy. This can be seen in the phase space plots from 641.32 fs onwards (after the arrival of the second pulse) in figure 5.14(b)-(c). The aluminium ions appear to be free streaming after the pulses have passed. As compared with shorter pulses, the 100 fs FWHM circularly polarised pulse drives a stronger shock wave in the plasma, and some peaks can be observed in the density profile. In the later stages of the interaction, the charge density relaxes again, as seen in 5.17. Further energy transfer to the heavier ions could be facilitated by two-streaming instabilities.

The energy spectrum in figure 5.14(j) features a prominent population of Al^{11+} ions around 70 MeV/u with an energy spread as narrow as 15%. The most-energetic ions reach energies up to 120 MeV/u, however the number of particles reaching this energy is almost negligible. The carbon ions originating from the contaminant layer are accelerated to up to 40 MeV/u. The spectrum is very similar to the picosecond case shown in figure 5.10(j). Both spectra feature the characteristic leading population of aluminium ions followed by the carbon ions. This feature is entirely lost in case of the 20 nm target (figure 5.16(j)) due to the not suitable preparation of the plasma by the first pulse. The spectrum in case of a 100 nm target (figure 5.15(j)) shows a monoenergetic peak albeit at much lower energy (around 10 MeV/u).

Conclusively, the proposed mechanism appears to be very effective for the acceleration of heavy ions, i.e. Al^{11+} in this particular case. While heavy ions can in principle

5. DOUBLE PULSE INTERACTION WITH THIN SOLID TARGETS

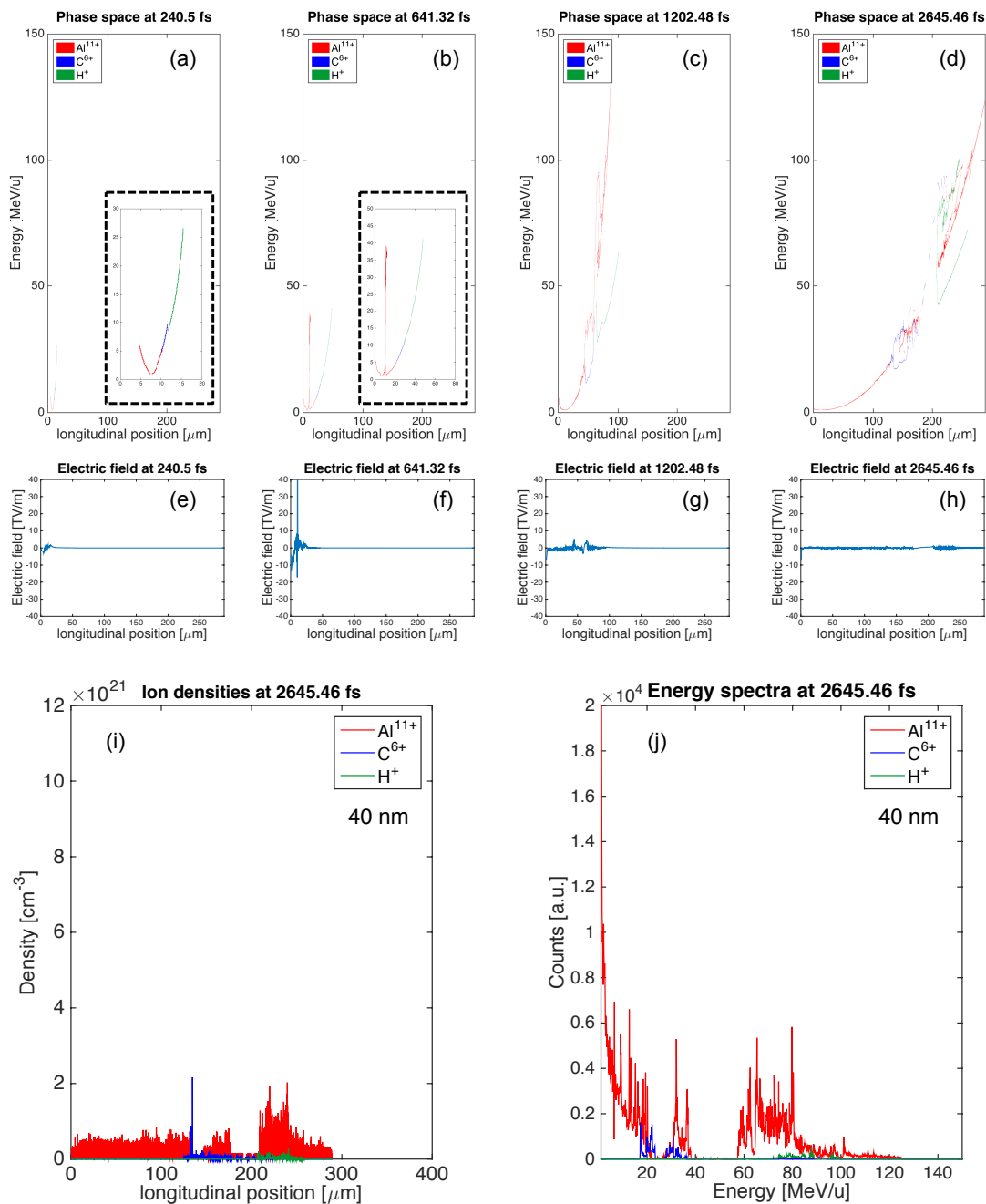


Figure 5.14: Overview linear-circular simulation with 40 nm target - femtosecond regime - Overview of the linear-circular double pulse run with femtosecond-range pulses and a 40 nm thick target. The phase spaces at four time steps (a-d) are shown with their corresponding longitudinal electric field values (e-h). The charge densities (i) and energy spectra (j) at the last time step are displayed on the bottom. See text for details.

5.2 Ion acceleration with double laser pulses of mixed polarisation

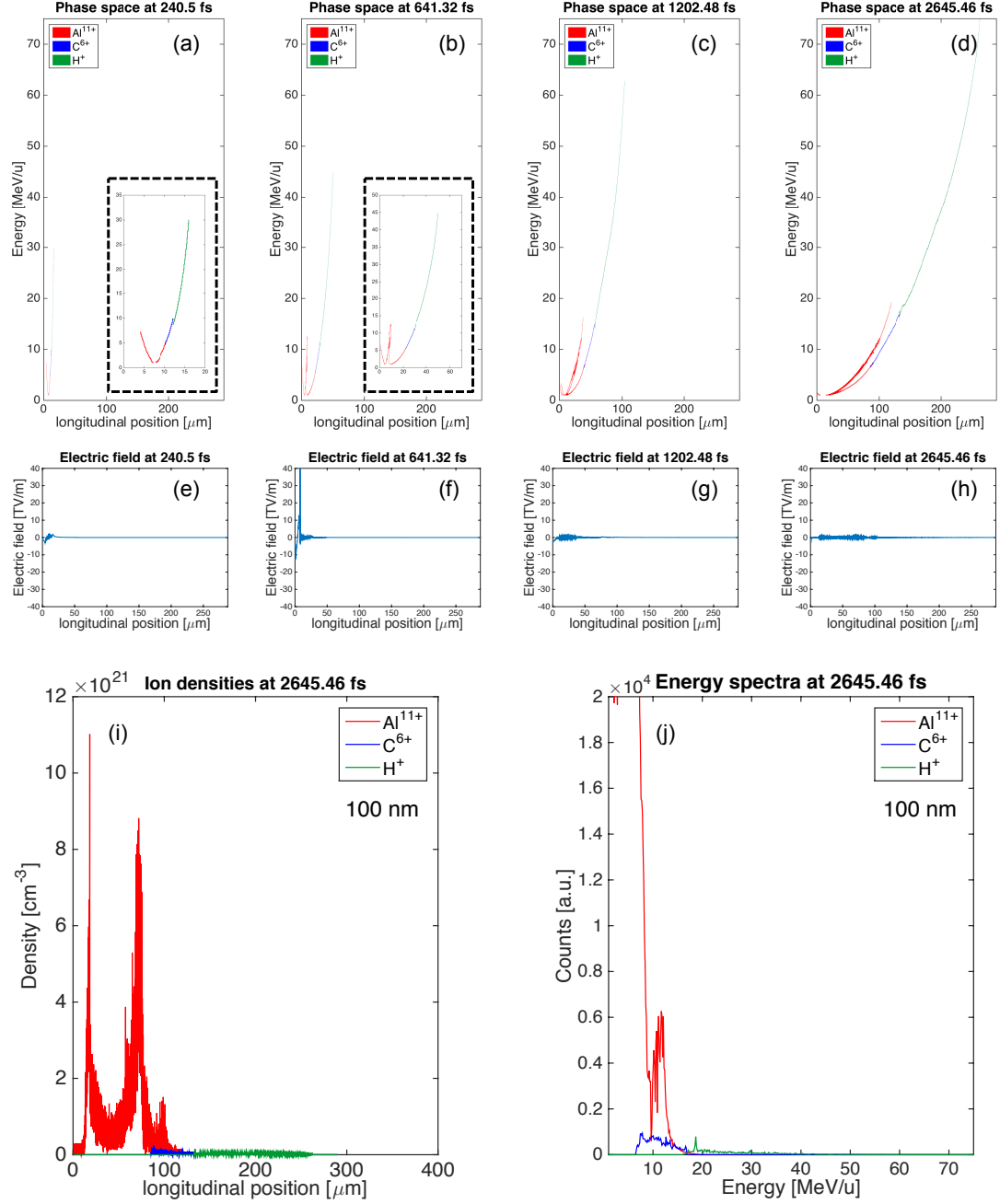


Figure 5.15: Overview linear-circular simulation with 100 nm target - femtosecond regime - Overview of the linear-circular double pulse run with femtosecond-range pulses and a 100 nm thick target. The phase spaces at four time steps (a-d) are shown with their corresponding longitudinal electric field values (e-h). The charge densities (i) and energy spectra (j) at the last time step are displayed on the bottom. See text for details.

5. DOUBLE PULSE INTERACTION WITH THIN SOLID TARGETS

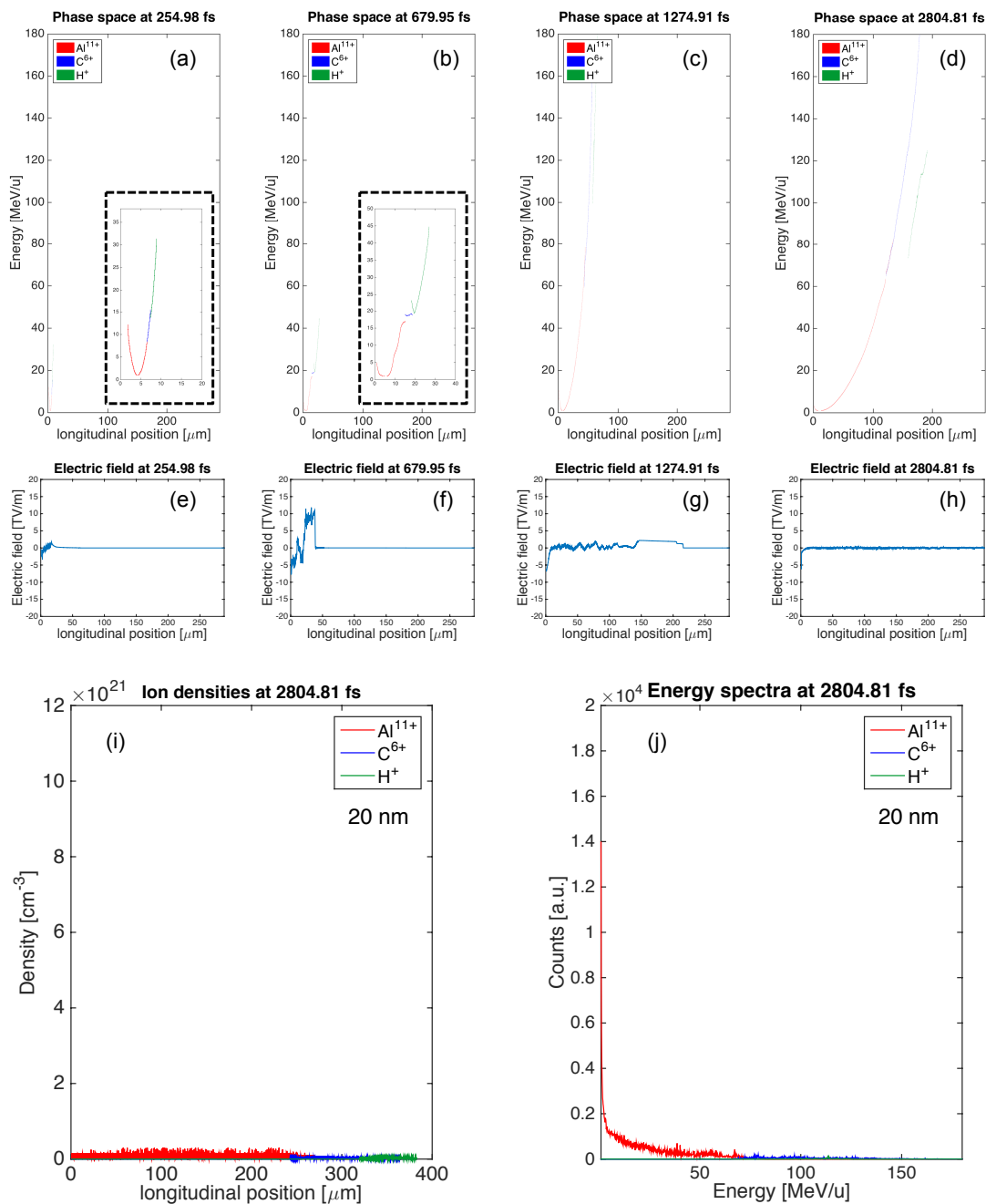


Figure 5.16: Overview linear-circular simulation with 20 nm target - femtosecond regime - Overview of the linear-circular double pulse run with femtosecond-range pulses and a 20 nm thick target. The phase spaces at four time steps (a-d) are shown with their corresponding longitudinal electric field values (e-h). The charge densities (i) and energy spectra (j) at the last time step are displayed on the bottom. See text for details.

5.2 Ion acceleration with double laser pulses of mixed polarisation

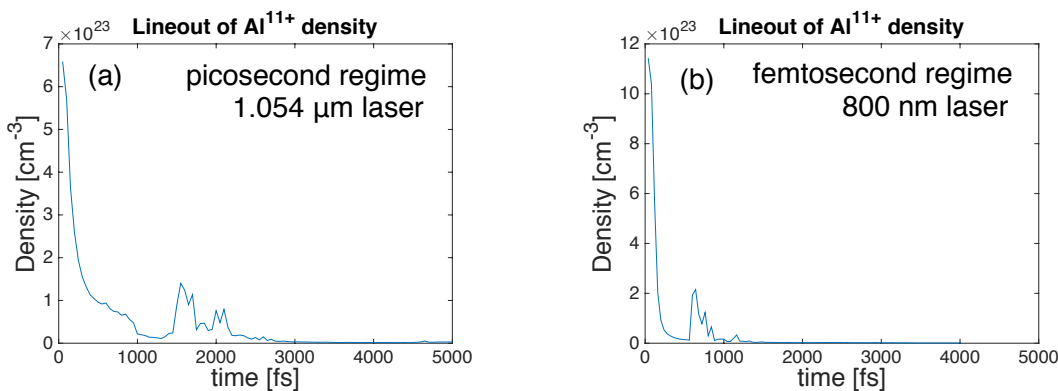


Figure 5.17: Charge density evolution in femtosecond and picosecond regime - Charge density evolution of the Al-ions with time from the interaction with double pulses of mixed polarisation in the (a) picosecond and (b) femtosecond regime.

be also accelerated in the TNSA regime, this usually requires careful target preparation by resistive or laser heating ((12) and references here-within) and the achieved energies are fairly low (~ 10 MeV). Alternative schemes, i.e. RPA, as discussed in section 4.1, show up an alternative route to stronger acceleration, however the laser intensity requirements are very high ($> 10^{22}$ Wcm⁻²). Therefore, the proposed scheme with a double pulse of mixed polarisation, is highly attractive for heavy ion acceleration with moderate intensities (10^{20} - 10^{21} Wcm⁻²). It has to be noted that these simulations were carried out in one dimension. For further studies, higher-dimensional (and computationally much more demanding) simulations should be performed, which could alter the dynamics. Multidimensional effects that could arise were discussed in section 3.2.4.

5.2.4 Summary

A new mechanism for the efficient acceleration of heavy ions has been proposed. By using a double pulse set-up, high-energetic particles (up to ~ 150 MeV/u) with moderate intensities ($\sim 10^{20}$ Wcm⁻² in picosecond regime, $\sim 10^{21}$ Wcm⁻² in femtosecond regime) can be generated. The ion spectra is very narrow (energy spread as narrow as 10%) and an efficient acceleration of heavier ions (Al¹¹⁺ and C⁶⁺) is observed as evidenced by the overtaking of the ions compared to the protons. This idea was motivated by experimental work towards ion acceleration with a double pulse with a fixed delay. While experimentally a linear-linear double pulse set-up was used, one-dimensional PIC simulations were performed with mixed polarisations (linear - circular). While a

5. DOUBLE PULSE INTERACTION WITH THIN SOLID TARGETS

linearly polarised pre-pulse is an ideal driver for plasma expansion, a second circularly polarised main pulse can drive a strong shock into the plasma thereby accelerating heavy ions to high energies. This novel scheme has been firstly demonstrated with one-dimensional simulations using picosecond long pulses, and a parameter study has shown that this mechanism is also accessible with femtosecond pulses.

6

Ion acceleration with the VEGA laser

6.1 Introduction

One of the motivations of the research reported in this thesis was to study the feasibility of carrying out laser-driven ion acceleration with the newly commissioned laser system VEGA at the Centro de Laseres Pulsados (CLPU). The investigations reported in the previous chapters provided insight into the sort of opportunities that such a system affords and the challenges it has to face. Among the first, one can mention the radiation pressure acceleration mechanism that can in principle produce beams of high-energy (>100 MeV/u) ions with low energy dispersion ($< 10\%$) (see section 4.1). The challenges include the coexistence of several acceleration mechanisms (TNSA, RPA, BOA) within the same interaction (see section 5.1), and the development of instabilities in the plasma (see section 4.2).

In the present chapter the capabilities of the VEGA laser system, that is currently being installed at the CLPU, to accelerate ions, are analysed. The VEGA laser system has some unique characteristics that could be exploited to make a major contribution to the development of laser-driven ion acceleration techniques. These characteristics are:

- High laser energy (up to 30 J)
- Ultra-short pulse duration (down to 30 fs)

6. ION ACCELERATION WITH THE VEGA LASER

- Ultra-high peak power (up to 1 PW)
- High beam quality (Strehl ratio > 0.9 with deformable mirror at the output)
- High focusing intensity ($> 10^{21} \text{Wcm}^{-2}$ [$a_0 > 22$])
- Ultra-high pulse contrast (ASE $< 10^{-12}$ at 100 ps; pre-pulse $< 10^{-9}$ at 11 ns)
- High repetition rate up to 10 Hz at 20 TW and 200 TW; up to 1 Hz at 1 PW)
- Three (fully synchronised) independent laser outputs of increasing power

As it has been discussed in previous chapters, the laser-based ion beam generation is a complex process and the different acceleration mechanisms depend very sensitively on the laser, target parameters and condition of the interaction. Also no clear line can be drawn between the on-set of the different acceleration mechanisms and it is difficult to unambiguously distinguish the signatures of each scheme. In principle, a variety of acceleration regimes can be accessed with the VEGA laser, but the ultra-high contrast and short pulse length makes the system especially apt for ion acceleration in the RPA Light-Sailing and Hole-Boring (collisionless shock acceleration) regime. For TNSA, longer and more energetic pulses are preferred.

The deformable mirror of VEGA 3 would be useful to produce near-diffraction limited focal spots (down to $r_0 \sim 1 \mu\text{m}$) and ultra-high intensities, as well as optimising the beam profile at the focus. The high repetition rate of the laser (up to 10 Hz at 20 TW and 200 TW; up to 1 Hz at 1 PW) suggests an implementation for applications which require a high-average proton and ion current. While solid targets are not ideal for the use with high-repetition rate, further targetry developments could pave the way for a successful implementation in the future. Moreover, an important aspect of a repetitive proton source is its stability. Regarding this, a laser pulse with the high contrast ratio achieved by a double CPA laser system with a saturable absorber, like VEGA, provides not only a higher maximum energy, but also a more stable operation of the proton source as compared with the set-ups that employ plasma mirrors.

The three fully synchronised independent laser outputs of VEGA make it possible to implement schemes of cascaded acceleration and double pulse set-ups. The novel scheme of collisionless shock acceleration with double pulses of mixed polarisation (i.e. linear pulse followed by circular) as introduced in section 5.2, could be experimentally implemented in VEGA, taking advantage of its independent synchronisable outputs.

6.2 Estimations of ion acceleration in VEGA

Parameter	Symbol	Unit	VEGA 1	VEGA 2	VEGA 3
Laser Energy	W_L	J	0.5	4	30
Laser Pulse Duration	τ	fs	30	30	30
Laser Power	P_0	PW	0.02	0.13	0.94
Focal Spot Radius	r_0	μm	5	5	5
Confocal Parameter	b	μm	196	196	196
Laser Intensity (Gaussian Profile)	I_0	W/cm ²	1.4E+19	1.1E+20	8.3E+20
Laser Intensity (Flat Top)	I_0	W/cm ²	2.0E+19	1.6E+20	1.2E+21

Table 6.1: VEGA laser parameters - Overview of achievable laser parameters with the VEGA laser system. Values are given for all three independent outputs VEGA 1, VEGA 2 and VEGA 3.

In the following the parameters achievable by each of the phases of VEGA will be considered separately. The corresponding powers and intensities are shown in table 6.1. These assume Gaussian pulses of 30 fs FWHM, focused down to a focal spot of radius 5 μm FWHM either with a Gaussian or a flat top spatial profile. It has to be mentioned that this is a conservative estimation. With the appropriate focusing system, corrective optics and alignment the focal spot could be reduced even further.

The potential performance of VEGA in laser-driven ion acceleration can be estimated in terms of maximum ion energy, conversion efficiency and shape of the energy spectrum. These were determined using scaling laws found in the literature and obtained through experimental measurements, PIC simulations, and analytical models based in different mechanisms.

6.2 Estimations of ion acceleration in VEGA

6.2.1 Target Normal Sheath Acceleration

According to the 1D TNSA model by Mora *et al.* (86), the ion energy at the expansion front at time t can be estimated as

$$\epsilon_i = 2Z_i T_e \left(\ln \left[\frac{\omega_{pi} t}{\sqrt{2} e_N} + \sqrt{\left(\frac{\omega_{pi} t}{\sqrt{2} e_N} \right)^2 + 1} \right] \right)^2 \quad (6.1)$$

Here T_e is the electron temperature ¹, $\omega_{pi} = (4\pi Z_i n_{e0} e^2 / m_i)^{0.5}$ is the ion plasma

¹Unless otherwise stated electron temperature is given as energy with the Boltzmann constant, k_b

6. ION ACCELERATION WITH THE VEGA LASER

frequency, n_{e0} is the electron density in the unperturbed plasma and $e_N = 2.71828$ is Euler's number.

In order to estimate the maximum ion energy, a few approximations may be made. The Mora model of TNSA assumes an isothermal plasma expansion and the hot electron temperature is assumed to be equal to the ponderomotive potential (182, 183, 184, 185, 186)

$$T_{e1} = \psi_{pond} = m_e c^2 \left[\sqrt{1 + a_0^2} - 1 \right] \quad (6.2)$$

However, for a shorter scale pre-plasma, which corresponds to higher contrast shorter duration laser pulses like those of VEGA, the hot electron temperature at intensities $> 10^{19} \text{ Wcm}^{-2}$ is significantly lower than the ponderomotive temperature, and can be estimated as (88)

$$T_{e2} \approx 0.47 m_e c^2 a_0^{2/3} \approx 0.22 \text{ MeV} (I_{18} \lambda_{\mu m})^{1/3} \quad (6.3)$$

Equation 6.1 predicts infinite ion energies for $t \rightarrow \infty$, therefore a limit to the acceleration time has to be introduced. A usual estimation is that the acceleration time is limited by the pulse duration τ_0 as (187)

$$t_{acc} \approx 1.3 \tau_0 \quad (6.4)$$

In order to get the cut-off energy from equation 6.1, the electron temperature T_e , a limit to the acceleration time t_{acc} , and the ion plasma frequency ω_{pi} are needed. The total number of electrons n_{e0} in the sheath volume is estimated by

$$n_{e0} = \frac{N_e}{c \tau_0 \pi r_s^2} \quad (6.5)$$

The total number of electrons N_e in the sheath is taken as the laser energy divided by the electron temperature and multiplied by a conversion efficiency η from laser energy into hot electrons that is estimated empirically as

$$N_e = \frac{\eta W_L}{T_e} \quad (6.6)$$

The conversion efficiency, η is given by

$$\eta = 1.2 \times 10^{15} \left(\frac{I_0}{\text{Wcm}^{-2}} \right)^{0.74} \quad (6.7)$$

as conversion factor.

6.2 Estimations of ion acceleration in VEGA

with maximum value $\eta = 0.5$ at $I_0 > I_{0*} \approx 5.7 \times 10^9 \text{ Wcm}^{-2}$ (188, 189)

The sheath volume is approximated as cylindrical. The sheath radius is estimated from the focal spot radius, the target thickness, and a half-divergence angle of the electron beam inside the target which is estimated as,

$$r_s = r_0 + l \tan\theta, \quad (6.8)$$

where r_0 is the focal spot radius, l is the target thickness, and the half-divergence angle of the electron beam inside the target θ is of the order of several to a few tens of degrees ($\theta = 8^\circ$ (162), $\theta = 25^\circ$ (190)). The length of the sheath is approximated as the pulse duration times the speed of light.

These approximations provide reasonable accurate estimations to the interaction of relatively long pulses (300 fs to a few ps) focused up to intensities of mid- 10^{19} Wcm^{-2} onto relatively thick ($> 10\mu\text{m}$) targets. A not too high pulse contrast is also required to produce a relatively large scale pre-plasma on the front side of the target (191). Therefore the estimations made with these models for the conditions of VEGA must be taken with special caution.

Table 6.2 shows the estimated achievable parameters with VEGA 1, VEGA 2 and VEGA 3 with $10 \mu\text{m}$ thick solid targets with $n_{e0} = 7.7 \times 10^{21} \text{ cm}^{-3}$. In general the highest proton energies are achieved with the smallest focal spot r_0 and target thickness l , but the minimum thickness is limited by the laser contrast.

The previous equations give the ion energy which can be achieved in a typical experiment with 'normal' ($\approx 10^6:1$ at 1 ps) pulse contrast choosing appropriate target and irradiation conditions. For ultra-high contrast lasers and sub- μm targets, the equations can still be used, but in this case the maximum energy of bound electrons differs from the other equation and needs to be measured or taken from simulations. The optimum laser pulse duration (to achieve maximum ion energy) using pulse energies of 0.5 -15 J, focused down to a spot of radius $r_0 \sim 1 \mu\text{m}$, onto $\sim 10 \mu\text{m}$ thick targets in the TNSA regime, is between 80 and 600 fs. Therefore the parameters of VEGA are far from the the optimum for TNSA. In the TNSA regime with lasers of moderate contrast the angle of incidence has a small effect on the ion acceleration(191). However in the case of a high-contrast laser pulse, the ion energy in the target normal direction does depend on the laser incidence angle (192). 3D PIC simulations (193) show that there is

6. ION ACCELERATION WITH THE VEGA LASER

Parameter	Equation	Symbol	Unit	VEGA 1	VEGA 2	VEGA 3
Laser Energy		W_L	J	0.5	4	30
Laser Intensity		I_0	W/cm ²	1.0E+19	1.0E+20	1.0E+21
Ponderomotive Energy (linear polarisation)		ϕ_{pond}	MeV	0.4	2.0	7.3
Hot Electron Temperature	6.2	T_{e1}	MeV	0.4	2.0	7.3
Hot Electron Temperature	6.3	T_{e2}	MeV	0.4	0.9	2.0
Acceleration Time	6.4	t_{acc}	fs	39	39	39
Target Thickness		l	μm	10	10	10
Half-divergence angle		q	°	15	15	15
Sheath Radius	6.8	r_s	μm	8	8	8
Conversion Efficiency into Hot Electrons	6.7	η		0.14	0.50	0.50
Number of Hot Electrons	6.6	N_e		1.0E+12	6.2E+12	1.3E+12
Density of Hot Electrons in the Sheath		n_{e0}	cm ⁻³	6.1E+20	3.8E+21	7.7E+21
Proton Plasma Frequency		ω_{pi}	s ⁻¹	3.3E+13	8.0E+13	1.2E+14
Ion (C ⁶⁺) Plasma Frequency		ω_{pi}	s ⁻¹	2.3E+13	5.7E+13	8.2E+13
Max. Proton Energy with T_{e1}	6.1	$\epsilon_{p,max}$	MeV	0.2	5	29
Max. Proton Energy with T_{e2}	6.1	$\epsilon_{p,max}$	MeV	0.2	2	8
Max. Ion (C ⁶⁺) Energy with T_{e1}	6.1	$\epsilon_{i,max}$	MeV	0.7	17	110
Max. Ion (C ⁶⁺) Energy with T_{e2}	6.1	$\epsilon_{i,max}$	MeV	0.7	8	31

Table 6.2: Estimations of TNSA acceleration with VEGA - Overview of achievable parameters with the VEGA laser system in the TNSA regime.

6.2 Estimations of ion acceleration in VEGA

an optimum incidence angle at which the ion energies can be significantly greater than those at normal incidence.

6.2.2 Light-Sailing RPA

A high-irradiance laser pulse with sufficiently large focal spot interacting with a thin foil pushes forward the electrons due to the radiation pressure (97). This acceleration mechanism approaches an ideal one and, if instabilities (see section 2.6) do not have time to develop, it can produce a quasi-monoenergetic ion spectrum. In RPA, the optimum relation between the laser amplitude and the electron areal density is $a_0 \approx \pi\sigma$. For the intensities achievable with each of the phases of VEGA, these optimum values are displayed in table 6.3 (assuming circular polarisation). Assuming the electron density of a fully ionised diamond-like carbon (DLC) target $n_e = 460n_{cr}$, these areal electron densities correspond to the target thickness also shown in table 6.3.

Parameter	Equation	Symbol	Unit	VEGA 1	VEGA 2	VEGA 3
Laser Intensity		I_0	W/cm ²	1.0E+19	1.0E+20	1.0E+21
Normalised Laser Amplitude (circular polarisation)	2.16	a_0		2	5	15
Optimum Areal Electron Density	3.1	σ_{opt}		0.5	2	5
Optimum Target Thickness (for fully ionised DLC)		l_{opt}	nm	1	3	8
Maximum Proton Energy	6.9	$\epsilon_{p,max}$	MeV	2	14	102
Maximum Ion (C ⁶⁺) Energy	6.9	$\epsilon_{i,max}$	MeV	5	45	376
Conversion Efficiency Protons	6.10	η		0.06	0.16	0.37
Conversion Efficiency Ions (C ⁶⁺)	6.10	η		0.03	0.09	0.23

Table 6.3: Estimations of RPA light-sailing acceleration with VEGA - Overview of achievable parameters with the VEGA laser system in the RPA laser light-sail regime.

The ion energy and efficiency in the optimum case ($a_0 \approx \pi\sigma$) can be estimated according to (97) by

$$\epsilon_{i,max}^* \approx 2m_i c^2 \frac{(\pi\mu a N)^2}{1 + 2\pi\mu a N} \quad (6.9)$$

$$\eta^* \approx \frac{2\pi\mu a N}{1 + 2\pi\mu a N} \quad (6.10)$$

where $N = c\tau/\lambda$ is the number of cycles in the pulse (for VEGA $N=11$), and $\mu = m_e Z_i/m_i$. With the parameters of VEGA in the optimum case ($a_0 = \pi\sigma$) this

6. ION ACCELERATION WITH THE VEGA LASER

model predicts the maximum ion energies shown in table 6.3. 2D PIC simulations show that the idealised 'light sail' model gives a good approximation for the maximum ion energy; however, it overestimates the efficiency (93).

6.2.3 Hole-Boring RPA

If an overdense target is relatively thick, it cannot be treated as a thin foil as in the 'light sail' regime. However the plasma is still pushed forward by the radiation pressure acceleration. In this hole-boring regime the 1D model predicts a monoenergetic ion spectrum. However in real-life multi-dimensional effects like instability development can cause the spectra to broaden. A circularly polarised pulse normally incident to the target is advantageous for the mechanism of hole boring, as in this case the plasma is heated less effectively (135, 194, 195). This mechanism is determined by the dimensionless piston parameter Ξ (see equation 2.55) The maximum kinetic ion energy is given by equation 2.61 and conversion efficiency given by this model are

$$\eta = 2\sqrt{\Xi}/(1 + 2\sqrt{\Xi}) \quad (6.11)$$

The ion energies are higher for smaller densities. However, the model is applicable for $n_e > (1 + a_0^2)^{\frac{1}{2}} n_{cr} \approx a_0 n_{cr}$ as it assumes total laser pulse reflection rather than relativistic transparency of a thick plasma. Assuming a near-critical density target of $n_e = 20n_{cr}$, the parameters of VEGA predict the values shown in table 6.4.

Parameter	Equation	Symbol	Unit	VEGA 1	VEGA 2	VEGA 3
Laser Intensity		I_0	W/cm ²	1.0E+19	1.0E+20	1.0E+21
Normalised Laser Amplitude (circular polarisation)	2.16	a_0		2	5	15
Pistoning Parameter (Protons)	2.55	Ξ		6.50E-05	6.50E-04	6.50E-03
Pistoning Parameter (C ⁶⁺)	2.55	Ξ		3.20E-05	3.20E-04	3.20E-03
Maximum Proton Energy	2.61	$\epsilon_{p,max}$	MeV	0.1	1.2	10
Maximum Ion (C ⁶⁺) Energy	2.61	$\epsilon_{i,max}$	MeV	0.7	7	65
Conversion Efficiency Protons	6.11	η		0.02	0.05	0.14
Conversion Efficiency Ions (C ⁶⁺)	6.11	η		0.01	0.03	0.1

Table 6.4: Estimations of RPA hole-boring acceleration with VEGA - Overview of achievable parameters with the VEGA laser system in the RPA hole-boring regime.

Ion acceleration attributed to collisionless shocks has been reported by Henig *et al.* (196) (protons up to 8 MeV using 0.6 J, 45 fs, 20 TW, 10^{20} Wcm⁻² laser irradiating

6.2 Estimations of ion acceleration in VEGA

overdense micro-sphere targets) and Wei *et al.* (197) (helium ions up to 13 MeV using 180 J, 0.5-0.7 ps, 0.25 PW laser irradiating an underdense gas jet target).

6.2.4 Experimental data under conditions achievable in VEGA

Experimental data collected from the literature performed under conditions similar to those achievable by each of the phases of VEGA, that is sub-100 fs pulses and energies lower than 0.5, 4, and 30 J is presented in table 6.5, 6.6 and 6.7, respectively. In the majority of experiments performed up to now from solid matter, the acceleration regime was close to the TNSA one. In this regime, the proton energy is proportional to the hot electron temperature, which in turn in the relativistic intensity regime is often proportional to the square root of intensity. Some proton energies significantly above the general trend have been obtained with ultra- high-contrast lasers, nanometre-scale foils, or by use of novel target techniques. The efficiency strongly depends upon other laser parameters and shooting conditions, especially the contrast ratio (198) and target thickness (91, 191, 198, 199, 200); higher contrast pulses and thinner targets tend to provide greater conversion efficiencies. On the other hand, the conversion efficiency into relatively low-energy ions can be increased by positioning the target out of focus, in which case the effect of larger spot area prevails over the effect of smaller intensity (201). The interaction with thinnest targets is the most promising route for ion acceleration from solid matter.

Reference	W_L (J)	τ (fs)	I_0 (W/cm ²)	Contrast	Target	d (μ m)	Angle ($^\circ$)	Energy (MeV/u)
Spencer <i>et al.</i> (202)	0.2	60	7.00E+18	1.00E+06	Mylar	23	0	1.5
Spencer <i>et al.</i> (202)	0.2	60	7.00E+18	1.00E+06	Al	12	0	0.9
Oishi <i>et al.</i> (164)	0.12	55	6.00E+18	1.00E+05	Cu	5	45	1.3
Neely <i>et al.</i> (198)	0.3	33	1.00E+19	1.00E+10	Al	0.1	30	4.0
Fukuda <i>et al.</i> (203)	0.15	40	7.00E+17	1.00E+06	CO ₂ +He	2000	0	15.0
Okihara <i>et al.</i> (204)	0.12	50	3.00E+18	1.00E+04	PTFE	75	0	5.0

Table 6.5: Experimental results with VEGA 1 parameters - List of experiments that were performed with similar parameters like the VEGA 1 output.

6. ION ACCELERATION WITH THE VEGA LASER

Reference	W_L (J)	τ (fs)	I_0 (W/cm ²)	Contrast	Target	d (μm)	Angle ($^\circ$)	Energy (MeV/u)
Kaluza <i>et al.</i> (162)	0.85	150	1.30E+19	2.00E+07	Al	20	30	4.0
Ceccotti <i>et al.</i> (205)	0.65	65	5.00E+18	1.00E+10	Mylar	0.1	45	5.3
Yogo <i>et al.</i> (206)	0.71	55	8.00E+18	1.00E+06	Cu	5	45	1.4
Yogo <i>et al.</i> (163)	0.8	45	1.50E+19	2.50E+05	Polymide	7.5	45	3.8
Nishiuchi <i>et al.</i> (207)	1.7	34	3.00E+19	2.50E+07	Polymide	7.5	45	4.0
Henig <i>et al.</i> (132)	0.7	45	5.00E+19	1.00E+11	DLC	0.0054	0	13.0
Zeil <i>et al.</i> (208)	3	30	1.00E+21	2.00E+08	Ti	2	45	17.0
Nishiuchi <i>et al.</i> (209)	7.5	40	1.00E+21	1.00E+10	Al	2	45	12.0

Table 6.6: Experimental results with VEGA 2 parameters -List of experiments that were performed with similar parameters like the VEGA 2 output.

Reference	W_L (J)	τ (fs)	I_0 (W/cm ²)	Contrast	Target	d (μm)	Angle ($^\circ$)	Energy (MeV/u)
Carroll <i>et al.</i> (192)	5	50	7.00E+20	1.00E+10	Al	0.1	0	7.5
MacKinnon <i>et al.</i> (17)	10	100	1.00E+20	1.00E+10	Al	3	22	24.0
Patel <i>et al.</i> (210)	10	100	5.00E+18	1.00E+07	Al	20	0	12.0
Prasad <i>et al.</i> (211)	12	50	5.00E+20	1.00E+10	Al	0.05 - 6	35	12.0
Ogura <i>et al.</i> (212)	7.5	40	1.00E+21	1.00E+10	SUS	2	45	40.0
Kim <i>et al.</i> (213)	27	30	1.00E+21	1.00E+11	Polymer	0.1	7	45.0
Green <i>et al.</i> (214)	10	45	1.00E+21	1.00E+10	Al	0.5	30	30.0
Bin <i>et al.</i> (215)	10	50	2.00E+20	1.00E+09	CNF	1	0	20.0

Table 6.7: Experimental results with VEGA 3 parameters - List of experiments that were performed with similar parameters like the VEGA 3 output.

6.3 Requirements for ion acceleration with VEGA

In order to obtain the maximum benefit from the unique characteristics of VEGA in terms of laser-driven ion acceleration, a series of experimental requirements must be taken into account.

6.3.1 Laser pulse parameters

The highest laser intensity is required to achieve larger ion energies in most acceleration regimes. This demands the use of off-axis parabolic mirrors with the shortest focal length possible (in practice $f/2$ or $f/3$). A wave front quality control with a deformable mirror helps to achieve the smallest focal spot (near diffraction limited) and highest intensity. The deformable mirror is also necessary to achieve the super-Gaussian or flat-top-like focal spot shapes required in the radiation pressure dominant regime of proton acceleration. The shape of the laser focal spot and target material affect the shape of the resulting proton beam too. Different polarisations on target are required to study its effect on the laser absorption by the plasma and employ the optimum. The TNSA mechanism benefits from a p-polarisation on target, whereas RPA requires a circularly polarised laser beam. A circularly polarised high power laser beam is achieved with a large-aperture $\lambda/4$ plate. A variable pulse duration (within a certain range) is beneficial to study the effect of the pulse duration on several acceleration mechanisms and fine tune the optimum duration whenever possible.

6.3.2 Pulse contrast

The preceding light may cause damage to the solid target before the intense main laser pulse arrives (see section 3.1.2). For relatively thick targets a few tens of μm scale pre-plasma can contribute positively to the ion acceleration because of stronger main pulse absorption and self-focusing, while the sufficient target thickness prevents rear surface deterioration. For this reason, a controllable pre-pulse or pedestal with variable delay and intensity is useful as well as for the novel scheme proposed in section 5.2. However, for most of the acceleration regimes, a low pulse contrast reduces the plasma fields which accelerate ions. Especially in the RPA light-sail regime, a sharp step-like density profile is required for the most efficient acceleration (as described in section 4.1). Also in the TNSA regime, a sharp plasma boundary at the target rear

6. ION ACCELERATION WITH THE VEGA LASER

side is required. Therefore, the laser contrast should be sufficiently high such that the target rear side remains unperturbed before the arrival of hot electrons. If the target is mainly perturbed by the ASE, the necessary ASE contrast for a given target thickness and material and ASE duration may be estimated as (216)

$$C_{ASE} = 8000 \frac{I_0}{\text{Wcm}^{-2}} \frac{\mu\text{m}}{\lambda_0} \tau_{ASE}^3 \left(\frac{\alpha \text{Pa}}{\rho_0 l (l - c_s \tau_{ASE})} \right)^{\frac{3}{2}} \quad (6.12)$$

where $\alpha \sim 1.4$ is an empirical constant, Pa represents pascal (pressure unit), c_s is the ion sound velocity, l the scale length and ρ_0 is the original material density. Assuming a duration of the ASE of $\tau_{ASE} = 0.5$ ns and a 6 μm aluminium target, the ASE minimum contrast would be 2×10^6 , 2×10^7 and 2×10^8 for 1×10^{19} Wcm^{-2} , 1×10^{20} Wcm^{-2} and 1×10^{21} Wcm^{-2} , respectively.

For the implementation of the radiation pressure acceleration regime, the front target surface should not be perturbed before the interaction with the main pulse. The contrast requirement is:

$$C = \frac{I_0 \tau_{pre}}{F_{DT}} \quad (6.13)$$

where τ_{pre} is the duration of the pre-pulse and F_{DT} is the damage threshold. This is in practice an even higher constraint on the pulse contrast.

The specifications of VEGA offer an ultra-high pulse contrast without the need of external contrast-enhancing devices. However, if it was needed, a single or double plasma mirror set-up could provide a contrast ratio of the order of 10^2 or 10^4 , respectively (106).

6.3.3 Targets

Many different types of targets, overdense and underdense, are commonly used in laser-plasma interaction experiments. These include thin foils (from few nm to μm), double layer targets, foam and foam-foil targets, tape targets and gas jets.

Materials used for solid targets are usually metals like aluminium, copper or gold, or plastics like Mylar and PTFE. Excellent results were obtained with diamond-like carbon (DLC), which was also used in the framework of this thesis to simulate the interaction with high intensity pulses (see section 4.1).

6.3 Requirements for ion acceleration with VEGA

For future experimental efforts and to make use of the high-repetition rate of the VEGA Petawatt, gas targets could become increasingly interesting. They usually consist of noble gases at high pressure expanded through a pulsed valve. Clusters are produced when mixing another gas with the noble gas and expanding the mixture at high pressure through the pulsed valve.

For ultra-thin solid foils sometimes the areal electron density (see equation 3.1) is more important than the thickness itself, whereas for micrometre targets this is usually not the case. The existence of an optimum target thickness is due to the geometrical factor (size of the sheath) (162, 191), the hot electron circulation (17, 217) and the stronger laser absorption in a partly expanded, near-critical density target (218, 219). For laser systems with a typical contrast of $\sim 10^7$, the optimum thickness is of several to a few tens of μm , as determined by the on-set of rear target side damage due to the ASE (see equation 6.12). For short pulse laser systems with contrast $\sim 10^{10}$ like VEGA the optimum target thickness is several tens to hundred nm determined by the target perturbation on the picosecond and sub-picosecond time scales.

Electron confinement effects lead to a larger hot electron density and therefore enhanced ion acceleration in the TNSA regime if the transverse size of the target is small enough. Further, a small transverse size of the target or light-ion or proton layer (dot) encourages a quasi-monoenergetic ion beam generation.

So-called mass-limited targets (MLT) could provide benefits under a wide range of experimental conditions. These benefits are larger hot electron densities and temperatures and more uniform hot electron distribution, which leads to increased proton energies and conversion efficiencies. It also generates a smaller proton beam divergence. Ideally, the target should completely be isolated, by levitating or injecting into the interaction region, for example a droplet target (220), or by employing thin support wires or spokes (221). Flat-top cone targets (222) may perform significantly better than thin foils in terms of maximum proton energy and conversion efficiency, however their fabrication and characterisation is much more demanding. In principle, all ultra-thin foils and complex targets like MLT, foam targets, etc. cannot be easily transported due to their fragility and require an in-situ target fabrication.

In order to use solid targets with the high-repetition rate offered by VEGA a means of delivering targets should be developed, which is highly non-trivial. It requires the mass production of targets, fast delivery into the interaction region, alignment into

6. ION ACCELERATION WITH THE VEGA LASER

focus and disposal of debris that otherwise may destroy adjacent targets and damage the focusing optics.

6.3.4 Plasma and particle beam diagnostics

In order to obtain a thorough understanding of the laser-target interaction during acceleration it is necessary to employ as many diagnostics as possible, including not only ion beam diagnostics (see section 3.1.4), but also full characterization of the laser pulse before and after the interaction (i.e. reflected, transmitted or scattered radiation parameters (223, 224), possible non-linear effects such as harmonics generation (134, 225, 226, 227), measurements of electron properties (228, 229, 230, 231, 232), time-resolved optical imaging (233), characterization of plasma densities and fields using interferometry (175, 234) or proton imaging/deflectometry (52), x-ray diagnostics (235) and so on.

For the characterisation of the charged particle beam, filtered stacks of nuclear track detectors such as CR-39 (236) or radiochromic films (RCFs) (237, 238, 239) are used as inexpensive 2D detectors without magnetic or electric fields. If the proton energy is larger than several MeV, the activation technique is also applicable for the stacked detectors (131, 240, 241). The activation technique can provide a very high dynamic range due to a high saturation level (242). Nuclear activation diagnostic can be selectively sensitive to some of the ion species (243, 244). These detectors are not affected by the powerful electromagnetic pulse (EMP) produced in the interaction, but they are off-line. In order to match the particle beam diagnostics with the high repetition rate of the laser, on-line electronic devices with a fast read-out time have to be used. This in turn requires a means to protect or screen out the electronics from the EMPs.

2D electronic detectors which provide short (a few seconds) readout times have been demonstrated: fast scintillator coupled to a CCD (116, 245) or micro-channel plate (MCP) coupled to a phosphor screen (as used in the conducted experimental campaigns, see section 3.1.4) and CCD (246, 247, 248, 249). The CCD should typically have a low noise and large gain, i.e. a suitable choice may be a cooled electron-multiplied CCD. Further, although the time gating is not absolutely necessary, it helps one to discriminate signals produced by protons, ions, electrons and X-rays (to all of which the scintillators and MCPs are sensitive), due to the different flight times, typically in the

nanosecond time scales for the protons and ions. The signal caused by electrons in these detectors can also be suppressed by magnets. The scintillators with different emission colours can be stacked to obtain several channels with different ion energies (250). The conventional technique, which was also used in the conducted experimental campaigns, to precisely identify the ion species as well as their energy spectra is the Thomson Parabola ion energy analyser (115, 116, 246, 248, 251, 252). It works with nuclear track detectors (e.g. CR-39), imaging plates (IP) (119, 253, 254), RCFs or MCPs as the recoding detector. Modified versions with angled electrodes have been used as high-resolution, high-dispersion Thomson Parabola for >100 MeV/nucleon ion energies (116) (see section 3.1.4.1). A TOF ion spectrometer (206, 255), due to its simple and fast readout, can be used as a real-time diagnostic with high repetition rate lasers. The measurement of the properties of electrons which are generated simultaneously with ions is also very important for understanding of proton and ion acceleration driven by intense lasers as has been demonstrated in chapter 4. Ideally, one should measure the electron spectrum and spatial distribution in the interaction region using, e.g., Thomson scattering (256, 257, 258), bremsstrahlung radiation (259, 260), optical transition radiation (229, 230, 232), Cerenkov radiation (261), or optical probe reflectometry (262). Some information can also be extracted analysing the spectra of electrons left at the target; the electron spectra can be obtained in this case with a magnetic electron energy analyser coupled with a scintillator or IP (117, 228, 263, 264).

6.4 Summary

Existing analytical scaling laws and numerical data were used to investigate the capabilities of laser-driven ion acceleration with the VEGA laser system at CLPU. While the TNSA is generally a robust and reliable mechanism, it works best for pulses between 80 fs and 600 fs and is therefore far from ideal for the VEGA system with its ultra-short (30 fs) pulse duration. Much more attractive in terms of ion acceleration, is the interaction with ultra-thin solid targets in the nanometre range. The most promising results are predicted in the radiation-pressure dominated regime, namely light-sailing with nano-foils and hole-boring with low-density targets (e.g. aerogels or foams (265)).

In the light-sailing RPA, analytical scaling laws predict energies up to 102 MeV and 376 MeV/u from the interaction with 8 nm thin fully ionised diamond-like-carbon

6. ION ACCELERATION WITH THE VEGA LASER

targets with an conversion efficiency of 0.37 and 0.23 for protons and carbon ions, respectively (see table 6.3). Due to the delicate nature of nanometre thin solid films, the contrast requirements are extremely stringent. A pulse contrast of up $10^{12} : 1$ can be demanded, which also makes VEGA a good candidate given its high contrast without the need of employing external contrast-enhancing devices. The numerical data presented in section 4.1 showed that the maximum energy scales as $E_{max} \propto I^2$, which coincides with the prediction by the light-sailing model and highlights the importance to achieve the highest laser intensities. With appropriate focusing VEGA can reach intensities up to 10^{22} Wcm^{-2} , which makes the exploration of the light-sailing regime attractive.

Hole-boring RPA could also be an attractive regime to be explored with the VEGA laser. As seen from table 6.4, energies up to 10 MeV and 65 MeV/u and conversion efficiencies up to 0.14 and 0.1 for protons and carbon ions, respectively. The energies are dependent on the pistoning parameter Ξ (see equation 2.55), and increase with smaller densities. Therefore the experimental study with aerogels or foam targets of reduced density with VEGA could yield high-energy ion beams.

Experimental set-ups like the one shown in section 5.1 allow the angular separation of ion beams originating from different acceleration processes (e.g. TNSA, RPA and BOA), facilitating the individual study. Such set-ups could also be implemented at the CLPU with the VEGA laser.

Finally, referring to section 5.1 and 5.2, VEGA is well suited to explore ion acceleration by the introduction of a controlled pre-pulse due to its individual outputs. As shown in section 5.2, a double pulse set-up with mixed polarisation could lead to generation of high-energy ($> 100 \text{ MeV/u}$) ion beams with moderate intensities ($\sim 10^{21} \text{ Wcm}^{-2}$ for VEGA parameters) and an energy spread as narrow as 10%, which also makes it very attractive for practical applications as discussed in section 1.2.

7

Conclusion and outlook

7.1 Conclusion

The presented thesis reports an investigation on laser-driven ion acceleration from ultrathin targets. The main objectives of the investigation were finding the conditions of the laser-plasma interaction that maximise the ion energy and minimise the energy spread in the generated ion beam, getting them closer to the parameters required to applications such as hadron therapy. The effects that determine and limit the ion beam parameters achievable in the interaction of high intensity laser beams with solid target were characterised. This includes an understanding of the on-set of relativistically-induced transparency, electron transport in the plasma, development of instabilities and occurrence of multiple acceleration mechanisms. Furthermore estimations about the performance of the VEGA laser system in laser-driven ion acceleration were obtained and a set of requirements in order to optimise its scientific exploitation was established. Therefore experimental and numerical data from the interaction of high intensity lasers with ultrathin solid targets was obtained. In particular, single pulse and double pulse laser schemes were investigated.

Numerical study of single laser pulse interactions with ultrathin solid targets

It has been shown that ions can be efficiently accelerated to 100 MeV/u in the Radiation Pressure Acceleration scheme using short femtosecond pulses with circular polarisation. The beam production also depends sensitively on the target thickness and composition.

7. CONCLUSION AND OUTLOOK

Optimum acceleration conditions were found for 40 nm thick diamond-like carbon foils. However there are a number of caveats that have to be overcome. High-resolution simulation runs revealed the development of transverse instabilities that have also been observed experimentally. Bubble-like structures are imprinted in the spatial density profile of the ion beams, which indicates the formation of Rayleigh-Taylor type instabilities.

Experimental investigation of electron dynamics at the on-set of Relativistically Induced Transparency

Beside the Radiation Pressure Acceleration mechanism, other schemes at the on-set of relativistically induced transparency have emerged, e.g. the Breakout Afterburner. Since the intensities of currently existing laser systems are not high enough to accelerate ions directly, the energy is always mediated via the plasma electrons. A thorough understanding of the electron dynamics is therefore required. The collective dynamics of electrons in relativistically transparent foils driven by a linearly polarised laser field was experimentally shown to exhibit a $\cos(2\theta)$ dependence, where θ is the angle between the electron radial momentum vector and the polarisation axis. This is manifested in a double lobe formation in the electron density distribution. It has been shown that the electron beam profile is sensitive to the laser polarisation direction and the percentage of the laser energy that is transmitted through the target.

Experimental investigation of double pulse interactions with ultrathin solid targets

In the framework of this thesis, also the interaction of double laser pulses with solid targets has been studied. Many ion acceleration mechanisms depend sensitively on the scale-length of the plasma. A first pulse can prepare the plasma to maximise the acceleration by the second pulse. An energy enhancement in ultrathin foils undergoing relativistically-induced transparency was investigated. In the case of a double pulse with two linearly polarised pulses the evolution between several acceleration mechanisms occurs over the duration of the laser pulse and the underlying phenomena can be investigated by angularly separating the different ion beam components. It was shown that the target expansion, controlled by varying the rising edge of intensity profile,

produces an extended plasma jet, which in turn allows better energy coupling to the proton population.

Numerical investigation of ion acceleration with double pulses of mixed polarisation

With the use of particle-in-cell simulations, a novel acceleration scheme with double pulses of mixed polarisation was identified that can operate in the femtosecond and picosecond pulse duration regime. In case of femtosecond pulses a first, moderate intensity linearly polarised pulse heats up the electron population causing the overdense target to expand, dragging the ions behind and preserving quasi-neutrality. After a time delay of around half a picosecond, a second pulse of higher intensity and circular polarisation, drives a collisionless shock in the pre-expanded and near-critical plasma that efficiently accelerates the remaining ions. This scheme predicts the generation of >100 MeV/u heavy-ions with intensities of 10^{21} Wcm⁻².

Performance of VEGA in laser-driven ion acceleration and experimental requirements

Finally, the obtained results and existing scaling laws were used to estimate the capabilities of the VEGA laser system in terms of ion acceleration. The ultra-short pulse duration, ultra-high intensity and the high contrast make VEGA an ideal system to accelerate ion the in the Radiation Pressure Acceleration scheme. Furthermore the three independent outputs allow the implementation of double-pulse set-ups, which could provide a pathway to efficient heavy-ion acceleration. Therefore the VEGA system is suitable for laser-driven ion acceleration, but effort is needed in terms of experimental set-up, target fabrication and optimisation, and diagnostics, to achieve ion beams which are useful for applications.

7.2 Outlook

At the present stage, the performance of a standard few μm -thick solid foil, irradiated with 'normal' ($\sim 10^6:1$) contrast laser pulses has been studied extensively and understood relatively well (89). The general conclusion obtained from experiments and simulations is that the use of thinner targets and higher pulse contrast is advantageous

7. CONCLUSION AND OUTLOOK

in terms of high maximum ion energy. Many ideas and techniques have been tested including the use of various advanced targets (16), circular polarization (132) (section 4.1), contrast improvement techniques (266), multi-pulse and multi-stage acceleration etc (166) (section 5.1 and 5.2).

Many models and simulations predict the generation of ion beams with energies well in excess of 100 MeV with already achievable laser energies and intensities ($\sim 10^{21} - 10^{22}$ Wcm⁻²) (section 4.1 and 5.2). However the experimentally obtained energies are not quite as high as the theoretical predicted energies. In particular there is the Radiation Pressure Acceleration light-sail that predicts the formation of quasi-monoenergetic (few % energy spread) ion beams with an energy of hundreds of MeV and a high efficiency, but inducing light-sail experimentally has proven very challenging.

Achieving the final stage of RPA is one of the most important immediate goals in the field of laser-driven ion acceleration; it includes tailoring of the laser pulse and target, avoiding or exploiting instabilities, finding optimum conditions, etc. Achieving (quasi-) monoenergetic ion beams is essential for some of the proposed applications of laser-driven ion sources such as hadron therapy. It involves achieving and optimising the acceleration mechanisms that predict monoenergetic spectra (92, 93, 267) and/or developing monochromatisation techniques for the ion beam (Phase rotation (268), laser-driven microlens (269), or permanent magnets and solenoids (270, 271, 272, 273)).

The interaction with gas and liquid targets will allow the use of laser pulses at a higher repetition rate. Therefore efficient acceleration mechanisms in the interaction of laser pulses with near-critical plasma will have to be identified and experimentally demonstrated.

The density of an originally solid target can also become close to the critical density or even underdense due to the pre-pulse or ASE irradiation (in few μm -thick targets) (274) or picosecond/femtosecond pedestal (in nanometre-thick targets) (218, 219), which further requires the demonstration of ion acceleration mechanisms in the underdense or near-critical regime.

A promising route is to use a pulsed high-pressure gas jet as target. A self-replenishable gas jet is ideal for applications where repetitive ion acceleration is required. Moreover, it is less demanding in terms of laser energy and pulse contrast, and it offers several additional advantages like adjustable density, contamination-free composition, and debris-free operation. In any case it is necessary to find the optimum

density profile, to demonstrate the scalability of the acceleration in near-critical plasmas to larger laser powers, and to search for conditions which lead to quasi-monoenergetic ion spectra.

Combining several techniques of laser-driven ion acceleration is also a potentially interesting line of research. For example, it is desirable to combine a clean (ultra-high contrast) laser pulse, focused to a sub- μm spot, with a nanometre-thick double-layer target or mass-limited targets (MLT).

Advances in laser-driven ion acceleration rely as much in the optimisation and development of novel target as in the laser technology itself. The general trend is to use thinner targets (which in turn require higher contrast pulses) and complex targets which typically comprise several components and have several geometrical parameters (275). Finding an optimum design for given laser parameters is a difficult task and should include analytical models, extensive simulations (276) and experiments. Without such optimization the high potential of complex targets cannot be fully exploited.

Another path for the optimization and control of laser-driven ion acceleration is the active tailoring of the driving laser pulses (optimisation of temporal shape on different time scales, spatial profile, polarisation, etc.) Much theoretical and experimental work is necessary to fully exploit the possibilities of available lasers. Another possibility which up to now has received relatively little attention in experiments is the employment of multi-pulse irradiation schemes (see section 5.1 and 5.2). Beam splitting and recombination (167) may increase the maximum proton energy and the conversion efficiency. Moreover, the low-energy parts of the proton spectra in the target normal direction may be suppressed at the optimal delays.

Cascaded (two stage) proton acceleration with two targets also allows spectrally controlling the proton beam (277). The central part of the proton beam accelerated from the first target and stretched by the time of flight dispersion is subsequently modified by the transient fields of a second target. Thus, a part of the spectrum, controllable with the optical delay between the two laser pulses, may be suppressed; part of the protons from a particular spectral region can be additionally accelerated, while the others are decelerated. Further development of multi-pulse and/or multi-stage techniques may allow ion or proton acceleration with relatively small energy bandwidth and narrow beam divergence up to higher energies without increasing the total laser energy (278, 279).

7. CONCLUSION AND OUTLOOK

In particular, mechanisms like the proposed collisionless shock acceleration with a double pulse laser set-up with mixed polarisation in section 5.2 are promising for future direction. The scheme has been demonstrated numerically with one-dimensional particle-in-cell simulations, and should therefore be tested in two-dimensional or three-dimensional simulations, and demonstrated experimentally (e.g. with Astra Gemini or VEGA).

Also the field of beam diagnostics has to be further explored. The measurement of ion beam properties in the multi-100 MeV/nucleon energy range is a potential issue due to smaller deflection by fields of the detectors and an expected strong background caused by simultaneously generated electrons, x-rays, neutrons, electromagnetic pulse, etc. The energy range of detectors presently used with laser-driven sources should be extended (115), or detectors used with conventional accelerators should be appropriately modified. Furthermore, the detectors should ideally provide 'on-line' capability in order to cope with the increasing repetition rate available in current high-power lasers.

At the moment-laser driven ion sources have some limitations (e.g. in terms of maximum energy and energy spread) which prevent their use in applications such as hadron therapy. However, the obtained experimental and numerical results have shown that there are a number of feasible acceleration schemes, leading to the generation of high-quality ion beams.

Publications

The following publications resulted from the work presented in this thesis:

Gray, R. J., MacLellan, D. A., Gonzalez-Izquierdo, B., Powell, H. W., Carroll, D. C., Murphy, C. D., **Stockhausen, L. C.**, Rusby, D. R., Scott, G. G., Wilson, R., Booth, N., Symes, S. J., Hawkes, S. J., Torres, R., Borghesi, M., Neely, D., McKenna, P. (2014). Azimuthal asymmetry in collective electron dynamics in relativistically transparent laserfoil interactions. *New Journal of Physics*, 112. doi:10.1088/1367-2630/16/9/093027

Stockhausen, L. C., Torres, R., Conejero Jarque, E. (2015). Simulations of ion acceleration from ultrathin targets with the VEGA petawatt laser. (Vol. 9514, p. 95141D). Presented at the SPIE Optics + Optoelectronics, SPIE. doi:10.1117/12.2178522

Powell, H. W., King, M., Gray, R. J., MacLellan, D. A., Gonzalez-Izquierdo, B., **Stockhausen, L. C.**, Hicks, G., Dover, N. P., Rusby, D. R., Carroll, D. C., Padda, H., Torres, R., Kar, S., Clarke, R. J., Musgrave, I. O., Najmudin, Z., Borghesi, M., Neely, D., McKenna, P. (2015). Proton acceleration enhanced by a plasma jet in expanding foils undergoing relativistic transparency. *New Journal of Physics*, 17(10), 110. doi:10.1088/1367-2630/17/10/103033

Stockhausen, L. C., Torres, R., Conejero Jarque, E. (2015). Simulations of radiation pressure ion acceleration with the VEGA Petawatt laser. *Nuclear Inst. and Methods in Physics Research*, A.

Stockhausen, L. C., Torres, R., Conejero Jarque, E. (in preparation). Collisionless shock ion acceleration with double laser pulses of mixed polarization.

7. CONCLUSION AND OUTLOOK

Bibliography

- [1] ALBERT EINSTEIN. **The Quantum Theory of Radiation.** *Physikalische Zeitschrift*, **18**(121):63–77, March 1917. 1
- [2] A L SCHAWLOW AND C H TOWNES. **Infrared and Optical Masers.** *Phys. Rev.*, **112**:1940–1949, 1958. 1
- [3] T H MAIMAN. **Stimulated Optical Radiation in Ruby.** *Nature*, **187**:494, August 1960. 1
- [4] F J MCCLUNG AND R W HELLWARTH. **Giant Optical Pulsations from Ruby.** *Applied Optics*, **1**(101):103–105, September 1962. 1
- [5] L E HARGROVE, R L FORK, AND M A POLLACK. **Locking of he-ne laser modes induced by synchronous intracavity modulation.** Technical report, July 1964. 1
- [6] DONNA STRICKLAND AND GERARD MOUROU. **Compression of amplified chirped optical pulses.** *Optics Communications*, **55**(6):447–449, 1985. 1, 46
- [7] ROLF WIDERÖE. **Über ein neues Prinzip zur Herstellung hoher Spannungen.** *Archiv für Elektrotechnik*, **21**(4):387–406, August 1928. 2
- [8] ERNEST O LAWRENCE AND M STANLEY LIVINGSTON. **The production of high speed light ions without the use of high voltages.** *Phys. Rev.*, **40**:19–35, 1932. 2
- [9] V I VEKSLER. **The principle of coherent acceleration of charged particles.** *The Soviet Journal of Atomic Energy*, 1957. 2
- [10] T TAJIMA AND J M DAWSON. **Laser electron accelerator.** *Physical Review Letters*, **43**(4):267, 1979. 2
- [11] VICTOR MALKA, JÉRÔME FAURE, YANN A GAUDUEL, ERIK LEFEBVRE, ANTOINE ROUSSE, AND KIM TA PHUOC. **Principles and applications of compact laser–plasma accelerators.** *Nature Physics*, **4**(6):447–453, 2008. 2
- [12] HIROYUKI DAIDO, MAMIKO NISHIUCHI, AND ALEXANDER S PIROZHKOV. **Review of laser-driven ion sources and their applications.** *Reports on Progress in Physics*, **75**(5):056401, April 2012. 2, 3, 20, 39, 151
- [13] M BORGHESI. **Laser-driven acceleration of ions: State of the art, perspectives and applications.** *Nuclear Inst. and Methods in Physics Research, A*, **179**:177–204, December 2013. 2
- [14] ANDREA MACCHI, MARCO BORGHESI, AND MATTEO PASSONI. **Ion acceleration by superintense laser-plasma interaction.** *Reviews of Modern Physics*, **85**(2):751–793, May 2013. 2, 3
- [15] R A SNAVELY, M H KEY, S P HATCHETT, T E COWAN, M ROTH, T W PHILLIPS, M A STOYER, E A HENRY, T C SANGSTER, AND M S SINGH. **Intense high-energy proton beams from petawatt-laser irradiation of solids.** *Physical Review Letters*, **85**(14):2945, 2000. 2, 3
- [16] S A GAILLARD, T KLUGE, K A FLIPPO, M BUSSMANN, B GALL, T LOCKARD, M GEISSEL, D T OFFERMANN, M SCHOLLMIEIER, Y SENTOKU, AND T E COWAN. **Increased laser-accelerated proton energies via direct laser-light-pressure acceleration of electrons in microcone targets.** *Physics of Plasmas*, **18**(5):056710, 2011. 2, 3, 121, 172
- [17] A MACKINNON, Y SENTOKU, P PATEL, D PRICE, S HATCHETT, M KEY, D ANDERSON, R SNAVELY, AND R FREEMAN. **Enhancement of Proton Acceleration by Hot-Electron Recirculation in Thin Foils Irradiated by Ultraintense Laser Pulses.** *Physical Review Letters*, **88**(21):215006, May 2002. 3, 162, 165
- [18] P MCKENNA, K W D LEDINGHAM, T MCCANNY, R P SINGHAL, I SPENCER, E L CLARK, F N BEG, K KRUSHELNICK, M S WEI, J GALY, J MAGILL, R J CLARKE, K L LANCASTER, P A NORREYS, K SPOHR, AND R CHAPMAN. **Effect of target heating on ion-induced reactions in high-intensity laser–plasma interactions.** *Applied Physics Letters*, **83**(14):2763, 2003. 3
- [19] M BORGHESI, J FUCHS, S V BULANOV, A J MACKINNON, P K PATEL, AND M ROTH. **Fast ion generation by high-intensity laser irradiation of solid targets and applications.** *Fusion Science and Technology*, **49**(3):412–439, 2006. 3
- [20] L YIN, B J ALBRIGHT, K J BOWERS, D JUNG, J C FERNÁNDEZ, AND B M HEGELICH. **Three-Dimensional Dynamics of Breakout Afterburner Ion Acceleration Using High-Contrast Short-Pulse Laser and Nanoscale Targets.** *Physical Review Letters*, **107**(4):045003, July 2011. 3, 109, 113
- [21] BENGT ELIASSON, CHUAN S LIU, XI SHAO, ROALD Z SAGDEEV, AND PADMA K SHUKLA. **Laser Radiation Pressure Acceleration of Monoenergetic Protons in an Ultra-Thin Foil.** **1188**:35, 2009. 3
- [22] A HENIG, D KIEFER, K MARKEY, D GAUTIER, K FLIPPO, S LETZRING, R JOHNSON, T SHIMADA, L YIN, B ALBRIGHT, K BOWERS, J FERNÁNDEZ, S RYKOVANOV, H C WU, M ZEPF, D JUNG, V LIECHTENSTEIN, J SCHREIBER, D HABS, AND B HEGELICH. **Enhanced Laser-Driven Ion Acceleration in the Relativistic Transparency Regime.** *Physical Review Letters*, **103**(4):045002, July 2009. 3, 109
- [23] QINGCAO LIU, MENG LIU, TONGPU YU, PENGJI DING, ZUOYE LIU, SHAOHUA SUN, XIAOLIANG LIU, XING LU, ZEQUIN GUO, AND BITAO HU. **Effect of target composition on proton acceleration in ultraintense laser-thin foil interaction.** *Physics of Plasmas*, **19**(9):093108, 2012. 3
- [24] ROBERT R WILSON. **Radiological use of fast protons.** *Radiology*, **47**:487–491, 1946. 3

BIBLIOGRAPHY

- [25] KEN LEDINGHAM, PAUL BOLTON, NAOYA SHIKAZONO, AND C M MA. **Towards Laser Driven Hadron Cancer Radiotherapy: A Review of Progress.** *Applied Sciences*, **4**(3):402–443, September 2014. 3, 4
- [26] LINDSEY A TORRE, FREDDIE BRAY, REBECCA L SIEGEL, JACQUES FERLAY, JOANNIE LORTET-TIEULENT, AND AHMEDIN JEMAL. **Global cancer statistics, 2012.** *CA: A Cancer Journal for Clinicians*, **65**(2):87–108, February 2015. 3
- [27] HYWEL OWEN, RANALD MACKEY, KEN PEACH, AND SUSAN SMITH. **Hadron accelerators for radiotherapy.** *Contemporary Physics*, **55**(2):55–74, March 2014. 3
- [28] A BRAHME, R LEWENSOHN, U RINGBORG, U AMALDI, F GERARDI, AND S ROSSI. **Design of a centre for biologically optimised light ion therapy in Stockholm.** *Nuclear Inst. and Methods in Physics Research B*, **184**:1–20, December 2001. 4
- [29] T HABERER. **Accelerators for Americas Future.** *Symmetry Magazine*, pages 1–8, August 2010. 5
- [30] STEPHANIE E COMBS, OLIVER JÄKEL, THOMAS HABERER, AND JÜRGEN DEBUS. **Radiotherapy and Oncology.** *Radiotherapy and Oncology*, **95**(1):41–44, April 2010. 4
- [31] S V BULANOV AND V S KHOROSHKOV. **Feasibility of Using Laser Ion Accelerators in Proton Therapy.** *Plasma Physics Reports*, **28**:1–5, May 2002. 6
- [32] S V BULANOV, T ZH ESIRKEPOV, F F KAMENETS, Y KATO, A V KUZNETSOV, K NISHIHARA, F PEGORARO, T TAJIMA, AND V S KHOROSHKOV. **Generation of High-Quality Charged Particle Beams during the Acceleration of Ions by High-Power Laser Radiation.** *Plasma Physics Reports*, **28**:1–18, December 2002. 6
- [33] STEPAN S BULANOV, ANDREI BRANTOV, VALERY YU BYCHENKOV, VLADIMIR CHVYKOV, GALINA KALINCHENKO, TAKESHI MATSUOKA, PASCAL ROUSSEAU, STEPHEN REED, VICTOR YANOVSKY, AND KARL KRUSHELNICK. **Accelerating protons to therapeutic energies with ultraintense, ultraclean, and ultrashort laser pulses.** *Medical physics*, **35**:1770, 2008. 6
- [34] E FOURKAL, B SHAHINE, M DING, J S LI, T TAJIMA, AND C M MA. **Particle in cell simulation of laser-accelerated proton beams for radiation therapy.** *Medical physics*, **29**(12):2788, 2002. 6
- [35] E FOURKAL, J S LI, M DING, T TAJIMA, AND C M MA. **Particle selection for laser-accelerated proton therapy feasibility study.** *Medical physics*, **30**(7):1660, 2003. 6
- [36] WEI LUO, EUGENE FOURKAL, JINSHENG LI, AND CHANG-MING MA. **Particle selection and beam collimation system for laser-accelerated proton beam therapy.** *Medical physics*, **32**(3):794, 2005. 6
- [37] E FOURKAL, J S LI, W XIONG, A NAHUM, AND C M MA. **Intensity modulated radiation therapy using laser-accelerated protons: a Monte Carlo dosimetric study.** Institute of Physics Publishing, 2003. 6
- [38] VICTOR MALKA, SVEN FRITZLER, ERIK LEFEBVRE, EMMANUEL D’HUMIÈRES, RÉGIS FERRAND, GEORGES GRILLON, CLAUDE ALBARET, SAMUEL MEYRONEINC, JEAN-PAUL CHAMBARET, ANDRÉ ANTONETTI, AND DANIELÉ HULIN. **Practicability of protontherapy using compact laser systems.** *Medical physics*, **31**(6):1587, 2004. 6
- [39] MASAO MURAKAMI, YOSHIO HISHIKAWA, SATOSHI MIYAJIMA, YOSHIKO OKAZAKI, KENNETH L SUTHERLAND, MITSUYUKI ABE, SERGEI V BULANOV, HIROYUKI DAIDO, TIMUR ZH ESIRKEPOV, JAMES KOGA, MITSURU YAMAGIWA, AND TOSHIKI TAJIMA. **Radiotherapy using a laser proton accelerator.** *arXiv.org*, April 2008. 6
- [40] S S BULANOV, E ESAREY, C B SCHROEDER, W P LEEMANS, S V BULANOV, D MARGARONE, G KORN, AND T HABERER. **Helium-3 and helium-4 acceleration by high power laser pulses for hadron therapy.** *Physical Review Special Topics - Accelerators and Beams*, **18**(6):061302, June 2015. 6
- [41] M ROTH, T E COWAN, M H KEY, S P HATCHETT, C BROWN, W FOUNTAIN, J JOHNSON, D M PENNINGTON, R A SNAVELY, S C WILKS, K YASUIKE, H RUHL, F PEGORARO, S V BULANOV, E M CAMPBELL, M D PERRY, AND H POWELL. **Fast Ignition by Intense Laser-Accelerated Proton Beams.** *Physical Review Letters*, **86**(3):436–439, January 2001. 7
- [42] V YU BYCHENKOV, W ROZMUS, A MAKSIMCHUK, DONALD P UMSTADTER, AND C E CAPJACK. **Fast Ignitor Concept with Light Ions.** *Plasma Physics Reports*, **27**, 2001. 7
- [43] M TABAK, J HAMMER, E GLINSKY, L WILLIAM, W L KRUEER, S C WILKS, J WOODWORTH, E M CAMPBELL, M D PERRY, AND R J MASON. **Ignition and high gain with ultrapowerful lasers.** pages 1–10, January 1994. 7
- [44] J J HONRUBIA, J C FERNÁNDEZ, M TEMPORAL, B M HEGELICH, AND J MEYER-TER VEHN. **Fast ignition of inertial fusion targets by laser-driven carbon beams.** *Physics of Plasmas*, **16**(10):102701, 2009. 7
- [45] M TEMPORAL, J J HONRUBIA, AND S ATZENI. **Numerical study of fast ignition of ablatively imploded deuterium–tritium fusion capsules by ultra-intense proton beams.** *Physics of Plasmas*, **9**(7):3098, 2002. 7
- [46] MAURO TEMPORAL. **Fast ignition of a compressed inertial confinement fusion hemispherical capsule by two proton beams.** *Physics of Plasmas*, **13**(12):122704, 2006. 7
- [47] J C FERNÁNDEZ, B J ALBRIGHT, F N BEG, M E FOORD, B M HEGELICH, J J HONRUBIA, M ROTH, R B STEPHENS, AND L YIN. **Fast ignition with laser-driven proton and ion beams.** *Nuclear Fusion*, **54**(5):054006, April 2014. 9
- [48] A YA FAENOV, T A PIKUZ, Y FUKUDA, M KANDO, H KOTAKI, T HOMMA, K KAWASE, T KAMESHIMA, A PIROZHKOV, A YOGO, M TAMPO, M MORI, H SAKAKI, I HAYASHI, T NAKAMURA, S A PIKUZ, V KARTASHEV, I YU SKOBELEV, A GIULIETTI, C A CHECCHETTI, A S BOLDAREV, V A GASILOV, A I MAGUNOV, S KAR, M BORGHESE, P BOLTON, H DAIDO, T TAJIMA, I KATO, AND S V BULANOV. **Ionography of nanostructures with the use of a laser plasma of cluster targets.** *JETP Letters*, **89**(10):485–491, July 2009. 9

- [49] A YA FAENOV, T A PIKUZ, Y FUKUDA, M KANDO, H KOTAKI, T HOMMA, K KAWASE, T KAMESHIMA, A PIROZHKOV, A YOGO, M TAMPO, M MORI, H SAKAKI, Y HAYASHI, T NAKAMURA, S A PIKUZ, I YU SKOBELEV, S V GASILOV, A GIULIETTI, C A CECCHETTI, A S BOLDAREV, V A GASILOV, A MAGUNOV, S KAR, M BORGHESI, P BOLTON, H DAIDO, T TAJIMA, Y KATO, AND S V BULANOV. **Submicron ionography of nanostructures using a femtosecond-laser-driven-cluster-based source.** *Applied Physics Letters*, **95**(10):101107, 2009. 9
- [50] L VOLPE, D BATANI, B VAUZOUR, PH NICOLAI, J J SANTOS, C REGAN, A MORACE, F DORCHIES, C FOURMENT, S HULIN, F PEREZ, S BATON, K LANCASTER, M GALIMBERTI, R HEATHCOTE, M TOLLEY, CH SPINDLOE, P KOESTER, L LABATE, L A GIZZI, C BENEDETTI, A SGATTONI, M RICHTETA, J PASLEY, F BEG, S CHAWLA, D P HIGGINSON, AND A G MACPHEE. **Proton radiography of laser-driven imploding target in cylindrical geometry.** *Physics of Plasmas*, **18**(1):012704, 2011. 9, 10
- [51] M BORGHESI, A SCHIAVI, D H CAMPBELL, M G HAINES, O WILLI, A J MACKINNON, L A GIZZI, M GALIMBERTI, R J CLARKE, AND H RUHL. *Proton imaging: a diagnostic for inertial confinement fusion/fast ignitor studies.* Institute of Physics Publishing, 2001. 9
- [52] A J MACKINNON, P K PATEL, R P TOWN, M J EDWARDS, T PHILLIPS, S C LERNER, D W PRICE, D HICKS, M H KEY, S HATCHETT, S C WILKS, M BORGHESI, L ROMAGNANI, S KAR, T TONCIAN, G PRETZLER, O WILLI, M KOENIG, E MARTINOLLI, S LEPAPE, A BENUZZI-MOUNAIX, P AUDEBERT, J C GAUTHIER, J KING, R SNAVELY, R R FREEMAN, AND T BOEHLLY. **Proton radiography as an electromagnetic field and density perturbation diagnostic (invited).** *Review of Scientific Instruments*, **75**(10):3531–3536, October 2004. 9, 166
- [53] M BORGHESI, D H CAMPBELL, A SCHIAVI, M G HAINES, O WILLI, A J MACKINNON, P PATEL, L A GIZZI, M GALIMBERTI, R J CLARKE, F PEGORARO, H RUHL, AND S BULANOV. **Electric field detection in laser-plasma interaction experiments via the proton imaging technique.** *Physics of Plasmas*, **9**(5):2214, 2002. 9
- [54] M BORGHESI, L ROMAGNANI, A SCHIAVI, D H CAMPBELL, M G HAINES, O WILLI, A J MACKINNON, M GALIMBERTI, L GIZZI, R J CLARKE, AND S HAWKES. **Measurement of highly transient electrical charging following high-intensity laser–solid interaction.** *Applied Physics Letters*, **82**(10):1529, 2003. 9
- [55] M BORGHESI, S V BULANOV, T ZH ESIRKEPOV, S FRITZLER, S KAR, T V LISEYKINA, V MALKA, F PEGORARO, L ROMAGNANI, J P ROUSSEAU, A SCHIAVI, O WILLI, AND A V ZAYATS. **Plasma Ion Evolution in the Wake of a High-Intensity Ultrashort Laser Pulse.** *Physical Review Letters*, **94**(19):195003, May 2005. 9
- [56] A J MACKINNON, P K PATEL, M BORGHESI, R C CLARKE, R R FREEMAN, H HABARA, S P HATCHETT, D HEY, D G HICKS, S KAR, M H KEY, J A KING, K LANCASTER, D NEELY, A NIKKRO, P A NORREYS, M M NOTLEY, T W PHILLIPS, L ROMAGNANI, R A SNAVELY, R B STEPHENS, AND R P J TOWN. **Proton Radiography of a Laser-Driven Implosion.** *Physical Review Letters*, **97**(4):045001, July 2006. 9
- [57] L ROMAGNANI, J FUCHS, M BORGHESI, P ANTICI, P AUDEBERT, F CECCHERINI, T COWAN, T GRISMAYER, S KAR, A MACCHI, P MORA, G PRETZLER, A SCHIAVI, T TONCIAN, AND O WILLI. **Dynamics of Electric Fields Driving the Laser Acceleration of Multi-MeV Protons.** *Physical Review Letters*, **95**(19):195001, October 2005. 9
- [58] L ROMAGNANI, S V BULANOV, M BORGHESI, P AUDEBERT, J C GAUTHIER, K LÖWENBRÜCK, A J MACKINNON, P PATEL, G PRETZLER, T TONCIAN, AND O WILLI. **Observation of Collisionless Shocks in Laser-Plasma Experiments.** *Physical Review Letters*, **101**(2):025004, July 2008. 9
- [59] S KAR, M BORGHESI, C A CECCHETTI, L ROMAGNANI, F CECCHERINI, T V LISEYKINA, A MACCHI, R JUNG, J OSTERHOLTZ, O WILLI, L A GIZZI, A SCHIAVI, M GALIMBERTI, AND R HEATHCOTE. **Dynamics of charge-displacement channeling in intense laser–plasma interactions.** *New Journal of Physics*, **9**(11):402–402, November 2007. 9
- [60] C A CECCHETTI, M BORGHESI, J FUCHS, G SCHURTZ, S KAR, A MACCHI, L ROMAGNANI, P A WILSON, P ANTICI, R JUNG, J OSTERHOLTZ, C A PIPAHL, O WILLI, A SCHIAVI, M NOTLEY, AND D NEELY. **Magnetic field measurements in laser-produced plasmas via proton deflectometry.** *Physics of Plasmas*, **16**(4):043102, 2009. 9
- [61] WILLIAM H SWEET. **The Uses of Nuclear Disintegration in the Diagnosis and Treatment of Brain Tumor.** *New England Journal of Medicine*, **245**(23):875–878, December 1951. 10
- [62] I SPENCER, K W D LEDINGHAM, R P SINGHAL, T MCCANNY, P MCKENNA, E L CLARK, K KRUSHELNICK, M ZEPF, F N BEG, M TATARAKIS, A E DANGOR, P A NORREYS, R J CLARKE, R M ALLOTT, AND I N ROSS. **Laser generation of proton beams for the production of short-lived positron emitting radioisotopes.** *Nuclear Inst. and Methods in Physics Research B*, 2001. 11
- [63] S FRITZLER, V MALKA, G GRILLON, J P ROUSSEAU, F BURGY, E LEFEBVRE, E D’HUMIÈRES, P MCKENNA, AND K W D LEDINGHAM. **Proton beams generated with high-intensity lasers: Applications to medical isotope production.** *Applied Physics Letters*, **83**(15):3039, 2003. 11
- [64] K W D LEDINGHAM, P MCKENNA, T MCCANNY, S SHIMIZU, J M YANG, L ROBSON, J ZWEIT, J M GILLIES, J BAILEY, G N CHIMON, R J CLARKE, D NEELY, P A NORREYS, J L COLLIER, R P SINGHAL, M S WEI, S P D MANGLES, P NILSON, K KRUSHELNICK, AND M ZEPF. **High power laser production of short-lived isotopes for positron emission tomography.** *Journal of Physics D: Applied Physics*, **37**(16):2341–2345, July 2004. 11
- [65] JOSE BENLUIRE. **The Laser Laboratory for Acceleration and Applications.** *International Conference on Accelerator Optimization*, pages 1–36, October 2015. 11
- [66] PAUL GIBBON. *Short Pulse Laser Interactions with Matter. An Introduction.* Imperial College Press, January 2005. 13, 23, 24
- [67] L V KELDYSH. **Ionization in the field of a strong electromagnetic wave.** *Soviet Physics JETP*, **20**, May 1965. 14
- [68] PETER MULSER AND DIETER BAUER. *High Power Laser-Matter Interaction.* Springer Science & Business Media, July 2010. 16

BIBLIOGRAPHY

- [69] I H HUTCHINSON. *Principles of Plasma Diagnostics*. Cambridge University Press, July 2005. 16
- [70] WILLIAM L KRUER. *The Physics of Laser Plasma Interactions*. Westview Press, January 2003. 16, 25
- [71] ANDREA MACCHI. *A Superintense Laser-Plasma Interaction Theory Primer*. Springer Science & Business Media, January 2013. 16, 33, 81
- [72] J D LAWSON. **LASERS AND ACCELERATORS**. *IEEE Trans. Nucl. Sci.*, **26**:4217–4219, 1979. 18
- [73] P M WOODWARD AND J D LAWSON. **The theoretical precision with which an arbitrary radiation-pattern may be obtained from a source of finite size**. *Journal of the Institution of Electrical Engineers - Part III: Radio and Communication Engineering*, **95**(37):363–370, September 1948. 18
- [74] PREDHIMAN KAW. **Relativistic Nonlinear Propagation of Laser Beams in Cold Overdense Plasmas**. *Physics of Fluids*, **13**(2):472, 1970. 26, 116
- [75] A I AKHIEZER, I A AKHIEZER, AND R V POLOVIN. *Non-Linear Theory and Fluctuations*. Plasma Electrodynamics. Elsevier, October 2013. 26, 116
- [76] S GUERIN, P MORA, J ADAM, A HERON, AND G LAVAL. **Propagation of ultraintense laser pulses through overdense plasma layers**. *Physics of Plasmas*, **3**(7):1–10, January 1996. 26
- [77] V A VSHIVKOV, N M NAUMOVA, F PEGORARO, AND S V BULANOV. **Nonlinear electrodynamics of the interaction of ultra-intense laser pulses with a thin foil**. *Physics of Plasmas*, **5**, July 1998. 27, 116
- [78] C A J PALMER, J SCHREIBER, S R NAGEL, N P DOVER, C BELLEI, F N BEG, S BOTT, R J CLARKE, A E DANGOR, S M HASSAN, P HILZ, D JUNG, S KNEIP, S P D MANGLES, K L LANCASTER, A REHMAN, A P L ROBINSON, C SPINDLOE, J SZERYPO, M TATARAKIS, M YEUNG, M ZEPF, AND Z NAIMUDIN. **Rayleigh-Taylor Instability of an Ultrathin Foil Accelerated by the Radiation Pressure of an Intense Laser**. *Physical Review Letters*, **108**(22):225002, May 2012. 29, 96, 127
- [79] G A RUEV, A V FEDOROV, AND V M FOMIN. **Development of the Richtmeyer-Meshkov instability during interaction of the mixing diffusion layer of two gases with transmitted and reflected shock waves**. *Doklady Physics*, **54**(8):381–383, August 2009. 29
- [80] R BANERJEE, L MANDAL, M KHAN, AND M R GUPTA. **Bubble and spike growth rate of Rayleigh Taylor and Richtmeyer Meshkov instability in finite layers**. *Indian Journal of Physics*, **87**(9):929–937, May 2013. 29, 96
- [81] O BUNEMAN. **Dissipation of Currents in Ionized Media**. *Phys. Rev.*, **115**:503–517, 1959. 29
- [82] L YIN, B J ALBRIGHT, B M HEGELICH, AND J C FERNÁNDEZ. **GeV laser ion acceleration from ultrathin targets: The laser break-out afterburner**. *Laser and Particle Beams*, **24**(2):291, 2006. 29, 40, 78, 109, 129
- [83] D V KOVALEV, A P SMIRNOV, AND YA S DIMANT. **Study of kinetic effects arising in simulations of Farley-Buneman instability**. *Plasma Physics Reports*, **35**(5):420–425, May 2009. 29
- [84] FRANCIS F CHEN. **Introduction to Plasma Physics and Controlled Fusion**, 1985. 30
- [85] C PEREGO, D BATANI, A ZANI, AND M PASSONI. **Target normal sheath acceleration analytical modeling, comparative study and developments**. *Review of Scientific Instruments*, **83**(2):02B502, 2012. 31
- [86] P MORA. **Plasma Expansion into a Vacuum**. *Physical Review Letters*, **90**(18):185002, May 2003. 31, 33, 155
- [87] J SCHREIBER, F BELL, F GRÜNER, U SCHRAMM, M GEISLER, M SCHNÜRER, S TER-AVETISYAN, B HEGELICH, J COBBLE, E BRAMBRINK, J FUCHS, P AUDEBERT, AND D HABS. **Analytical Model for Ion Acceleration by High-Intensity Laser Pulses**. *Physical Review Letters*, **97**(4):045005, July 2006. 31, 33
- [88] S C WILKS, W L KRUER, M TABAK, AND A B LANGDON. **Absorption of ultra-intense laser pulses**. *Physical Review Letters*, **69**:1383–1386, 1992. 31, 156
- [89] H SCHWOERER, S PFOTENHAUER, O JÄCKEL, K U AMTHOR, B LIESFELD, W ZIEGLER, R SAUERBREY, K W D LEDINGHAM, AND T ESIRKEPOV. **Laser-plasma acceleration of quasi-monoenergetic protons from microstructured targets**. *Nature*, **439**(7075):445–448, January 2006. 31, 93, 171
- [90] T E COWAN, J FUCHS, H RUHL, Y SENTOKU, A KEMP, P AUDEBERT, M ROTH, R STEPHENS, I BARTON, A BLAŽEVIĆ, E BRAMBRINK, J COBBLE, J C FERNÁNDEZ, J C GAUTHIER, M GEISSEL, M HEGELICH, J KAAE, S KARSCH, G P LE SAGE, S LETZRING, M MANCLOSSI, S MEYRONEINC, A NEWKIRK, H PÉPIN, AND N RENARD-LEGALLOUDEC. **Ultra-low emittance, high current proton beams produced with a laser-virtual cathode sheath accelerator**. *Nuclear Instruments and Methods in Physics Research Section A: Accelerators, Spectrometers, Detectors and Associated Equipment*, **544**(1-2):277–284, May 2005. 33, 100
- [91] L ROBSON, P T SIMPSON, R J CLARKE, K W D LEDINGHAM, F LINDAU, O LUNDH, T MCCANNY, P MORA, D NEELY, C G WAHLSTRÖM, M ZEPF, AND P MCKENNA. **Scaling of proton acceleration driven by petawatt-laser-plasma interactions**. *Nature Physics*, **3**(1):58–62, December 2006. 33, 77, 121, 161
- [92] H HABARA, K LANCASTER, S KARSCH, C MURPHY, P NORREYS, R EVANS, M BORGHESE, L ROMAGNANI, M ZEPF, T NORIMATSU, Y TOYAMA, R KODAMA, J KING, R SNAVELY, K AKLI, B ZHANG, R FREEMAN, S HATCHETT, A MACKINNON, P PATEL, M KEY, C STOECKL, R STEPHENS, R FONSECA, AND L SILVA. **Ion acceleration from the shock front induced by hole boring in ultraintense laser-plasma interactions**. *Physical Review E*, **70**(4):046414, October 2004. 33, 34, 121, 172
- [93] ANDREA MACCHI, SILVIA VEGHINI, AND FRANCESCO PEGORARO. **“Light Sail” Acceleration Reexamined**. *Physical Review Letters*, **103**(8):085003, August 2009. 34, 160, 172

- [94] A SGATTONI, S SINIGARDI, AND A MACCHI. **High energy gain in three-dimensional simulations of light sail acceleration.** *Applied Physics Letters*, **105**(8):084105, August 2014. 34
- [95] A P L ROBINSON, P GIBBON, M ZEPF, S KAR, R G EVANS, AND C BELLEI. **Relativistically correct hole-boring and ion acceleration by circularly polarized laser pulses.** *Plasma Physics and Controlled Fusion*, **51**(2):024004, January 2009. 36, 142
- [96] A P L ROBINSON, M ZEPF, S KAR, R G EVANS, AND C BELLEI. **Radiation Pressure Acceleration of Thin Foils with Circularly Polarized Laser Pulses.** *New Journal of Physics*, August 2008. 39, 78
- [97] T ESIRKEPOV, M BORGHESE, S BULANOV, G MOUROU, AND T TAJIMA. **Highly Efficient Relativistic-Ion Generation in the Laser-Piston Regime.** *Physical Review Letters*, **92**(17):175003, April 2004. 40, 78, 84, 88, 159
- [98] L YIN, B J ALBRIGHT, D JUNG, R C SHAH, S PALANIYAPPAN, K J BOWERS, A HENIG, J C FERNÁNDEZ, AND B M HEGELICH. **Break-out afterburner ion acceleration in the longer laser pulse length regime.** *Physics of Plasmas*, **18**(6):063103, 2011. 40, 74, 78, 105, 119, 138
- [99] B J ALBRIGHT, L YIN, KEVIN J BOWERS, B M HEGELICH, K A FLIPPO, T J T KWAN, AND J C FERNÁNDEZ. **Relativistic Buneman instability in the laser breakout afterburner.** *Physics of Plasmas*, **14**(9):094502, 2007. 40, 129, 135
- [100] J E MURRAY AND W H LOWDERMILK. **Nd: YAG regenerative amplifier.** *Journal of Applied Physics*, 1980. 46
- [101] W H LOWDERMILK AND J E MURRAY. **The multipass amplifier: Theory and numerical analysis.** *Journal of Applied Physics*, 1980. 46
- [102] D F HOTZ. **Gain Narrowing in a Laser Amplifier.** *Applied Optics*, **4**:1–1, September 1965. 47
- [103] A DUBIETIS, G JONUSAUSKAS, AND A PISKARSKAS. **Powerful femtosecond pulse generation by chirped and stretched pulse parametric amplification in BBO crystal.** *Optics Communications*, **88**:1–4, October 1991. 47
- [104] TIMUR ZH ESIRKEPOV, JAMES K KOGA, ATSUSHI SUNAHARA, TOSHIMASA MORITA, MASAHARU NISHIKINO, KEI KAGEYAMA, HIDEO NAGATOMO, KATSUNOBU NISHIHARA, AKITO SAGISAKA, HIDEYUKI KOTAKI, TATSUFUMI NAKAMURA, YUJI FUKUDA, HAJIME OKADA, ALEXANDER S PIROZHKOV, AKIFUMI YOGO, MAMIKO NISHIUCHI, HIROMITSU KIRIYAMA, KIMINORI KONDO, MASAKI KANDO, AND SERGEI V BULANOV. **Nuclear Instruments and Methods in Physics Research A.** *Nuclear Inst. and Methods in Physics Research, A*, **745**(C):150–163, May 2014. 52
- [105] V YANOVSKY, M D PERRY, C G BROWN, M D FEIT, AND A M RUBENCHICK. **Plasma Mirrors for Short Pulse Lasers.** Technical report, September 1997. 53
- [106] C THAURY, F QUÉRÉ, J P GEINDRE, A LÉVY, T CECCOTTI, P MONOT, M BOUGEARD, F RÉAU, P D’OLIVEIRA, P AUDEBERT, R MARJORIBANKS, AND PH MARTIN. **Plasma mirrors for ultrahigh-intensity optics.** *Nature Physics*, **3**(6):424–429, April 2007. 53, 164
- [107] C RÖDEL, M HEYER, M BEHMEKE, M KÜBEL, O JÄCKEL, W ZIEGLER, D EHRT, M C KALUZA, AND G G PAULUS. **High repetition rate plasma mirror for temporal contrast enhancement of terawatt femtosecond laser pulses by three orders of magnitude.** *Applied Physics B*, **103**(2):295–302, November 2010. 53
- [108] MJV STREETER, P S FOSTER, AND F H CAMERON. **Astra gemini compact plasma mirror system.** *Central Laser Facility . . .*, 2009. 53
- [109] YONGZHI WANG, JINGUI MA, JING WANG, PENG YUAN, GUO-QIANG XIE, XU-LEI GE, FENG LIU, XIAOHUI YUAN, HEYUAN ZHU, AND LIEJIA QIAN. **Single-shot measurement of ≥ 1010 pulse contrast for ultra-high peak-power lasers.** *Scientific Reports*, **4**, January 2014. 53
- [110] CHRIS HOOKER, YUNXIN TANG, OLEG CHEKHLOV, JOHN COLLIER, EDWIN DIVALL, KLAUS ERTEL, STEVE HAWKES, BRYN PARRY, AND P P RAJEEV. **Improving coherent contrast of petawatt laser pulses.** pages 1–11, January 2011. 54
- [111] Y J GU, Z ZHU, X F LI, Q YU, S HUANG, F ZHANG, Q KONG, AND S KAWATA. **Stable long range proton acceleration driven by intense laser pulse with underdense plasmas.** *Physics of Plasmas*, **21**(6):063104, June 2014. 54
- [112] A LIFSCHITZ, F SYLLA, S KAHALY, A FLACCO, M VELTICHEVA, G SANCHEZ-ARRIAGA, E LEFEBVRE, AND V MALKA. **Ion acceleration in underdense plasmas by ultra-short laser pulses.** *New Journal of Physics*, pages 1–11, March 2014. 54
- [113] M TAYYAB, S BAGCHI, B RAMAKRISHNA, T MANDAL, A UPADHYAY, R RAMIS, J A CHAKERA, P A NAIK, AND P D GUPTA. **Role of target material in proton acceleration from thin foils irradiated by ultrashort laser pulses.** *Physical Review E*, **90**(2):023103, August 2014. 55
- [114] T M IVKOVA, V K LIECHTENSTEIN, AND E D OLSHANSKI. **Preparation and application of ultra-thin superstrong diamond-like carbon targets for laboratory and space experiments.** *Nuclear Inst. and Methods in Physics Research, A*, **362**:77–80, March 1995. 55
- [115] D JUNG, R HÖRLEIN, D KIEFER, S LETZRING, D C GAUTIER, U SCHRAMM, C HÜBSCH, R ÖHM, B J ALBRIGHT, J C FERNÁNDEZ, D HABS, AND B M HEGELICH. **Development of a high resolution and high dispersion Thomson parabola.** *Review of Scientific Instruments*, **82**(1):013306, 2011. 56, 167, 174
- [116] D C CARROLL, P BRUMMITT, D NEELY, FILIP LINDAU, OLLE LUNDH, C G WAHLSTRÖM, AND P MCKENNA. **A modified Thomson parabola spectrometer for high resolution multi-MeV ion measurements—Application to laser-driven ion acceleration.** *Nuclear Inst. and Methods in Physics Research, A*, **620**(1):23–27, August 2010. 58, 166, 167
- [117] KAZUO A TANAKA, TOSHINORI YABUCHI, TAKASHI SATO, RYOSUKE KODAMA, YONEYOSHI KITAGAWA, TERUYOSHI TAKAHASHI, TOSHIKI IKEDA, YOSHIHIDE HONDA, AND SHUICHI OKUDA. **Calibration of imaging plate for high energy electron spectrometer.** *Review of Scientific Instruments*, **76**(1):013507, 2005. 61, 167

BIBLIOGRAPHY

- [118] B HIDDING, G PRETZLER, M CLEVER, F BRANDL, F ZAMPONI, A LÜBCKE, T KÄMPFER, I USCHMANN, E FÖRSTER, U SCHRAMM, R SAUERBREY, E KROUPP, L VEISZ, K SCHMID, S BENAVIDES, AND S KÄRSCH. **Novel method for characterizing relativistic electron beams in a harsh laser-plasma environment.** *Review of Scientific Instruments*, **78**(8):083301, 2007. 61
- [119] A MANCIC, J FUCHS, P ANTICI, S A GAILLARD, AND P AUDEBERT. **Absolute calibration of photostimulable image plate detectors used as (0.5–20MeV) high-energy proton detectors.** *Review of Scientific Instruments*, **79**(7):073301–073301–6, 2008. 61, 167
- [120] C G FREEMAN, G FIKSEL, C STOECKL, N SINENIAN, M J CANFIELD, G B GRAEPER, A T LOMBARDO, C R STILLMAN, S J PADALINO, C MILEHAM, T C SANGSTER, AND J A FRENJE. **Calibration of a Thomson parabola ion spectrometer and Fujifilm imaging plate detectors for protons, deuterons, and alpha particles.** *Review of Scientific Instruments*, **82**(7):073301, 2011. 61
- [121] HAMAMATSU. **MCP & MCP ASSEMBLY.** pages 1–16, May 2009. 62
- [122] P WANABONGSE, B SOLA, J JAMSANGTONG, AND S RATANABUSSAYAPORN. **Calibration of CR-39 solid state nuclear track detector.** *Indian Journal of Physics*, **83**(6):833–837, 2009. 63
- [123] D S HEY, M H KEY, A J MACKINNON, A G MACPHEE, P K PATEL, R R FREEMAN, L D VAN WOERKOM, AND C M CASTANEDA. **Use of GafChromic film to diagnose laser generated proton beams.** *Review of Scientific Instruments*, **79**(5):053501, 2008. 64
- [124] J ZIEGLER. www.srim.org [online]. 65
- [125] RICARDO A FONSECA, LUIS O SILVA, FRANK S TSUNG, VIKTOR K DECYK, WEI LU, CHUANG REN, WARREN B MORI, S DENG, S LEE, AND T KATSIOULEAS. **OSIRIS: A three-dimensional, fully relativistic particle in cell code for modeling plasma based accelerators.** pages 342–351, 2002. 67, 80
- [126] TSUNEHIKO N KATO. **Energy Loss of High-Energy Particles in Particle-in-Cell Simulation.** *arXiv.org, physics.comp-ph*, 2013. 68
- [127] C K BIRDSALL AND A B LANGDON. *Plasma Physics via Computer Simulation.* CRC Press, October 2004. 70
- [128] S C WILKS, A B LANGDON, T E COWAN, M ROTH, M SINGH, S HATCHETT, M H KEY, D PENNINGTON, A MACKINNON, AND R A SNAVELY. **Energetic proton generation in ultra-intense laser–solid interactions.** *Physics of Plasmas*, **8**(2):542, 2001. 77
- [129] A MACCHI AND C BENEDETTI. **Ion acceleration by radiation pressure in thin and thick targets.** *Nuclear Instruments and Methods in Physics . . .*, 2010. 77
- [130] CHARLOTTE A J PALMER, N P DOVER, I POGORELSKY, M BABZIEN, G I DUDNIKOVA, M ISPIRIYAN, M N POLYANSKIY, J SCHREIBER, P SHKOLNIKOV, V YAKIMENKO, AND Z NAJMUDIN. **Monoenergetic Proton Beams Accelerated by a Radiation Pressure Driven Shock.** *Physical Review Letters*, **106**(1):014801, January 2011. 78
- [131] P MCKENNA, F LINDAU, O LUNDH, D NEELY, A PERSSON, AND C G WAHLSTRÖM. **High-intensity laser-driven proton acceleration: influence of pulse contrast.** *Philosophical Transactions of the Royal Society A: Mathematical, Physical and Engineering Sciences*, **364**(1840):2945–2948, March 2006. 78, 166
- [132] A HENIG, S STEINKE, M SCHNÜRER, T SOKOLLIK, R HÖRLEIN, D KIEFER, D JUNG, J SCHREIBER, B M HEGELICH, X Q YAN, J MEYER-TER VEHN, T TAJIMA, P V NICKLES, W SANDNER, AND D HABS. **Radiation-Pressure Acceleration of Ion Beams Driven by Circularly Polarized Laser Pulses.** *Physical Review Letters*, **103**(24):245003, December 2009. 78, 80, 121, 162, 172
- [133] T ESIRKEPOV, M YAMAGIWA, AND T TAJIMA. **Laser Ion-Acceleration Scaling Laws Seen in Multiparametric Particle-in-Cell Simulations.** *Physical Review Letters*, **96**(10):105001, March 2006. 79
- [134] R HÖRLEIN, B DROMEY, D ADAMS, Y NOMURA, S KAR, K MARKEY, P FOSTER, D NEELY, F KRAUSZ, G D TSAKIRIS, AND M ZEPF. **High contrast plasma mirror: spatial filtering and second harmonic generation at 10 19Wcm².** *New Journal of Physics*, **10**(8):083002, August 2008. 79, 166
- [135] ANDREA MACCHI, FEDERICA CATTANI, TATIANA V LISEYKINA, AND FULVIO CORNOLTI. **Laser Acceleration of Ion Bunches at the Front Surface of Overdense Plasmas.** *Physical Review Letters*, **94**(16):165003, April 2005. 79, 160
- [136] LUCA C STOCKHAUSEN, RICARDO TORRES, AND ENRIQUE CONEJERO JARQUE. **Simulations of radiation pressure ion acceleration with the VEGA Petawatt laser.** *Nuclear Inst. and Methods in Physics Research, A*, November 2015. 80
- [137] LUCA C STOCKHAUSEN, RICARDO TORRES, AND ENRIQUE CONEJERO JARQUE. **Simulations of ion acceleration from ultrathin targets with the VEGA petawatt laser.** In KENNETH W D LEDINGHAM, KLAUS SPOHR, PAUL MCKENNA, PAUL R BOLTON, ERIC ESAREY, CARL B SCHROEDER, AND FLORIAN J GRÜNER, editors, *SPIE Optics + Optoelectronics*, page 95141D. SPIE, May 2015. 80
- [138] ANDREA MACCHI. **Theory of light sail acceleration by intense lasers: an overview.** *High Power Laser Science and Engineering*, **2**:e10, April 2014. 84
- [139] V I BEREZHIANI AND N L SHATASHVILI. **On the “vacuum heating” of plasma in the field of circularly polarized laser beam.** *Europhysics Letters (EPL)*, **76**(1):70–73, January 2007. 86
- [140] ANDREA MACCHI, SILVIA VEGHINI, TATYANA V LISEYKINA, AND FRANCESCO PEGORARO. **Radiation pressure acceleration of ultrathin foils.** *New Journal of Physics*, **12**(4):045013, April 2010. 88
- [141] DINO A JAROSZYNSKI, R BINGHAM, AND R A CAIRNS. *Laser-Plasma Interactions.* Taylor & Francis, 2009. 88
- [142] E G GAMALY. **Instability of the overdense plasma boundary induced by the action of a powerful photon beam.** *Physical Review E*, **48**:1–2, October 1993. 96

- [143] F PEGORARO AND S V BULANOV. **Photon Bubbles and Ion Acceleration in a Plasma Dominated by the Radiation Pressure of an Electromagnetic Pulse.** *Physical Review Letters*, **99**(6):065002, August 2007. 96
- [144] A SGATTONI, S SINGARDI, L FEDELI, F PEGORARO, AND A MACCHI. **Laser-driven Rayleigh-Taylor instability: Plasmonic effects and three-dimensional structures.** *Physical Review E*, **91**(1):013106, January 2015. 96
- [145] D WU, C Y ZHENG, B QIAO, C T ZHOU, X Q YAN, M Y YU, AND X T HE. **Suppression of transverse ablative Rayleigh-Taylor-like instability in the hole-boring radiation pressure acceleration by using elliptically polarized laser pulses.** *Physical Review E*, **90**(2):023101, August 2014. 104
- [146] P A NORREYS, M SANTALA, E CLARK, M ZEPF, I WATTS, F N BEG, K KRUSHELNICK, M TATARAKIS, A E DANGOR, X FANG, P GRAHAM, T MCCANNY, R P SINGHAL, K W D LEDINGHAM, A CRESWELL, D C W SANDERSON, J MAGILL, A MACHACEK, J S WARK, R ALLOTT, B KENNEDY, AND D NEELY. **Observation of a highly directional g-ray beam from ultrashort, ultraintense laser pulse interactions with solids.** 1999. 105
- [147] ANTOINE ROUSSE, KIM TA PHUOC, RAHUL SHAH, ALEXANDER PUKHOV, ERIC LEFEBVRE, VICTOR MALKA, SERGEY KISELEV, FRÉDÉRIC BURGY, JEAN-PHILIPPE ROUSSEAU, DONALD UMSTADTER, AND DANIELE HULIN. **Production of a keV X-Ray Beam from Synchrotron Radiation in Relativistic Laser-Plasma Interaction.** *Physical Review Letters*, **93**(13):135005, September 2004. 105
- [148] S KNEIP, C MCGUFFEY, J L MARTINS, S F MARTINS, C BELLEI, V CHVYKOV, F DOLLAR, R FONSECA, C HUNTINGTON, G KALINTCHENKO, A MAKSIMCHUK, S P D MANGLES, T MATSUOKA, S R NAGEL, C A J PALMER, J SCHREIBER, K TA PHUOC, A G R THOMAS, V YANOVSKY, L O SILVA, K KRUSHELNICK, AND Z NAJMUDIN. **Bright spatially coherent synchrotron X-rays from a table-top source.** *Nature Physics*, **6**(12):980–983, October 2010. 105
- [149] SILVIA CIPICCIA, MOHAMMAD R ISLAM, BERNHARD ERSFELD, RICHARD P SHANKS, ENRICO BRUNETTI, GREGORY VIEUX, XUE YANG, RIJU C ISSAC, SAMUEL M WIGGINS, GREGOR H WELSH, MARIA-PIA ANANIA, DZMITRY MANEUSKI, RACHEL MONTGOMERY, GARY SMITH, MATTHIAS HOEK, DAVID J HAMILTON, NUNO R C LEMOS, DAN SYMES, PATTATHIL P RAJEEV, VAL O SHEA, JOÃO M DIAS, AND DINO A JAROSZYNSKI. **Gamma-rays from harmonically resonant betatron oscillations in a plasma wake.** *Nature Physics*, **7**(11):867–871, September 2011. 105
- [150] B DROMEY, S RYKOVANOV, M YEUNG, R HÖRLEIN, D JUNG, D C GAUTIER, T DZELZAINIS, D KIEFER, S PALANIYAPPAN, R SHAH, J SCHREIBER, H RUHL, J C FERNÁNDEZ, C L S LEWIS, M ZEPF, AND B M HEGELICH. **Coherent synchrotron emission from electron nanobunches formed in relativistic laser-plasma interactions.** *Nature Physics*, **8**(11):804–808, October 2012. 105
- [151] A R BELL AND JOHN G KIRK. **Possibility of Prolific Pair Production with High-Power Lasers.** *Physical Review Letters*, **101**(20):200403, November 2008. 105
- [152] A R BELL AND R J KINGHAM. **Resistive Collimation of Electron Beams in Laser-Produced Plasmas.** *Physical Review Letters*, **91**(3):035003, July 2003. 105
- [153] R J GRAY, D A MACLELLAN, B GONZALEZ-IZQUIERDO, H W POWELL, D C CARROLL, C D MURPHY, L C STOCKHAUSEN, D R RUSBY, G G SCOTT, R WILSON, N BOOTH, D R SYMES, S J HAWKES, R TORRES, M BORGHESI, D NEELY, AND P MCKENNA. **Azimuthal asymmetry in collective electron dynamics in relativistically transparent laser-foil interactions.** *New Journal of Physics*, pages 1–12, September 2014. 105, 129
- [154] C S BRADY AND T D ARBER. **An ion acceleration mechanism in laser illuminated targets with internal electron density structure.** *Plasma Physics and Controlled Fusion*, **53**(1):015001, November 2010. 105, 128
- [155] W L KRUEER AND K ESTABROOK. **J B heating by very intense laser light.** *Physics of Fluids (1958-1988)*, 1985. 109
- [156] AAKASH A SAHAI, FRANK S TSUNG, ADAM R TABLEMAN, WARREN B MORI, AND THOMAS C KATSIOULEAS. **Relativistically induced transparency acceleration of light ions by an ultrashort laser pulse interacting with a heavy-ion-plasma density gradient.** *Physical Review E*, **88**(4):043105, February 2014. 109
- [157] S KAR, K F KAKOLEE, B QIAO, A MACCHI, M CERCHEZ, D DORIA, M GEISSLER, P MCKENNA, D NEELY, J OSTERHOLZ, R PRASAD, K QUINN, B RAMAKRISHNA, G SARRI, O WILLI, X Y YUAN, M ZEPF, AND M BORGHESI. **Ion Acceleration in Multispecies Targets Driven by Intense Laser Radiation Pressure.** *Physical Review Letters*, **109**(18):185006, November 2012. 109
- [158] D JUNG, B J ALBRIGHT, L YIN, D C GAUTIER, R SHAH, S PALANIYAPPAN, S LETZRING, B DROMEY, H C WU, T SHIMADA, R P JOHNSON, M ROTH, J C FERNÁNDEZ, D HABS, AND B M HEGELICH. **Beam profiles of proton and carbon ions in the relativistic transparency regime.** *New Journal of Physics*, **15**(12):123035, December 2013. 109, 113, 127, 129
- [159] B M HEGELICH, I POMERANTZ, L YIN, H C WU, D JUNG, B J ALBRIGHT, D C GAUTIER, S LETZRING, S PALANIYAPPAN, R SHAH, K ALLINGER, R HÖRLEIN, J SCHREIBER, D HABS, J BLAKENEY, G DYER, L FULLER, E GAUL, E MCCARY, A R MEADOWS, C WANG, T DITMIRE, AND J C FERNÁNDEZ. **Laser-driven ion acceleration from relativistically transparent nanotargets.** *New Journal of Physics*, **15**(8):085015, August 2013. 109, 113
- [160] S P D MANGLES, A G R THOMAS, M C KALUZA, O LUNDH, F LINDAU, A PERSSON, F S TSUNG, Z NAJMUDIN, W B MORI, C G WAHLSTRÖM, AND K KRUSHELNICK. **Laser-Wakefield Acceleration of Monoenergetic Electron Beams in the First Plasma-Wave Period.** *Physical Review Letters*, **96**(21):215001, May 2006. 112
- [161] F CATTANI, A KIM, D ANDERSON, AND M LISAK. **Threshold of induced transparency in the relativistic interaction of an electromagnetic wave with overdense plasmas.** *Physical Review E*, **62**:1–4, June 2000. 116
- [162] M KALUZA, J SCHREIBER, M I K SANTALA, G D TSAKIRIS, K EIDMANN, J MEYER-TER VEHN, AND K J WITTE. **Influence of the Laser Prepulse on Proton Acceleration in Thin-Foil Experiments.** *Physical Review Letters*, **93**(4):045003, July 2004. 121, 136, 157, 162, 165

BIBLIOGRAPHY

- [163] A YOGO, H DAIDO, S V BULANOV, K NEMOTO, Y OISHI, T NAYUKI, T FUJII, K OGURA, S ORIMO, A SAGISAKA, J L MA, T ZH ESIRKEPOV, M MORI, M NISHIUCHI, A S PIROZHKO, S NAKAMURA, A NODA, H NAGATOMO, T KIMURA, AND T TAJIMA. **Laser ion acceleration via control of the near-critical density target.** *Physical Review E*, **77**(1):016401, January 2008. 121, 162
- [164] Y OISHI, T NAYUKI, T FUJII, Y TAKIZAWA, X WANG, T YAMAZAKI, K NEMOTO, T KAYOJI, T SEKIYA, K HORIOKA, Y OKANO, Y HIRONAKA, K G NAKAMURA, K KONDO, AND A A ANDREEV. **Dependence on laser intensity and pulse duration in proton acceleration by irradiation of ultrashort laser pulses on a Cu foil target.** *Physics of Plasmas*, **12**(7):073102, 2005. 121, 161
- [165] F L ZHENG, S Z WU, H ZHANG, T W HUANG, M Y YU, C T ZHOU, AND X T HE. **Preplasma effects on the generation of high-energy protons in ultraintense laser interaction with foil targets.** *Physics of Plasmas*, **20**(12):123105, 2013. 121
- [166] A ROBINSON, M SHERLOCK, AND P NORREYS. **Artificial Collimation of Fast-Electron Beams with Two Laser Pulses.** *Physical Review Letters*, **100**(2):025002, January 2008. 121, 137, 172
- [167] K MARKEY, P MCKENNA, C M BRENNER, D C CARROLL, M M GÜNTHER, K HARRIS, S KAR, K LANCASTER, F NÜRNBERG, M N QUINN, A P L ROBINSON, M ROTH, M ZEPF, AND D NEELY. **Spectral Enhancement in the Double Pulse Regime of Laser Proton Acceleration.** *Physical Review Letters*, **105**(19):195008, November 2010. 121, 131, 137, 173
- [168] ZS LECZ AND A ANDREEV. **Shock wave acceleration of protons in inhomogeneous plasma interacting with ultrashort intense laser pulses.** *Physics of Plasmas*, **22**(4):043103, April 2015. 121
- [169] H W POWELL, M KING, R J GRAY, D A MACLELLAN, B GONZALEZ-IZQUIERDO, L C STOCKHAUSEN, G HICKS, N P DOVER, D R RUSBY, D C CARROLL, H PADDA, R TORRES, S KAR, R J CLARKE, I O MUSGRAVE, Z NAJMUDIN, M BORGHESI, D NEELY, AND P MCKENNA. **Proton acceleration enhanced by a plasma jet in expanding foils undergoing relativistic transparency.** *New Journal of Physics*, **17**(10):1–10, October 2015. 122
- [170] CH ZIENER, P S FOSTER, E J DIVALL, C J HOOKER, M H R HUTCHINSON, A J LANGLEY, AND D NEELY. **Specular reflectivity of plasma mirrors as a function of intensity, pulse duration, and angle of incidence.** *Journal of Applied Physics*, **93**(1):768, 2003. 123
- [171] D GWYNNE, S KAR, D DORIA, H AHMED, M CERCHEZ, J FERNÁNDEZ, R J GRAY, J S GREEN, F HANTON, D A MACLELLAN, P MCKENNA, Z NAJMUDIN, D NEELY, J A RUIZ, A SCHIAVI, M STREETER, M SWANTUSCH, O WILLI, M ZEPF, AND M BORGHESI. **Modified Thomson spectrometer design for high energy, multi-species ion sources.** *Review of Scientific Instruments*, **85**(3):033304, March 2014. 126
- [172] A ALEJO, S KAR, H AHMED, A G KRYGIER, D DORIA, R CLARKE, J FERNÁNDEZ, R R FREEMAN, J FUCHS, A GREEN, J S GREEN, D JUNG, A KLEINSCHMIDT, C L S LEWIS, J T MORRISON, Z NAJMUDIN, H NAKAMURA, G NERSISYAN, P NORREYS, M NOTLEY, M OLIVER, M ROTH, J A RUIZ, L VASSURA, M ZEPF, AND M BORGHESI. **Characterisation of deuterium spectra from laser driven multi-species sources by employing differentially filtered image plate detectors in Thomson spectrometers.** *Review of Scientific Instruments*, **85**(9):093303, September 2014. 126
- [173] R SANGINÉS AND H SOBRAL. **Two-color interferometry and shadowgraphy characterization of an orthogonal double-pulse laser ablation.** *Journal of Applied Physics*, **110**(3):033301, 2011. 126
- [174] ALEXANDER BUCK, MARIA NICOLAI, KARL SCHMID, CHRIS M S SEARS, ALEXANDER SÁVERT, JULIA M MIKHAILOVA, FERENC KRAUSZ, MALTE C KALUZA, AND LASZLO VEISZ. **Real-time observation of laser-driven electron acceleration.** *Nature Physics*, **7**(7):543–548, March 2011. 126
- [175] S KAR, M BORGHESI, S V BULANOV, M H KEY, T V LISEYKINA, A MACCHI, A J MACKINNON, P K PATEL, L ROMAGNANI, A SCHIAVI, AND O WILLI. **Plasma Jets Driven by Ultraintense-Laser Interaction with Thin Foils.** *Physical Review Letters*, **100**(22):225004, June 2008. 126, 166
- [176] N P DOVER, M J V STREETER, C A J PALMER, H AHMED, B ALBERTAZZI, M BORGHESI, D C CARROLL, J FUCHS, R HEATHCOTE, P HILZ, K F KAKOLEE, S KAR, R KODAMA, A KON, D A MACLELLAN, P MCKENNA, S R NAGEL, M NAKATSUTSUMI, D NEELY, M M NOTLEY, R PRASAD, G SCOTT, M TAMPO, M ZEPF, J SCHREIBER, AND Z NAJMUDIN. **Buffered spectrally-peaked proton beams in the relativistic-transparency regime.** *arXiv.org*, June 2014. 127, 131
- [177] S V BULANOV, D V DYLOV, T ESIRKEPOV, F F KAMENETS, AND I V SOKOLOV. **Ion Acceleration in a Dipole Vortex in a Laser Plasma Corona.** *Particle Acceleration in Plasma*, **31**:1–14, May 2005. 131
- [178] TATSUFUMI NAKAMURA, SERGEI V BULANOV, TIMUR ZH ESIRKEPOV, AND MASAKI KANDO. **High-Energy Ions from Near-Critical Density Plasmas via Magnetic Vortex Acceleration.** *Physical Review Letters*, **105**(13):135002, September 2010. 132
- [179] R J GRAY, D C CARROLL, X H YUAN, C M BRENNER, M BURZA, M COURY, K L LANCASTER, X X LIN, Y T LI, D NEELY, M N QUINN, O TRESCA, C G WAHLSTRÖM, AND P MCKENNA. **Laser pulse propagation and enhanced energy coupling to fast electrons in dense plasma gradients.** *New Journal of Physics*, **16**(11):1–13, November 2014. 136
- [180] S KAR, K F KAKOLEE, M CERCHEZ, D DORIA, A MACCHI, P MCKENNA, D NEELY, J OSTERHOLZ, K QUINN, B RAMAKRISHNA, G SARRI, O WILLI, X H YUAN, M ZEPF, AND M BORGHESI. **Experimental investigation of hole boring and light sail regimes of RPA by varying laser and target parameters.** *Plasma Physics and Controlled Fusion*, **55**(12):124030, November 2013. 137
- [181] T SCHLEGEL, N NAUMOVA, V T TIKHONCHUK, C LABAUNE, I V SOKOLOV, AND G MOUROU. **Relativistic laser piston model: Ponderomotive ion acceleration in dense plasmas using ultraintense laser pulses.** *Physics of Plasmas*, **16**(8):083103, 2009. 142

- [182] M CARRIÉ, E LEFEBVRE, A FLACCO, AND V MALKA. **Influence of subpicosecond laser pulse duration on proton acceleration.** *Physics of Plasmas*, **16**(5):053105, 2009. 156
- [183] M G HAINES, M S WEI, F N BEG, AND R B STEPHENS. **Hot-Electron Temperature and Laser-Light Absorption in Fast Ignition.** *Physical Review Letters*, **102**(4):045008, January 2009. 156
- [184] TSUYOSHI TANIMOTO, H HABARA, R KODAMA, M NAKATSUTSUMI, KAZUO A TANAKA, K L LANCASTER, J S GREEN, R H H SCOTT, M SHERLOCK, PETER A NORREYS, R G EVANS, M G HAINES, S KAR, M ZEPF, J KING, T MA, M S WEI, T YABUCHI, F N BEG, M H KEY, P NILSON, R B STEPHENS, H AZECHI, K NAGAI, T NORIMATSU, K TAKEDA, J VALENTE, AND J R DAVIES. **Measurements of fast electron scaling generated by petawatt laser systems.** *Physics of Plasmas*, **16**(6):062703, 2009. 156
- [185] ERIK LEFEBVRE, LAURENT GREMILLET, ANNA LEVY, RACHEL NUTER, PATRIZIO ANTICI, MICHAËL CARRIÉ, TIBERIO CECOTTI, MATHIEU DROUIN, JULIEN FUCHS, VICTOR MALKA, AND DAVID NEELY. **Proton acceleration by moderately relativistic laser pulses interacting with solid density targets.** *New Journal of Physics*, **12**(4):045017, April 2010. 156
- [186] F N BEG, A R BELL, A E DANGOR, AND C N DANSON. **A study of picosecond laser–solid interactions up to 1019 W cm².** *Physics of Plasmas*, 1997. 156
- [187] V MALKA AND J L MIQUEL. **Experimental Confirmation of Ponderomotive-Force Electrons Produced by an Ultrarelativistic Laser Pulse on a Solid Target.** *Physical Review Letters*, **77**(1):1–4, July 1996. 156
- [188] T FEURER, W THEOBALD, R SAUERBREY, AND I USCHMANN. **Onset of diffuse reflectivity and fast electron flux inhibition in 528-nm-laser–solid interactions at ultrahigh intensity.** *Physical Review E*, 1997. 157
- [189] M H KEY, K ESTABROOK, B HAMMEL, ET AL. **Hot electron production and heating by hot electrons in fast ignitor research.** 2008. 157
- [190] J FUCHS, T E COWAN, P AUDEBERT, H RUHL, L GREMILLET, A KEMP, M ALLEN, A BLAŽEVIĆ, J C GAUTHIER, M GEISSEL, M HEGELICH, S KARSCH, P PARKS, M ROTH, Y SENTOKU, R STEPHENS, AND E M CAMPBELL. **Spatial Uniformity of Laser-Accelerated Ultrahigh-Current MeV Electron Propagation in Metals and Insulators.** *Physical Review Letters*, **91**(25):255002, December 2003. 157
- [191] J FUCHS, P ANTICI, E D'HUMIÈRES, E LEFEBVRE, M BORGHESI, E BRAMBRINK, C A CECCHETTI, M KALUZA, V MALKA, M MANCLOSSI, S MEYRONEINC, P MORA, J SCHREIBER, T TONCIAN, H PÉPIN, AND P AUDEBERT. **Laser-driven proton scaling laws and new paths towards energy increase.** *Nature Physics*, **2**(1):48–54, December 2005. 157, 161, 165
- [192] D C CARROLL, O TRESCA, R PRASAD, L ROMAGNANI, P S FOSTER, P GALLEGOS, S TER-AVETISYAN, J S GREEN, M J V STREETER, N DOVER, C A J PALMER, C M BRENNER, F H CAMERON, K E QUINN, J SCHREIBER, A P L ROBINSON, T BAEVA, M N QUINN, X H YUAN, Z NAJMUDIN, M ZEPF, D NEELY, M BORGHESI, AND P MCKENNA. **Carbon ion acceleration from thin foil targets irradiated by ultrahigh-contrast, ultraintense laser pulses.** *New Journal of Physics*, **12**(4):045020, April 2010. 157, 162
- [193] T MORITA, T ZH ESIRKEPOV, S V BULANOV, J KOGA, AND M YAMAGIWA. **Tunable High-Energy Ion Source via Oblique Laser Pulse Incident on a Double-Layer Target.** *Physical Review Letters*, **100**(14):145001, April 2008. 157
- [194] XIAOMEI ZHANG, BAIFEI SHEN, XUEMEI LI, ZHANGYING JIN, AND FENGCHAO WANG. **Multistaged acceleration of ions by circularly polarized laser pulse: Monoenergetic ion beam generation.** *Physics of Plasmas*, **14**(7):073101, 2007. 160
- [195] XIAOMEI ZHANG, BAIFEI SHEN, XUEMEI LI, ZHANGYING JIN, FENGCHAO WANG, AND MENG WEN. **Efficient GeV ion generation by ultraintense circularly polarized laser pulse.** *Physics of Plasmas*, **14**(12):123108, 2007. 160
- [196] A HENIG, D KIEFER, M GEISLER, S RYKOVANOV, R RAMIS, R HÖRLEIN, J OSTERHOFF, ZS MAJOR, L VEISZ, S KARSCH, F KRAUSZ, D HABS, AND J SCHREIBER. **Laser-Driven Shock Acceleration of Ion Beams from Spherical Mass-Limited Targets.** *Physical Review Letters*, **102**(9):095002, March 2009. 160
- [197] M S WEI, S P D MANGLES, Z NAJMUDIN, B WALTON, A GOPAL, M TATARAKIS, A E DANGOR, E L CLARK, R G EVANS, S FRITZLER, R J CLARKE, C HERNANDEZ-GOMEZ, D NEELY, W MORI, M TZOUFRAS, AND K KRUSHELNICK. **Ion Acceleration by Collisionless Shocks in High-Intensity-Laser–Underdense-Plasma Interaction.** *Physical Review Letters*, **93**(15):155003, October 2004. 161
- [198] D NEELY, P FOSTER, A ROBINSON, F LINDAU, O LUNDH, A PERSSON, C G WAHLSTRÖM, AND P MCKENNA. **Enhanced proton beams from ultrathin targets driven by high contrast laser pulses.** *Applied Physics Letters*, **89**(2):021502, 2006. 161
- [199] K V SAFRONOV, D A VIKHLYAEV, A G VLADIMIROV, D S GAVRILOV, S A GOROKHOV, A G KAKSHIN, E A LOBODA, V A LYKOV, E S MOKICHEVA, A V POTAPOV, V A PRONIN, V N SAPRYKIN, P A TOLSTOUKHOV, O V CHEFONOV, AND M N CHIZHKOV. **Experimental study of the acceleration of protons emitted from thin foils irradiated by ultrahigh-contrast laser pulses.** *JETP Letters*, **88**(11):716–719, May 2009. 161
- [200] K V SAFRONOV, D A VIKHLYAEV, A G VLADIMIROV, D S GAVRILOV, S A GOROKHOV, A G KAKSHIN, E A LOBODA, V A LYKOV, E S MOKICHEVA, A V POTAPOV, V A PRONIN, V N SAPRYKIN, P A TOLSTOUKHOV, O V CHEFONOV, AND M N CHIZHKOV. **Proton acceleration from targets irradiated by ultraintense high-contrast laser pulses in the SOKOL-P facility.** *Plasma Physics Reports*, **36**(5):443–445, May 2010. 161
- [201] J S GREEN, D C CARROLL, C BRENNER, B DROMEY, P S FOSTER, S KAR, Y T LI, K MARKEY, P MCKENNA, D NEELY, A P L ROBINSON, M J V STREETER, M TOLLEY, C G WAHLSTRÖM, M H XU, AND M ZEPF. **Enhanced proton flux in the MeV range by defocused laser irradiation.** *New Journal of Physics*, **12**(8):085012, August 2010. 161

BIBLIOGRAPHY

- [202] I SPENCER, K W D LEDINGHAM, P MCKENNA, T MCCANNY, R P SINGHAL, P S FOSTER, D NEELY, A J LANGLEY, E J DIVALL, C J HOOKER, R J CLARKE, P A NORREYS, E L CLARK, K KRUSHELNICK, AND J R DAVIES. **Experimental study of proton emission from 60-fs, 200-mJ high-repetition-rate tabletop-laser pulses interacting with solid targets.** *Physical Review E*, **67**(4):046402, April 2003. 161
- [203] Y FUKUDA, A YA FAENOV, M TAMPO, T A PIKUZ, T NAKAMURA, M KANDO, Y HAYASHI, A YOGO, H SAKAKI, T KAMESHIMA, A S PIROZHKO, K OGURA, M MORI, T ZH ESIRKEPOV, J KOGA, A S BOLDAREV, V A GASILOV, A I MAGUNOV, T YAMAUCHI, R KODAMA, P R BOLTON, Y KATO, T TAJIMA, H DAIDO, AND S V BULANOV. **Energy Increase in Multi-MeV Ion Acceleration in the Interaction of a Short Pulse Laser with a Cluster-Gas Target.** *Physical Review Letters*, **103**(16):165002, October 2009. 161
- [204] SHIN-ICHIRO OKIHARA, MASATOSHI FUJIMOTO, HIRONORI TAKAHASHI, KOJI MATSUKADO, SHINJI OHSUKA, SHIN-ICHIRO AOSHIMA, SHIGETOSHI OKAZAKI, TOSHIKI ITO, AND YUTAKA TSUCHIYA. **Generation of over 5MeV carbon ions from a fibrous polytetrafluoroethylene film irradiated with a 2.4TW, 50fs tabletop laser.** *Applied Physics Letters*, **89**(12):121502, 2006. 161
- [205] T CECCOTTI, A LÉVY, H POPESCU, F RÉAU, P D'OLIVEIRA, P MONOT, J GEINDRE, E LEFEBVRE, AND PH MARTIN. **Proton Acceleration with High-Intensity Ultrahigh-Contrast Laser Pulses.** *Physical Review Letters*, **99**(18):185002, October 2007. 162
- [206] AKIFUMI YOGO, HIROYUKI DAIDO, ATSUSHI FUKUMI, ZHONG LI, KOICHI OGURA, AKITO SAGISAKA, ALEXANDER S PIROZHKO, SHU NAKAMURA, YOSHIHISA IWASHITA, TOSHIYUKI SHIRAI, AKIRA NODA, YUJI OISHI, TAKUYA NAYUKI, TAKASHI FUJII, KOSHICHI NEMOTO, IL WOO CHOI, JAE HEE SUNG, DO-KYEONG KO, JONGMIN LEE, MINORU KANEDA, AND AKIO ITOH. **Laser prepulse dependency of proton-energy distributions in ultraintense laser-foil interactions with an online time-of-flight technique.** *Physics of Plasmas*, **14**(4):043104, 2007. 162, 167
- [207] M NISHIUCHI, H DAIDO, A YOGO, S ORIMO, K OGURA, J MA, A SAGISAKA, M MORI, A S PIROZHKO, H KIRIYAMA, S V BULANOV, T ZH ESIRKEPOV, I W CHOI, C M KIM, T M JEONG, T J YU, J H SUNG, S K LEE, N HAFZ, K H PAE, Y C NOH, D K KO, J LEE, Y OISHI, K NEMOTO, H NAGATOMO, K NAGAI, AND H AZUMA. **Efficient production of a collimated MeV proton beam from a polyimide target driven by an intense femtosecond laser pulse.** *Physics of Plasmas*, **15**(5):053104, 2008. 162
- [208] K ZEIL, S D KRAFT, S BOCK, M BUSSMANN, T E COWAN, T KLUGE, J METZKES, T RICHTER, R SAUERBREY, AND U SCHRAMM. **The scaling of proton energies in ultrashort pulse laser plasma acceleration.** *New Journal of Physics*, **12**(4):045015, April 2010. 162
- [209] M NISHIUCHI, H SAKAKI, S MAEDA, A SAGISAKA, A S PIROZHKO, T PIKUZ, A FAENOV, K OGURA, M KANASAKI, K MATSUKAWA, T KUSUMOTO, A TAO, T FUKAMI, T ESIRKEPOV, J KOGA, H KIRIYAMA, H OKADA, T SHIMOMURA, M TANOUÉ, Y NAKAI, Y FUKUDA, S SAKAI, J TAMURA, K NISHIO, H SAKO, M KANDO, T YAMAUCHI, Y WATANABE, S V BULANOV, AND K KONDO. **Multi-charged heavy ion acceleration from the ultra-intense short pulse laser system interacting with the metal target.** *Review of Scientific Instruments*, **85**(2):02B904, February 2014. 162
- [210] P PATEL, A MACKINNON, M KEY, T COWAN, M FOORD, M ALLEN, D PRICE, H RUHL, P SPRINGER, AND R STEPHENS. **Isochoric Heating of Solid-Density Matter with an Ultrafast Proton Beam.** *Physical Review Letters*, **91**(12):125004, September 2003. 162
- [211] R PRASAD, A A ANDREEV, S TER-AVETISYAN, D DORIA, K E QUINN, L ROMAGNANI, C M BRENNER, D C CARROLL, N P DOVER, D NEELY, P S FOSTER, P GALLEGOS, J S GREEN, P MCKENNA, Z NAJMUDIN, C A J PALMER, J SCHREIBER, M J V STREETER, O TRESKA, M ZEPF, AND M BORGHESI. **Fast ion acceleration from thin foils irradiated by ultra-high intensity, ultra-high contrast laser pulses.** *Applied Physics Letters*, **99**(12):121504, 2011. 162
- [212] KOICHI OGURA, MAMIKO NISHIUCHI, ALEXANDER S PIROZHKO, TSUYOSHI TANIMOTO, AKITO SAGISAKA, TIMUR ZH ESIRKEPOV, MASAKI KANDO, TOSHIYUKI SHIZUMA, TAKEHITO HAYAKAWA, AND HIROMITSU KIRIYAMA. **Proton acceleration to 40 MeV using a high intensity, high contrast optical parametric chirped-pulse amplification/Ti:sapphire hybrid laser system.** *Optics Letters*, **37**(14):2868–2870, 2012. 162
- [213] I JONG KIM, KI-HONG PAE, CHUL MIN KIM, HYUNG TAEK KIM, JAE HEE SUNG, SEONG KU LEE, TAE JUN YU, IL WOO CHOI, CHANG-LYOUL LEE, KEE HWAN NAM, PETER V NICKLES, TAE MOON JEONG, AND JONGMIN LEE. **Transition of Proton Energy Scaling Using an Ultrathin Target Irradiated by Linearly Polarized Femtosecond Laser Pulses.** *Physical Review Letters*, **111**(16):165003, October 2013. 162
- [214] J S GREEN, A P L ROBINSON, N BOOTH, D C CARROLL, R J DANCE, R J GRAY, D A MACLELLAN, P MCKENNA, C D MURPHY, D RUSBY, AND L WILSON. **High efficiency proton beam generation through target thickness control in femtosecond laser-plasma interactions.** *Applied Physics Letters*, **104**(21):214101, May 2014. 162
- [215] J H BIN, W J MA, H Y WANG, M J V STREETER, C KREUZER, D KIEFER, M YEUNG, S COUSENS, P S FOSTER, B DROMEY, X Q YAN, R RAMIS, J MEYER-TER VEHN, M ZEPF, AND J SCHREIBER. **Ion Acceleration Using Relativistic Pulse Shaping in Near-Critical-Density Plasmas.** *Physical Review Letters*, **115**(6):064801, August 2015. 162
- [216] O LUNDH, F LINDAU, A PERSSON, C G WAHLSTRÖM, P MCKENNA, AND D BATANI. **Influence of shock waves on laser-driven proton acceleration.** *Physical Review E*, **76**(2):026404, August 2007. 164
- [217] Y SENTOKU, T E COWAN, A KEMP, AND H RUHL. **High energy proton acceleration in interaction of short laser pulse with dense plasma target.** *Physics of Plasmas*, **10**(5):2009, 2003. 165
- [218] P ANTICI, J FUCHS, E D'HUMIÈRES, E LEFEBVRE, M BORGHESI, E BRAMBRINK, C A CECCHETTI, S GAILLARD, L ROMAGNANI, Y SENTOKU, T TONCIAN, O WILLI, P AUDEBERT, AND H PÉPIN. **Energetic protons generated by ultra-high contrast laser pulses interacting with ultrathin targets.** *Physics of Plasmas*, **14**(3):030701, 2007. 165, 172

- [219] P ANTICI, J FUCHS, E D'HUMIÈRES, J ROBICHE, E BRAMBINK, S ATZENI, A SCHIAVI, Y SENTOKU, P AUDEBERT, AND H PÉPIN. **Laser acceleration of high-energy protons in variable density plasmas.** *New Journal of Physics*, **11**(2):023038, February 2009. 165, 172
- [220] S TER-AVETISYAN, M SCHNÜRER, P V NICKLES, M KALASHNIKOV, E RISSE, T SOKOLLIK, W SANDNER, A ANDREEV, AND V TIKHONCHUK. **Quasimonoenergetic Deuteron Bursts Produced by Ultraintense Laser Pulses.** *Physical Review Letters*, **96**(14):145006, April 2006. 165
- [221] C STRANGIO, A CARUSO, D NEELY, P L ANDREOLI, R ANZALONE, G CRISTOFARI, E DEL PRETE, G DI GIORGIO, C MURPHY, C RICCI, R STEVENS, M TOLLEY, AND R CLARKE. **Production of multi-MeV per nucleon ions in the controlled amount of matter mode (CAM) by using causally isolated targets.** 2007. 165
- [222] K A FLIPPO, E D'HUMIÈRES, S A GAILLARD, J RASSUCHINE, D C GAUTIER, M SCHOLLMEIER, F NÜRNBERG, J L KLINE, J ADAMS, B ALBRIGHT, M BAKEMAN, K HARRES, R P JOHNSON, G KORCAN, S LETZRING, S MALEKOS, N RENARD-LEGALLOUDEC, Y SENTOKU, T SHIMADA, M ROTH, T E COWAN, J C FERNÁNDEZ, AND B M HEGELICH. **Increased efficiency of short-pulse laser-generated proton beams from novel flat-top cone targets.** *Physics of Plasmas*, **15**(5):056709, 2008. 165
- [223] A S PIROZHKOV, I W CHOI, J H SUNG, S K LEE, T J YU, T M JEONG, I J KIM, N HAFZ, C M KIM, K H PAE, Y C NOH, D K KO, J LEE, A P L ROBINSON, P FOSTER, S HAWKES, M STREETER, C SPINDLOE, P MCKENNA, D C CARROLL, C G WAHLSTRÖM, M ZEPF, D ADAMS, B DROMEY, K MARKEY, S KAR, Y T LI, M H XU, H NAGATOMO, M MORI, A YOGO, H KIRIYAMA, K OGURA, A SAGISAKA, S ORIMO, M NISHIUCHI, H SUGIYAMA, T ZH ESIRKEPOV, H OKADA, S KONDO, S KANAZAWA, Y NAKAI, A AKUTSU, T MOTOMURA, M TANOUÉ, T SHIMOMURA, M Ikegami, I DAITO, M KANDO, T KAMESHIMA, P BOLTON, S V BULANOV, H DAIDO, AND D NEELY. **Diagnostic of laser contrast using target reflectivity.** *Applied Physics Letters*, **94**(24):241102, 2009. 166
- [224] S PALANIYAPPAN, R C SHAH, R JOHNSON, T SHIMADA, D C GAUTIER, S LETZRING, D JUNG, R HÖRLEIN, D T OFFERMANN, J C FERNÁNDEZ, AND B M HEGELICH. **Pulse shape measurements using single shot-frequency resolved optical gating for high energy (80 J) short pulse (600 fs) laser.** *Review of Scientific Instruments*, **81**(10):10E103, 2010. 166
- [225] U TEUBNER, K EIDMANN, U WAGNER, U ANDIEL, F PISANI, G D TSAKIRIS, K WITTE, J MEYER-TER VEHN, T SCHLEGEL, AND E FÖRSTER. **Harmonic Emission from the Rear Side of Thin Overdense Foils Irradiated with Intense Ultrashort Laser Pulses.** *Physical Review Letters*, **92**(18):185001, May 2004. 166
- [226] I W CHOI, I J KIM, K H PAE, K H NAM, C L LEE, H YUN, H T KIM, S K LEE, T J YU, J H SUNG, A S PIROZHKOV, K OGURA, S ORIMO, H DAIDO, AND J LEE. **Simultaneous generation of ions and high-order harmonics from thin conjugated polymer foil irradiated with ultrahigh contrast laser.** *Applied Physics Letters*, **99**(18):181501, 2011. 166
- [227] M J V STREETER, P S FOSTER, F H CAMERON, M BORGHESE, C BRENNER, D C CARROLL, E DIVALL, N P DOVER, B DROMEY, P GALLEGOS, J S GREEN, S HAWKES, C J HOOKER, S KAR, P MCKENNA, S R NAGEL, Z NAJMUDIN, C A J PALMER, R PRASAD, K E QUINN, P P RAJEEV, A P L ROBINSON, L ROMAGNANI, J SCHREIBER, C SPINDLOE, S TER-AVETISYAN, O TRESKA, M ZEPF, AND D NEELY. **Relativistic plasma surfaces as an efficient second harmonic generator.** *New Journal of Physics*, **13**(2):023041, February 2011. 166
- [228] Z LI, H DAIDO, A FUKUMI, A SAGISAKA, K OGURA, M NISHIUCHI, S ORIMO, Y HAYASHI, M MORI, M KADO, S V BULANOV, T ZH ESIRKEPOV, Y OISHI, T NAYUKI, T FUJII, K NEMOTO, S NAKAMURA, AND A NODA. **Measurements of energy and angular distribution of hot electrons and protons emitted from a p- and s-polarized intense femtosecond laser pulse driven thin foil target.** *Physics of Plasmas*, **13**(4):043104, 2006. 166, 167
- [229] M MANCLOSSI, J J SANTOS, D BATANI, J FAURE, A DEBAYLE, V T TIKHONCHUK, AND V MALKA. **Study of Ultraintense Laser-Produced Fast-Electron Propagation and Filamentation in Insulator and Metal Foil Targets by Optical Emission Diagnostics.** *Physical Review Letters*, **96**(12):125002, March 2006. 166, 167
- [230] J J SANTOS, A DEBAYLE, PH NICOLAI, V TIKHONCHUK, M MANCLOSSI, D BATANI, A GUENNIE-TAFO, J FAURE, V MALKA, AND J J HONRUBIA. **Fast-electron transport and induced heating in aluminum foils.** *Physics of Plasmas*, **14**(10):103107, 2007. 166, 167
- [231] D KIEFER, A HENIG, D JUNG, D C GAUTIER, K A FLIPPO, S A GAILLARD, S LETZRING, R P JOHNSON, R C SHAH, T SHIMADA, J C FERNÁNDEZ, V KH LIECHTENSTEIN, J SCHREIBER, B M HEGELICH, AND D HABS. **First observation of quasimonoenergetic electron bunches driven out of ultra-thin diamond-like carbon (DLC) foils.** *The European Physical Journal D*, **55**(2):427–432, July 2009. 166
- [232] C BELLEI, S R NAGEL, S KAR, A HENIG, S KNEIP, C PALMER, A SÄVERT, L WILLINGALE, D CARROLL, B DROMEY, J S GREEN, K MARKEY, P SIMPSON, R J CLARKE, H LOWE, D NEELY, C SPINDLOE, M TOLLEY, M C KALUZA, S P D MANGLES, P MCKENNA, P A NORREYS, J SCHREIBER, M ZEPF, J R DAVIES, K KRUSHELNICK, AND Z NAJMUDIN. **Micron-scale fast electron filaments and recirculation determined from rear-side optical emission in high-intensity laser–solid interactions.** *New Journal of Physics*, **12**(7):073016, July 2010. 166, 167
- [233] D R SYMES, U WEGNER, H C AHLSEWED, M J V STREETER, P L GALLEGOS, E J DIVALL, R A SMITH, P P RAJEEV, AND D NEELY. **Ultrafast gated imaging of laser produced plasmas using the optical Kerr effect.** *Applied Physics Letters*, **96**(1):011109, 2010. 166
- [234] A SAGISAKA, A S PIROZHKOV, H DAIDO, A FUKUMI, Z LI, K OGURA, A YOGO, Y OISHI, T NAYUKI, T FUJII, K NEMOTO, S ORIMO, M NISHIUCHI, Y HAYASHI, M MORI, M KADO, S NAKAMURA, A NODA, I W CHOI, J H SUNG, D K KO, AND J LEE. **Development of a two-color interferometer for observing wide range electron density profiles with a femtosecond time resolution.** *Applied Physics B*, **84**(3):415–419, June 2006. 166
- [235] S A GAILLARD, K A FLIPPO, M E LOWENSTERN, J E MUCINO, J M RASSUCHINE, D C GAUTIER, J WORKMAN, AND T E COWAN. **Proton acceleration from ultrahigh-intensity short-pulse laser-matter interactions with Cu micro-cone targets at an intrinsic 10 8contrast.** *Journal of Physics: Conference Series*, **244**(2):022034, September 2010. 166

BIBLIOGRAPHY

- [236] E C H SILK AND R S BARNES. **Examination of fission fragment tracks with an electron microscope.** *Philosophical Magazine*, **4**(44):970–972, August 1959. 166
- [237] W L McLAUGHLIN, C YUN-DONG, C G SOARES, A MILLER, G VAN DYK, AND D F LEWIS. **Sensitometry of the response of a new radiochromic film dosimeter to gamma radiation and electron beams.** *Nuclear Instruments and Methods in Physics Research Section A: Accelerators, Spectrometers, Detectors and Associated Equipment*, **302**:1–12, June 1991. 166
- [238] S M VATNITSKY, RWM SCHULTE, AND R GALINDO. **Radiochromic film dosimetry for verification of dose distributions delivered with proton-beam radio-surgery.** *Physics in medicine . . .*, 1997. 166
- [239] AZAM NIROOMAND-RAD, CHARLES ROBERT BLACKWELL, BERT M COURSEY, KENNETH P GALL, JAMES M GALVIN, WILLIAM L McLAUGHLIN, ALI S MEIGOONI, RAVINDER NATH, JAMES E RODGERS, AND CHRISTOPHER G SOARES. **Radiochromic film dosimetry: Recommendations of AAPM Radiation Therapy Committee Task Group 55.** *Medical physics*, **25**(11):2093–2115, November 1998. 166
- [240] S P HATCHETT, C G BROWN, T E COWAN, E A HENRY, J JOHNSON, M H KEY, J A KOCH, A B LANGDON, B F LASINSKI, R W LEE, A J MACKINNON, D M PENNINGTON, M D PERRY, T W PHILLIPS, M ROTH, T C SANGSTER, M S SINGH, R A SNAVELY, M A STOVER, S C WILKS, AND K YASUIKE. **Electron, photon, and ion beams from the relativistic interaction of Petawatt laser pulses with solid targets.** *Physics of Plasmas (1994-present)*, **7**(5):2076–2082, 2000. 166
- [241] M I K SANTALA, M ZEPF, F N BEG, E L CLARK, A E DANGOR, K KRUSHELNICK, M TATARAKIS, I WATTS, K W D LEDINGHAM, T MCCANNY, I SPENCER, A C MACHACEK, R ALLOTT, R J CLARKE, AND P A NORREYS. **Production of radioactive nuclides by energetic protons generated from intense laser-plasma interactions.** *Applied Physics Letters*, **78**(1):19, 2001. 166
- [242] R J CLARKE, P T SIMPSON, S KAR, J S GREEN, C BELLEI, D C CARROLL, B DROMEY, S KNEIP, K MARKEY, P MCKENNA, W MURPHY, S NAGEL, L WILLINGALE, AND M ZEPF. **Nuclear activation as a high dynamic range diagnostic of laser-plasma interactions.** *Nuclear Instruments and Methods in Physics Research Section A: Accelerators, Spectrometers, Detectors and Associated Equipment*, **585**(3):117–120, February 2008. 166
- [243] D T OFFERMANN, K A FLIPPO, S A GAILLARD, D C GAUTIER, S LETZRING, J C COBBLE, G WURDEN, R P JOHNSON, T SHIMADA, D S MONTGOMERY, R P GONZALES, T HURRY, F ARCHULETA, M J SCHMITT, S-M REID, T BARTAL, M S WEI, D P HIGGINSON, F N BEG, M GEISSEL, AND M SCHOLLMEIER. **Carbon ion beam focusing using laser irradiated, heated diamond hemispherical shells.** *Journal of Physics: Conference Series*, **244**(2):022053, September 2010. 166
- [244] D T OFFERMANN, K A FLIPPO, J COBBLE, M J SCHMITT, S A GAILLARD, T BARTAL, D V ROSE, D R WELCH, M GEISSEL, AND M SCHOLLMEIER. **Characterization and focusing of light ion beams generated by ultra-intensely irradiated thin foils at the kilojoule scale.** *Physics of Plasmas*, **18**(5):056713, 2011. 166
- [245] A P L ROBINSON, D NEELY, P MCKENNA, AND R G EVANS. **Spectral control in proton acceleration with multiple laser pulses.** *Plasma Physics and Controlled Fusion*, **49**(4):373–384, February 2007. 166
- [246] W MROZ, P NOREK, A PROKOPIUK, P PARYS, M PFEIFER, L LASKA, M STOECKLI, D FRY, AND K KASUYA. **Method of processing ion energy distributions using a Thomson parabola ion spectrograph with a microchannelplate image converter camera.** *Review of Scientific Instruments*, **71**(3):1–5, March 2000. 166, 167
- [247] SARGIS TER-AVETISYAN, MATHIAS SCHNÜRER, AND PETER V NICKLES. **Time resolved corpuscular diagnostics of plasmas produced with high-intensity femtosecond laser pulses.** *Journal of Physics D: Applied Physics*, **38**(6):863–867, March 2005. 166
- [248] K HARRES, M SCHOLLMEIER, E BRAMBRINK, P AUDEBERT, A BLAŽEVIĆ, K FLIPPO, D C GAUTIER, M GEISSEL, B M HEGELICH, F NÜRNBERG, J SCHREIBER, H WAHL, AND M ROTH. **Development and calibration of a Thomson parabola with microchannel plate for the detection of laser-accelerated MeV ions.** *Review of Scientific Instruments*, **79**(9):093306, 2008. 166, 167
- [249] R PRASAD, D DORIA, S TER-AVETISYAN, P S FOSTER, K E QUINN, L ROMAGNANI, C M BRENNER, J S GREEN, P GALLEGOS, M J V STREETER, D C CARROLL, O TRESCA, N DOVER, C A J PALMER, J SCHREIBER, D NEELY, Z NAJMUDIN, P MCKENNA, M ZEPF, AND M BORGHESI. **Nuclear Instruments and Methods in Physics Research A.** *Nuclear Inst. and Methods in Physics Research, A*, **623**(2):712–715, November 2010. 166
- [250] J S GREEN. **Multi-channel system for imaging laser accelerated proton beams.** *Central Laser Facility Annual Report*, pages 1–4, December 2009. 167
- [251] J J THOMPSON. **Rays of Positive Electricity and Their Application to Chemical Analysis**, October 1991. 167
- [252] J N OLSEN. **Ion-expansion energy spectra correlated to laser plasma parameters.** *Journal of Applied Physics*, **44**(5):2275, 1973. 167
- [253] Y AMEMIYA AND J MIYAHARA. **Imaging plate illuminates many fields.** 1988. 167
- [254] MICHIAKI MORI, MASAKI KANDO, ALEXANDER S PIROZHKOV, YUKIO HAYASHI, AKIFUMI YOGO, NORIHISA YOSHIMURA, KOICHI OGURA, MAMIKO NISHIUCHI, AKITO SAGISAKA, SATOSHI ORIMO, MASATAKA KADO, ATSUSHI FUKUMI, ZHONG LI, SHU NAKAMURA, AKIRA NODA, AND HIROYUKI DAIDO. **New Detection Device for Thomson Parabola Spectrometer for Diagnosis of the Laser-Plasma Ion Beam.** *Plasma and Fusion Research*, **1**:042–042, 2006. 167
- [255] SHU NAKAMURA, YOSHIHISA IWASHITA, AKIRA NODA, TOSHIYUKI SHIRAI, HIROMU TONGU, ATSUSHI FUKUMI, MASATAKA KADO, AKIFUMI YOGO, MICHIAKI MORI, SATOSHI ORIMO, KOICHI OGURA, AKITO SAGISAKA, MAMIKO NISHIUCHI, YUKIO HAYASHI, ZHONG LI, HIROYUKI DAIDO, AND YOSHIO WADA. **Real-Time Optimization of Proton Production by Intense Short-Pulse Laser with Time-of-Flight Measurement.** *Japanese Journal of Applied Physics*, **45**(No. 34):L913–L916, August 2006. 167

- [256] T E GLOVER, T D DONNELLY, E A LIPMAN, A SULLIVAN, AND R W FALCONE. **Subpicosecond Thomson Scattering Measurements of Optically Ionized Helium Plasmas.** *Physical Review Letters*, **73**:1–4, July 1994. 167
- [257] S H GLENZER, W E ALLEY, AND K G ESTABROOK. **Thomson scattering from laser plasmas.** *Physics of Plasmas*, 1999. 167
- [258] P TOMASSINI, M GALIMBERTI, A GIULIETTI, D GIULIETTI, L A GIZZI, AND L LABATE. **Spectroscopy of laser-plasma accelerated electrons: A novel concept based on Thomson scattering.** *Physics of Plasmas*, **10**(4):917, 2003. 167
- [259] C D CHEN, J A KING, M H KEY, K U AKLI, F N BEG, H CHEN, R R FREEMAN, A LINK, A J MACKINNON, A G MACPHEE, P K PATEL, M PORKOLAB, R B STEPHENS, AND L D VAN WOERKOM. **A Bremsstrahlung spectrometer using k-edge and differential filters with image plate dosimeters.** *Review of Scientific Instruments*, **79**(10):10E305, 2008. 167
- [260] A G MACPHEE, K U AKLI, F N BEG, C D CHEN, H CHEN, R CLARKE, D S HEY, R R FREEMAN, A J KEMP, M H KEY, J A KING, S LE PAPE, A LINK, T Y MA, H NAKAMURA, D T OFFERMANN, V M OVCHINNIKOV, P K PATEL, T W PHILLIPS, R B STEPHENS, R TOWN, Y Y TSUI, M S WEI, L D VAN WOERKOM, AND A J MACKINNON. **Diagnostics for fast ignition science (invited).** *Review of Scientific Instruments*, **79**(10):10F302, 2008. 167
- [261] S TER-AVETISYAN, M SCHNÜRER, T SOKOLLIK, P V NICKLES, W SANDNER, H R REISS, J STEIN, D HABS, T NAKAMURA, AND K MIMA. **Proton acceleration in the electrostatic sheaths of hot electrons governed by strongly relativistic laser-absorption processes.** *Physical Review E*, **77**(1):016403, January 2008. 167
- [262] P ANTICI, J FUCHS, M BORGHESI, L GREMILLET, T GRISMAYER, Y SENTOKU, E D'HUMIÈRES, C A CECCHETTI, A MANCIC, A C PIPAHLE, T TONCIAN, O WILLI, P MORA, AND P AUDEBERT. **Hot and Cold Electron Dynamics Following High-Intensity Laser Matter Interaction.** *Physical Review Letters*, **101**(10):105004, September 2008. 167
- [263] HUI CHEN, ANTHONY J LINK, ROGER VAN MAREN, PRAVESH K PATEL, RONNIE SHEPHERD, SCOTT C WILKS, AND PETER BEIERSDORFER. **High performance compact magnetic spectrometers for energetic ion and electron measurement in ultraintense short pulse laser solid interactions.** *Review of Scientific Instruments*, **79**(10):10E533, 2008. 167
- [264] HUI CHEN, NORMAN L BACK, TERESA BARTAL, F N BEG, DAVID C EDER, ANTHONY J LINK, ANDREW G MACPHEE, YUAN PING, PETER M SONG, ALAN THROOP, AND LINN VAN WOERKOM. **Absolute calibration of image plates for electrons at energy between 100keV and 4MeV.** *Review of Scientific Instruments*, **79**(3):033301, 2008. 167
- [265] M PASSONI, A ZANI, A SGATTONI, D DELLASEGA, A MACCHI, I PRENCIPE, V FLOQUET, P MARTIN, T V LISEYKINA, AND T CECCOTTI. **Energetic ions at moderate laser intensities using foam-based multi-layered targets.** *Plasma Physics and Controlled Fusion*, **56**(4):045001, March 2014. 167
- [266] G G SCOTT, V BAGNOUD, C BRABETZ, R J CLARKE, J S GREEN, R I HEATHCOTE, H W POWELL, B ZIELBAUER, T D ARBER, P MCKENNA, AND D NEELY. **Optimization of plasma mirror reflectivity and optical quality using double laser pulses.** *New Journal of Physics*, **17**(3):1–10, March 2015. 172
- [267] T ESIRKEPOV, R BINGHAM, S BULANOV, T HONDA, K NISHIHARA, AND F PEGORARO. **Coulomb explosion of a cluster irradiated by a high intensity laser pulse.** *Laser and Particle Beams*, **18**:503–506, February 2000. 172
- [268] SHU NAKAMURA, MASAHIRO IKEGAMI, YOSHIHISA IWASHITA, TOSHIYUKI SHIRAI, HIROMU TONGU, HIKARU SOUDA, HIROYUKI DAIDO, MICHIAKI MORI, MASATAKA KADO, AKITO SAGISAKA, KOICHI OGURA, MAMIKO NISHIUCHI, SATOSHI ORIMO, YUKIO HAYASHI, AKIFUMI YOGO, ALEXANDER S PIROZHKOV, SERGEI V BULANOV, TIMUR ESIRKEPOV, AKIRA NAGASHIMA, TOYOAKI KIMURA, TOSHIKI TAJIMA, TAKESHI TAKEUCHI, ATSUSHI FUKUMI, ZHONG LI, AND AKIRA NODA. **High-Quality Laser-Produced Proton Beam Realized by the Application of a Synchronous RF Electric Field.** *Japanese Journal of Applied Physics*, **46**(No. 29):L717–L720, July 2007. 172
- [269] T TONCIAN. **Ultrafast Laser-Driven Microlens to Focus and Energy-Select Mega-Electron Volt Protons.** *Science*, **312**(5772):410–413, April 2006. 172
- [270] M SCHOLLMEIER, S BECKER, M GEISSEL, K FLIPPO, A BLAŽEVIĆ, S GAILLARD, D GAUTIER, F GRÜNER, K HARES, M KIMMEL, F NÜRNBERG, P RAMBO, U SCHRAMM, J SCHREIBER, J SCHÜTRUMPF, J SCHWARZ, N TAHIR, B ATHERTON, D HABS, B HEGELICH, AND M ROTH. **Controlled Transport and Focusing of Laser-Accelerated Protons with Miniature Magnetic Devices.** *Physical Review Letters*, **101**(5):055004, August 2008. 172
- [271] S TER-AVETISYAN, M SCHNÜRER, R POLSTER, P V NICKLES, AND W SANDNER. **First demonstration of collimation and monochromatisation of a laser accelerated proton burst.** *Laser and Particle Beams*, **26**(04):637, November 2008. 172
- [272] M NISHIUCHI, I DAITO, M IKEGAMI, H DAIDO, M MORI, S ORIMO, K OGURA, A SAGISAKA, A YOGO, A S PIROZHKOV, H SUGIYAMA, H KIRIYAMA, H OKADA, S KANAZAWA, S KONDO, T SHIMOMURA, M TANOUÉ, Y NAKAI, H SASAO, D WAKAI, H SAKAKI, P BOLTON, I W CHOI, J H SUNG, J LEE, Y OISHI, T FUJII, K NEMOTO, H SOUDA, A NODA, Y ISEKI, AND T YOSHIYUKI. **Focusing and spectral enhancement of a repetition-rated, laser-driven, divergent multi-MeV proton beam using permanent quadrupole magnets.** *Applied Physics Letters*, **94**(6):061107, 2009. 172
- [273] M NISHIUCHI, H SAKAKI, T HORI, P R BOLTON, K OGURA, A SAGISAKA, A YOGO, M MORI, S ORIMO, A S PIROZHKOV, I DAITO, H KIRIYAMA, H OKADA, S KANAZAWA, S KONDO, T SHIMOMURA, M TANOUÉ, Y NAKAI, H SASAO, D WAKAI, H DAIDO, K KONDO, H SOUDA, H TONGU, A NODA, Y ISEKI, T NAGAFUCHI, K MAEDA, K HANAWA, T YOSHIYUKI, AND T SHIRAI. **Measured and simulated transport of 1.9 MeV laser-accelerated proton bunches through an integrated test beam line at 1 Hz.** *Physical Review Special Topics - Accelerators and Beams*, **13**(7):071304, July 2010. 172

BIBLIOGRAPHY

- [274] K MATSUKADO, T ESIRKEPOV, K KINOSHITA, H DAIDO, T UTSUMI, Z LI, A FUKUMI, Y HAYASHI, S ORIMO, M NISHIUCHI, S V BULANOV, T TAJIMA, A NODA, Y IWASHITA, T SHIRAI, T TAKEUCHI, S NAKAMURA, A YAMAZAKI, M IKEGAMI, T MIHARA, A MORITA, M UESAKA, K YOSHII, T WATANABE, T HOSOKAI, A ZHIDKOV, A OGATA, Y WADA, AND T KUBOTA. **Energetic Protons from a Few-Micron Metallic Foil Evaporated by an Intense Laser Pulse.** *Physical Review Letters*, **91**(21):215001, November 2003. 172
- [275] MALAY DALUI, W M WANG, T MADHU TRIVIKRAM, SUBHRANGSHU SARKAR, SHEROY TATA, J JHA, P AYYUB, Z M SHENG, AND M KRISHNAMURTHY. **Preferential enhancement of laser-driven carbon ion acceleration from optimized nanostructured surfaces.** *Scientific Reports*, pages 1–11, July 2015. 173
- [276] HIDEO NAGATOMO, TOMOYUKI JOHZAKI, KUNIOKI MIMA, AND HITOSHI SAKAGAMI. **Multi-scale Simulations for Laser Plasma Physics.** pages 243–250. Springer Berlin Heidelberg, Berlin, Heidelberg, October 2009. 173
- [277] S M PFOTENHAUER, O JÄCKEL, J POLZ, S STEINKE, H-P SCHLENVOIGT, J HEYMANN, A P L ROBINSON, AND M C KALUZA. **A cascaded laser acceleration scheme for the generation of spectrally controlled proton beams.** *New Journal of Physics*, **12**(10):103009, October 2010. 173
- [278] H Y WANG, C LIN, B LIU, Z M SHENG, H Y LU, W J MA, J H BIN, J SCHREIBER, X T HE, J E CHEN, M ZEPF, AND X Q YAN. **Laser-driven three-stage heavy-ion acceleration from relativistic laser-plasma interaction.** *Physical Review E*, **89**(1):013107, January 2014. 173
- [279] KYUNG NAM KIM, KITAE LEE, SEONG HEE PARK, JI YOUNG LEE, YOUNG UK JEONG, NIKOLAY VINOKUROV, AND YONG GI KIM. **Generation of a quasi-monoenergetic high energy proton beam from a vacuum-sandwiched double layer target irradiated by an ultraintense laser pulse.** *Physics of Plasmas*, **21**(4):043110, April 2014. 173